Molecular characterisation of the placental-pancreatic islet axis

Faheem Seedat

St Edmund's Hall

&

Nuffield Department of Women's & Reproductive Health

University of Oxford

Supervised by: Prof. Manu Vatish, Prof. John Todd, Prof. Alisha N Wade, Dr Maria I Stefana, and Dr Neva Kandzija

A thesis submitted for the degree of Doctor of Philosophy

Hilary Term, 2025

47,921 words

Declaration

This thesis is submitted to the University of Oxford, in partial fulfilment of the requirements for the degree of Doctor of Philosophy.

This thesis is entirely my own work, and except where otherwise stated, describes my own research.

Acknowledgements

The DPhil journey is not one that can be undertaken alone. Bringing it to fruition is deeply dependent on the support of supervisors, colleagues, friends, and family. My experience was no different, and I am profoundly grateful to the many individuals who enriched, contributed to, and supported my journey.

To Professor Manu Vatish, I could not have asked for a better supervisor. Thank you for always being available and for going above and beyond to support both my academic journey and my personal trials and tribulations over these past few years. Your willingness to offer advice and support, no matter how trivial or serious the matter, has been invaluable. The greatest compliment I can give is that every conversation we have had over these years has left me feeling positive, motivated, and reassured that I can achieve the goals I set for myself. To Professor John Todd, thank you for welcoming me into the DIL group and for fostering an environment where my work could grow and develop. Your continual guidance and input throughout my project have been truly instrumental. I am especially grateful for your openness and readiness to support my work at every stage. To Dr Irina Stefana, thank you for taking me under your wing when I had very little scientific knowledge! I am deeply grateful for the guidance and training you provided throughout my DPhil, especially at the outset, when the transition to laboratory science felt so daunting. I also greatly appreciate your encouragement and support in pushing the boundaries of my project, allowing me the freedom to explore and expand it as far as my scientific curiosity took me. I will miss our debates about experimental design, and the lessons you taught me about appropriate controls will stay with me for years to come. To Dr Neva Kandzija, thank you for always being a sounding board for new ideas and for providing astute guidance on what to pursue and what to set aside. Your positivity and persistent encouragement, even when things were

challenging, made a significant difference in keeping me motivated. I will always remember our first experiment together—labelling extracellular vesicles with PKH26 and filtering them—which marked the beginning of my hands-on laboratory journey. It has been truly wonderful to work on projects together, and I am deeply grateful for your support throughout. To Professor Alisha Wade, thank you for setting this entire journey in motion by introducing me to the key mentors who helped start my DPhil journey—it was serendipitous in many ways. I am deeply grateful for your input, guidance, and support throughout. Thank you for your invaluable contributions and for being part of this journey.

To all the members of Team Manu, a heartfelt thank you. To Dr Wei Zhang, thank you for always being available whenever I needed scientific advice or extra support. To Catarina Palma dos Reis and Emily Hyde, it was a pleasure sharing this journey with you both as fellow students in the same year—going through the ups and downs together made the experience all the more memorable. A special thanks to Shuhan Jiang, Maryam Rahbar, and Prassana Logenthiran, who played an instrumental role in teaching me placental perfusion and other laboratory techniques—I am deeply grateful for the time and effort you dedicated to providing this training and guidance. To Emily Mazey, I truly appreciate your help in the lab with protocols and samples, which you provided so generously without expecting anything in return. To Gabriel Jones and Will Cooke, thank you for always being available to offer advice and guidance. To Bryony Davies, Michelle Ma, Morganne Wilbourne, Angga Lokeswara, Asselzhan Sarbalina, and Sarah Hutchinson, it has been wonderful meeting, collaborating, and working alongside you all. Your support and camaraderie have made this journey all the more enjoyable.

To the DIL group, thank you for welcoming me so warmly into the team. To Michael Ellis, I am truly grateful for all your help when I first joined. Your patience and willingness to train me in nearly every laboratory technique played an immense role in allowing my project to move forward. I now look back and smile at how we would complain that the EndoCs just 'don't grow fast enough.' I also deeply appreciate your calm and collected nature, even when I was convinced the experiments weren't going well—it always made a difference. To Katie Holden, it has been a pleasure working together, and it's been lots of fun trying to figure out and debating whether the antibody actually worked or not! To Christina Hubbart, thank you for always ensuring the laboratory ran so efficiently and for making sure I had all the support I needed, both in the lab and the office, so I could focus entirely on the science. A big thank you to the other DIL team members: Ricardo Ferreira, Marcin Pekalski, Holly Roach, and Heather McMurray.

To Dr James Bancroft and Edward Drydale, thank you for always being so accommodating and available for anything microscopy related. It has always been great fun chatting with you both—about science and beyond. To Dr Taha Elajnaf, I truly appreciate your kindness, and collaboration; your willingness to help has made a real difference. A heartfelt thank you also to my other collaborators: Dr Avigail Taylor, Ms Svenja Hester, and Dr Simon Davis.

To my wife, Nureen, this journey would not have been possible without you. Your unwavering support and love have been my anchor throughout. I am truly grateful for the sacrifices you have made to ensure that we, as a family, could have this experience. Your ability to keep us rooted and united as a family fills me with admiration every day. To my sons, Rayyan, Marwan, and Sinan, it has been a joy to watch you grow together. Your resilience and the way you have embraced the challenge of moving to a new country at such

a young age have been nothing short of remarkable. To my parents, I am deeply grateful for your unwavering support and guidance. It is your sacrifices that laid the foundation for this journey, and for that, I will always be thankful.

For Nureen, Rayyan, Marwan, Sinan, and my parents.

Abstract

TITLE: Molecular characterisation of the placental-pancreatic islet axis

NAME AND COLLEGE: Dr Faheem Seedat, St Edmund's Hall

DEGREE: DPhil in Women's and Reproductive Health

TERM AND YEAR OF SUBMISSION: Hilary 2024

During pregnancy adaptive changes support foetal growth and prepare the mother for childbirth. This includes the pancreatic islets, in which insulin secretion from β cells doubles by the third trimester. When these adaptations fail, gestational diabetes mellitus can occur, negatively impacting outcomes. These islet adaptations are closely linked to placental growth, with insulin secretion increasing as the placenta develops and returning to normal post-delivery. In mouse models, placental signals, such as hormones and extracellular vesicles (EVs), enhance islet function and β-cell mass. However, it remains unclear if these mechanisms apply to humans. This thesis investigates islet changes during human pregnancy *ex vivo*, using rare pancreatic tissue from pregnant women, and explores the role of placental small EVs (psEVs) in β-cell biology using a human-based model system. In the first part of the study, human islets were isolated using laser capture microdissection and analysed via liquid chromatography-mass spectrometry (LC-MS/MS), generating the largest dataset of proteins from islets isolated from pregnant women to date with over 7,000 proteins detected. Comparative analysis between pregnant and non-pregnant samples identified differences in only four proteins. Immunohistochemistry, coupled with unbiased computational analysis, revealed that whole islet, α-, and β-cell areas increased during pregnancy due to an increase in cell number, similar to findings in mice. However, unlike in mice, serotonin 2B receptor was absent in human β cells, and prolactin receptor expression remained unchanged. A notable increase in glucagon-like peptide-1 (GLP-1) within α cells was observed, which may enhance β-cell function through paracrine signalling. In the second part of the study, psEVs were isolated from human placentae and

their effects tested *in vitro* on a human β-cell line, EndoC-βH3. psEVs increased β-cell insulin gene expression and insulin content but did not enhance glucose-stimulated insulin secretion. Proteomic analysis via LC-MS/MS identified an increase in Annexin A1 (ANXA1) in psEV-treated Endoc-βH3 cells, suggesting a potential mechanistic role in psEV-mediated effects. In conclusion, islet adaptations in human pregnancy differ to those in mice and psEVs increase insulin content potentially through ANXA1.

List of abbreviations

ACHOIS	Australian Carbohydrate Intolerance Study in Pregnant Women
ACN	Acetronitrile
ADA	American Diabetes Association
ADIPS	Australasian Diabetes in Pregnancy Society
Alix	ALG-2-Interacting Protein X
AMY2A	Amylase 2A
ANOVA	Analysis of variance
ANXA1	Annexin A1
ATP	Adenosine triphosphate
B4GALT4	β1,4-galactosyltransferase 4
BCA	Bicinchoninic acid
Bcl-6	B-cell lymphoma 6 protein
BMI	Body mass index
bp	Base pairs
BSA	Bovine serum albumin
C19	Chromosome 19
C-AA	Chloroacetamide
Ca	Carcinoma
cAMP	Cyclic adenosine monophosphate
CHG	Centre for Human Genetics
CREBRF	CREB3 regulatory factor
CRHR	Corticotropin-releasing hormone receptor
CDK2	Cyclin-dependent kinase 2

CDK5	Cyclin-dependent kinase 5
cDNA	Complementary deoxyribonucleic acid
CGM	Continuous glucose monitoring
ChAT	Choline acetyltransferase
CHGA	Chromogranin A
CHGB	Chromogranin B
CHRNA3	Cholinergic receptor nicotinic alpha 3 subunit
ChT1	Choline transporter 1
CLDN15	Claudin 15
CO_2	Carbon dioxide
CLIC1	Chloride intracellular channel protein
Cre-ERT2	Cyclisation recombination-estrogen receptor T2
CRYBA2	Crystallin beta A2
CSHL1	Chorionic somatomammotropin hormone-like 1
CTSZ	Cathepsin Z
ddH2O	Double-distilled water
DDM	n-Dodecyl-β-D-Maltoside
DEG	Differentially expressed gene
DIA-NN	Data-independent acquisition software by neural networks
diaPASEF	Data-independent acquisition parallel accumulation serial fragmentation
DMEM	Dulbecco's modified eagle medium
DMSO	Dimethyl sulfoxide
DNase	Deoxyribonuclease
DPP-IV	Dipeptidyl peptidase IV

DNA	Deoxyribonucleic acid
EBCOG	European Board and College of Obstetrics and Gynaecology
EDTA	Ethylenediaminetetraacetic acid
ESCRT	Endosome sorting complexes required for transport
EV(s)	Extracellular vesicle(s)
FASP	Filter-aided sample preparation
FC	Fold change
FDR	False discovery rate
FFPE	Formalin-fixed paraffin-embedded
FIGO	International Federation of Gynecology and Obstetrics
FOXO1	Forkhead box protein O1
FOXM1	Forkhead box protein M1
fPBS	Filtered phosphate buffered saline
GA	Gestational age
GABA	Gamma-amino butyric acid
GABA-A	Gamma-amino butyric acid receptor A
GAD	Glutamic acid decarboxylase
GCG	Glucagon
GCGR	Glucagon receptor
GCT	Glucose challenge test
GDM	Gestational diabetes mellitus
GLI3	GLI family zinc finger 3
GLP-1	Glucagon-like peptide 1
GLP-1R	Glucagon-like peptide-1 receptor
GLUT1	Glucose transporter 1

GLUT4	Glucose transporter type 4
GO	Gene ontology
GSIS	Glucose-stimulated insulin secretion
HAPO	Hyperglycaemia and Adverse Pregnancy Outcomes
HbA1c	Haemoglobin A1c
HCL	Hydrochloric acid
HEK293T	Human embryonic kidney 293T
HG	High glucose
HIER	Heat-induced epitope retrieval
hiFBS	Heat-inactivated foetal bovine serum
HIPAA	Health Insurance Portability and Accountability Act
5-HTP	5 – hydroxytryptophan
HTR1D	Serotonin 1D receptor gene
5-HT1D	Serotonin 1D receptor
HTR2B	Serotonin 2B receptor gene
5-HT2B	Serotonin 2B receptor
HTR3A	Serotonin 3 receptor gene
5-HT3	Serotonin 3 receptor
IADPSG	International Association of the Diabetes and Pregnancy Study Groups
IGF1R	Insulin-like growth factor 1 receptor
IHC	Immunohistochemistry
IHC-IF	Immunofluorescence labelling of tissue sections
INS	Insulin gene
INSR	Insulin receptor

IQR	Interquartile range
IRS-1	Insulin receptor substrate-1
ISEV	International Society for Extracellular Vesicles
IVD	Isovaleryl-CoA dehydrogenase
JAK	Janus kinase
JAK2	Janus kinase 2
JDS	Japan Diabetes Society
KO	Knockout
LC-MS/MS	Liquid chromatography-tandem mass spectrometry
LCM	Laser capture microdissection
LGA	Large-for-gestational-age
MAPK	Mitogen-activated protein kinase
MATN2	Matrilin-2
MafB	Musculoaponeurotic fibrosarcoma oncogene homolog B
M3R	Muscarinic receptor
MCL	Markov cluster algorithm
NG	Normal glucose
NGS	Next-generation sequencing
NICE	National Institute for Health and Care Excellence
NIH	National Institutes of Health
NP	Network for Pancreatic Organ Donors with Diabetes
nPOD	Normal pregnancy
ns	Not significant
NTA	Nanoparticle tracking analysis
OGC	Oxford Genomics Centre

OGTT	Oral glucose tolerance test
PBS	Phosphate buffered saline
PBT	PBS with 0.1% Tween 20
PCA	Principal component analysis
PCR	Polymerase chain reaction
PEN	Polyethylene naphthalate
Pen/Strep	Penicillin/streptomycin
PIGF	Placental growth factor
PI3K	Phosphoinositide 3-kinases
PKA	Protein kinase A
PL	Placental lactogen
PLAP	Placental alkaline phosphatase
PLC	Phospholipase C
PNET	Pancreatic neuroendocrine tumour
PRKACA	Protein kinase CAMP-activated catalytic subunit alpha
PRKACB	Protein kinase CAMP-activated catalytic subunit beta
PRKACG	Protein kinase CAMP-activated catalytic subunit gamma
PRL	Prolactin
PRLR	Prolactin receptor
psEVs	Placental small extracellular vesicles
qPCR	Quantitative polymerase chain reaction
RBC	Red blood cells
RBCsEVs	Red blood cell small extracellular vesicles
RCT	Randomised controlled trial
RIN	RNA integrity number

RIPA	Radio-immunoprecipitation assay
RNA-seq	RNA sequencing
RT-qPCR	Reverse transcription quantitative polymerase chain reaction
SD	Standard deviation
sEV carrier control	Small extracellular vesicle carrier control
sEVs	Small extracellular vesicles
SLC2A1	Solute carrier family 2, facilitated glucose transporter member 1
SSTR	Somatostatin receptor
STAT	Signal transducer and activator of transcription
STAT5	Signal transducer and activator of transcription 5
STMN1	Stathmin 1
SV40LT	SV40 large T-antigen
TAE	Tris-acetate-EDTA
TBP	TATA-Box Binding Protein
TBS	Tris-buffered saline
TBS-T	Tris-buffered saline with Tween 20
TCEP	Tris(2-carboxyethyl) phosphine
TEAB	Triethylammonium bicarbonate
TFA	Trifluoroacetic acid
TOBOGM	Treatment of Booking Gestational Diabetes Mellitus
TPH	Tryptophan hydroxylase
TSG101	Tumour susceptibility gene 101 protein
UK	United Kingdom
USA	United States of America
UV	Ultraviolet

vAChT	Vesicular acetylcholine transporter
VEGF-A	Vascular endothelial growth factor A
WGA	Wheat germ agglutinin
WHO	World Health Organisation
WT	Wild-type

Table of contents

Chapter 1

Introduction

1.1 Physiological changes in human pregnancy

Pregnancy is a dynamic state marked by significant anatomical and physiological changes in the mother to ensure the developing foetus receives the necessary nutrients for growth, while also preparing the mother for the demands of delivery and lactation (1, 2). Nearly every organ system undergoes alterations to support these needs. For example, the cardiovascular and respiratory systems adapt to increase maternal cardiac output and ventilation, while the haematological system adapts to expand blood volume, and the renal system enhances filtration through the glomeruli (1, 2). The endocrine system, which regulates essential biological processes such as nutrient metabolism, reproduction, growth, and the stress response, also undergoes several adaptations during pregnancy. A critical area of change is the system involved in nutrient metabolism, specifically the pancreatic islets of Langerhans, which house the hormone-producing cells responsible for glucose homeostasis. Glucose is the primary fuel for foetal development, and pancreatic islets must adapt during pregnancy to maintain an adequate glucose supply for the growing foetus (1, 2).

1.2 Pancreatic islets of Langerhans

1.2.1 Islet distribution and structure

The human pancreas contains both endocrine and exocrine tissue. The hormone-producing endocrine cells are located within the islets of Langerhans. It is estimated that the human pancreas contains between 1 and 14.8 million islets, which collectively occupy a total volume of 0.5–2 cm^3, representing 1–3% of the total pancreatic volume (3-5). These islets are approximately spherical in shape, with an average volume of 0.00069 µL (3). The reported mean diameter of islets varies; while studies using 3D volumetric reconstruction imaging indicate diameters between 68 µm and 109 µm, older studies using 2D imaging techniques suggest larger diameters, ranging from 130 µm to as much as 300 µm (5). The

surface area of islets typically ranges from 1,000 to 10,000 μm² for 66% of islets, with 9% having a surface area under 1,000 μm², and 24% exceeding 10,000 μm². Islets with a surface area greater than 100,000 μm² are generally considered to be clusters rather than individual islets (4).

Islets are scattered throughout the head, body, and tail of the pancreas, though reports on their distribution are somewhat conflicting. Earlier studies using large-scale image capture reported a two-fold increase in the number of islets in the pancreatic tail. However, more recent studies using 3D volumetric reconstruction imaging suggest a more uniform distribution of islets from the head to the tail of the pancreas (4-6).

The endocrine pancreas contains several types of hormone-secreting cells, each responsible for producing specific hormones. These include α cells, which secrete glucagon; β cells, which secrete insulin; δ cells, which secrete somatostatin; γ cells, which secrete pancreatic polypeptide; and ε cells, which secrete ghrelin. Of these, α cells make up approximately 30% of the islet cells, β cells 60%, δ cells 5%, with γ and ε cells comprising the remainder (3, 5, 7).

1.2.2 Islet hormones and glucose homeostasis

Plasma glucose levels are tightly regulated within a narrow normal range through the interplay between insulin and glucagon. Insulin lowers plasma glucose by promoting cellular uptake of glucose, while glucagon raises plasma glucose by stimulating glucose release from the liver (8, 9).

β cells secrete insulin in response to elevated plasma glucose levels, typically after a meal. Glucose uptake by β cells triggers glycolysis, producing adenosine triphosphate (ATP), which closes potassium channels, causing depolarisation and the opening of voltage-gated calcium channels. The resulting calcium influx triggers the release of insulin-containing vesicles into the bloodstream. In contrast, α cells secrete glucagon in response to low glucose levels. In α cells, reduced ATP production leads to the closure of potassium channels, depolarisation, calcium influx, and the exocytosis of glucagon-containing vesicles into the bloodstream (8, 9).

Insulin is transported to muscle and adipose tissue, where it binds to the insulin receptor, a tyrosine kinase receptor. This activates the insulin receptor signalling pathway, including the phosphoinositide 3-kinases (PI3K) and protein kinase B (AKT) pathways, stimulating the insertion of glucose transporter type 4 (GLUT4) channels into the cell membrane. These channels facilitate glucose uptake from the bloodstream into the cells.

Glucagon binds to its G-protein-coupled receptor, predominantly expressed in the liver, but also found in the kidneys, gastrointestinal tract, and pancreas. This activates the cyclic adenosine monophosphate (cAMP) and phospholipase C (PLC) signalling pathways, which regulate target gene expression. The overall effect is to increase glucose production through gluconeogenesis (new glucose synthesis) or glycogenolysis (the breakdown of glycogen, the carbohydrate storage molecule). Additionally, glucagon promotes the breakdown of lipids and amino acids to support gluconeogenesis.

During hyperglycaemia, insulin inhibits glucagon secretion, while in hypoglycaemia, low glucose levels suppress insulin secretion and stimulate glucagon release. Glucagon, in turn,

promotes insulin secretion by activating glucagon receptors on β cells, which triggers intracellular signalling pathways, such as the cAMP pathway, that enhance insulin release (8, 9).

1.3 Glucose homeostasis in pregnancy

Normal pregnancy induces significant changes in glucose metabolism (10). Glucose is the primary fuel source for the developing foetus, and glucose homeostasis is carefully regulated to ensure a continuous supply (11, 12). Since glucose transfer across the placenta occurs via passive diffusion, it is crucial that maternal glucose levels are sufficient to maintain a consistent maternal-foetal gradient (12). This gradient facilitates the efficient transfer of glucose to the foetus, ensuring proper foetal growth and development. These changes vary across trimesters (11, 13). In early pregnancy, fasting glucose levels decrease due to haemodilution resulting from the expansion of maternal blood volume (11, 13). Fasting glucose levels remain low during the second trimester and decline further in the third trimester, as the foetus continues to utilise glucose for growth and development during gestation (11, 13). To compensate for the low fasting glucose levels and ensure a consistent maternal-foetal gradient is maintained, hepatic gluconeogenesis increases (11, 12). Additionally, postprandial glucose levels rise with placental development and continue to increase throughout pregnancy (11, 12). These mechanisms help maintain maternal glucose levels, ensuring sufficient transplacental glucose transfer to the foetus throughout gestation.

1.3.1 Insulin resistance in pregnancy

Insulin resistance progressively increases throughout pregnancy, limiting glucose uptake by maternal tissues (11, 12). This helps maintain elevated postprandial glucose levels, which is essential for sustaining the maternal-foetal transplacental glucose gradient (12). Early in

pregnancy, insulin resistance decreases; however, with the onset of placental development, this quickly changes, and insulin resistance begins to rise (11). Over the course of pregnancy, insulin resistance increases by 40–80% in a linear fashion, correlating with placental growth, and reverses after delivery (10, 14, 15). This rise is primarily driven by the secretion of placental hormones, such as human placental lactogen, growth hormone variant, prolactin, progesterone, oestrogen, and cortisol, which interfere with insulin signalling (10-14). Additionally, other factors like leptin and tumour necrosis factor alpha, produced both by the placenta and maternal adipose tissue, contribute to maternal insulin resistance (11, 14). Elevated circulating free fatty acids, resulting from pregnancy-associated maternal adiposity and subsequent lipolysis, further exacerbate insulin resistance during pregnancy (14).

1.3.2 Insulin secretion in pregnancy

Insulin secretion also increases progressively throughout pregnancy, also rising in a linear fashion throughout gestation (10, 11, 13, 14). Initially, it was believed that this increase was purely a compensatory response to the rise in insulin resistance, necessary to maintain maternal euglycemia (10, 11, 16). However, recent evidence suggests that insulin secretion begins to rise independently of changes in insulin resistance as insulin levels increase early in pregnancy, well before the more pronounced insulin resistance typically seen in the second and third trimesters (10, 16). A recent longitudinal study of 34 women with normal pregnancies, using an intravenous glucose tolerance test, quantified these changes in insulin secretion. *Powe et al.* observed that insulin secretion increased by approximately 54.82% from pre-pregnancy to early pregnancy, and by a further 28.33% from early to late pregnancy. Overall, insulin secretion nearly doubled, increasing by approximately 98.67% from pre-pregnancy to late pregnancy (15).

1.3.3 Glucagon secretion in pregnancy

Unlike the extensive research on insulin, there is limited literature exploring the changes in glucagon during pregnancy and its contribution to glucose metabolism. A study involving 156 pregnant women, using postprandial samples from 5 to 40 weeks of gestation, observed no significant changes in glucagon concentrations between pregnant and non-pregnant women during the first and third trimesters (17). However, a moderate increase in glucagon levels was observed between weeks 16 and 28 of pregnancy (17). A second study of 16 pregnant women demonstrated no increase in fasting glucagon levels compared to non-pregnant women (18). Conversely, other studies have reported elevated postprandial glucagon levels in late gestation compared to non-pregnant controls (19). More research is needed to clarify the precise circulating levels of glucagon and to better understand its role in glucose regulation during pregnancy.

1.4 Pancreatic islet adaptations during pregnancy

Rodent models have revealed numerous molecular adaptations in islets that support the increased insulin demands of pregnancy. There is an overall increase in islet β-cell mass, accompanied by enhanced islet vascularisation to improve nutrient and oxygen delivery. β-cells increase in size and β-cell proliferation also rises. β cells demonstrate a heightened glucose-stimulated insulin secretion (GSIS) response, with a lower threshold for GSIS activation. Insulin gene expression, synthesis, and overall insulin content are all increased to ensure sufficient insulin availability. β-cell glucose metabolism is augmented by the upregulation of glucokinase and glucose transporter proteins, which enhances glucose sensing, and uptake. Enhanced gap-junctional coupling between β-cells further supports coordinated insulin release, optimising the islet response to fluctuating glucose levels and

aiding in maintaining maternal glucose homeostasis throughout pregnancy (11, 13). How these adaptations translate to human pregnancy is still not fully understood.

1.4.1 Role of the placenta in affecting islet physiology during pregnancy

During pregnancy, the placenta functions as a vital endocrine organ that not only supports the developing foetus but also significantly influences maternal physiology (10). Insulin physiology and placental development are intrinsically linked, with insulin secretion progressively increasing alongside placental growth until delivery, then returning to pre-pregnancy levels following birth and the removal of the placenta (15, 20). Placental-derived signalling molecules drive the adaptations in maternal β-cells that enhance insulin secretion (11, 13, 20). These placenta specific molecules include hormones secreted by the placenta and extracellular vesicles released from the placenta that act on maternal pancreatic islets, inducing adaptive physiological changes necessary to meet the metabolic demands of pregnancy (10, 11, 13, 20). Additionally, there is a dynamic feedback loop in which maternal signals can influence placental development, establishing a constantly evolving interplay from the first trimester onwards. This balance is tightly regulated and is sensitive to the maternal metabolic environment, ensuring that maternal and placental functions are harmonised throughout pregnancy (10, 11, 13, 20).

1.4.2 Structural alterations

Rodent studies have demonstrated that β-cell mass increases 3- to 4-fold during pregnancy, predominantly due to β-cell proliferation (11, 13, 21, 22). Similarly, α-cell mass in mice also increases more than 2-fold by late gestation due to proliferation (23-25). Data are sparse describing changes of other islet cell types during pregnancy.

Two studies have examined changes in β-cell mass during human pregnancy. *Van Assche et al*. investigated β-cell area in pancreatic tissue from five pregnant women (four in the third trimester and one in the second trimester, with a mean gestational age of 32.2 weeks) compared to non-pregnant controls. The authors observed a 2.4-fold increase in β-cell area in the pregnant group ($p < 0.005$), suggesting significant β-cell expansion during pregnancy (26). *Butler et al.* conducted a more recent study examining β-cell area in 18 pregnant women (eight in the second trimester, eight in the third trimester, and two in the first trimester, with a mean gestational age of 24.6 weeks). Their findings showed a 1.4-fold increase in β-cell area in the pregnant group compared to non-pregnant controls. Additionally, islet density (the number of islets per area measured) was higher in pregnancy, with islets being the same size or smaller than those observed in non-pregnant women. The pregnant group also had a greater number of individual β-cells and insulin-positive duct cells. However, no differences were observed between pregnant and non-pregnant groups in β-cell proliferation (measured by Ki-67 staining), β-cell apoptosis (measured by TUNEL staining), or β-cell size, indicating no evidence of cell hypertrophy. Given the absence of evidence for cell proliferation or hypertrophy, alongside an increase in insulin-positive duct cells (with ducts known to serve as sites for new islet cell formation) and individual β-cells, the authors proposed that neogenesis may be the primary mechanism underlying the increased β-cell mass observed during pregnancy (27). Notably, no studies to date have examined changes in α-cell mass during human pregnancy.

1.4.3 Molecular changes

1.4.3.1 Lactogenic signalling

Lactogenic hormones, specifically placental lactogen (PL) and prolactin, are secreted by the placenta and play a key role in pregnancy by supporting maternal islet adaptations (13, 25).

PL is exclusively produced by the placenta, while prolactin, although primarily secreted by the anterior pituitary, sees its pituitary-derived secretion decrease by mid-gestation, making the placenta the predominant source during late gestation (11). Among placental hormones, lactogens are the most extensively studied for their impact on islet adaptation in rodent models. Both PL and prolactin exert their effects through binding to the prolactin receptor (PRLR), which is expressed on rodent β-cells (11).

The rise in PL secretion during gestation correlates with increased insulin secretion observed during rat pregnancy, and pregnancy associated β cell changes coincide with the increase in PL levels (28). Studies using lactogenic hormones, including PL and prolactin, demonstrate that these hormones enhance insulin secretion and promote β-cell proliferation, mass expansion, and survival (29). Overexpression of PL in mouse islets led to a twofold increase in insulin content and β-cell mass, as well as enhanced insulin secretion (30).

The PRLR is expressed on rodent β cells, and signalling by PL and prolactin through the PRLR is critical for pregnancy-related β cell adaptations (11, 29). Global *PRLR* knockout mice *($PRLR^{-/-}$)* exhibit reduced insulin content, impaired insulin secretion, and diminished β-cell mass. $PRLR^{-/-}$ mice are infertile and studies in heterozygous global *PRLR* knockout mice ($PRLR^{+/-}$) reveal glucose intolerance and reduced β-cell mass, attributed to decreased β-cell proliferation (31). Additionally, in mice with a β-cell specific PRLR knockout allele, $PRLR^{+/-}$ β cells, exhibit reduced insulin secretion and β-cell mass during pregnancy, leading to glucose intolerance in pregnancy (32-34).

Several studies have investigated the signalling pathways activated by lactogens following PRLR binding that contribute to enhanced insulin production, insulin secretion, and β-cell

proliferation observed in rodents (11, 13, 25). One key pathway identified is the activation of the enzyme tryptophan hydroxylase 1 (TPH1), which increases serotonin synthesis to promote β-cell proliferation (25, 32, 35). Another critical signalling mechanism following PRLR activation involves the upregulation of transcription factors, including signal transducer and activator of transcription 5 (STAT5), menin, forkhead box protein O1 (FOXO1), forkhead box protein M1 (FOXM1), B-cell lymphoma 6 protein (Bcl-6), musculoaponeurotic fibrosarcoma oncogene homolog B (MafB) (32, 35-39). Given the increase in β-cell proliferation during mouse pregnancy, changes in cell cycle regulation are also prominent, with increased expression of cell cycle cyclins (A2, B1, B2, and D1), activation of cyclin-dependent kinases, and modulation of cell cycle inhibitors such as p21, p27, and p57 have all been identified as being altered by lactogenic signalling (21, 32, 35, 36). Among these pathways, the promotion of β-cell proliferation during pregnancy by serotonin is particularly noteworthy.

1.4.3.2 Serotonin

TPH1 is the rate-limiting enzyme that catalyses the conversion of tryptophan to serotonin. During pregnancy, *TPH1* is among the most highly expressed genes in pancreatic islets, and its expression is upregulated through activation of the PRLR signalling pathway. Both PL and prolactin activate PRLR, which, in turn, initiate the Janus kinase 2 (JAK2) and signal transducer and activator of transcription 5 (STAT5) signalling cascade. This activation leads to increased synthesis of TPH1, ultimately elevating intra-islet serotonin levels (11-13, 34, 40).

Several studies in mice have demonstrated that intra-islet serotonin functions in an autocrine and paracrine manner, enhancing both β-cell proliferation and insulin secretion during

pregnancy (11-13, 40, 41). In addition, *Bennet et al.* reported that serotonin also enhances GSIS in human islets (42).

There are 14 cell surface G-protein coupled serotonin receptors each mediating distinct functions, and β cells are known to express several of these receptors (43). Mechanistic studies have sought to elucidate the role of these receptors in aiding β-cell proliferation and insulin secretion following activation by serotonin. Amongst these receptors, the serotonin 1D (5-HT1D) receptor, serotonin 2B (5-HT2B) receptor, and serotonin 3 (5-HT3) receptor have been extensively studied for their effects on β-cell function. In mouse islets, *Kim et al.* observed that during mid-gestation, the expression of *HTR2B*, the gene coding the 5-HT2B receptor, was upregulated, correlating with increased β-cell proliferation. However, by late gestation *HTR2B* expression decreased and instead *HTR1D*, the gene coding the 5-HT1D receptor, expression increased, which was associated with β-cell regression in mouse islets (44). The role of the 5-HT2B receptor in enhancing β-cell mass was confirmed in a separate study, which demonstrated that β-cell mass was reduced by 55% in *HTR2B* knockout mice (*HTR2B*$^{-/-}$), resulting in glucose intolerance, although GSIS from their pancreatic islets remained unaffected (41). Regarding the 5-HT3 receptor, *Ohara-Imaizumi et al*. compared pregnant and non-pregnant wild-type and *HTR3A* knockout mice (*HTR3A*$^{-/-}$) (the gene encoding a subunit of the 5-HT3 receptor) and observed that elevated intra-islet serotonin levels during pregnancy activated the 5-HT3 receptor to enhance GSIS (45).

Taken together, activation of the 5-HT1D receptor has been associated with β-cell regression, while activation of the 5-HT2B receptor promotes β-cell proliferation, and stimulation of the 5-HT3 receptor enhances insulin secretion. Based on these functional roles and the observed changes in receptor levels throughout gestation, a mechanistic model has

been proposed in which receptor abundance dynamically shifts to support pregnancy-related adaptations in β-cells. Specifically, during mid-gestation, increased 5-HT2B receptor expression promotes β-cell proliferation and insulin secretion, while 5-HT1D receptor levels decrease, reducing signals for β-cell regression. Postpartum, this balance reverses, with a decline in 5-HT2B receptor expression and increased 5-HT1D receptor abundance facilitating β-cell regression. Meanwhile, 5-HT3 receptor expression remains unchanged during pregnancy, and serotonin signalling via this receptor continues to enhance insulin secretion (Figure 1.1) (44, 45).

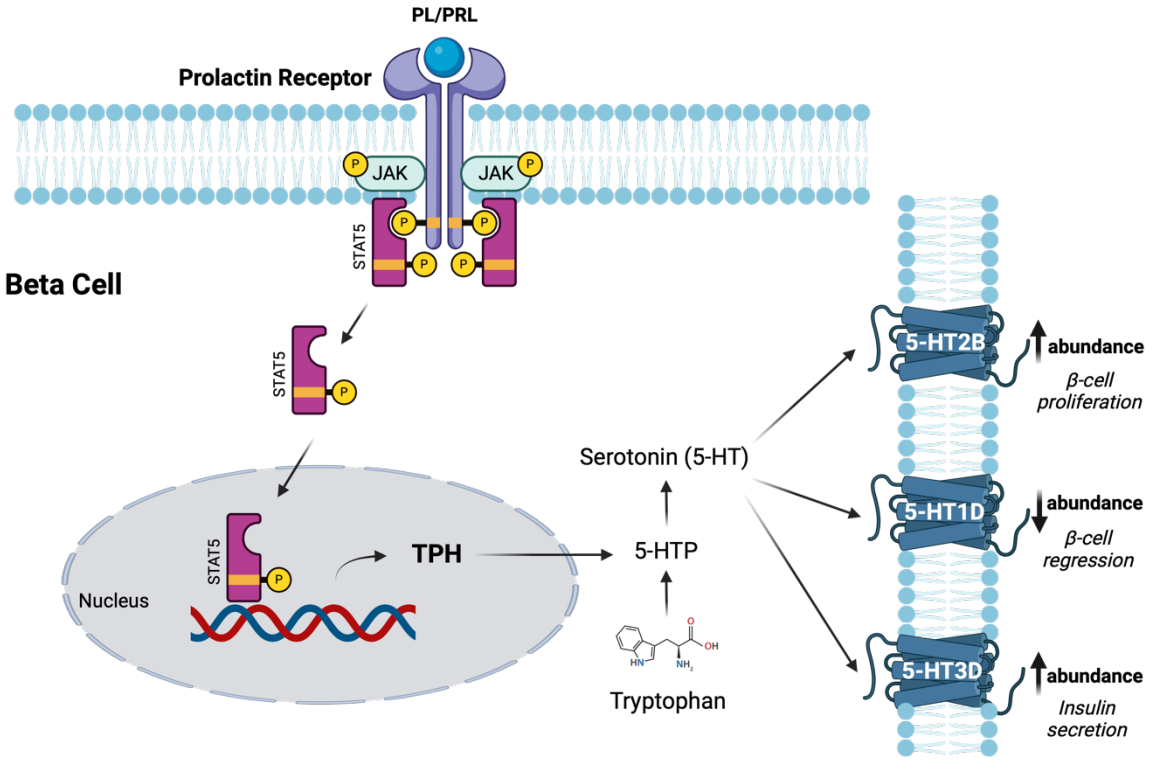

Figure 1.1. This schematic illustrates the proposed signalling pathway of the lactogenic and serotonin pathways in pancreatic β-cells during mid-gestation. Activation of the prolactin receptor (PRLR) by placental lactogen (PL) and prolactin (PRL) triggers the Janus kinase 2 (JAK2) and signal transducer and activator of transcription 5 (STAT5) pathway. This leads to an upregulation of tryptophan hydroxylase 1 (TPH1), which catalyses the conversion of tryptophan into active serotonin (5-HT). During pregnancy, expression of serotonin receptors adapts, with an increase in the abundance of the serotonin 2B (5-HT2B) and serotonin 3D (5-HT3D) receptors, while serotonin 1D (5-HT1D) receptor levels, which are linked with β-cell regression, decrease. Autocrine and paracrine signalling by serotonin through the 5-HT2B receptor enhances β-cell proliferation, while activation of the 5-HT3D receptor promotes insulin secretion during mid-pregnancy. This pathway underscores the complex regulatory adaptations of β-cells to meet the metabolic demands of pregnancy. Created with BioRender.com released under a Creative Commons Attribution-NonCommercial-NoDerivs 4.0 International license.

*5-HTP – 5 – hydroxytryptophan, JAK- Janus kinase, PL - placental lactogen, PRL – prolactin, STAT - signal transducer and activator of transcription, 5-HT1D - serotonin 1D receptor, 5-HT2B - serotonin 2B receptor, TPH1 - tryptophan hydroxylase 1.

It is notable that a recent study by *Goyvaerts et al.* found no reduction in β-cell proliferation during normal pregnancy in *TPH1* knockout mice (*TPH1*$^{-/-}$), 129P2/OlaHsd mice (which are unable to upregulate islet TPH1 during pregnancy), or *HTR2B*-deficient mice (46). Moreover, genetic variants in *TPH1* and *HTR2B* were not associated with gestational diabetes mellitus (GDM) in pregnant women (47). These findings contrast with earlier studies that highlighted the critical role of lactogenic and serotonin signalling pathways in promoting β-cell proliferation during pregnancy. Given these contrasting observations and the fact that similar mechanisms in human islets remain incompletely understood, further investigation is necessary to clarify the role of serotonin and its associated receptors during human pregnancy.

1.4.3.3 Other proposed mechanisms

Additional hormones secreted by the placenta that contribute to maternal β-cell adaptations in pregnancy include growth hormone, oestrogen, and progesterone (11, 13). Growth hormone signalling via its receptor also activates the 5-HT2B receptor to increase β-cell proliferation in mice (41). Other signalling molecules influencing β-cell function in pregnancy include vascular endothelial growth factor A (VEGF-A), adiponectin, and placental growth factor (PIGF) (11, 13). Recent findings also highlight roles for oxytocin and melatonin (from the pineal gland) in pregnancy associated β-cell adaptations (25). Locally produced islet factors, such as kisspeptin, leptin, urocortin, and hepatocyte growth factor, have also been shown to play significant roles in these adaptive processes during pregnancy (11, 13).

It is notable that all the mechanisms discussed above have been described in rodent models, and their applicability to human pregnancy remains to be elucidated.

1.4.4 Changes in the islet proteome

There are just a few studies that have characterised the islet proteome and of these just a single study, conducted in mice, has evaluated the islet proteome during pregnancy (22). To date, no studies have been performed in human islets from pregnant women.

Horn et al. compared the islet proteome of pregnant mice at day 14.5 gestation to non-pregnant littermates (22). The authors used two complementary proteomic techniques to assess protein expression in pancreatic islets from pregnant and non-pregnant mice to identify proteins contributing to pregnancy associated β-cell mass expansion in mice. First, the authors employed *in vivo* pulsed stable isotope labelling to track newly synthesised proteins during the initial 14.5 days of pregnancy, allowing them to capture dynamic protein synthesis. In parallel, islets were isolated and *ex vivo* dimethyl labelling used to measure overall protein abundance in the islets specifically at gestational day 14.5. To isolate islets the pancreas was inflated with with Liberase TL/DNase I enzyme solution, followed by stopping the reaction with Hanks buffered salt solution. The digested pancreatic tissue was filtered through 100 μm and 70 μm strainers to retain the islets, which were then handpicked and snap frozen. By integrating these two methods, the study was able to capture both the dynamic synthesis of proteins and the broader changes in protein abundance associated with β-cell mass expansion during pregnancy. A false discovery rate of 0.15 and log2 fold change of 0.2 was applied for the analysis. When examining *de novo* protein synthesis in islets during mouse pregnancy, 617 unique proteins were identified exclusively in the pregnant group. Additionally, an analysis of relative protein abundance in islets on day 14.5 of gestation revealed 427 proteins that were significantly different between pregnant and non-pregnant mice. Comparing the *de novo* synthesized proteins with those showing significant changes in overall abundance revealed 170 proteins that were differentially regulated in both

analyses. These proteins were then compared to differentially expressed genes identified by a complementary transcriptomic analysis of the same set of mouse islets collected at day 14.5 of pregnancy. Of the 170 proteins, 89 were also regulated at the RNA level. A three-dimensional plot of the 20 most highly upregulated proteins highlighted Matrilin-2 (MATN2), Insulin-like Growth Factor Binding Protein 5 (IGFBP5), Chromogranin B (CHGB), and Isovaleryl-CoA Dehydrogenase (IVD)—proteins previously shown to support islet mass expansion in mice—alongside novel candidates Chloride Intracellular Channel Protein 1 (CLIC1) and Stathmin 1 (STMN1), as key contributors to islet expansion during mouse pregnancy (22).

1.5 Extracellular vesicles

1.5.1 Classification and biogenesis

Extracellular vesicles (EVs) are cell-derived particles surrounded by a lipid bilayer and which lack a functional nucleus which prevents them from self-replicating (48). EVs carry proteins, lipids, and genetic material, collectively known as cargoes (48, 49).

EVs can be classified based on their size, cellular or tissue origin, biochemical characteristics, or the pathways involved in their biogenesis. Small EVs (sEVs) measure less than 200 nm, whereas medium/large EVs range from 200 to 1000 nm. EVs originating from the placenta may be referred to as placental EVs. Their biochemical classification includes the expression of specific surface markers, such as $CD63^+$/$CD9^+$ (48, 49).

Distinct pathways of biogenesis result in the formation of different EV types. By biogenesis, EVs are classified into three groups: exosomes, microvesicles and apoptotic bodies (50-52). Each originates from a unique cellular process that is responsible for their formation.

Microvesicles are formed from the cell surface by outward budding of the cell membrane in response to intracellular calcium influx, similarly, apoptotic bodies are also formed by outward blebbing following cytoplasmic fragmentation during apoptosis (50). Exosomes, in contrast, are formed by a more complex process derived from the endolysosomal pathway. During exosome formation, the cell membrane invaginates to form an early endosome. Early endosomes fuse to form the late endosome which leads to invagination of the endosomal membrane to form intraluminal vesicles. This results in the formation of multivesicular endosomes, also termed multivesicular bodies. This process is coordinated by the endosome sorting complexes required for transport machinery (ESCRT). Multivesicular bodies fuse with the cell membrane to release exosomes extracellularly or fuse with lysosomes to be degraded (Figure 1.2) (50, 51).

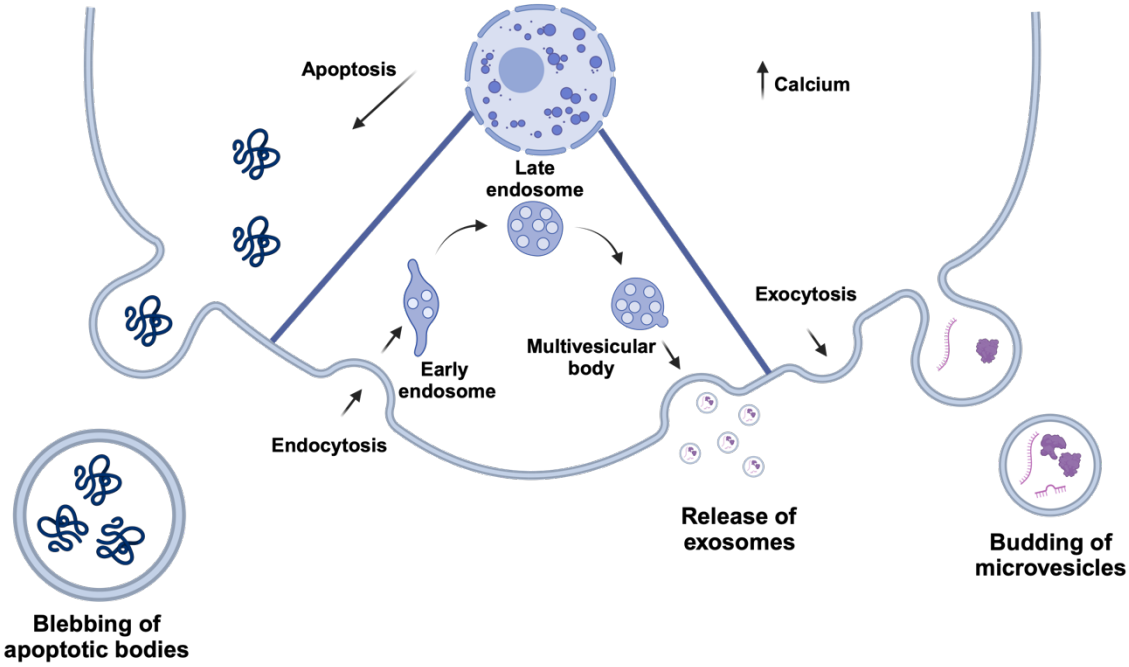

Figure 1.2. Schematic representing the biogenesis of extracellular vesicles. Microvesicles are formed by budding of the cell membrane in response to a rise in intracellular calcium. Exosomes are formed via the endolysosomal pathway and are released from multivesicular bodies. Apoptotic bodies are secreted following cell apoptosis. Created with BioRender.com released under a Creative Commons Attribution-NonCommercial-NoDerivs 4.0 International license.

Exosomes, microvesicles and apoptotic bodies differ in size, biomarker abundance, and contents (51, 53). The distinct features of each are detailed in Table 1.1. However, some overlap exists in the characteristics of the different EV biogenic-subtype markers (48). It is recommended that terms linked to biogenesis pathways should not be used to define or classify EVs in research studies. Instead, it is recommended that EVs should be described by their physical characteristics such as size (48). This is because EV biomarkers lack specificity, and commonly used EV isolation techniques are unable to separate EVs based on their biogenesis, resulting in a heterogeneous pool. For example, techniques used to isolate EVs under 200 nm may isolate both exosomes and microvesicles. In this scenario, the International Society of Extracellular Vesicles recommends that it is more accurate to refer to the EV population studied as small EVs rather than exosomes (48, 49). In line with these guidelines, in this thesis, EVs are classified by their size and tissue of origin. For example, sEVs or medium/large EVs from the placenta or red blood cells.

Table 1.1: Characteristics of exosomes, microvesicles, and apoptotic bodies.

	Size (nm)	Biomarkers	Contents
Exosomes	50 - 150	Tetraspanins - CD63, CD9, CD81; ESCRT components - ALIX, Tsg101, syntenin	RNAs - mRNA, miRNA, and other non-coding RNAs Proteins - cytoplasmic, membrane
Microvesicles	100 - 1,000	Integrins, selectins, CD40, tissue factor	RNAs - mRNA, miRNA, and other non-coding RNAs Proteins - cytoplasmic, membrane
Apoptotic bodies	100 - 5,000	Annexin V, C3b, histone coagulation factor	Nuclear fractions, cell organelles

*ESCRT - endosome sorting complexes required for transport, Alix – ALG-2-interacting protein X, Tsg101 – tumour susceptibility gene 101.

1.5.2 Extracellular vesicle mediated cell signaling

EVs are recognised as mediators of intercellular communication and are able to affect the function of target cells in distant tissues (51, 53). The function of target cells may be altered in two ways. EV surface protein or lipid ligands can interact directly with cell surface receptors or EVs can transfer their cargoes, including miRNA, mRNA, and proteins, to recipient cells to alter cell function (51, 52, 54, 55). EVs are shown to contribute to immune regulation, cancer progression, and metabolic control and can affect cellular mechanisms responsible for maintaining normal cell physiology or they may directly contribute to pathological processes (51).

1.6 Extracellular vesicles in pregnancy

1.6.1 The placenta

The placenta is essential for foetal growth and development. It is a temporary organ, formed during pregnancy and removed afterward (56, 57). The placenta facilities the transfer of oxygen and nutrients, such as glucose, from the mother to the growing foetus, while removing foetal waste (56, 57). Additionally, during pregnancy, the placenta also produces and releases hormones, growth factors and EVs into the maternal circulation to support key maternal adaptations (56, 57).

The placenta begins to form after the blastocyst implants into the maternal endometrium around day six to seven post-conception. Structurally, it is a disc-shaped organ attached to the maternal surface via the basal plate and connected to the foetus through the chorionic plate via the umbilical cord (56, 57). Maternal spiral arteries project into the intervillous space, filling it with maternal blood that carries oxygen and fresh nutrients (56, 57).

Foetal vessels form a branching, tree-like structure known as chorionic villi. Chorionic villi attach to the chorionic plate, extend into the intervillous space, with their terminal branches consisting of foetal capillaries (56, 57). Foetal capillaries increase the vascular surface area for efficient nutrient and gas exchange. Almost all exchange between mother and foetus occurs at the level of the chorionic villi (foetal vessels) which are bathed in maternal blood (Figure 1.3) (56, 57).

The foetal blood, however, remains separated from direct contact with maternal blood by the syncytiotrophoblast layer, which form the walls of the chorionic villi. This cell layer, which regulates the transfer of molecules between the maternal and foetal circulations, is continuously replenished from an underlying pool of cytotrophoblast cells (56, 57). Moreover, the syncytiotrophoblast is responsible for releasing hormones, growth factors, and EVs into the maternal circulation (56, 57).

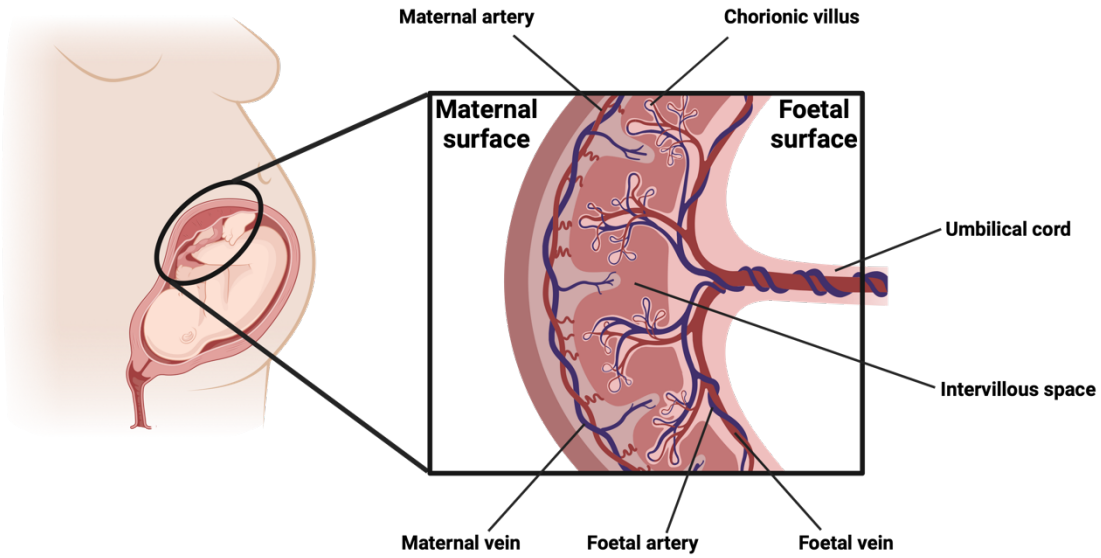

Figure 1.3. Schematic illustrating the anatomical structure of the human placenta. Created with BioRender.com released under a Creative Commons Attribution-NonCommercial-NoDerivs 4.0 International license.

1.6.2 Placental extracellular vesicles

Placental EVs, also termed syncytiotrophoblast-derived EVs as they originate from the synytiotrophoblast layer, have distinct cargoes compared to EVs originating from other tissues (56). Placental EVs carry placental-specific proteins such as placental alkaline phosphatase (PLAP), synctin-1 and the placental-specific genetic material, including the functional Chromosome 19 (C19) miRNA cluster encoding 59 mature miRNAs (57-59).

It is well described that placental EVs are detected in maternal circulation (60). Placental EVs have been detected from as early as six weeks of gestation and as the placenta grows the secretion of placental EVs steadily increases with a 20-fold rise in the number of circulating placental EVs reported by 28 weeks (57, 61). At 40 weeks, up to a quarter of all circulating sEVs are placental in origin (62). Following delivery, levels of placental EVs in circulation decline rapidly (61).

No studies have directly examined the biodistribution of placental EVs in humans due to safety and ethical concerns of using fluorescently tagged EVs or other methodologies during human pregnancy. Studies that have examined EV biodistribution *in vivo* have been conducted in mice where EVs are infused via tail vein injections. The lung capillary bed is the first site EVs encounter before broader systemic dissemination (63). When examining placental EVs, high concentrations of both placental medium/large EVs and sEVs are consistently detected in the lungs and liver (64). It is hypothesised that the high EV concentrations observed in the liver are due to phagocytosis by Kupffer cells, to clear EVs from the circulation. Detection of placental EVs in more distant organs, such as the spleen and kidneys, has been inconsistent, however just a few studies have examined the biodistribution of placental EVs (64). When evaluating EVs from other sources, which have

been studied more extensively, medium/large EVs are not reliably detected in peripheral organs like the spleen or kidneys. However, sEVs have been consistently found in these organs (63). Studies in the nano-signalling field suggest that sEVs exhibit increased cellular motility, enhancing their uptake and enabling more effective cargo delivery to distant sites (65). A recent study detected injected fluorescently labelled psEVs in mice pancreata, confirming that psEVs are indeed able to reach the pancreas *in vivo* (66). Taken together, this evidence suggests that EV size influences biodistribution patterns. Considering that placental EVs are likely to behave similarly to other EV types, it is likely that smaller placental EVs have a greater potential to reach distant tissues, particularly the pancreas, however further research is needed in this area.

Placental EVs also act as signaling molecules, playing a role in physiological adaptations in pregnancy as well as in pregnancy-related diseases (54, 57). Placental EVs contribute to maternal-embryo communication and act locally to alter maternal endometrial cells to aid in placental development (57, 60, 67). In circulation, placental EVs affect maternal vasculature by altering endothelial cell migration in pregnancy. Pathological effects of placental EVs are implicated in pregnancy related diseases like GDM, pre-eclampsia, and during viral infections (57, 60, 67).

1.6.2 Methods to isolate and enrich placental extracellular vesicles

Placental EVs have been isolated from several different sources, including from placental tissue itself, from primary placental or placenta-derived cell lines, or from the maternal circulation (60, 68-72).

Three main techniques have been described for isolating placental EVs directly from placental tissue (68-70, 72). The first is mechanical disruption, which involves dissecting a piece of placental tissue, chopping it into small pieces, washing it, and filtering it to produce an eluate from which placental EVs are isolated. Although this method is technically the simplest, it often results in the release of a large number of necrotic EVs, which may not accurately reflect the physiological EV release occurring *in vivo* and may be contaminated by EVs from other cell-types (68, 72). Another method is placental explant culture, an *in vitro* technique where placental tissue is harvested, washed, and placed onto specialised inserts within culture dishes. Media is added to the wells to cover the explants, which are incubated for 24–72 hours. After incubation, the media is collected and purified to isolate placental EVs. However, this approach can result in contamination of EVs from non-syncytiotrophoblast sources such as immune cells, endothelial cells, and stromal cells, affecting the purity of the final EV preparation. Variations in media types and culture durations across different studies contribute to the variability in the placental EVs collected (70, 71). The third technique is placental perfusion, an *ex vivo* method that mimics *in utero* placental physiology. A fresh placenta is used, with a single cotyledon selected and cannulated on the foetal surface while the maternal surface is perfused with media through cannulae inserted into the placental tissue. The placenta is perfused for three hours, after which the maternal perfusate, representing maternal blood containing the products released by the placenta into the maternal circulation, is collected and purified (69, 72). While this technique offers the most physiological approach to isolating placental EVs, it is technically demanding, with success rates ranging from 35% to 70% (72). It also requires an undamaged placenta delivered by caesarean section, which can be difficult to obtain, and may be contaminated by EVs from red blood cells due to the unavoidable presence of maternal blood in the placental vessels (72).

Isolation of placental EVs from the culture media used to maintain primary placental or placental- derived cell lines offer a useful, more accessible, and technically simpler method to obtain purely placental EVs. However, these EVs may not accurately reflect the true physiological changes occurring in the placenta *in utero*, particularly in the context of disease states (72). Isolating placental EVs from circulation by processing plasma collected from pregnant women often results in low yields compared to other methodologies (71). Additionally, these samples can be contaminated by EVs from other sources, as well as by lipoproteins, which complicates the isolation process and affects the purity of the final EV preparation (73, 74).

The EV containing product of the methods used described above is then processed using different techniques to enrich placental EVs each of which varies in complexity, purity and yield. One of the most used techniques is density ultracentrifugation, which separates EVs based on their density through high-speed centrifugation. Density ultracentrifugation with a sucrose cushion is also used, which enhances purity by introducing a sucrose gradient, allowing for more precise separation based on buoyant density, but this method can be time-consuming. Size exclusion chromatography offers a gentler method that separates particles by size as they pass through a porous column, preserving EV integrity, though it may result in lower yields. Immunoprecipitation uses antibodies that target specific surface markers on EVs (e.g., $CD63^+$, $CD81^+$) to selectively isolate EV subtypes with high specificity, although it requires well-characterised markers and can be expensive (75, 76).

1.6.3 Placental extracellular vesicles and gestational diabetes mellitus

In GDM, the placenta undergoes macroscopic and molecular alterations. Placental weight and gross morphology are affected and at the molecular level, the placenta's transcriptome,

proteome, metabolome, and miRNA profile are also altered (77). This leads to differences in the quantity and molecular composition of circulating placental EVs in women with GDM (77). These changes may affect the signalling roles of GDM placental EVs, influencing maternal and foetal health during gestation.

In GDM pregnancy the total number of circulating EVs, irrespective of their source, increases across gestation (78). More specifically, the number of circulating placental EVs (defined as PLAP-positive EVs) is significantly higher in GDM compared to normal pregnancy. Even when considering sEVs alone, placental sEVs (psEVs) increase 2.2-fold, 1.5-fold and 1.8-fold higher in GDM during the first, second and third trimesters, respectively, compared to normal pregnancy (77). Interestingly, primary placental cell and explant cultures from GDM placentae produce a greater number of placental EVs compared to cells or tissue from placentae from normal pregnancy (77). This suggests that GDM alters placental EV biogenic machinery to increase EV production.

There has been significant interest and research focused on examining the cargo of EVs in GDM to identify differences compared to normal pregnancy. In particular, miRNAs and proteins have been extensively studied to understand how their composition may be altered in GDM. Studies using next-generation sequencing have identified unique miRNA cargo in the placental EVs from GDM compared to normal pregnancy, which have been linked to alterations in glucose homeostasis, insulin secretion, and insulin signalling (77-79). Regarding miRNA's involved in the regulation of insulin secretion, miR-122-5p, 132-3p, 29b-3p, 182-3p, and 29a- 3p are upregulated in early pregnancy in GDM placental EVs (80).

Several studies have used liquid chromatography-mass spectrometry (LC-MS/MS) to characterise the proteins carried by placental EVs. Differences in the proteomic profile of GDM placental EV cargoes in relation to normal pregnancy have been observed (61, 77, 79). In our research group, a proteomic analysis of placental EVs identified 56 differentially abundant proteins in GDM medium/large placental EVs compared to normal pregnancy, however, no differences in GDM sEVs compared to normal pregnancy sEVs were observed (81).

GDM placental EVs exhibit functional effects and are linked to an increased pro-inflammatory milieu due to increased cytokine release (61, 82). Additionally, they are associated with oxidative stress and endothelial cell dysfunction (82). Furthermore, GDM placental EVs contribute to insulin resistance through impaired insulin signalling in skeletal muscle, leading to reduced glucose uptake, largely due to decreased phosphorylation of insulin receptor substrate-1 (IRS-1) and AKT (77, 78).

1.6.4 Placental extracellular vesicles and β-cell adaptations in pregnancy

As already discussed, the rise in the number of psEVs during gestation correlates with the increase in insulin secretion observed in pregnancy (83) and there is evidence suggesting that placental EVs also modulate β-cell function.

A next-generation sequencing study investigated the miRNA profile of GDM psEVs in early pregnancy, focusing on their relationship with pancreatic β-cell function. In the GDM group the concentration of psEVs positively correlated with reduced β-cell function. The study identified nine differentially expressed miRNAs in psEVs from women with GDM and reduced β-cell function, compared to controls with normal β-cell function. Among

these, miR-7704 and miR-4706 were downregulated and were also found in psEVs from women with normal pregnancies who had reduced β-cell function. miR-3665 was consistently downregulated in psEVs from pregnant women with GDM with both normal and reduced β-cell function. Of the remaining six miRNAs uniquely associated with GDM and reduced β-cell function, miR-455-3p was upregulated, while miR-2277-5p, miR-6087, miR-6729-5p, miR-6750-5p, and miR-1469 were all downregulated. These miRNAs were found to regulate 129 genes, which enriched pathways in sphingolipid metabolism and signalling, as well as interleukin-17 signalling which relate to biosynthesis and immune tolerance (84).

A functional study investigated the effects of psEVs on insulin secretion in mouse islets. At 24 – 28 weeks of gestation, psEVs were isolated from plasma of women with healthy normal pregnancies and GDM. These psEVs were then continuously infused into late-gestation pregnant mice (starting at gestational day 13.5) using a mini-osmotic pump for four days. On day 17.5, plasma insulin levels were measured and GSIS using the isolated mouse islets was evaluated *in vitro*. Mice infused with psEVs from healthy normal pregnancies showed an increase in plasma insulin levels, whereas those infused with GDM psEVs did not exhibit any change in insulin levels. Similarly, islets from mice infused with normal pregnancy psEVs demonstrated enhanced GSIS at both 2.8 mM and 16.7 mM glucose concentrations. In contrast, no significant change in insulin secretion was observed in islets from mice who received GDM psEVs under the same conditions following GSIS. These findings suggest that psEVs from normal pregnancies promote insulin secretion in β cells, while GDM psEVs fail to elicit the same effect, potentially attenuating insulin release (85).

The effects of normal pregnancy and GDM psEVs isolated from human and mouse placental explants on mice islets and the mouse β cell line, Mouse Insulinoma (MIN) 6, have also been evaluated. In this model, GDM was mimicked by feeding pregnant mice a high-fat diet, confirmed through glucose and insulin tolerance tests. Mouse islets treated with mouse psEVs isolated from GDM-exposed mice exhibited reduced insulin content, decreased GSIS, and increased apoptosis *in vitro*. *Wang et al.* also studied GDM psEVs isolated from human placentae and observed that miR-320b was upregulated, a microRNA also found to be elevated in the plasma of newly diagnosed patients with type 2 diabetes mellitus. The authors then increased miR-320b levels in MIN6 cells and mouse islets through transfection, which resulted in decreased GSIS and increased apoptosis, though insulin synthesis and content remained unaffected. These findings suggest that miR-320b, carried by human GDM psEVs, may play a critical role in β-cell dysfunction observed in GDM (66).

In our research group, *Kandzija et al.* identified that both medium/large-placental EVs and psEVs express dipeptidyl peptidase IV (DPP-IV), an enzyme responsible for degrading glucagon-like peptide-1 (GLP-1). GLP-1 is an incretin hormone known to stimulate GSIS and promote β-cell proliferation and survival (86). The study demonstrated that DPP-IV carried by placental EVs is active, can be inhibited by DPP-IV inhibitors, and is capable of breaking down GLP-1 *in vitro*. Furthermore, DPP-IV-expressing placental EVs, identified by PLAP-positive markers, were detected in the plasma of pregnant women. When comparing DPP-IV activity between normal pregnancy and GDM, placental EVs from GDM pregnancies exhibited significantly higher activity—2-fold greater in medium/large EVs and 5-fold greater in psEVs. Moreover, DPP-IV expression in GDM medium/large EVs was almost 9-fold higher than in normal pregnancy. However, due to the limitations of flow cytometry, it was not possible to reliably analyse DPP-IV expression on psEVs (87).

Taken together the published data suggest that, like placental hormones, psEVs from normal pregnancies enhance β-cell function in mouse models, while GDM-derived psEVs contribute to β-cell dysfunction, impairing insulin secretion, and promoting β-cell damage.

1.7 Gestational diabetes mellitus

GDM is defined as an elevated blood glucose that first appears during pregnancy but does not meet the criteria for overt diabetes (10, 88). GDM is the most common medical complication of pregnancy and according to the International Diabetes Federation (IDF) affects approximately one in seven live births globally (10, 89). GDM is a complex, multifactorial disorder affecting the homeostasis of insulin, glucose, and other energy sources during pregnancy which may persist after childbirth (14). The condition poses significant health risks for both mother and child both during and after pregnancy (10). It also represents a considerable financial burden, with annual costs estimated at $1.6 billion in the United States of America (USA) and $5.5 billion in China (10, 88). The prevalence of GDM is rising worldwide, driven by several factors such as increasing rates of type 2 diabetes mellitus, obesity in women of reproductive age, and advancing maternal age (14).

1.7.1 Classification

The classification and diagnostic criteria for diabetes in pregnancy have evolved significantly over time, becoming more refined. Contemporary classification systems and terminology describing diabetes in pregnant women now more clearly differentiate between women with pregestational diabetes who conceive and those with hyperglycaemia first detected in pregnancy (10, 14). Pregestational diabetes includes type 1 diabetes mellitus,

type 2 diabetes mellitus, and other types of diabetes such as cystic fibrosis-related diabetes, steroid/medication-induced diabetes, and monogenic diabetes.

Hyperglycaemia first diagnosed in pregnancy is now subclassified into two separate categories, namely “overt diabetes mellitus during pregnancy” and GDM (10, 14). In some instances, the term “diabetes mellitus in pregnancy” is used to represent “overt diabetes mellitus in pregnancy” (14).

GDM, specifically, is recognised as a heterogeneous condition, with variations in both the timing of diagnosis—either early or later in pregnancy—and underlying pathophysiology, which may involve insulin resistance or deficiency.

Based on the timing of diagnosis, GDM can be classified as either early- or late-onset. Early GDM is diagnosed before 20 weeks of gestation, whilst late GDM is identified between 24 and 28 weeks after negative screening for early-onset GDM (10, 14).

Early-onset GDM is associated with a greater need for insulin, and higher complication rates (10, 14). The impact of late-onset GDM on pregnancy outcomes is well-documented. The Hyperglycaemia and Adverse Pregnancy Outcomes (HAPO) study revealed a linear relationship between maternal glycaemia and complications arising later in pregnancy (90).

1.7.2 Epidemiology

GDM affects up to 14% of pregnancies globally (10, 14, 88). In some regions, particularly where screening practices are more rigorous, this figure can rise up to 40% (88). Early-onset GDM contributes to 30–70% cases and complicates up to 37% of all pregnancies (10, 14,

91). The prevalence of a subset of early-onset GDM who are diagnosed before 12 weeks gestation ranges between 0.7% and 14.2% (10). However, the overall prevalence of GDM, in both the early- and late-onset groups, varies significantly between countries, from as low as 0.7% to as high as 36.8% (14, 88). These variations are influenced by differences in screening methods, diagnostic criteria, and the underlying population's risk factors, including socioeconomic and cultural determinants (88).

Ethnicity influences GDM prevalence, with genetic, biological, and socioeconomic factors all contributing to risk. Susceptibility to GDM is increased by genetic alleles, such as the Pacific-specific CREB3 Regulatory Factor (CREBRF) rs373863828 allele in Polynesian women (88). Ethnic differences in patterns of diagnosis are also observed; for example, Asian women are more likely to be diagnosed based on the oral glucose tolerance test (OGTT), while European women a more commonly diagnosed using fasting glucose levels (88).

Geographically, GDM prevalence is lowest in North America and the Caribbean (7.1%) and Europe (5.4–11.7%), while the highest rates are seen in the Middle East and North Africa (27.6%) (88). Prevalence is lowest in middle-income countries while low- and high-income countries exhibit similar rates of GDM (88). However, there remains a scarcity of comprehensive global studies on GDM prevalence, leaving gaps in our understanding of its true prevalence.

1.7.3 Pathophysiology

GDM is primarily characterised by the inability of insulin secretion to adequately compensate for the increasing insulin resistance that occurs during pregnancy (10, 14). This

can be due to pre-existing defects in insulin secretion, which are unmasked by the rise in insulin resistance that occurs from mid to late pregnancy or increases in insulin resistance that are greater that can be counterbalanced by normal insulin secretion (10, 14). This resembles type 2 diabetes mellitus, where a relative insulin secretory deficit arises in the setting of increased insulin resistance coupled with impaired β-cell function and mass (10, 14). This imbalance leads to decreased glucose uptake, increased hepatic gluconeogenesis, and maternal hyperglycaemia (10, 14).

However, it is increasingly recognised that the pathophysiology of GDM is complex with distinct subtypes that differ—ranging from a primarily insulin resistance subtype to a predominant insulin deficient subtype (10, 14). These may be present early during pregnancy or only emerge at a later point in gestation (10, 14). The contribution of insulin resistance and deficiency vary between women with GDM. Insulin resistance is prevalent in 50–60% of GDM cases, while insulin deficiency affects 15–30%, irrespective of whether the diagnosis is made in early or late pregnancy (10, 14). Notably, insulin resistance tends to be associated with a higher risk of complications, whereas insulin deficiency, if adequately treated, results in outcomes comparable to pregnancies without GDM (10, 14). This heterogeneity underlines the importance of differentiating between insulin-resistant and insulin-deficient forms of GDM.

1.7.3.1 Insulin resistance

Women with GDM often exhibit insulin resistance even before pregnancy and during pregnancy the severity and level of resistance varies depending on the GDM subtype. Genetic and non-genetic factors may contribute to insulin resistance. For example, genetic abnormalities in glucokinase gene regulation affect glucose sensing while non-genetic

contributors include obesity, lack of physical activity, and unhealthy lifestyle choices (10, 14). Metabolomic studies show dietary choices play a role as elevated triglycerides and branched-chain amino acids are strongly associated with insulin resistance (10, 14).

1.7.3.2 Insulin deficiency

With respect to insulin deficiency, many women who develop GDM may have underlying or pre-existing β-cell dysfunction, which could be present even before pregnancy and may become evident early in gestation, independent of changes in insulin resistance. Pre-pregnancy hyperlipidaemia and elevated serum triglycerides cause lipotoxic damage to β-cells further impairing insulin secretion, while GSIS is altered due to fatty acids (14).

During pregnancy, insulin deficiency has genetic and pregnancy-related determinants. Before pregnancy, genetic factors—such as shared β-cell loci between GDM and type 2 diabetes mellitus — can predispose women to insulin deficiency (10, 14). β-cell dysfunction may also be influenced by alterations in circulating hormones during pregnancy, such as leptin, which may impair β-cell function to reduce insulin secretion and contribute to GDM onset (10, 14). Failure of β-cell mass expansion is also thought to be a key factor in this process (14).

1.7.3.3 Placental biology in gestational diabetes mellitus

The placenta is altered in GDM pregnancies and is intricately linked to the associated pathophysiology. In early GDM, placental alterations may affect the release of hormones and EVs, which impact the maternal adaptation to pregnancy (10). By term, multiple structural and functional changes occur in GDM placentae. Metabolic disturbances lead to the accumulation of triglycerides, glycogen, and collagen within the placenta, which results

in excess maternal nutrient supply and foetal hyperinsulinaemia (10). Terminal villi undergo hypervascularisation to compensate for oxygen deficits caused by foetal hyperinsulinaemia which develops as early as 14 weeks of gestation (10).

Furthermore, epigenetic changes and modifications in placental signalling pathways, including those involving insulin, insulin-like growth factors, cytokines, mTOR, and PPAR activators also occur (10). Metabolic and pro-inflammatory factors, as well as exosomal miRNAs, also play significant roles in these processes (10). These changes reflect the placenta's response to a compromised *in utero* environment, aiming to alter maternal adaptation to pregnancy and support foetal development and growth despite metabolic challenges.

1.7.4 Risk factors for gestational diabetes mellitus

Risk factors for GDM can be categorised as either modifiable or non-modifiable. Modifiable factors include maternal body mass index (BMI) (overweight (BMI 25–29.99 kg/m^2) or obesity (BMI $\geq$ 30 kg/m^2)), physical inactivity, and exposure to passive smoking. In contrast, non-modifiable factors are a history of GDM in a previous pregnancy, which is the strongest risk factor for GDM, advancing maternal age, a family history of diabetes mellitus, hypothyroidism, a history of stillbirth, preterm delivery, congenital malformations, and previous macrosomia (10, 14). Furthermore, maternal hypertension, both before and during early pregnancy, increases the risk of GDM development (14).

Ethnicities at increased risk for development of type 2 diabetes mellitus, such as South and Far-east Asians, Hispanic, Black and Native Americans, Aboriginal and Torres Strait Islanders, and Middle Easterners are also associated with an increased risk of GDM (10, 14).

Additionally, studies indicate an association between polycystic ovary syndrome and GDM, although this link is significantly reduced after adjusting for maternal BMI (10, 14). Other recognised risk factors include multiparity, twin pregnancies, a history of perinatal complications, maternal small-for-gestational-age or large-for-gestational-age (LGA) births, low-fibre and high-glycaemic load diets, higher dietary fat intake, lower carbohydrate intake, and the use of medications such as glucocorticoids and antipsychotic agents (10, 14).

1.7.5 Screening and diagnostic challenges

The current diagnosis of GDM is primarily based on the OGTT which is supported by the findings in the landmark HAPO study which evaluated over 25,000 pregnant women at 24–32 weeks' gestation using the 75 g, 2-hour OGTT (90). The study found a continuous, positive linear relationship between maternal fasting, 1-hour, and 2-hour glucose levels and an increased risk for adverse perinatal outcomes (90). Haemoglobin A1c is considered insufficiently sensitive to be used as a screening tool for the diagnosis of GDM (88). Screening approaches and diagnostic thresholds for GDM remain a contentious issue with guideline recommendations differing globally (14, 88, 91). Screening for GDM is recommended between 24 and 28 weeks of gestation (14, 88). The accepted criteria from several organisations and guidelines for the diagnosis of GDM and overt diabetes in pregnancy are detailed in Table 1.2.

Table 1.2: Current recommendations for the diagnosis of gestational diabetes mellitus.

1-step approach		
Method	**Diagnosis**	**Organisation**
75 g 2-hour OGTT		
Fasting glucose 5.1 - 6.9 mmol/L 1-hour glucose > 10 mmol/L 2-hour glucose 8.5 - 11 mmol/L	GDM	IADPSG (92), EBCOG (93), WHO (94), FIGO (95), ADIPS (96), ADA (97), JDS (98), Endocrine Society (99)
75 g 2-hour OGTT		
Fasting glucose ≥ 5.6 mmol/L 2-hour glucose ≥ 7.8 mmol/L	GDM	NICE (100)
75 g 2-hour OGTT		
Fasting glucose ≥ 7.0 mmol/L 2-hour glucose ≥ 11.1 mmol/L Random glucose ≥ 11.1 mmol/L Haemoglobin A1c ≥ 6.5%	Overt diabetes in pregnancy, Diabetes mellitus in pregnancy, Type 2 diabetes mellitus	IADPSG, EBCOG, WHO, FIGO, ADIPS, ADA
2-step approach		
Method	**Diagnosis**	**Organisation**
50 g 1-hour GCT ≥ 7.8 mmol/L	Move to second step	ADA
100 g 3-hour OGTT		
Fasting glucose ≥ 5.3 mmol/L 1-hour glucose > 10 mmol/L 2-hour glucose ≥ 8.6 mmol/L 3-hour glucose ≥ 7.8 mmol/L	GDM	ADA

*ADA - American Diabetes Association, ADIPS - Australian Diabetes in Pregnancy Association, EBCOG - European Board and College of Obstetrics and Gynaecology, FIGO

- International Federation of Gynecology and Obstetrics , GCT - Glucose Challenge Test, GDM - Gestational Diabetes Mellitus, IADPSG - International Association of the Diabetes and Pregnancy Study Groups, JDS - Japan Diabetes Society, NICE - National Institute for Health and Care Excellence, OGTT - Oral Glucose Tolerance Test, WHO - World Health Organization.

There is ongoing debate regarding who should undergo screening. This stems from the finding that the HAPO study did not identify specific glucose thresholds at which complications increased significantly (90). Universal screening using the one-step approach is endorsed by several leading organisations, including the International Association of Diabetes and Pregnancy Study Groups (IADPSG), the World Health Organization (WHO), the International Federation of Gynaecology and Obstetrics (FIGO), and is also supported by the American Diabetes Association (ADA), the Endocrine Society, the Australasian Diabetes in Pregnancy Society (ADIPS), the Japan Diabetes Society (JDS), and the European Board and College of Obstetrics and Gynaecology (EBCOG). However, despite this widespread endorsement, the one-step approach has not been universally adopted (14, 88, 91). For example, the National Institutes of Health (NIH) does not currently recommend universal screening, citing a lack of randomised controlled trial (RCT) evidence showing substantial benefit (14, 88). In low- and middle-income countries, universal screening poses practical challenges due to limited healthcare resources (14, 88, 91). Therefore, many regions adopt a risk-based screening approach, focusing on women with known risk factors for GDM.

It also remains unclear which approach, the one-step or two-step method, is superior. Meta-analyses comparing the two have found no significant differences in pregnancy complications using either approach, despite the one-step approach diagnosing 6.6% more cases of GDM than the two-step approach (14, 88). The Gestational Diabetes Mellitus Study of Detection Thresholds (GEMS) trial found that while the one-step approach doubled the prevalence of GDM diagnoses, it did not lead to better pregnancy outcomes compared to the two-step approach (101). The Pragmatic Randomised Clinical Trial of Screening in Gestational Diabetes Mellitus (ScreenR2GDM), a recent large-scale RCT in the USA,

compared the one-step and two-step screening approaches in nearly 24,000 women. While the one-step approach doubled the rate of GDM diagnoses (16.5% vs. 8.5%), there were no significant differences in pregnancy complications, including LGA infants, gestational hypertension, or caesarean section delivery rates (102). These findings have reignited the debate on the cost-effectiveness and clinical benefit of the one-step approach. Despite this, the one-step approach is more widely used due to its' simplicity and ease of administration compared to the two-step approach.

The timing of GDM testing is also not clear. Early GDM screening, based on criteria from the International Association of Diabetes and Pregnancy Study Groups (IADPSG), has shown inconsistent results, with repeat testing in early and late pregnancy lacking reproducibility (14, 88). This is partly due to the natural decline in maternal fasting glucose from six weeks gestation onward. The IADPSG has since adjusted the early pregnancy fasting glucose threshold to 5.9 mmol/L to address these variations (14, 88). Early screening for GDM remains a contentious issue and while early diagnosis and treatment have shown benefits, early screening alone has not been linked to improved perinatal outcomes (14, 88).

1.7.6 Complications

The likelihood of adverse pregnancy outcomes is increased in GDM, and elevated maternal glucose levels are linearly associated with an increased risk of perinatal complications, both in early and late pregnancy (14, 88, 90). This relationship continues post-pregnancy, with long-term cardio-metabolic risks for both the mother and the child (10, 14, 88). Although the type and severity of complications can vary based on the geographic region, obesity rates, screening practices, and obstetric care (88).

1.7.6.1 Short-term complications

Women with GDM face an elevated risk of several obstetric complications (14, 88). These include a higher likelihood of interventions such as induction of labour, assisted deliveries, and caesarean section, as well as delivery-related complications like perineal lacerations and uterine rupture (14, 88). These risks are largely driven by conditions such as foetal macrosomia and polyhydramnios and occur even when non-insulin therapies are initiated between 24- and 28-weeks' gestation (14, 88). The need for insulin treatment itself further increases the risk of complications, doubling the rate of neonatal intensive care admissions (103).

GDM is also strongly associated with pre-eclampsia, linked to impaired placentation and compromised placental function due to insulin resistance and inflammatory pathway activation (14). Other maternal complications include polyhydramnios, urinary tract or vaginal infections, postpartum haemorrhage, and difficulties with breastfeeding initiation or maintenance (14, 88). GDM can also affect psychological well-being, with women with GDM experiencing higher rates of depression, anxiety, and stress (88). Feelings of stigma, guilt, and shame are also common in these women (88). Additionally, GDM has been linked to poorer oral health outcomes, including gingivitis, tooth erosion, dental caries, and periodontitis (88).

For the foetus, GDM significantly increases the risk of preterm birth, LGA status and neonatal intensive care unit admission, particularly when insulin treatment is required during pregnancy (14, 88). Neonates are also at a higher risk of respiratory distress syndrome, transient tachypnea of the newborn, birth trauma, hypoglycaemia, polycythaemia, jaundice, and stillbirth (14, 88). Additionally, GDM increases the likelihood of congenital

malformations, cardiomyopathy, and various forms of birth trauma, such as shoulder dystocia, bone fractures, and brachial plexus injuries (14, 88).

A systematic review of 26 studies further highlights that early GDM presents a greater risk for several complications, including caesarean sections, LGA births, preterm delivery, congenital abnormalities, hypertension, pre-eclampsia, shoulder dystocia, and induction of labour, in comparison to late-onset GDM (104). Early GDM is also associated with higher rates of perinatal mortality, neonatal morbidity, and insulin use compared to GDM diagnosed at 24–28 weeks (105).

1.7.6.2 Long-term complications

In the long term, women with GDM are at a markedly increased risk of developing type 2 diabetes mellitus, cardiovascular diseases, and metabolic syndrome (10, 14). Women with a history of GDM are 7–10 times more likely to develop type 2 diabetes mellitus within five years postpartum, with a tenfold increase in lifetime risk (10, 14). Furthermore, about 31% of type 2 diabetes mellitus cases in women of reproductive age are attributable to GDM (10, 14). Cardiovascular disease risk is doubled in the first decade after pregnancy, with higher incidences of hypertension, dyslipidaemia, coronary heart disease, stroke, and heart failure (10, 14). Additionally, GDM recurrence rates range from 30% to 84% in subsequent pregnancies (10, 14).

The long-term effects of GDM also extend to the offspring as the maternal diabetic environment can affect foetal organ development and foetal programming leading to long-term health challenges for the child (10, 14). Children born to mothers with GDM have a higher risk of obesity, type 2 diabetes mellitus, and cardiovascular diseases later in life (10,

14). The HAPO study demonstrated a direct correlation between maternal glucose levels and the risk of childhood obesity and impaired glucose tolerance in offspring (90). Other long-term effects include neurodevelopmental defects such as autism spectrum disorder and attention-deficit hyperactivity disorder (10, 14). Structural and functional alterations in organ development due to GDM are linked to epigenetic changes, including DNA methylation, histone modifications, and non-coding RNAs, which can influence metabolic outcomes and increase the risk of metabolic syndrome, hyperinsulinaemia, and hypertension in the child (10, 14).

1.7.7 Therapy

The primary goal of GDM therapy is to achieve maternal normoglycaemia, as maintaining near-normal glucose levels can help reduce excessive foetal growth and significantly lowers the risk of complications for both mother and child (14, 88).

The Australian Carbohydrate Intolerance Study in Pregnant Women (ACHOIS) trial, a landmark RCT involving 1,000 participants, was the first to demonstrate the benefits of treating GDM in reducing perinatal complications (106). Women who received a combination of dietary advice, self-monitoring of blood glucose, and insulin therapy (if required) to achieve glucose targets experienced significantly fewer serious perinatal complications compared to those who received routine care (106). Furthermore, the intervention reduced rates of macrosomia, pre-eclampsia and improved maternal quality of life (106).

Numerous RCTs and meta-analyses have confirmed that treating GDM, even when diagnosed later in pregnancy, reduces the risk of complications (14, 88). More recently, the

focus has shifted to the potential benefits of early treatment in women with GDM. The Treatment of Booking Gestational Diabetes Mellitus (TOBOGM) trial demonstrated that women diagnosed with early GDM who received treatment before 20 weeks—particularly around 14 weeks—experienced better pregnancy outcomes compared to those whose diagnosis and treatment were delayed (107). Early identification and intervention in GDM improve maternal quality of life, increase breastfeeding initiation rates, and even reduce the risk of postpartum depression (14).

1.7.7.1 Self-monitoring of blood glucose

Monitoring blood glucose levels through self-monitoring of blood glucose is essential, although glucose targets for treatment vary internationally (14). Some evidence suggests that lower glucose targets may improve outcomes, though this has not yet been confirmed in large RCTs (14). Use of continuous glucose monitoring (CGM) is not widely supported by current evidence (88).

Treatment targets for fasting, 1-hour, and 2-hour postprandial plasma glucose levels are generally consistent across different guidelines. The American Diabetes Association (ADA), National Institute for Health and Care Excellence (NICE), and Japan Diabetes Society (JDS) all recommend aiming for a fasting plasma glucose level below 5.3 mmol/L. In contrast, the Australasian Diabetes in Pregnancy Society (ADIPS) suggests a slightly lower target of under 5.0 mmol/L. For 1-hour postprandial glucose, the ADA, NICE, and JDS recommend a target of under 7.8 mmol/L, while ADIPS advises aiming for under 7.4 mmol/L. Regarding 2-hour postprandial glucose, the ADA, JDS, and ADIPS all recommend a target of under 6.7 mmol/L, with NICE recommending a slightly lower target of under 6.4 mmol/L (96-98, 100).

1.7.7.2 Lifestyle intervention

Lifestyle interventions and medical nutrition therapy are the cornerstone of managing GDM. Globally, the first-line approach focuses on modifying carbohydrate intake, as carbohydrates are the primary determinant of maternal postprandial glucose levels. Medical nutrition therapy aims to improve the quality and distribution of carbohydrates, emphasising low glycaemic index foods. While no specific dietary regimen is universally preferred, current guidelines recommend that carbohydrates make up between 33–55% of total energy intake (14, 88, 107).

1.7.7.3 Medical management

For medical management, insulin remains the treatment of choice when lifestyle interventions fail to maintain glucose levels within target ranges. Both human and analogue insulin are used, with regimens tailored to the individual and their socio-economic circumstances (14, 88, 107). Metformin is considered a safe and effective alternative to insulin, with systematic reviews and meta-analyses showing that it reduces adverse maternal and neonatal outcomes compared to insulin and carries a lower risk of hypoglycaemia. However, metformin can cross the placenta, raising concerns about potential long-term effects on offspring, particularly related to metabolic programming (14, 88, 107). Glyburide, a sulfonylurea, has been shown to improve glycaemia but is associated with higher neonatal morbidity compared to insulin, limiting its widespread use. Other drugs, such as GLP-1 agonists and DPP-IV inhibitors, are not recommended due to insufficient safety data (14, 88, 107).

1.7.7.4 Obstetric management

Obstetric management of GDM requires early evaluation, risk factor stratification, and tailored treatment plans. Detailed ultrasounds between 18–20 weeks and foetal surveillance from 38 weeks, including cardiotocography and biophysical profiles, are recommended, though evidence on their impact on foetal outcomes is unclear. The timing of delivery remains complex, depending on maternal glucose control and foetal factors. Current guidelines recommend delivery by 41 weeks for women managing GDM with diet alone, and between 39 and 40 weeks for women requiring pharmacotherapy. However, the approach must be individualised to each clinical and resource setting, as intensive surveillance may not be practical in low-resource environments (14, 88, 107).

1.7.7.5 Long-term management

Long-term management of women with GDM involves close monitoring postpartum, with a repeat OGTT or fasting glucose test recommended at 6–12 weeks after delivery to assess maternal glucose status (14, 91). Women should also undergo regular assessments of cardiometabolic health and implement lifestyle changes to reduce their elevated risk of type 2 diabetes mellitus and cardiovascular disease (91). Supporting family-wide lifestyle improvements, including healthy diet, physical activity, and weight management for both the mother and her offspring, is essential for reducing long-term health risks (91).

1.8 Models to study islet and β-cell function in human pregnancy

1.8.1 Limitations of mouse models

1.8.1.1 Human versus mouse islets

Although human and mouse islets secrete insulin and glucagon to maintain glucose homeostasis they differ significantly in several respects.

In terms of cellular composition, β cells constitute the majority of cells in both human and mouse islets, yet mouse islets have a higher proportion of β cells, comprising about 75 ± 10% of the total islet volume, compared to 55 ± 17% in human islets (108). Conversely, α cells make up a larger portion of human islets, accounting for approximately 40 ± 19%, whereas they represent only 15 ± 6% in mouse islets (109-112). δ cells also differ between the species, comprising up to 22% of human islets, but under 10% in mice, whilst the other cell types represent < 1% of total islet composition in both species (113) (Figure 1.4)

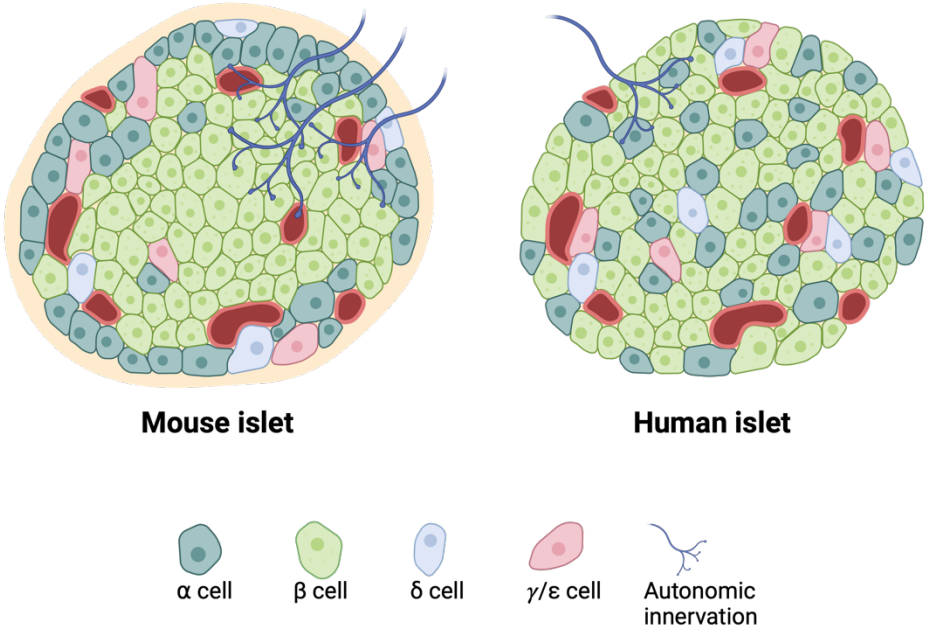

Figure 1.4. Schematic comparing the architecture and innervation of pancreatic islets in mice and humans. Mouse islets display a more organised architecture with a mantle of α, γ, and ε cells around the periphery surrounding an inner core of β cells, while human islet cells are more interspersed. Additionally, mouse islets are more densely innervated, whereas innervation in human islets is comparatively sparse. Created with BioRender.com released under a Creative Commons Attribution-NonCommercial-NoDerivs 4.0 International license.

Architecturally, mouse islets typically feature a core of β cells, encircled by a peripheral "mantle" of α, δ, and other cell types. In human islets, however, this arrangement is more integrated, with α and δ cells interspersed throughout the islet, appearing in both the islet centre and periphery (114). This interspersed organisation in human islets impacts islet cellular interactions, as a larger proportion of β cells maintain heterotypic contacts—direct interactions with other cell types—compared to mouse islets. In humans, 71-80% of β cells are in direct contact with other islet cell types, whereas in mice, 71% of β cells primarily form homotypic contacts (direct contact with β cells), while only 28% of β cells form heterotypic contacts (111, 112). Furthermore, in human islets some β cells have even been shown to partially envelop α cells, which is not the case in mouse islets (13, 109, 110, 113, 115-118).

The internal structure of supporting tissues within islets differs between humans and mice. Typically, blood is supplied to the islet core and flows outward to the periphery via the microvasculature. In mouse islets, the distinct core-mantle arrangement means that β-cell secretory products are transported from the core to the peripheral α and δ cells, allowing β-cell products to influence these cell types sequentially. In contrast, the dispersed arrangement of cells within human islets enables simultaneous exposure of all cell types to both the blood flow and the secretory products from all the different islet cell types (13). In mice, β cells in the islet core lack their own basement membrane and are in direct contact with the vascular basement membrane surrounding the islet capillaries. The vascular basement membrane maintains islet blood vessels and provides growth factors necessary for preserving islet cell characteristics and supporting β-cell proliferation. Human islets, in contrast, contain two distinct basement membrane layers: the vascular basement membrane

and a peri-islet basement membrane. This peri-islet basement membrane extends into the islet along vascular pathways and expresses a unique set of laminin isoforms (109).

Pancreatic islets are innervated by the autonomic nervous system, but the patterns and functional implications of this innervation differ between humans and mice. In mice, both sympathetic and parasympathetic axons directly innervate the islet blood vessels and islet cells, with equal parasympathetic input to α and β cells, while sympathetic input predominantly innervates α cells. This direct innervation modulates hormone secretion and blood flow, and autonomic signals play a significant role in maintaining GSIS in mouse β cells. In contrast, parasympathetic innervation in human islets is sparse and the sympathetic nervous system, primarily, innervates the vascular smooth muscle cells, suggesting that islet function is modulated indirectly by changes in blood flow rather than direct neuronal control. Notably, human α cells have been found to express vesicular acetylcholine transporter (vAChT), choline transporter 1 (ChT1), and choline acetyltransferase (ChAT), indicating that they can synthesise and release acetylcholine. Acetylcholine release from α cells enhances insulin secretion from β cells, effectively replacing the parasympathetic input seen in rodents. This divergence in innervation patterns suggests that, while direct autonomic input fine-tunes hormone secretion and blood flow in mouse islets, human islets may rely more on acetylcholine-mediated intra-islet paracrine signalling for coordinated regulation (109, 110, 113).

The regenerative capacity of β cells through proliferation is well documented in mice, but remains controversial in humans, as adult human β cells are largely quiescent, with a replication rate of less than 0.1% (13, 109, 110, 113, 115-118). Unlike mouse β cells, human β cells show minimal proliferation under most conditions, largely due to age-dependent

epigenetic regulation of specific genes (119). Additionally, the genetic profile regulating β-cell proliferation differs significantly between humans and mice (119). Instead, it has been proposed that in humans islet mass expansion may result from neogenesis, involving the formation of new islets, rather than from β-cell replication as seen in rodents (27, 120).

The differences in cytoarchitecture, vasculature and innervation mean that intra-islet cell signalling and ultimately regulation of β cell function differ between mice and humans. With a higher α:β cell ratio, greater direct contact between different islet cell types, distinct vascular and autonomic nerve supply, and a limited role for β-cell regeneration, paracrine signalling within islets (Figure 1.5) has emerged as a crucial mechanism influencing β-cell function (121). Due to these differences, it remains unclear whether observations in β cell and islet mouse models are applicable to human biology. These differences underscore the importance of cautious interpretation when translating findings from mouse models to human biology.

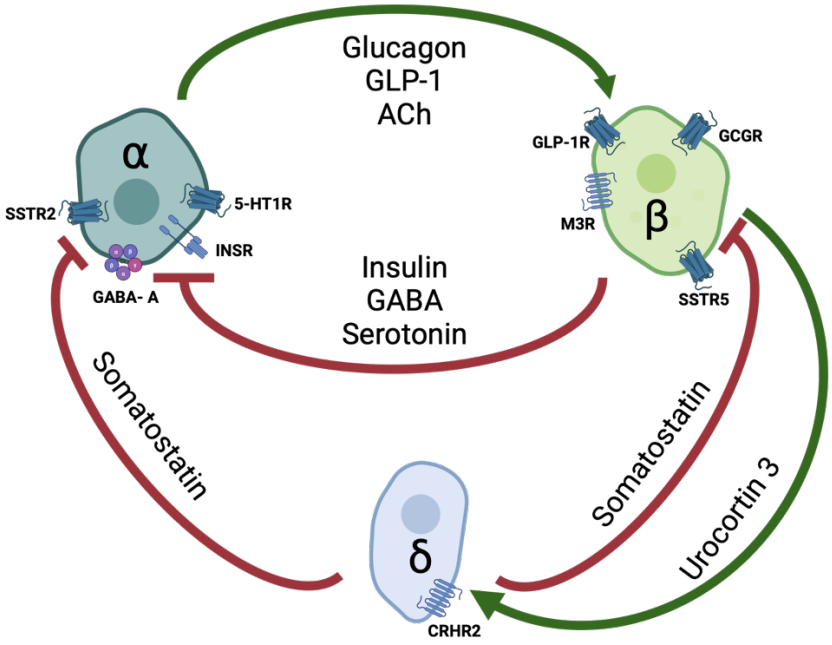

Figure 1.5. A schematic illustrating the mechanisms of intra-islet paracrine signalling among human islet cell types. Green arrows indicate stimulatory signals, while red arrows represent inhibitory signals. Glucagon, glucagon-like peptide-1 (GLP-1), and acetylcholine (ACh) secreted by α cells, stimulate β cells to enhance insulin secretion. In turn, β cells release insulin, gamma amino butyric acid (GABA), and serotonin, which inhibit α cell activity and reduce glucagon secretion. Additionally, β cells secrete urocortin to activate δ cells, prompting them to release somatostatin. Somatostatin, produced by δ cells, exerts an inhibitory effect on both α and β cells, helping to modulate hormone release (110, 121). Created with BioRender.com released under a Creative Commons Attribution-NonCommercial-NoDerivs 4.0 International license.

*Ach - acetylcholine, CRHR – corticotropin-releasing hormone receptor, GABA - gamma amino butyric acid, GABA-A gamma amino butyric acid receptor A, GLP-1 – glucagon-like peptide-1, GLP-1R - GLP-1 receptor, GCGR - Glucagon receptor, 5-HT1R - 5-hydroxy tryptamine receptor 1, INSR – insulin receptor, M3R - muscarinic receptor, SSTR somatostatin receptor.

1.8.1.2 Human versus mouse pregnancy

While mouse models have significantly advanced scientific understanding, there are concerns about their limitations in accurately reflecting human physiology, as work done in mice does not always directly translate to efficacy in humans (122). This limitation is particularly relevant in pregnancy research, where structural and functional differences between mice and humans mean that mouse models may not be ideal for understanding pregnancy-related adaptations in humans (123).

Key differences between mice and humans include variations in placental structure, function, and foeto-placental development (111, 112). Structurally, while both species have haemochorial placentas, where maternal blood is in direct contact with the chorionic trophoblast, human placentas are discoid in shape, whereas mouse placentas are labyrinthine (123). Additionally, humans have a single syncytiotrophoblast layer directly bathed in maternal blood, supporting nutrient and gas exchange. In contrast, the mouse placenta has three distinct layers separating maternal and foetal blood: the syncytiotrophoblast, cytotrophoblast, and an endothelial layer. Nutrient exchange also varies; in humans, blood enters the intervillous space for diffusion, while in mice, exchange occurs between foetal and maternal capillaries within the labyrinthine structure (123).

The degree of trophoblast invasion following placentation also differs. The human placenta is deeply invasive, with trophoblasts penetrating the endometrial layer to access spiral arteries, ensuring sufficient blood flow to support the developing foetus. In mice, however, trophoblast invasion is more superficial, reflecting the lower nutritional demands of smaller foetuses (123).

Functionally, the endocrine roles of the placenta differ between the species. In mice, the placenta prominently secretes placental lactogens and prolactin, which are critical for pancreatic islet adaptations during mouse pregnancy. In humans, however, the placenta produces high levels of human chorionic gonadotropin, progesterone, as well as placental lactogen, each playing essential roles in maintaining pregnancy and supporting maternal metabolic adaptations (123).

In later stages of pregnancy, the use of mouse models has been criticised for additional limitations. Since organ development in mice largely occurs after birth, mice may not adequately model late-pregnancy conditions that involve complex placental interactions, such as pre-eclampsia, foetal growth restriction, and GDM (111, 112). These distinctions highlight that while mouse models provide valuable insights, caution is warranted when extrapolating findings to late-stage pregnancy adaptations and diseases in human pregnancy.

While mouse models have been essential in providing foundational insights into islet adaptations during pregnancy, the distinct differences between human and mouse islet biology—as well as between human and mouse pregnancies—underscore the importance of complementary studies using human tissues. Additionally, it remains controversial whether enhanced β-cell function via β cell mass expansion from proliferation is crucial in human pregnancy (13). Therefore, it is crucial to investigate these mechanisms in human model systems to determine the extent to which findings in mice translate to human pregnancy.

1.8.2 Human-based model systems

1.8.2.1 Human tissue

Research in islet biology is particularly challenging when it comes to human studies, as obtaining well-preserved pancreatic tissue is difficult. This is primarily because pancreatic samples can only be collected post-mortem, and not all autopsy samples are suitable as the post-mortem release of pancreatic digestive enzymes leads to rapid auto-digestion of the tissue. This process causes necrosis, disrupts the architecture of the islets, and degrades islet proteins. (108). Furthermore, studying human pregnancy poses significant practical and ethical challenges, particularly when it comes to obtaining pancreatic tissue from pregnant women.

The Network for Pancreatic Organ Donors with Diabetes (nPOD) at the University of Florida, USA, is the largest global repository of human pancreatic tissue. nPOD collects pancreata from heart-beating organ donors, with cold ischemia times kept under 24 hours from acquisition to processing. This rapid handling minimises post-mortem pancreatic necrosis, preserving high-quality tissue for research purposes. nPOD is one of the few global repositories that provides pancreatic tissue from pregnant women with well-preserved islet architecture and protein expression (124, 125).

1.8.2.2 EndoC-βH3, a human β cell line

The lack of an adequate human β-cell line and challenges in accessing human islets have meant that much of the research using β cells has traditionally depended on mouse islets or mouse-derived cell lines. Mouse β cells are not representative of human β cells, and exhibit transcriptomic differences compared to human β cells (126, 127). Moreover, mouse β-cell lines are not derived from primary rodent β cells but instead originate from insulinoma cells

(a β-cell neuroendocrine tumour), which may not accurately represent normal mouse β-cell physiology, let alone human β-cell biology (128). This obstacle, however, has been addressed to some extent with the development of the human β-cell line, EndoC-βH3. (126, 127). The EndoC-βH3 human β-cell line is derived from human foetal pancreatic tissue, it retains many features of primary human β cells and serves as a valuable *in vitro* model for investigating human β-cell function (126). Using this cell line offers more translatable insights when investigating the mechanisms regulating β-cell biology.

1.9 Hypothesis and aims of this thesis

My hypothesis is that the human islet proteome undergoes significant alterations during pregnancy, leading to changes that alter islet function. Specifically, I hypothesised that the abundance of the PRLR increases in human pregnancy, similar to observations in murine pregnancy. However, in contrast to mice, where β-cells undergo proliferation, the abundance of the 5-HT2B receptor in human β-cells is not increased, as human β-cells are not well described to exhibit proliferation. Additionally, I hypothesised that psEVs influence the biology of pancreatic β-cells and may play a role in enhancing β-cell function during pregnancy.

Aim 1: To characterise the islet proteome of islets from pregnant women and identify changes in protein abundance compared to islets isolated from matched non-pregnant controls. This aim focuses on uncovering specific pregnancy-induced proteomic adaptations in human islets.

Aim 2: To utilise non-biased, reproducible computational analyses to measure, quantify, and compare the structure of islets from pregnant women and non-pregnant controls, including

the whole islet area, α-cell and β-cell area, and the abundance of the PRLR and 5-HT2B receptor.

Aim 3: To investigate the effects of psEVs on the transcriptome and proteome of EndoC-BH3 cells, with the goal of understanding the molecular mechanisms by which psEVs modulate β-cell function.

Aim 4: To evaluate whether psEVs impact insulin gene expression, insulin content, and GSIS in EndoC-BH3 cells, providing insights into the potential functional role of psEVs in modulating β-cell activity during pregnancy.

Chapter 2

General materials and methods

2.1 General methods

2.1.1 Immunoblotting

Laemmli sample buffer (4X) (Bio-Rad, cat. no. 1610747), containing 100 µL of β–2-mercaptoethanol (Sigma, cat. no. M6250) per 900 µL of sample buffer, was added at a 1:3 ratio to cell lysates (40 µg) or small extracellular vesicles (sEVs) (20 µg). Samples were boiled at 90°C for 10 minutes. Boiled samples were separated on 4-15% Mini-PROTEAN TGX precast gel cassettes (Bio-Rad, cat. no. 4568084, 10-well gels, and 4561086, 15-well gels). A Mini Trans-BLOT Cell (Bio-Rad, cat. no. 1703930) was used to transfer proteins onto a polyvinylidene difluoride membrane (Merck Millipore, cat. no. IPFL00010). Membranes were blocked with 5% ECL Prime blocking agent (Cytiva, cat. no. RPN418) for 1 hour and incubated with primary antibodies overnight at 4°C. Membranes were washed in 10% tris-buffered saline (TBS) (Thermo Fisher Scientific, J60764.K2) with 0.1% Tween 20 (TBS-T) (Bio-Rad, cat. no. 1610781) and incubated in secondary antibodies for 1 hour at room temperature. After washing with 10% TBS-T, membranes were then dried in 100% methanol (Sigma, cat. no. 34860), imaged using the Licor Odyssey® CLx Infrared Imaging System (LI-COR Biosciences), and visualised using Image Studio™ software (v5.5.4) (LI-COR Biosciences, available at https://www.licor.com/bio/image-studio-lite/).

2.2.2 Immunocytochemistry

Cells cultured in µ-slide 8-well glass bottom chamber slides (Ibidi, cat. no. 80827) were fixed and permeabilised using 4% paraformaldehyde (Thermo Fisher Scientific, cat. no. 043368.9M). In experiments in which fluorescent dyes were used to label cellular structures, the cells were incubated with the dyes for 15 minutes then washed with phosphate buffered saline (PBS) (Gibco, cat. no. 10010023). In experiments where no further antibody immunostaining was necessary, the cells were imaged at this stage.

In experiments in which fluorescent dyes were not used, this step was omitted. For antibody immunostaining, samples were blocked with 10% goat serum (Sigma, cat. no. G6767) and 0.1% Tween 20 in PBS for 1 hour at room temperature. Primary antibodies were then added and incubated overnight at 4°C. The following morning, the wells were washed with PBS containing 0.1% Tween 20 (PBT) before secondary antibodies were added and incubated at room temperature for 30 minutes. Following this incubation step, the wells were washed with PBT before imaging.

2.2.3 Immunohistochemistry

Slides with formalin-fixed paraffin-embedded (FFPE) tissue sections and cell pellets were used for immunohistochemistry. Immunofluorescence labelling of tissue sections are termed IHC-IF, whilst IHC refers to chromogenic immunolabelling of tissue sections.

2.1.3.1 Immunofluorescence labelling of formalin-fixed paraffin embedded tissue sections and cell pellets

FFPE tissue sections and FFPE cell pellets were first dewaxed and rehydrated. FFPE tissue sections and cell pellets were incubated twice in Histo-Clear (National Diagnostics, cat. no. HS-200) for 5 minutes followed by incubation in a graded ethanol series (Thermo Fisher Scientific, cat. no. 397690025) (100%, 90%, 70% ethanol, and 100% methanol for 1 minute each; final wash in double-distilled water (ddH_2O) for 5 minutes). Antigens were unmasked using heat-induced epitope retrieval (HIER). Slides were incubated in 1X citrate pH 6 (Sigma, cat. no. C9999) or 1X tris-ethylenediaminetetraacetic acid (EDTA) pH 9 (Abcam, cat. no. ab93684) and heated to 100°C for 20 minutes using a microwave. Tissue sections and cell pellets were then blocked with 5% goat serum for 20 minutes at room temperature followed by incubation with primary antibodies overnight at 4°C in a humidity chamber.

Tissue sections and cell pellets were then incubated in secondary antibodies at room temperature for 30 minutes. DAPI (1 μg/mL; Thermo Fisher Scientific, cat. no. 62248) was used to label nuclei. 10% TBS-T was used to wash slides following each antibody incubation step. Autofluorescence was quenched by incubating tissue sections for 5 minutes with the Vector® TrueVIEW® autofluorescence quenching kit (Vector Laboratories, cat. no. SP-8500-15) followed by a 5-minute wash in PBS. Coverslips were mounted onto the slides (Fischer Scientific, cat. no. 12373128) using fluorescent mounting medium (Agilent, cat. no. S302380-2). The slides were dried overnight and then imaged.

2.2.3.2 Chromogenic immunolabelling of formalin-fixed paraffin embedded tissue sections and cell pellets

FFPE tissue sections and cell pellets were dewaxed and rehydrated as described above, with 50% ethanol substituted for 100% methanol. Antigen retrieval was performed as previously described. The VECTASTAIN® Elite® ABC Universal PLUS Kit, Peroxidase (Horse Anti-Mouse/Rabbit IgG) (Vector Laboratories, cat. no. PK-8200) was used for chromogenic immunolabelling of FFPE tissue sections and cell pellets. Endogenous peroxidases were quenched using BLOXALL Blocking Solution for 10 minutes followed by blocking in 2.5% horse serum for 20 minutes at room temperature. Primary antibodies were incubated overnight at 4°C followed by incubation in prediluted biotinylated horse anti-mouse/rabbit IgG secondary antibody for 30 minutes at room temperature. Tissue sections and cell pellets were then incubated in VECTASTAIN Elite ABC Reagent for 30 minutes and the signal developed using ImmPACT 3,3'-Diaminobenzidine (DAB) EqV solution. Slides were washed three times in PBS after incubation in primary and secondary antibodies. Nuclei were counterstained with haematoxylin (Vector Laboratories, cat. no. H3502) followed by dehydration in a graded ethanol series (50%, 70%, 90%, and 100% for a minute each).

Clearing in Histo-Clear for 10 minutes twice was performed, and coverslips mounted using DPX mountant (Sigma, cat. no. 06522) before imaging.

2.4 RNA isolation from cell lines

Cell culture media was removed from dishes and the cells were washed twice in PBS. TRIzol Reagent (Life Technologies, cat. no. 15596026) was added to the cells and then incubated on ice for 10 minutes. Lysed cells were then collected in a DNase free eppendorf tube (Eppendorf, cat. no. 0030108051). RNA, from these samples, was extracted and purified using the Direct-zol RNA Miniprep kit (Zymo Research, cat. no. R2070). An equal volume of 95-100% ethanol was added to the sample lysed in TRIzol reagent and mixed thoroughly. Each sample was then transferred to a Zymo-Spin IICR column which was placed in a collection tube and centrifuged (Eppendorf centrifuge 5417R) at 16,000 *g* for 30 seconds. A maximum of 700 µL could be added to the column and this step was repeated until all the sample volume was processed. For all steps, samples were centrifuged at 16,000 *g* for 30 seconds unless otherwise specified. RNA wash buffer was then added to each column and centrifuged. To remove residual genomic DNA, DNase I was diluted in DNA digestion buffer (1:16) and applied to each column, followed by a 15-minute incubation at room temperature. Direct-zol RNA prewash buffer was added to each column and centrifuged, and this step was repeated. RNA wash buffer was once again added to each column and centrifuged for 2 minutes. Finally, each column was placed in a DNase free eppendorf tube and 50 µL of nuclease-free water added to the column, which was centrifuged to elute isolated RNA from the column.

Eluted RNA quality was then analysed. RNA purity was assessed using the NanoDrop™ 8000 spectrophotometer (Thermo Fisher Scientific, cat. no. ND-8000-GL) using 1 µL of

eluted RNA, measuring 260/280 and 260/230 absorbance ratios. RNA concentrations quantified using the Qubit® 2.0 fluorometer (Thermo Fisher Scientific, cat. no. Q32866) and Qubit™ RNA HS Assay Kit (Thermo Fisher Scientific, cat. no. Q32852). When using the Qubit fluorometer, the Qubit working solution was first prepared by adding Qubit RNA HS reagent to Qubit RNA HS buffer (1:200). Standards were prepared by adding 10 µL of each standard to 190 µL of Qubit working solution. For each sample, 1 µL of eluted RNA was added to 199 µL of Qubit working solution. Standards and samples were then vortexed for 3-5 minutes, incubated for 2 minutes at room temperature, and analysed using the Qubit fluorometer.

2.5 Complementary DNA synthesis from mRNA

The complementary DNA (cDNA) template was produced from extracted RNA using the Lunascript® RT supermix kit (New England Biolabs, cat. no. E3010). Lunascript RT supermix 1X (4 µL) was added to RNA and nuclease free water to a total volume of 20 µL. For each sample, the volume of RNA and nuclease free water added was adjusted to ensure equal RNA concentrations across all samples. The reactions were incubated in the applied biosystems Veriti thermal cycler (Thermo Fisher Scientific, cat. no. 4375305). The settings applied were as follows: primer annealing was held at 25°C for 2 minutes, followed by cDNA synthesis at 55°C for 10 minutes, and finally heat inactivation at 95°C for 1 minute. Transcribed cDNA was diluted 1:5.

2.6 Reverse transcription quantitative polymerase chain reaction

Transcribed cDNA was mixed with TaqMan^{TM} fast advanced master mix (2X) (Thermo Fisher Scientific, cat. no. 4444557), TaqMan^{TM} primers (20X) and nuclease free water (Invitrogen, cat. no. AM3395) to a total reaction volume of 10 µL per well of the reaction

plate (Thermo Fisher Scientific, 10-well plates, cat. no. 4346907 and 384-well plates, cat. no. 4309849). In all reactions, the TaqMan™ primer for the gene of interest and the TaqMan™ primer for the house keeping gene were added to each well. Cq values for the gene of interest was acquired in the FAM channel whilst Cq values for the housekeeping gene were acquired in the VIC channel to ensure Cq values for both primers were measured from the same well. All polymerase chain reactions (PCR) were performed in triplicate and an equal concentration of cDNA used across all reactions. No template controls and no reverse transcriptase controls were used for each sample type and each primer. The analysis was performed using the QuantStudio™ 6 Flex Real-Time PCR system (Thermo Fisher Scientific) and the reverse transcription quantitative polymerase chain reaction (RT-qPCR) was run as follows: polymerase activation was held at 95°C for 20 seconds, followed by 40 cycles of PCR during which 1 second was spent on denature at 95°C, and anneal/extend at 60°C for 20 seconds. Cq values were generated by the QuantStudio™ 6 Flex Real-Time PCR system software, Design & Analysis (v2.6.0). The raw data were exported, and fold changes were calculated using the $2^{-\Delta\Delta Ct}$ method.

2.7 Protein extraction from cell lines

Cell culture media was removed from dishes and cells washed twice in cold PBS. Radio-Immunoprecipitation Assay (RIPA) lysis and extraction buffer (1X) (Thermo Fisher Scientific, cat. no. 89900), containing 1X protease inhibitor (Roche, cat. no. 11873580001) and 1X phosphate inhibitor (Roche, cat. no. 4906837001), was added to cell containing dishes and incubated on ice for 15 minutes. Whole-cell lysates were scraped from culture dishes and collected in low protein binding microcentrifuge tubes (Thermo Fisher Scientific, cat. no. 90410). Collected whole-cell lysates were then centrifuged at 20,000 *g* for 20

minutes at 4°C (Eppendorf centrifuge 5417R). The supernatant was collected, and protein concentrations quantified using a bicinchoninic acid (BCA) assay.

2.8 Bicinchoninic acid assay

Protein concentrations were quantified using the Pierce™ BCA Protein Assay Kit (Thermo Fisher Scientific, cat. no. 23227). Protein concentration standards (2 mg/mL, 1.5 mg/mL, 1 mg/mL, 0.75 mg/mL, 0.5 mg/mL, 0.25 mg/mL and 0.125 mg/mL) were created by diluting 2 mg/mL of bovine serum albumin in ddH_2O. For the blank sample, ddH_2O alone was used. Samples were diluted 1:10 in ddH_2O. Standards, the blank and samples, 12.5 µL each, were loaded in duplicate onto a 96-well flat bottom plate (TPP®, cat. no. Z707902) and 100 µL of BCA reagent (BCA solution and copper II sulphate solution (50:1)) was added to each well. The plate was incubated for 30 minutes at 37°C. Following incubation, the FLUOstat OPTIMA plate reader (BMG Labtech) was used to read the absorbance at 562 nm. Protein concentration of samples was extrapolated based on spectrophotometer readings detected in the standards and these values corrected for the 1:10 dilution.

2.9 Statistical analysis

Prism 10 (GraphPad, 2024) software was used to present all data graphically and perform statistical analyses. Statistical tests were selected based on the characteristics of the acquired data and the comparisons required. Normality of the data was assessed using the Shapiro–Wilk test against a Gaussian distribution. For two-group comparisons, normally distributed data were analysed using the unpaired Student's t-test, while non-parametric data were assessed with the Mann-Whitney test. For comparisons involving more than two groups, parametric data were analysed using a one-way ANOVA and where two independent variables or repeated measures were present, a two-way ANOVA or mixed-effects model

was applied. Post-hoc tests used to compare individual groups included: Dunnett's multiple comparisons test when comparing individual groups to the control group, Šídák's multiple comparisons test for a small number of specific comparisons, and Tukey's multiple comparisons test when all individual groups were compared to each other. For data that did not follow a normal distribution and involved more than two groups, the Kruskal-Wallis test was used, followed by Dunn's multiple comparisons test for post-hoc analysis. Statistical significance was defined as a p-value of less than 0.05.

Chapter 3

Laser-capture microdissection and proteomic profiling of islets from pregnant women

3.1 Introduction

In Chapter 1, I discussed the adaptations human pancreatic islets undergo during pregnancy to increase maternal insulin secretion, thereby maintaining normoglycaemia and compensating for pregnancy-associated peripheral insulin resistance (11, 13). During human pregnancy, insulin secretion increases by 50% in early gestation and by 100% in late gestation (15). These findings indicate that pregnancy enhances islet-cell function. Uncovering the mechanisms driving this islet plasticity could aid in developing pharmacotherapies to increase insulin secretion, providing potential treatment options for individuals with diabetes mellitus.

Furthermore, I also highlighted the consequences of inadequate insulin secretion during pregnancy, which leads to gestational diabetes mellitus (GDM), defined as the onset of hyperglycaemia first detected during pregnancy (129). Additionally, I reviewed the range of maternal and foetal complications associated with GDM. Understanding the molecular mechanisms driving pregnancy-related islet adaptations is critical not only for advancing our understanding of GDM but also for designing therapies to improve maternal and foetal outcomes.

The literature review in Chapter 1 provided an overview of the mechanisms proposed to explain the adaptive changes in islets during pregnancy. Much of this research has been conducted using *in vitro* and *in vivo* mouse models, which have limitations as models of human pregnancy (111, 112). Moreover, I discussed the biological differences between mouse and human islets, emphasising the need for caution when translating findings from mouse models to human biology (109, 110, 113, 118). Although studies in mice have offered

important foundational insights, it is crucial to explore these mechanisms in human systems to verify if the findings apply to human pregnancy.

Much of what we know about the global changes that occur in islets during pregnancy stems from studies that have examined transcriptomic profiles in islets from pregnant versus non-pregnant mice (21, 44, 130, 131). However, mRNA expression levels do not always correlate with protein expression (132). Additionally, little is understood about the specific alterations that occur in human islets to enhance insulin secretion during normal pregnancy, or about the potential failure of these adaptations that lead to GDM. In general, the study of protein expression in human islets from pregnant women remains limited. Notably, only one study has conducted comprehensive proteomic profiling of mouse islets during pregnancy, and, to the best of my knowledge, no similar research has been carried out using human pancreatic tissue from pregnant women (22). Profiling the proteome of islets in human pregnancy could provide valuable insights into the mechanisms driving pregnancy-related adaptations and improve our understanding of islet function and plasticity.

Studying islet biology is inherently difficult due to the limited availability of well-preserved pancreatic tissue. Unlike many other tissues, pancreatic samples can only be collected postmortem. Unfortunately, autopsy specimens are not ideal, as the release of digestive enzymes from the exocrine pancreas triggers rapid auto-digestion, leading to tissue necrosis, disruption of islet structure, and degradation of islet proteins (108). Furthermore, research on human pregnancy faces additional practical and ethical challenges, making it even more difficult to obtain pancreatic tissue from pregnant women.

The Network for Pancreatic Organ Donors with Diabetes (nPOD) at the University of Florida, USA, is the world's largest repository of human pancreatic tissue, with samples collected from heart-beating donors and processed within 24 hours to minimise cold ischemia. This rapid preservation reduces postmortem pancreatic necrosis, ensuring the availability of high-quality tissue. Among the few biorepositories worldwide, nPOD is the only one known to provide well-preserved pancreatic samples from pregnant women, maintaining intact islet architecture and protein expression that accurately reflect *ex vivo* conditions (124, 125).

In this chapter, I aimed to characterise the broader protein expression profiles of pancreatic islets from pregnant women using liquid chromatography-mass spectrometry (LC-MS/MS). I also aimed to identify any differentially expressed proteins by comparing the protein profiles of islets from pregnant women to those from matched non-pregnant controls. I would utilise formalin-fixed paraffin-embedded (FFPE) pancreatic tissue sections acquired from the nPOD biorepository and isolate the islets using laser-capture microdissection (LCM). LCM is a powerful tool for isolating specific cell populations from complex tissues while maintaining their natural environment, enabling precise molecular analyses (133, 134). This technique can be employed to isolate islets from pancreatic tissues for further investigation.

3.1.1 Aims

The aims of this chapter were to:

1. Isolate islets from FFPE pancreatic tissue using LCM.
2. Use LC-MS/MS to analyse the proteome of the isolated islets.

3. Characterise the proteome of islets isolated from the FFPE pancreatic tissue from pregnant women.
4. Compare protein abundance in islets from pregnant women to non-pregnant women.
5. Compare protein abundance in islets from women with normal pregnancies to those with GDM.

3.2 Materials and methods

3.2.1 Donor tissues

This project received approval from the South Central – Oxford A Research Ethics Committee (REFS 18/SC/0559). The nPOD biorepository provided pre-processed FFPE pancreatic tissue sections, along with demographic, clinical, and laboratory data for each donor. All donor information was de-identified by nPOD in accordance with the Health Insurance Portability and Accountability Act (HIPAA) regulations in the USA. The biorepository contained FFPE pancreatic tissue sections from eight pregnant donors, seven of whom were in the third trimester, and one in the first trimester. To maintain consistency for group comparisons, the first trimester donor was excluded. Pregnant donors were further classified based on the presence of GDM, as confirmed by clinical records provided by the nPOD biorepository documenting a history of GDM diagnosis and treatment during the current pregnancy. Non-pregnant control donors were matched to pregnant donors as closely as possible in terms of age, race, and body mass index (BMI), given the availability of control samples. For pregnant donors the pregnancy BMI is provided.

3.2.2 Sample size calculation

Owing to the rarity of FFPE pancreatic tissue samples from pregnant women, I was unable to obtain additional samples beyond those provided by the nPOD biorepository, despite reaching out to other well-established repositories and scientists in the field. Consequently, I opted to use all the samples of pancreata from pregnant women available in the nPOD biorepository for this study, as no others were accessible. Therefore, an initial sample size calculation to determine the minimum number of participants was not performed due to limited sample availability.

3.2.3 Laser-capture microdissection

Polyethylene naphthalate (PEN) membrane-covered microscope slides (1.0) (Carl Zeiss, cat. no. 15350731) were irradiated with 254 nm UV light for 30 minutes, as per the manufacturer's recommendations, to improve tissue adherence and sterilise the slides. The slides were then shipped to the nPOD biorepository in Florida, USA. FFPE pancreatic tissue sections, 10 µm thick, were mounted onto the PEN membrane-covered slides and dried overnight at 56°C by the nPOD facility to further enhance tissue adherence, before being returned to Oxford.

LCM was performed in collaboration with Dr Simon Davis and Professor Roman Fischer at the Target Discovery Institute (TDI), Nuffield Department of Medicine, University of Oxford.

FFPE tissue sections were de-paraffinised by two washes in xylene (2 minutes each) (Sigma, cat. no. 108298), followed by a series of graded ethanol and double-distilled water (ddH_2O) washes (100%, 90%, and 70% ethanol for 1 minute each, with a final 5-minute wash in ddH_2O). The slides were then dried and stored at -80°C until the day of LCM. The Leica LMD7 system was used for LCM, I identified islets via brightfield and fluorescence imaging (laser excitation wavelength of 495 nm) at 20x magnification. For each donor, 235,000 µm² of both islet and exocrine tissues were microdissected and collected. Exocrine tissue (areas with primarily acinar cells) was used as an internal control to confirm the purity of the isolated islet tissue. For each donor a single tissue section was used, islets were selected at random and dissected islets were separated by a minimum of 200 µm to ensure each dissected region represented a distinct islet. The LCM settings included: power at 45, aperture at 9, speed of 5, middle pulse count of 2, final pulse of 15, head current at 100%,

and pulse frequency of 3773 Hz. The dissected tissue was collected in 40 µL of acetonitrile in a 96-well PCR plate (Eppendorf, cat. no. 0030129580). To ensure tissue was positioned at the bottom of the wells, 110 µL of acetonitrile was added, the plate was sealed, centrifuged at 2,000 *g* for 5 minutes, and dried in a vacuum centrifuge at 40°C. The plate was stored at -20°C until further processing.

3.2.4 Liquid chromatography-mass spectrometry

LC-MS/MS was also performed in collaboration with Dr Simon Davis and Professor Roman Fischer at the Target Discovery Institute (TDI), Nuffield Department of Medicine, University of Oxford.

The protein digestion and LC-MS/MS experiment was performed by Dr Simon Davis as follows. To minimise sample losses, a single step digestion was performed (135). To the dried samples, 20 µL lysis buffer was added to each well of the plate, the plate was sealed and then incubated at 95°C for 90 minutes. The lysis buffer consisted of 0.013 % n-Dodecyl-β-D-Maltoside (DDM, Thermo Scientific, cat. No. 89902), 50 mM triethylammonium bicarbonate (TEAB, Sigma, cat. No. 18597) in LC-MS-grade water. Samples were cooled to 20°C and normalised to 20 µL with LC-MS-grade water. Five µL 60 % acetonitrile, 50 mM TEAB was added to the plate, the plate sealed and incubated at 75°C for 30 minutes. The samples were cooled to 20°C and centrifuged at 2000 *g* for 1 minute. Four µL of 50 mM TEAB was added to dilute the acetonitrile to 10 % and 1 µL of 8 ng/µL Trypsin/LysC enzyme mix (Promega, cat. No. V5073) in 50 mM TEAB was added to the samples. The plate was sealed and incubated at 37°C overnight in a thermomixer with a heated lid (Eppendorf, cat. No. 5382000031). The digestion was quenched by adding formic acid (Fischer scientific, cat. No. 10596814) to 1%.

Samples (2 µL) were loaded on Evotip Pure C18 tips (Evosep, EV2011) following the manufacturer's protocol. Tips were rinsed with 20 µL Solvent B by centrifugation, conditioned by soaking in 1-propanol, equilibrated with 20 µL Solvent A by centrifugation, loaded with 2 µL of sample and 18 µL of solvent A, then centrifuged, washed with 20 µL solvent A by centrifugation, and wet with 100 µL solvent A and a brief centrifugation step for 10 seconds. All centrifugation steps were 60 seconds at 800 *g* unless stated otherwise.

Peptides were analysed with an Evosep One LC system (EvoSep) coupled to a timsTOF Ultra mass spectrometer (Bruker) using the Whisper 40 samples per day method and a 75 µm x 150 mm C18 column with 1.7 µm particles and an integrated Captive Spray Emitter (IonOpticks). Buffer A was 0.1% formic acid in water and Buffer B was 0.1% formic acid in acetonitrile. Data were collected using data-independent acquisition parallel accumulation serial fragmentation (diaPASEF) (136) with one MS frame and nine diaPASEF frames per cycle with an accumulation and ramp time of 100 milliseconds, for a total cycle time of 1.07 seconds. The diaPASEF frames were separated into three ion mobility windows, in total covering the 400 – 1000 m/z mass range with 25 m/z-wide windows between an ion mobility range of 0.64–1.4 Vs/cm^2. The collision energy was ramped linearly over the ion mobility range, with 20 eV applied at 0.6 Vs/cm^2 to 59 eV at 1.6 Vs/cm^2.

Mass spectrometry raw files were analysed in DIA-NN (v1.8.1) (137) using an in-silico spectral library generated by DIA-NN with default settings (one missed cleavage, N-terminal methionine excision was allowed, carbamidomethylation of cysteine was not allowed) using a Uniprot human FASTA file containing 20383 reviewed sequences with common contaminants added. MS1 and MS2 accuracies were set to 15 ppm, all other settings were left as default.

3.2.4.1 Data analysis

I analysed the LC-MS/MS data using Perseus (v2.0.11), a data analysis and visualisation tool for proteomics data with a comprehensive suite of functionalities for pre-processing data, conducting quality control, and performing statistical tests for differential expression (138).

The data were log2 transformed and organised into four categories: pregnant islet, pregnant exocrine, control islet, and control exocrine. After removing incomplete rows from each group, 6,292 proteins per donor were retained for further comparison across both the islet and exocrine groups. To demonstrate the purity of islet isolation, the combined islet groups (pregnant and control islets) were compared to the combined exocrine groups (pregnant and control exocrine tissue). Owing to evidence of exocrine contamination in the islet samples, a single donor and its matched control (nPOD IDs 6226 and 6559) were excluded from the analysis. In total, data from 12 donors were included for analysis.

To identify islet-specific proteins expressed during pregnancy, the pregnant islet group was compared to the pregnant exocrine group. To assess whether protein expression was altered in islets or exocrine tissue during pregnancy, comparisons were made between pregnant versus control islet groups, as well as between pregnant versus control exocrine tissue groups. Within the pregnant islet group, GDM cases were compared to normal pregnancies.

Between-group comparisons were conducted using permutation-based testing to adjust for multiple comparisons. A false discovery rate (FDR) of < 0.05 and an S0 value of 0.01 (26) were applied to islet-exocrine comparisons, comparisons between pregnant and non-pregnant islets, and comparisons between GDM and normal pregnancies within the islet

group. The FDR reflects the adjusted p-value after correcting for multiple comparisons. Principal component analysis (PCA) was carried out using the built-in PCA function. Volcano plots were generated by plotting the negative log10 of the FDR against the log2 fold change of the normalised mean MS intensities. A negative log10 FDR of >1.3 is equivalent to a $p < 0.05$. Hierarchical clustering analysis was performed for the 25 proteins with the largest positive and negative log2 FCs when comparing all islet proteins versus all exocrine proteins and when comparing islet proteins from pregnant women versus exocrine proteins from pregnant women, respectively. A subset table with these proteins and their corresponding MS intensities for each condition was created. The data were normalised using z-scores, and a heatmap was generated via hierarchical clustering with the following parameters: Euclidean distance, average linkage, and no constraints.

3.2.4.2 Protein network visualisation

Protein network visualisation and an over-representation analysis were conducted using Cytoscape (v3.10.2) in combination with the STRING database, which includes both known and predicted protein-protein interactions (STRING, v2023) (139). Physical interactions between differentially expressed proteins were utilised to construct interaction networks. Over-representation analysis focused on proteins with a log2 fold change (FC) > 1 and FDR < 0.05, representing islet-specific proteins. The total set of proteins detected in the experiment served as the background proteome for enrichment analysis, and redundancy filtering was applied to prioritise the most significant and biologically relevant pathways, preventing an overly extensive and potentially overwhelming list. Pathways enriched for GO biological processes, as well as those from Reactome and KEGG databases, with an FDR < 0.05, were considered significant.

Protein network clusters were identified using the Markov Cluster Algorithm (MCL) via the clusterMaker2 app, with a granularity (inflation value) set at four, allowing the identification of clusters of densely interconnected proteins within the networks (140). These clusters were visualised, and networks with three or more proteins contributing to enriched pathways were further examined. Enriched pathways were overlaid onto the protein networks, highlighting the proteins involved in each pathway to offer deeper insights into the biological processes that underlie islet function in third-trimester pregnant women.

3.3 Results

3.3.1 Donor characteristics

Table 3.1 provides a comparative overview of the demographic and clinical characteristics between the pregnant donors and non-pregnant controls. Pregnant donors were older and had a higher body mass index than the non-pregnant controls, however neither difference was statistically significant ($p = 0.15$ and $p = 0.07$, respectively). With regard to BMI, only the pregnancy BMI is provided due to the circumstances under which donor tissues are acquired, making pre-pregnancy BMI unavailable. Both groups had the same number of Far-east Asian and Latin-American donors, however the pregnant group had one more African American donor and one fewer Caucasian donor than the non-pregnant group. The median gestational age of pregnant donors was 33 weeks (Interquartile range [IQR] = 32 – 40), reflecting their third-trimester status. Pregnant and non-pregnant donors had similar haemoglobin A1c ($p = 0.91$) and C-peptide levels ($p > 0.99$). Anti-GAD antibodies and insulinitis, detected on histology, were detected in two pregnant donors, while neither were detected in the non-pregnant group. Table 3.2 presents the descriptive characteristics pertaining to each donor in detail.

Table 3.1: Comparison of the characteristics of pregnant women and non-pregnant controls who donated their pancreata.

	Non-pregnant (n=7)	Pregnant (n=7)	p-value
Age (years)	25 (21-33)	33 (28-26)	0.15
Ethnicity - no. (%)			
African American	2 (28)	3 (42)	>0.99
Asian	1 (14)	1 (14)	
Caucasian	2 (28)	1 (14)	
Hispanic	2 (28)	2 (28)	
Body mass index (kg/m^2)	28.3 (24-31.3)	34.4 (27.2-45)	0.07
Gestational age at delivery (weeks)	-	33 (32-40)	N/A
Haemoglobin A1c (%)	5.4 (5.2-5.9)	5.4 (5-6.6)	0.91
C-Peptide (ng/ml)	7 (1.9-8.1)	6.4 (1.8-10.5)	>0.99
Anti-GAD antibody positive - no. (%)	0 (0)	2 (29)	0.46
Insulinitis (Histology) - no. (%)	0 (0)	2 (29)	0.46

*data are described using median/interquartile range (IQR). Continuous data were compared using the two-sided Mann-Whitney test and categorical data, presented as numbers (no.) and percentages (%), were compared using two-sided Fisher's exact tests. Reproduced from a manuscript accepted for publication in *Nature Communications, Seedat et al.* (2025).

Table 5.2: Descriptive characteristics of women who donated their pancreata.

nPOD ID	Classification	Age (years)	Ethnicity	Gestational age (weeks)	BMI (kg/m^2)	C-peptide (ng/ml)	HbA1c (%)	Antibody status	GDM therapy	Cause of death	Number of islets isolated for analysis
6226	Normal pregnancy	38	Far east Asian	32.1	27.2	3.87	5.3	Neg	-	Subarachnoid haemorrhage	10
6257	Normal pregnancy	19	American Indian/Alaska native	12	45.9	23.18	Unknown	Neg	-	Head trauma	-
6310	Normal pregnancy	28	Latin American	40	22.4	10.54	Unknown	GADA	-	Cerebrovascular accident	12
6363	Normal pregnancy	36	African American	34	45	1.47	5.5	Neg	-	Subarachnoid haemorrhage	11
6383	Normal pregnancy	22	African American	40	34.4	7.26	4.9	Neg	Unknown	Intracerebral haemorrhage	10
6082	GDM pregnancy	33	Caucasian	33	34.4	12.27	Unknown	Neg	Metformin	Intracerebral haemorrhage	11
6239	GDM pregnancy	35	African American	29	50.9	6.4	Unknown	Neg	Insulin	Hypoxia and sudden cardiac arrest	9
6405	GDM pregnancy	29	Latin American	32	42.5	1.84	7	GADA, IA2A, ZnT8A	-	Intracerebral haemorrhage	12
6559	No diabetes	23	Far east Asian	-	26.3	7.02	5.3	Neg	-	Cerebral tumour with brain herniation	10
6479	No diabetes	21	Latin American	-	20.9	1.74	5	Neg	-	Cerebral anoxia	11
6425	No diabetes	38	Caucasian	-	28.3	8.06	6	Neg	-	Cerebral anoxia	10
6253	No diabetes	19	African American	-	34.3	7.22	Unknown	Neg	-	Head trauma	9
6251	No diabetes	33	Caucasian	-	29.5	1.92	5.3	Neg	-	Head trauma	12
6331	No diabetes	27	African American	-	24	3.01	5.4	Neg	-	Cerebral anoxia	10
6401	No diabetes	25	Latin American	-	31.3	12.81	5.8	Neg	-	Head trauma	9

*BMI – body mass index, GDM – gestational diabetes mellitus, HbA1c – haemoglobin A1c, IHC-IF – immunofluorescence of tissue sections, LCM – laser capture microdissection. Reproduced from a manuscript accepted for publication in *Nature Communications, Seedat et al.* (2025).

3.3.2 Isolation and deep proteomic profiling of human islets and exocrine tissue using laser-capture microdissection and liquid chromatography-mass spectrometry

Proteins were extracted by lysing the samples, which were then subjected to unbiased proteomic analysis using LC-MS/MS. This was followed by between group comparisons of the quantified protein abundances.

The workflow that was used is illustrated in Figure 3.1. Microscope images of islets, identified using brightfield and fluorescent microscopy, are shown before LCM in Figure 3.2A, and after microdissection in Figure 3.2B.

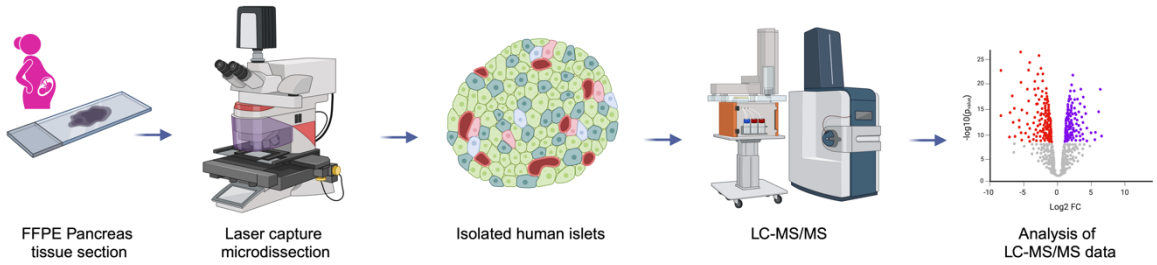

Figure 3.1. Schematic illustrating the experimental workflow used to identify pancreatic islets in pancreas FFPE tissue sections using brightfield and fluorescent microscopy, followed by LCM, proteomic characterisation via LC-MS/MS, and analysis of differential protein expression. Created with BioRender.com released under a Creative Commons Attribution-NonCommercial-NoDerivs 4.0 International license. Reproduced from a manuscript accepted for publication in *Nature Communications, Seedat et al.* (2025). This content is distributed under the Creative Commons Attribution License (CC BY 4.0).

*FFPE – formalin-fixed paraffin-embedded, LCM – laser-capture microdissection, LC-MS/MS – liquid-chromatography mass spectrometry

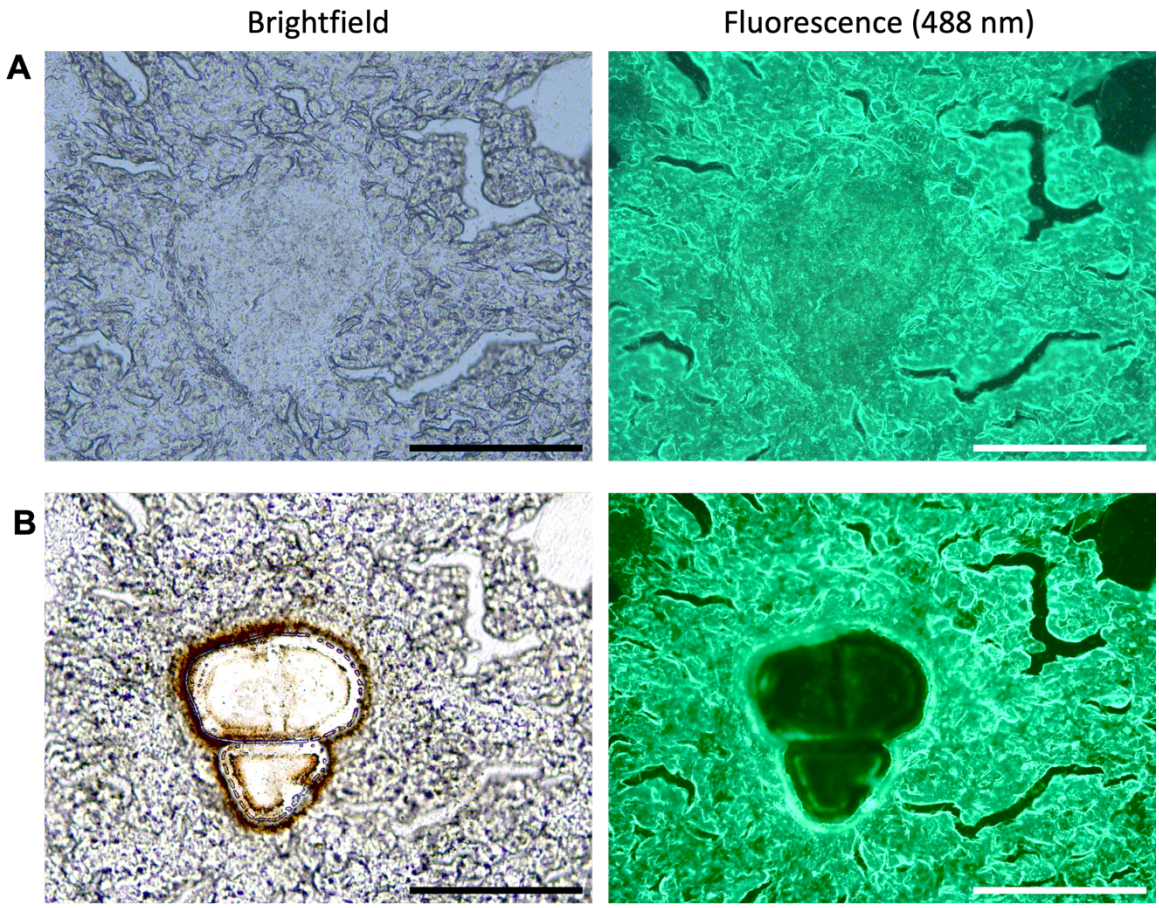

Figure 3.2. Identification of islets by microscopy using brightfield (left) and fluorescence (488 nm excitation channel) (right). Images of islets are at 20x magnification. **A.** Images acquired before laser-capture microdissection (LCM) and **B.** post-LCM are shown. Scale bar = 200 µm. Reproduced from a manuscript accepted for publication in *Nature Communications, Seedat et al.* (2025). This content is distributed under the Creative Commons Attribution License (CC BY 4.0).

A similar number of proteins was detected in all samples (Figure 3.3). Per donor, the mean number of proteins identified in isolated islets was 7,388 proteins (SD = 83), and 7,124 (SD = 120) in exocrine tissues.

The purity of islet isolation through LCM was demonstrated by the clear separation between islet and exocrine tissue clusters in the principal component analysis (Figure 3.4). To further verify the isolation purity, the proteomic profiles of all islet samples (both pregnant and non-pregnant) were compared to those of all exocrine samples. Several proteins specific to islets were highly expressed in islet samples compared to exocrine tissues (Figure 3.5). Notably, insulin (INS), glucagon (GCG), and chromogranin A and B (CHGA and CHGB) were abundant in the isolated islets. In contrast, proteins associated with acinar cell-secreted enzymes, such as amylase (AMY2A), lipase (PNLIPRP1), trypsin (PRSS1, PRSS2, PRSS3), and chymotrypsin-like elastases (CELA2A, CELA2B, CELA3B, and CTRL), were prevalent in exocrine tissue but absent from islet samples (Figure 3.5). Hierarchical clustering of the 50 proteins with the most significant positive and negative log2 FCs (Figure 3.6) further confirmed the islet isolation purity, as islet-specific proteins were abundant in islet samples, while exocrine-specific proteins were mainly found in exocrine samples. The clear visual distinction between the two tissue types reinforces the success of the isolation procedure and highlights the distinct proteomic profiles of islet and exocrine tissue.

A subsequent pathway analysis of significantly upregulated proteins in the islets revealed a corresponding enrichment of islet-specific pathways (Figure 3.7). These pathways were associated with insulin processing and secretion regulation, as well as broader categories pertinent to secretory cells, such as vesicular transport and exocytosis regulation, which are crucial to the hormone-secreting functions of islet cells (113).

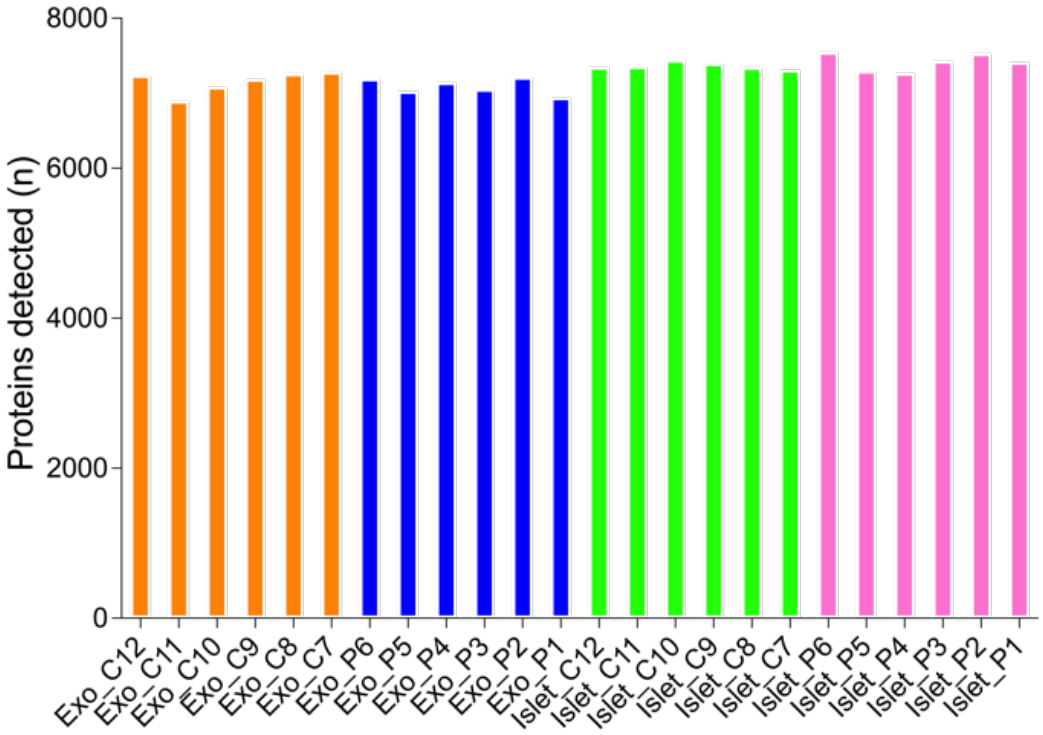

Figure 3.3. Number (n) of proteins detected per islet and exocrine sample following analysis by liquid chromatography-mass spectrometry. Isolated islets from pregnant cases are represented in pink and from control cases in green, while exocrine tissue samples from pregnant cases are shown in blue and the controls in orange. Reproduced from a manuscript accepted for publication in *Nature Communications, Seedat et al.* (2025). This content is distributed under the Creative Commons Attribution License (CC BY 4.0).

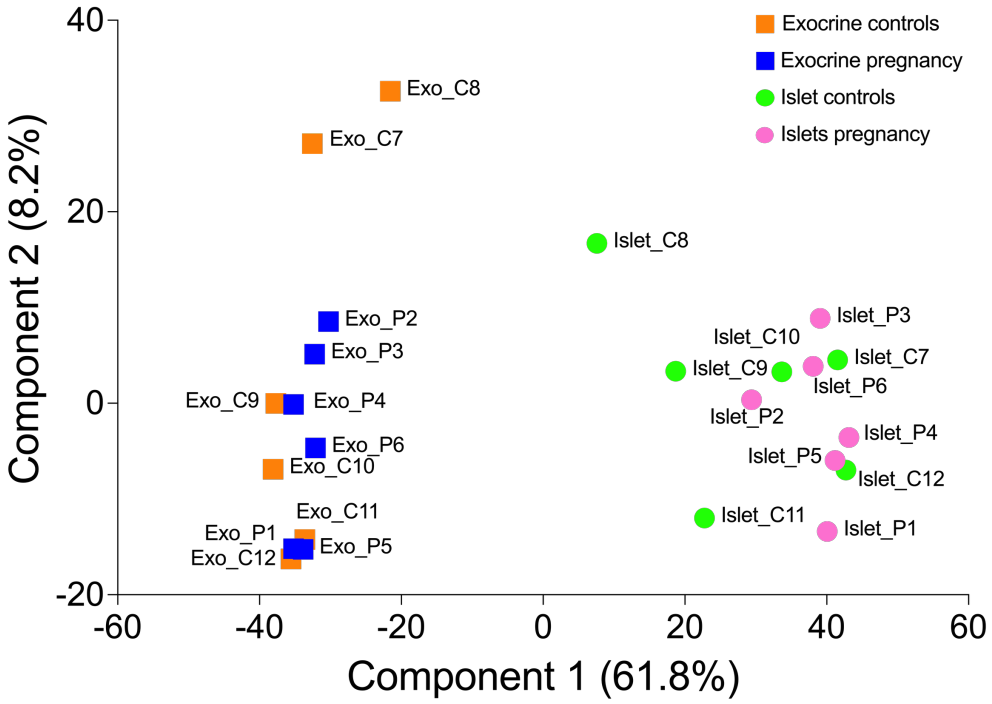

Figure 3.4. Principal component analysis plot of the islet and exocrine samples analysed by liquid chromatography-mass spectrometry. Isolated islets are represented as circles (pregnant cases in pink, controls in green), while exocrine tissue samples are shown as squares (pregnant cases in blue, controls in orange). A clear separation between the islet and exocrine clusters is observed. Reproduced from a manuscript accepted for publication in *Nature Communications, Seedat et al.* (2025).

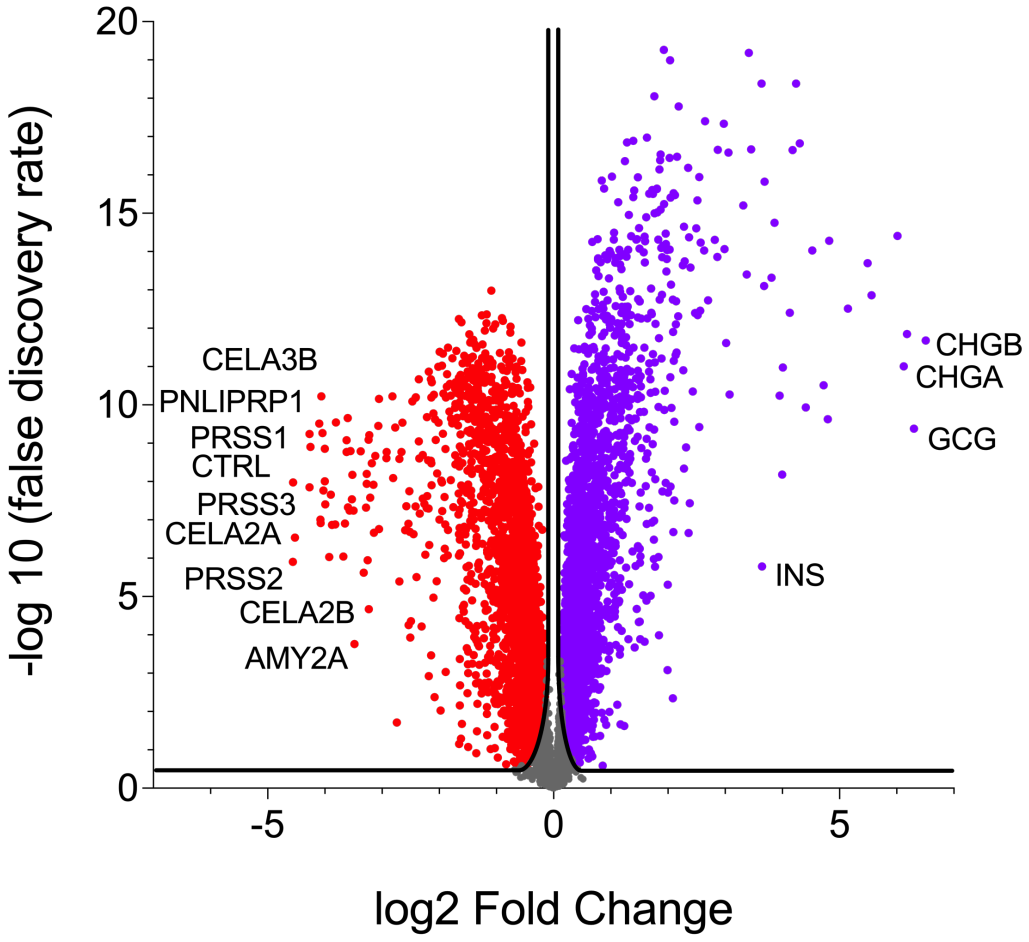

Figure 3.5. Volcano plot comparing protein expression between isolated islets and exocrine tissue demonstrates the identification of islet specific proteins within isolated islets. Significantly upregulated proteins belonging to islets are shown in purple, and downregulated proteins belonging to exocrine tissue in red. Selected proteins with a log2 fold change > 3 or < −3 are labelled. False discovery rate (FDR) < 0.05 = - log10 FDR > 1.3, S0 = 0.01. Reproduced from a manuscript accepted for publication in *Nature Communications, Seedat et al.* (2025). This content is distributed under the Creative Commons Attribution License (CC BY 4.0).

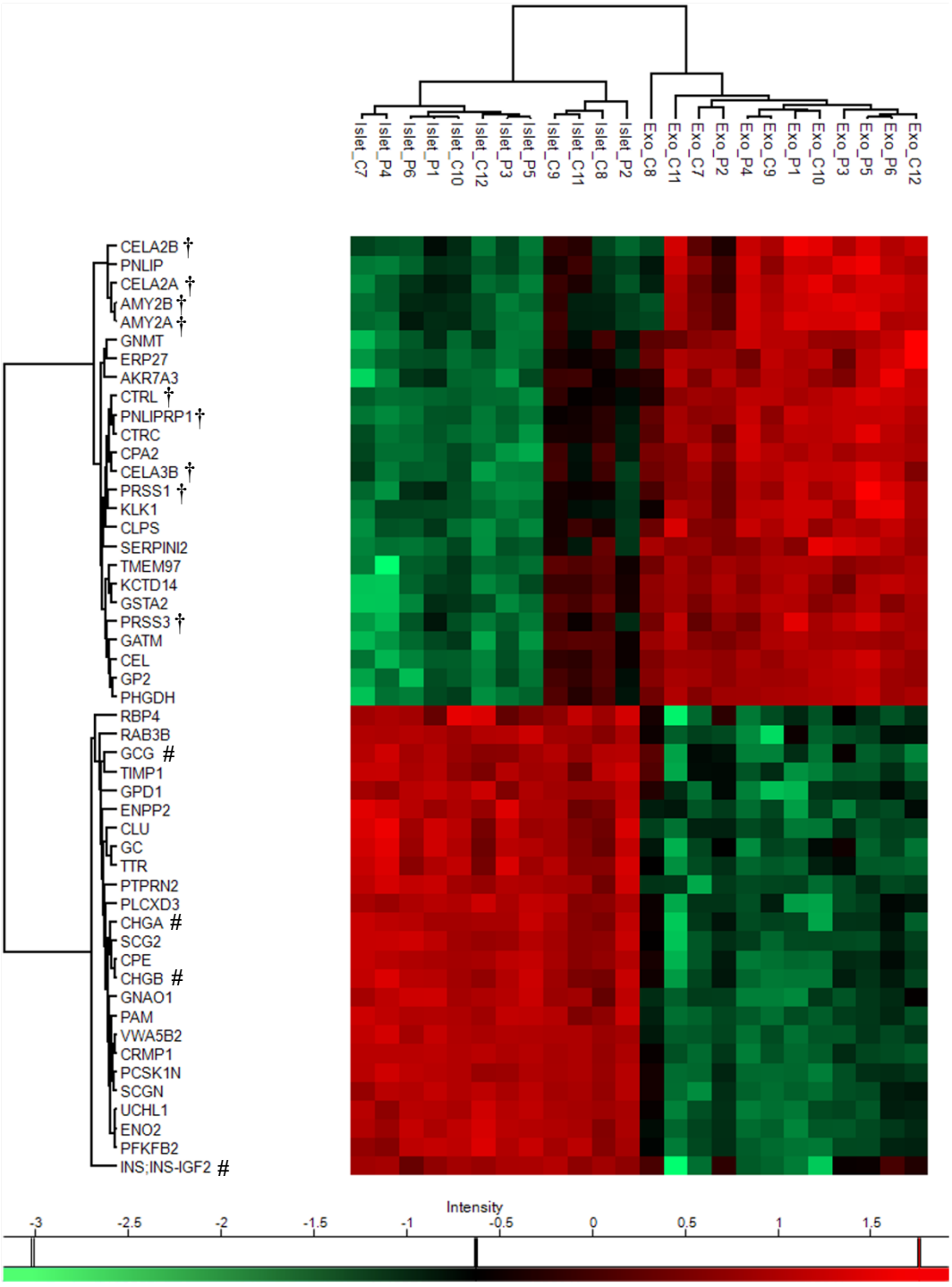

Figure 3.6. Hierarchical clustering of the 50 proteins with the greatest positive (n=25) and negative (n=25) log2 fold changes when comparing all isolated islets to all isolated exocrine tissues, regardless of pregnancy status. Warmer colours (red) represent higher expression, while cooler colours (green) indicate lower expression. The "#" symbol indicates the islet-specific proteins, including insulin (INS), glucagon (GCG), and chromogranin A and B

(CHGA and CHGB). The "†" symbol denotes the exocrine-specific proteins, including amylase (AMY2A and AMY2B), lipase (PNLIPRP1), trypsin (PRSS1 and PRSS3), and chymotrypsin-like elastases (CELA2A, CELA2B, CELA3B, and CTRL).

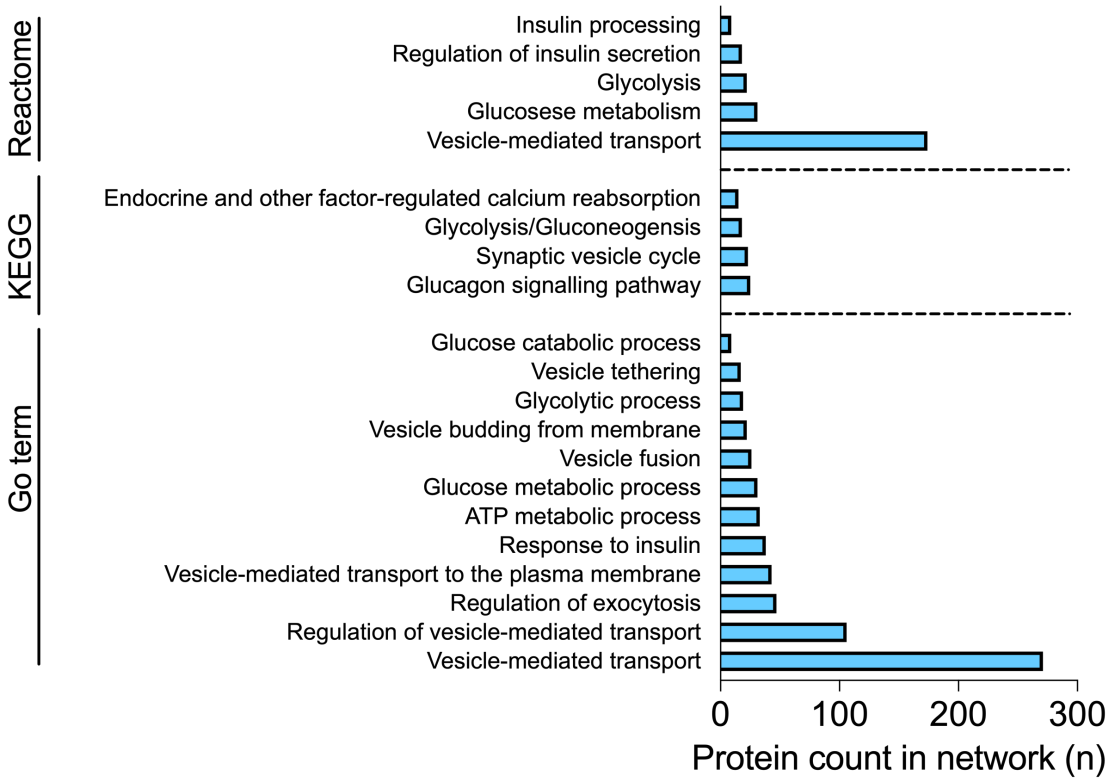

Figure 3.7. Overrepresentation analysis of enriched pathways from the Reactome, KEGG, and GO Biological Processes databases. Numerous pathways directly relating to islet function are observed. Pathways with a false discovery rate (FDR) < 0.05 are shown. Reproduced from a manuscript accepted for publication in *Nature Communications, Seedat et al.* (2025).

3.3.3 Characterisation of the human islet proteome during pregnancy

Proteins expressed in islets isolated from the pancreata of pregnant women were compared to those from exocrine tissue of pregnant women. A total of 4,136 proteins were significantly differentially expressed between the pregnant islet samples and pregnant exocrine tissue samples. Of these, 2,057 proteins were enriched in the islets, with 446 exhibiting a log2 FC greater than 1 (Figure 3.8). Hierarchical clustering of the 50 proteins with the largest positive and negative log2 FCs between islets and exocrine tissue in pregnant women is displayed in Figure 3.9. Pathway analysis revealed six pathways enriched in islet functional biology (Figure 3.10).

Network clustering identified 69 clusters, four of which contained three or more proteins associated with the enriched pathways (Figure 3.11). Cluster one comprised several subunits of the Vacuolar-type proton ATPase, which were linked to ion channel transport, synaptic vesicle, lysosome, and phagosome pathways. Cluster two consisted of various Guanine nucleotide-binding proteins (G proteins), contributing to pathways involved in energy metabolism integration and neuronal system function. Cluster three included proteins responsible for synaptic vesicle docking, fusion, and transport. Finally, cluster four was primarily made up of ATP-binding cassette proteins, particularly sub-family member nine, also known as sulfonylurea receptor two (Figure 3.11).

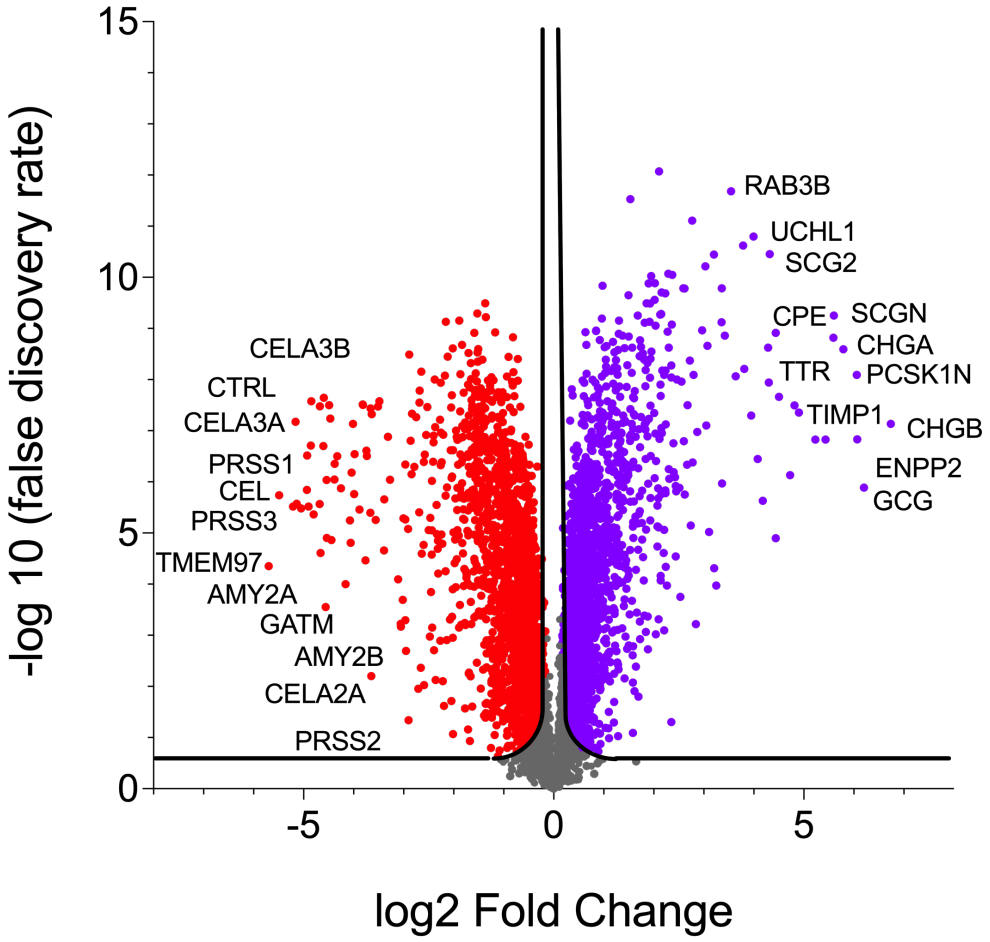

Figure 3.8. Volcano plot of proteins expressed in islets from pregnant women compared to exocrine tissue. Significantly upregulated proteins are shown in purple, and downregulated proteins in red. Selected proteins with a log2 fold change >4 or <−4 are labelled. False discovery rate (FDR) < 0.05 = - log10 FDR > 1.3, S0 = 0.01. Reproduced from a manuscript accepted for publication in *Nature Communications, Seedat et al.* (2025). This content is distributed under the Creative Commons Attribution License (CC BY 4.0).

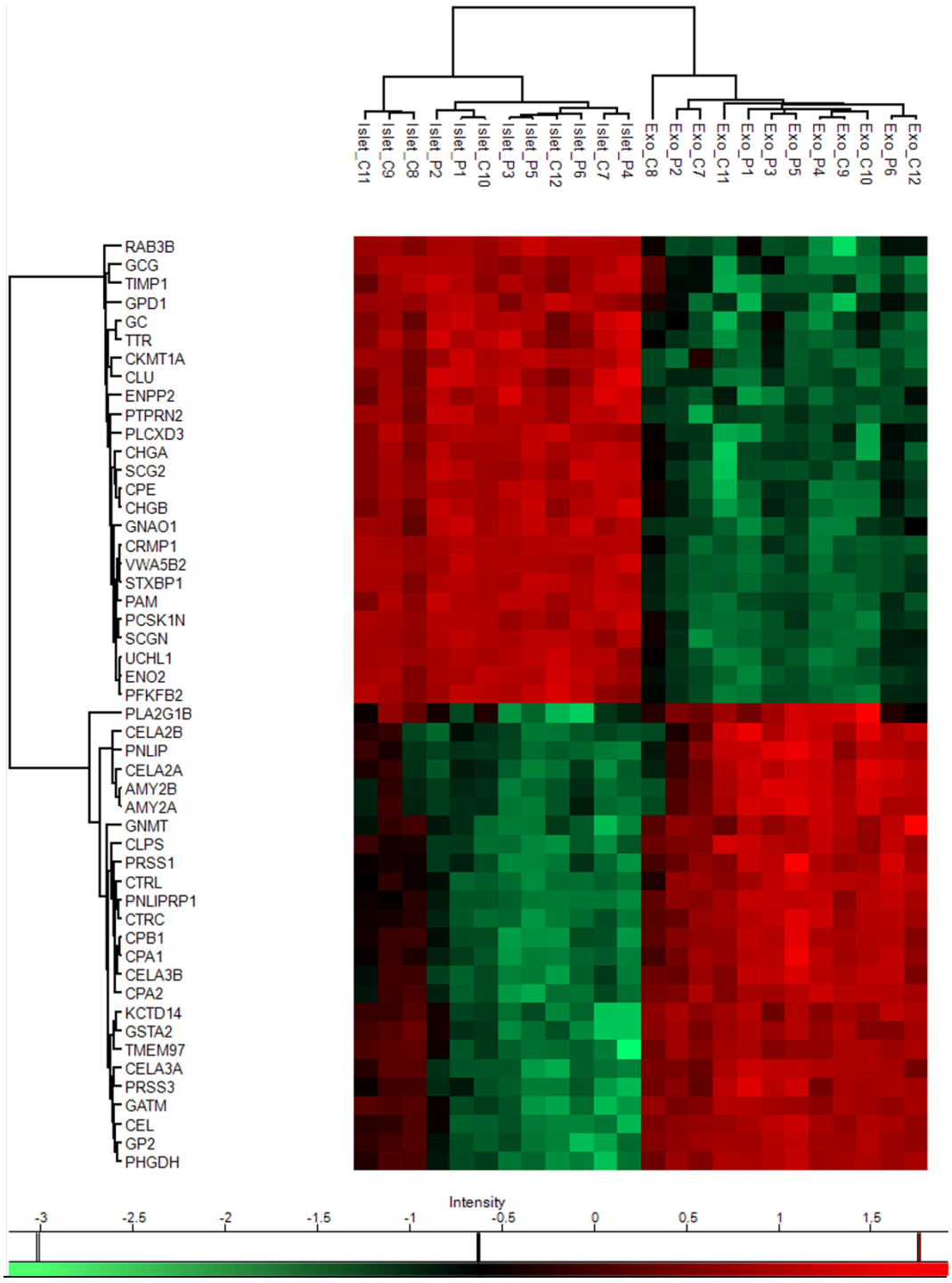

Figure 3.9. Hierarchical clustering of the 50 proteins with the greatest positive (n=25) and negative (n=25) log2 fold changes when comparing islets isolated from pancreata of pregnant women to the pancreatic exocrine tissue isolated from pregnant women. Warmer colours (red) represent higher expression, while cooler colours (green) indicate lower expression.

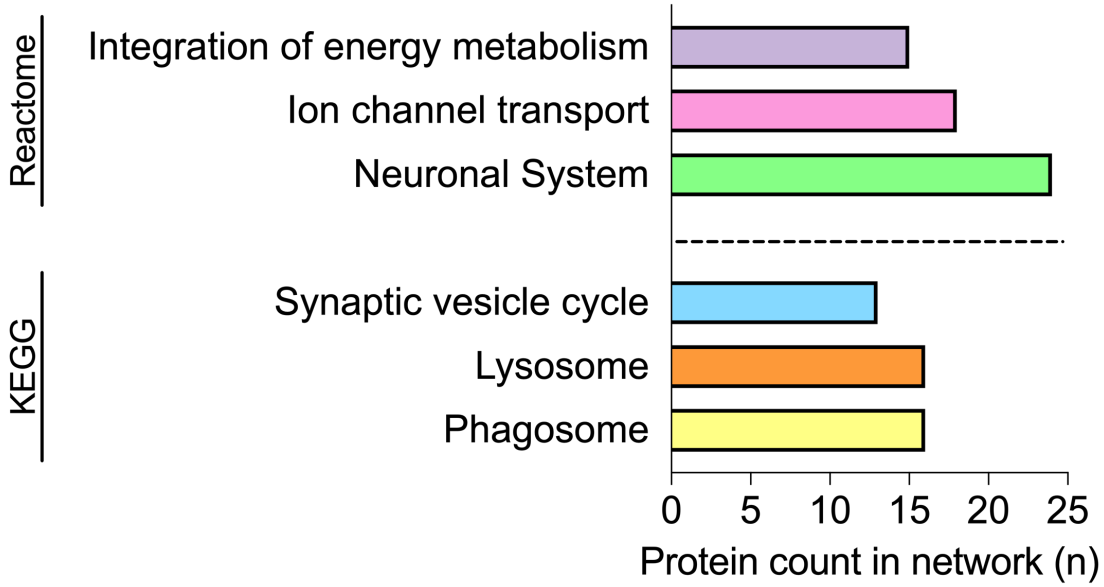

Figure 3.10. Over-representation analysis of enriched pathways from the KEGG and Reactome databases. Upregulated proteins with log2 fold change >1 expressed in islets from pregnant women were analysed using STRING for physical protein interactions.

False discovery rate (FDR) < 0.05. Colours of enriched pathways correspond to the colours of proteins nodes depicted in Figure 3.11. Reproduced from a manuscript accepted for publication in *Nature Communications, Seedat et al.* (2025). This content is distributed under the Creative Commons Attribution License (CC BY 4.0).

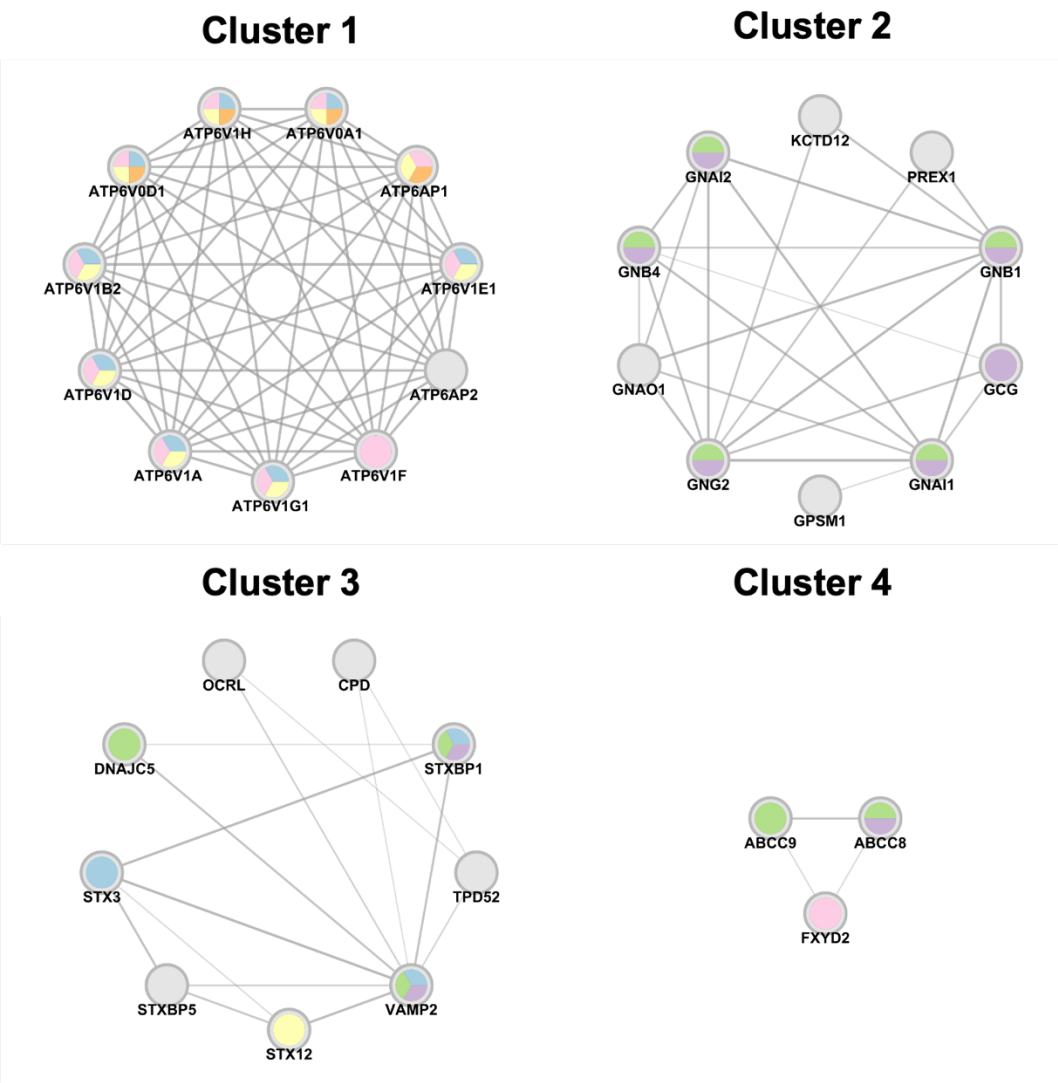

Figure 3.11. Protein networks clustered by physical interactions between nodes. Networks with three or more proteins in enriched pathways are shown. Protein labels are displayed, and node colours correspond to the colours of enriched pathways depicted in Figure 3.10. Reproduced from a manuscript accepted for publication in *Nature Communications, Seedat et al.* (2025). This content is distributed under the Creative Commons Attribution License (CC BY 4.0).

3.3.4 Identification of differentially expressed proteins in pancreatic islets during pregnancy

Proteins from islets of pregnant women were compared to those from non-pregnant control islets. Out of the 7,546 proteins detected in human islet samples, cathepsin Z (CTSZ) (log2 FC = 1.36, -log10 FDR = 4.98), β1,4-galactosyltransferase 4 (B4GALT4) (log2 FC = 0.59, -log10 FDR = 4.44), cyclin-dependent kinase 5 (CDK5) (log2 FC = 0.32, -log10 FDR = 4.82), and laminin subunit alpha 4 (LAMA4) (log2 FC = -0.66, -log10 FDR = 3.98) were differentially expressed in islets from third-trimester pregnant women compared to non-pregnant controls (Figure 3.12). No physical interactions were identified between these differentially expressed proteins (Figure 3.13). Additionally, no differences in protein expression was observed in exocrine tissue when comparing pregnant and non-pregnant controls, nor in the islets when comparing normal pregnancy to GDM donors.

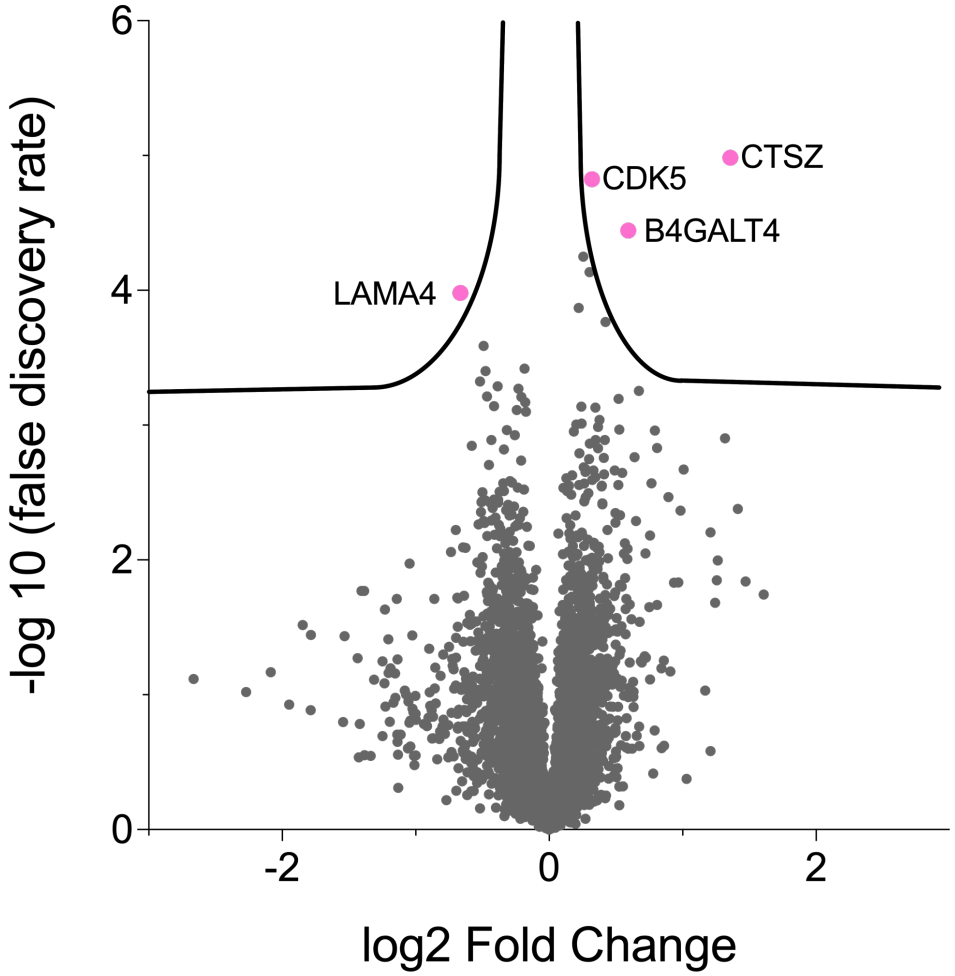

Figure 3.12. Volcano plot illustrating differential protein expression in islets from pregnant women compared to non-pregnant controls. Significantly expressed proteins are shown in pink and are labelled. False discovery rate (FDR) < 0.05 = - log10 FDR > 1.3, S0 = 0.01. Reproduced from a manuscript accepted for publication in *Nature Communications, Seedat et al.* (2025). This content is distributed under the Creative Commons Attribution License (CC BY 4.0).

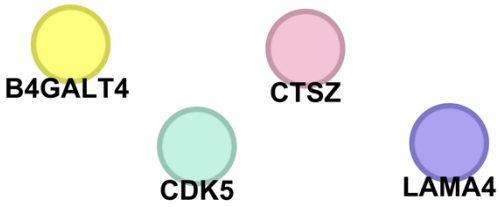

Figure 3.13. Analysis of physical protein network interactions of differentially expressed proteins analysed using the STRING database showing no interactions. False discovery rate (FDR) < 0.05. Reproduced from a manuscript accepted for publication in *Nature Communications, Seedat et al.* (2025). This content is distributed under the Creative Commons Attribution License (CC BY 4.0).

3.4 Discussion

In this chapter, I used LCM to isolate islets from FFPE pancreatic sections from both pregnant women and matched non-pregnant controls, followed by their proteomic characterisation using LC-MS/MS. By comparing islets to exocrine tissues for all cases and specifically amongst the pregnant cases, I identified enriched pathways and protein clusters related to typical islet functions (8, 9, 141). Additionally, the study revealed how proteins in the interacting cluster networks are linked to islet-specific biological pathways in the pregnant group. Protein profiles from islets in pregnant versus non-pregnant groups were compared, revealing only four proteins that were differentially expressed in pregnant islets, with no significant differences observed in the exocrine tissue.

A key strength of this study is the depth of proteomic analysis achieved. FFPE is the most widely used tissue preservation method and is more accessible than other methods. Advances in techniques for identifying proteins from FFPE samples using LC-MS/MS have enabled comprehensive analysis, even with limited material from LCM experiments (133, 142-147). Although these techniques have been used in other research areas, this is the first study to successfully isolate and analyse protein expression in pancreatic islets FFPE tissue using LC-MS/MS. Previous studies using fresh frozen tissue for LCM and LC-MS/MS have detected between 1,000 and 2,000 proteins in islets from patients with type 1 diabetes mellitus (148, 149), more than 3,000 proteins in rat islets using nanoPOTS technology (150), and 6,873 proteins in pooled mouse islets after purification with Liberase I and ultracentrifugation (151). The Human Protein Atlas has identified 3,708 proteins within the pancreas (152), while a spatial proteomics study using fresh frozen human pancreas tissue identified over 6,000 proteins per sample (153). A recent study analysing fresh-frozen islets from 90 donors, both with and without type 2 diabetes mellitus, reported the detection of

approximately 8,000 proteins on average (154). Despite using FFPE tissue, this study detected more than 7,000 proteins per sample, representing the largest dataset of islet and exocrine proteins derived from islets of pregnant women to date. To my knowledge, this is the first study to achieve such depth in the quantification of pancreatic islet and exocrine proteins using FFPE pancreatic tissue and is comparable to studies of human and mouse pancreatic cryosections.

In comparison to a previous study by *Horn et al.*, which analysed islets from pregnant and non-pregnant mice and identified 427 differentially expressed proteins (log_2 FC > 0.2, FDR < 0.15) at day 14.5 of gestation (22), I detected only four differentially expressed proteins in islets from pregnant women. It should be noted that the mouse study used a more relaxed FDR and a lower log2 FC threshold. Moreover, rather than collection of islets from pancreas tissue via LCM followed by LC-MS/MS, *Horn et al.* isolated islets from mouse pancreata using Liberase TL/DNase I enzyme digestion, followed by filtration to retain islets, which were then snap-frozen. These methodological differences, species-specific variations, as well as biological differences between human and mouse pregnancies, likely account for the larger number of differentially expressed proteins in the mouse study. The limited number of altered proteins in human islets, despite their ability to nearly double insulin secretion by late pregnancy, suggests that proteomic changes during human pregnancy are few (15). However, I recognise that dynamic proteomic changes, which may contribute to islet adaptations during pregnancy, might not have been captured in this study. This is because the use of FFPE pancreatic tissue sections did not allow for the study of protein turnover.

The differentially expressed proteins identified in islets from pregnant women, compared to non-pregnant controls, are associated with cellular processes that may influence islet

adaptation during pregnancy. Cathepsin Z, although not directly linked to islet function or diabetes mellitus, plays a role in immune processes and promotes pancreatic neuroendocrine tumour (PNET) development through heterotypic cell signalling (155). CDK5 has been shown to support β-cell survival, enhance proliferation, regulate insulin gene transcription, and promote insulin secretion, in addition to contributing to PNET formation (156-162). Laminin subunit alpha 4 (LAMA4) is linked to β-cell proliferation and insulin secretion (163). Further research is needed to understand how these proteins contribute to islet adaptations in human pregnancy.

No differences were found in protein expression between islets from women with normal pregnancies and those with GDM. GDM arises when insulin secretion fails to compensate for increased insulin resistance during pregnancy (15). Clinical data show no significant differences in first-phase insulin response or insulin secretion during pregnancy between women with and without GDM. However, GDM is associated with lower insulin secretion when comparing pregnancies in women with GDM to non-diabetic pregnant women who have risk factors for hyperglycaemia (15, 164). It is now recognized that GDM has a heterogeneous pathophysiology, with early- and late-onset forms and both insulin-deficient and insulin-resistant subtypes (10). These differences suggest that GDM likely affects islets in various ways, with disturbances differing between subtypes. These disturbances may be subtle and difficult to detect, possibly involving genetic mutations, post-translational modifications, or external stressors like oxidative stress, which could contribute to islet dysfunction in GDM and explain the absence of differences in the islet proteome between GDM and normal pregnancy (40).

The limited sample size in this study reflects the challenge of obtaining high-quality pancreatic tissue from pregnant women. This limited sample size introduced heterogeneity within this cohort and the variability in ethnicity, BMI, GDM status, anti-GAD antibody status, and insulinitis among donors may have contributed to detecting only a few differentially expressed proteins. Greater collaboration between researchers and clinicians is needed to increase access to such samples for future studies. This is particularly important for comparing GDM and normal pregnancy, as the small sample size in this study necessitates cautious interpretation of the data and although these findings offer important initial insights, further studies with larger cohorts are required to confirm these results and establish more conclusive evidence on the effects of GDM on islet adaptations during pregnancy. In future studies it would be valuable to examine pancreas samples from women at different stages of pregnancy; however, high-quality first- and second-trimester tissue was unavailable for this study. The use of immunofluorescence with islet-specific markers like insulin and glucagon would enhance the accuracy of islet isolation via LCM compared to relying solely on brightfield microscopy and islet autofluorescence. Attempts to use immunofluorescence were hampered by damage to the PEN slide membrane during heat-mediated antigen retrieval, making it difficult to reliably separate islet and exocrine tissue during LCM. Efforts to reduce membrane disruption during antigen retrieval were unsuccessful (165).

The successful LC-MS/MS analysis of islet proteins from FFPE pancreatic sections, rather than cryosections, following islet isolation by LCM represents an advancement in islet research. Given the limited availability of pancreatic tissue samples, particularly cryosections, this approach may broaden opportunities for new studies in islet biology.

Although pregnancy is a highly dynamic state, this study identified relatively few changes in islet protein expression during pregnancy, suggesting that human islet adaptations during pregnancy are more subtle than those observed in mouse models. The data presented in this chapter offer new insights into pancreatic islet changes during pregnancy and highlight the importance of using human-based model systems or tissues for studying islet biology.

Chapter 4

Analysis of whole islet, α and β cell area, and the expression of prolactin and serotonin 2B receptors in islets during human pregnancy

4.1 Introduction

In Chapter 3, I utilised formalin-fixed paraffin-embedded (FFPE) human pancreatic tissue from the Network for Pancreatic Organ Donors with Diabetes (nPOD) biorepository to examine the proteomic profile of islets isolated from pregnant women. Although significant physiological adaptations occur during pregnancy, the proteome of islets from pregnant women showed few differences compared to non-pregnant controls, with just four differentially expressed proteins identified. These findings suggest that, unlike in mouse models, the molecular adaptations in human islets during pregnancy may be more subtle and refined.

In Chapter 1, I reviewed the limited data on islet adaptations during pregnancy, including the only two previous studies on human samples, which report a 1.4- to 2.4-fold increase in pancreatic β-cell area during pregnancy (26, 27). I also discussed the molecular mechanisms thought to regulate β-cell adaptations during pregnancy, which have mainly been investigated in mouse models. In mice, the expansion of β cells during pregnancy is well-documented and is primarily driven by lactogenic hormones such as prolactin and placental lactogen. These hormones interact with the prolactin receptor (PRLR) on β cells, initiating signalling pathways that stimulate cell proliferation and enhance insulin secretion (13, 129). Additionally, lactogenic signals trigger serotonin production in β cells via the upregulation of tryptophan hydroxylase (TPH), which further supports β-cell proliferation and function (11, 13). Serotonin, acting through the serotonin 2B (5-HT2B) receptor—which is upregulated during pregnancy and decreases post-partum—also promotes β-cell expansion (11, 13). While these processes are well understood in mice, less is known about α-cell changes during pregnancy, although studies have shown that mouse α cells increase in both size and number during pregnancy (40).

It remains uncertain if similar β-cell adaptive mechanisms in the PRLR and 5-HT2B receptor occur in humans during pregnancy. As highlighted in Chapters 1 and 3, using mouse models to study human pregnancy presents key limitations, especially regarding β-cell adaptations. One notable difference lies in the regenerative capacity of β cells: while mouse β cells can proliferate efficiently, human β cells remain mostly quiescent, with replication rates lower than 0.1%. (109, 110, 113, 118). Furthermore, there is ongoing debate about whether β-cell replication is a critical factor behind the enhanced β-cell function and insulin secretion observed in human pregnancy (13). This distinction becomes especially relevant when considering the roles of prolactin (PRLR) and serotonin (5-HT2B) receptors in human islets, which are crucial for β-cell mass expansion in mice.

Given these uncertainties and the findings from Chapter 3, which showed that human islets undergo significantly fewer proteomic changes during pregnancy compared to mouse islets, this chapter aims to assess changes in α and β cell areas in pregnancy and determine whether the molecular adaptations seen in mice are also present in human islets. A key focus is on the roles of the PRLR and 5-HT2B receptor in human islet adaptations. However, neither the PRLR nor 5-HT2B receptor was identified in the islets of pregnant or non-pregnant women in the proteomics dataset presented in Chapter 3. This may be due to the limitations of the proteomic analysis, which may not have been sensitive enough to detect low abundant islet proteins. Moreover, the lack of single-cell resolution made it challenging to differentiate between different islet cell types, complicating the analysis of these specific receptors.

In this chapter, my objective was to examine pregnancy-related changes in pancreatic islet cell metrics, focusing on both entire islets and specific α and β cell populations. To do so I

employed immunofluorescence (IHC-IF) to label the FFPE pancreatic tissue sections from the nPOD biorepository. To enhance reproducibility and reduce bias, I utilised high-resolution imaging of complete tissue slides, coupled with automated image segmentation and quantification. Additionally, I validated antibodies to assess the expression of low-abundance proteins, specifically the PRLR and 5-HT2B receptor, in human α and β cells during pregnancy. By combining whole-slide high-resolution imaging with antibody validation, I aimed to offer an unbiased analysis of islet metrics and to assess the abundance of PRLR and 5-HT2B receptor in human islets during pregnancy.

4.1.1 Aims

The aims of this chapter were to:

1. Assess and compare pancreatic islet cell metrics (whole islet, α-cell and β-cell areas) between pregnant cases and non-pregnant controls.
2. Validate antibodies for the PRLR and 5-HT2B receptors for subsequent analysis.
3. Evaluate PRLR and 5-HT2B receptor abundance in α and β cells, comparing pregnant cases to non-pregnant controls.

4.2 Materials and methods

4.2.1 Donor tissues

Details of the donors from the nPOD biorepository are provided in Chapter 3 (Tables 3.1 and 3.2).

4.2.2 Cell culture

HAP1 parental control cells (cat. no. C631, RRID: CVCL_Y019) and PRLR knockout (KO) cells with a 25 base pair (bp) deletion (cat. no. HZGHC003937c0061, RRID: CVCL_TH11) were purchased from Horizon Discovery. The *PRLR*-edited cell line, generated using CRISPR/Cas9 technology with the guide RNA sequence AACCCTACCTGTGGATTAAA, resulted in a 25 bp deletion in exon 6 of the *PRLR* gene, causing frame shifts and multiple stop codons downstream. Both cell lines were maintained in Iscove's Modified Dulbecco's Medium (Sigma, cat. no. I3390) supplemented with 10% heat-inactivated foetal bovine serum (hiFBS) (Sigma, cat. no. F9665) and 1% Pen/Strep (100 U/mL penicillin and 100 µg/mL streptomycin), as per the supplier's instructions. Cells were passaged every 2-3 days upon reaching 70-75% confluence and used for experiments at approximately 70% confluence.

HeLa cells (cat. no. 93021013, RRID: CVCL_0030), SH-SY5Y cells (cat. no. 94030304, RRID: CVCL_0019), MCF7 cells (cat. no. 86012803, RRID: CVCL_0031), and U2OS cells (cat. no. 92022711, RRID: CVCL_0042) were all obtained from the European Collection of Authenticated Cell Cultures via Sigma-Merck. HeLa cells were maintained in low glucose DMEM with GlutaMAX and pyruvate (Gibco, cat. no. 21885-108), 10% hiFBS, and 1% Pen/Strep. They were passaged every 2-3 days at a 1:4 ratio upon reaching 75-80% confluence. SH-SY5Y cells were cultured in a 1:1 mixture of DMEM and F12 medium

(Gibco, cat. no. 11330057) with 10% hiFBS and no antibiotics. They were passaged every five days at a 1:5 ratio upon reaching 90% confluence. MCF7 cells were maintained in low glucose DMEM with GlutaMAX and pyruvate, 10% hiFBS, and 1% Pen/Strep. They were split every 3-4 days at a 1:3 ratio upon reaching ~80% confluence. U2OS cells were maintained in McCoy's 5A (modified) Medium (Gibco, cat. no. 16600082) with 10% hiFBS and 1% Pen/Strep. They were passaged every 3-4 days at a 1:4 ratio upon reaching 75-80% confluence.

EndoC-βH3 cells (obtained from Human Cell Design, France) were cultured in low glucose DMEM with GlutaMAX and pyruvate, supplemented with 2% bovine serum albumin (BSA) (Roche, cat. no. 10775835001), 10 mM nicotinamide (Sigma, cat. no. N3376), 50 μM β-2 mercaptoethanol (Gibco, cat. no. 31350010), 5.5 μg/mL transferrin (Sigma, cat. no. T8158), 6.6 ng/mL sodium selenite (Sigma, cat. no. 214485), and 1% Pen/Strep. Cells were differentiated by adding 4-hydroxitamoxifen (1 μL/10 mL) to culture media for 21 days.

All cell lines were maintained at 37°C in a humidified incubator with air and 5% carbon dioxide (CO_2) and, except HAP1 cell lines, collected for experiments upon reaching 85-90% confluence.

4.2.3 Sequencing of the PCR-amplified cDNA from HAP1 cells

Sequencing of PCR-amplified cDNA from HAP1 cells was performed with the assistance of Ms Katie Holden.

RNA was isolated from parental wild-type (WT) and PRLR knockout (KO) HAP1 cells following the protocol outlined in Chapter 2. cDNA was then synthesised from 1 μg of RNA

using the LunaScript® RT SuperMix Kit (New England Biolabs, cat. no. E3010) as described in Chapter 2. The cDNA was then amplified by PCR using OneTaq® Hot Start DNA Polymerase (New England Biolabs, cat. no. M0484), 10 µM of forward and reverse primers were added to 12.5 µL of OneTaq Hot Start 2X Master Mix with standard buffer and the volume was increased to 25 µL using nuclease-free water from the kit. The reactions were incubated in the applied biosystems Veriti thermal cycler (Thermo Fisher Scientific, cat. no. 4375305) using the following protocol: an initial denaturation step at 94°C for 30 seconds. This was followed by 30 cycles of denaturation at 94°C for 15-30 seconds, annealing at 45-68°C for 15-60 seconds, and extension at 68°C for 1 minute per kilobase of target DNA. After the cycling steps, a final extension was carried out at 68°C for 5 minutes. PCR products were then collected for further processing.

PCR products were separated by agarose gel electrophoresis. A 1% agarose gel was prepared by dissolving agarose powder (Sigma, cat. no. A9539) in 1X Tris-acetate ethylenediaminetetraacetic acid (EDTA) (TAE) buffer, followed by staining with SYBR™ Safe (Thermo Fisher Scientific, cat. no. S33111). The gel was cast and allowed to solidify before being submerged in 1X TAE buffer in an electrophoresis chamber (Bio-Rad, cat. no. 1704401). PCR samples were mixed with 6X loading dye and loaded into the gel along with a DNA ladder (Thermo Fisher Scientific, cat. no. 10488090) for size comparison. The gel was run at 100 V for 45 minutes, and DNA bands were visualised using a UV transilluminator.

The bands of interest were excised and purified using the QIAquick® Gel Extraction Kit (QIAGEN, cat. no. 28704). To extract the DNA fragments, the gel slice was weighed, and 1 volumes of diffusion buffer were added per volume of gel (100 µL of buffer for every 100

mg of gel). The sample was incubated at 50°C for 30 minutes, followed by centrifugation for 1 minute at 10,000 *g*. The supernatant was carefully removed and passed through a disposable plastic column to eliminate any residual polyacrylamide. The volume of the recovered supernatant was measured, and three volumes of Buffer QG were added to one volume of supernatant. The mixture was checked to ensure the colour was yellow; if it appeared orange or violet, 10 µL of 3 M sodium acetate (pH 5.0) was added to adjust the colour to yellow.

Next, a QIAquick Spin Column was placed in a provided 2 mL collection tube. The sample was applied to the column and centrifuged at 10,000 *g* for 30–60 seconds to bind the DNA. The flow-through was discarded, and the column was placed back into the same collection tube. To wash the column, 0.75 mL of Buffer PE was added, and the column was centrifuged again for 30–60 seconds at 10,000 *g*. After discarding the flow-through, the column was centrifuged for an additional minute at maximum speed to remove residual ethanol from Buffer PE.

The QIAquick Spin Column was then transferred to a clean 1.5 mL microcentrifuge tube. To elute the DNA, 50 µL of Buffer EB (10 mM Tris·Cl, pH 8.5) was added to the centre of the column and centrifuged for 1 minute at 10,000 *g*.

Purified PCR products were submitted for Sanger sequencing to Genewiz using the same primers as those employed in the PCR amplification. The primer sequences were as follows: CTGCCTTCTGAATGGACAGTT (forward; exon 3) and CCACAGAGATCCACACGGTTG (reverse; exon 8).

4.2.4 FFPE embedded cell pellets

Eight T175 flasks of both PRLR KO cells and parental HAP1 cells were utilised to create FFPE cell pellets. Cells were detached using 10 mM EDTA (Sigma, cat. no. E9884) and pelleted by centrifugation at 930 *g* for 5 minutes. The pellets were then washed with phosphate-buffered saline (PBS) (Gibco, cat. no. 10010023). The cells were fixed overnight in neutral buffered formalin (Sigma, cat. no. HT501128). After fixation, the pellets were processed, trimmed, embedded, sectioned into 4 μm thick slices, and mounted onto slides by the Translational Histopathology Laboratory at the University of Oxford, following established protocols (166). FFPE T47D cell pellets were sourced from Amsbio, UK (cat. no. 3010-0620).

4.2.5 Protein extractions and immunoblotting

Proteins were extracted from cell lines and protein concentration quantified as described in Chapter 2.

Cell lysates (40ug), full length 5-HT2B recombinant protein (20ng) (Abnova, H00003357-P01), and the PRLR overexpression human embryonic kidney (HEK293T) cell lysate (5ug) (Origene cat. no. LY424444) were analysed by immunoblotting. Immunoblotting was performed as described in Chapter 2 and the antibodies used are detailed Table 4.1.

Table 4.1: Antibodies used for immunoblotting and immunofluorescence.

	Concentration	Manufacturer	Catalog Number	Species	Clonality	Immunoblotting Dilution	Immunofluorescence Dilution
Primary antibodies							
Anti-DYKDDDDK Tag	54 µg/mL	Cell Signalling Technology	8146	Mouse	Monoclonal	-	1 in 250
Anti-GAPDH	1 mg/mL	Abcam	ab9485	Rabbit	Polyclonal	1 in 1000	-
Anti-Glucagon	7 mg/mL	Sigma	G2654	Mouse	Monoclonal	-	1 in 1000
Anti-Glucagon	0.303 mg/mL	Abcam	Ab92517	Rabbit	Monoclonal	-	1 in 1000
Anti-Glucagon-like peptide-1 (GLP-1)	1.0 6mg/mL	Abcam	ab26278	Mouse	Monoclonal	-	1 in 500
Anti-Insulin (Autostainer link 48)	-	Agilent	IR00261-2	Guinea pig	Polyclonal	-	Undiluted
Anti-Ki67 (Alexa Fluor ® 555)	0.5 mg/mL	Abcam	ab215226	Rabbit	Monoclonal	-	1 in 250
Anti-Prolactin receptor	100 µg/mL	Cell Signalling Technology	13552	Rabbit	Monoclonal	1 in 500	1 in 50
Anti-Serotonin receptor 5B	200 µg/mL	Santa Cruz Biotechnology	sc-376878	Mouse	Monoclonal	1 in 250	1 in 50
Secondary antibodies for immunoblotting							
IRDye 680 anti-Mouse IgG	10 mg/mL	LI-COR Biosciences	926-68072	Donkey	-	1in 10000	-
IRDye 800 anti-Rabbit IgG	10 mg/mL	LI-COR Biosciences	926-32213	Donkey	-	1in 10000	-
Secondary antibodies for immunofluorescence							
Goat anti-Mouse IgG (H+L) Highly Cross-Adsorbed Secondary Antibody, Alexa Fluor™ Plus 488	2 mg/mL	Invitrogen	A32723	Goat	Polyclonal	-	1 in 400
Goat anti-Rabbit IgG (H+L) Highly Cross-Adsorbed Secondary Antibody, Alexa Fluor™ Plus 488	2 mg/mL	Invitrogen	A32731	Goat	Polyclonal	-	1 in 400
Goat anti-Mouse IgG (H+L) Highly Cross-Adsorbed Secondary Antibody, Alexa Fluor™ Plus 555	2 mg/mL	Invitrogen	A21424	Goat	Polyclonal	-	1 in 400
Goat anti-Rabbit IgG (H+L) Highly Cross-Adsorbed Secondary Antibody, Alexa Fluor™ Plus 555	2 mg/mL	Invitrogen	A32732	Goat	Polyclonal	-	1 in 400
Goat anti-Guinea Pig IgG (H+L) Highly Cross-Adsorbed Secondary Antibody, Alexa Fluor™ Plus 647	2 mg/mL	Invitrogen	A21450	Goat	Polyclonal	-	1 in 400
VectaFluor™ Excel Amplified Anti-Rabbit IgG, DyLight™ 488 Antibody Kit	-	Vector Laboratories	DK-1488	-	-	-	Undiluted

4.2.6 Immunofluorescence labelling of formalin-fixed paraffin embedded tissue sections and formalin-fixed paraffin embedded cell pellets

Immunofluorescence labelling of tissue sections (IHC-IF) and cell pellets was performed as described in Chapter 2. The details of the primary and secondary antibodies used to label the PRLR, the 5HT2B receptor, Ki-67, and glucagon-like peptide-1 (GLP-1) are provided in Table 4.1. Following initial labelling of the PRLR, the 5-HT2B receptor, Ki-67, and GLP-1, respectively, FFPE tissue sections were subsequently sequentially labelled for either glucagon or insulin, or both (glucagon followed by insulin). For glucagon and insulin, primary antibodies were incubated at room temperature for 2 hours each followed by incubation with secondary antibodies as described in Chapter 2.

In order to amplify the signal when labelling islets for PRLR, the protocol was modified by using the VectaFluor™ Excel Amplified Anti-Rabbit IgG, DyLight™ 488 Antibody Kit (Vector Laboratories, cat. no. DK-1488), as per manufacturer instructions, in lieu of 5% goat serum and the secondary antibodies.

4.2.7 Chromogenic immunolabelling of formalin-fixed paraffin embedded tissue sections and formalin-fixed paraffin embedded cell pellets

Chromogenic immunolabelling of tissue sections (IHC) to label FFPE tissue sections and cell pellets for PRLR was performed as described in Chapter 2. The anti-PRLR antibody used is shown in Table 5.1.

4.2.8 Image acquisition and quantitative data analysis

4.2.8.1 Image acquisition

Image acquisition was performed in collaboration with Dr James Bancroft and Edward Drydale (Cellular Imaging Core Facility, CHG, Oxford UK).

Imaging of IHC-IF labelled FFPE tissue sections and cell pellets was performed using an Olympus SpinSR SoRa spinning disc confocal microscope, fitted with a 10x 0.4 numerical aperture air objective and the 50 µm pinhole disc of a Yokogawa CSU-W1 spinning disc unit. The system included a Hammamatsu ORCA Fusion BT camera, with excitation lasers at 405 nm, 488 nm, 561 nm, and 640 nm.

Images labelled using IHC-DAB were captured using an Olympus VS200 research slide scanner, equipped with a 20x 0.8 numerical aperture air objective, and controlled by the VS2000 ASW software.

4.2.8.2 Image analysis pipeline

A comprehensive analysis pipeline was developed and applied to all IHC-IF images of whole pancreas tissue sections. To process and analyse the images, I utilised a sequence of operations using Arivis Vision4D (v 4.1.2) image analysis software. Initially, a closing operation was applied to the glucagon and insulin channels to remove small gaps and connect disjointed objects, followed by a mean filter to reduce noise and smooth the image. The 488 channels (anti-PRLR, anti-5-HT2B receptor, and anti-GLP-1) underwent a mean filter to enhance signal quality. Thresholding was then applied to the insulin and glucagon channels to identify their respective signals, which were subsequently combined to form a complete islet signal (to define a whole islet). A size filter was used to exclude non-specific

staining smaller than 1000 μm², ensuring that only genuine islet structures were analysed. Another closing operation was performed to refine islet shapes, followed by intersections with glucagon and insulin channels to isolate regions expressing both hormones. The islets were then compartmentalised into whole islets, α cells (glucagon positive cells), β cells (insulin positive cells), and bihormonal cells (expressing both glucagon and insulin), allowing for detailed morphological and quantitative analysis.

Object math was employed to differentiate exocrine tissue from islet compartments, and to quantify these areas. The longest axis of the islet was measured for islet diameter. To identify nuclei within islets, a watershed function was applied, followed by a size filter to exclude objects larger than 10 μm. Nuclei counts and diameters within α cells, β cells, and whole islets were quantified. All data were exported to Microsoft Excel for further analysis.

To address differences in total tissue area across sections, various normalisation techniques were applied to whole islet, α cell, β cell, bihormonal cell, and GLP-1 positive areas prior to comparisons. The areas of whole islets, α cells, β cells, bihormonal cells, and GLP-1 positive regions were expressed as a ratio to the total exocrine area per section, termed fractional area. The mean areas of these regions were calculated by dividing the measured area by the number of islets per tissue section. Additionally, the proportions of α cells, β cells, bihormonal cells, and GLP-1 positive regions relative to the total islet area were determined, as well as the proportion of GLP-1 positive area relative to the total α cell area. The number of islets was then normalised to the tissue section area to represent islet density.

To estimate α and β cell sizes, their total measured areas were divided by the number of nuclei in the corresponding regions, and the nuclei counts for α and β cells were expressed

as percentages of the total islet nuclei per section. Data were plotted, and statistical comparisons between groups were performed using Prism 10.

4.2.8.3 Colocalisation analysis

Colocalisation analysis of the 5-HT2B receptor and insulin channels in whole pancreatic tissue sections was conducted using Arivis Vision4D image analysis software's built-in colocalisation tool. The software automatically applied auto thresholds for the 5-HT2B receptor and insulin channels. Scatter plots comparing the 5-HT2B receptor signal with the insulin channel were generated, and Manders' coefficients were calculated. Specifically, Manders' coefficient M1, indicating the proportion of the insulin signal overlapping with the 5-HT2B receptor signal, and Manders' coefficient M2, representing the proportion of the 5-HT2B receptor signal overlapping with the insulin signal, were computed.

4.2.9 Statistics

Statistical comparisons were conducted using the appropriate tests, as described in Chapter 2, depending on the data distribution and experimental design. Statistical significance was defined as $p < 0.05$.

4.3 Results

4.3.1 Donor characteristics

The details comparing pregnant donors and non-pregnant controls are presented in Table 3.1 in Chapter 3. Table 4.2 shows the symbols that are used to represent each data point in the figures presented in this chapter, these correspond with the nPOD identifying numbers of each case. The descriptive characteristics of each donor, which match with their nPOD identifying number, are presented in Table 3.2 in Chapter 3.

Table 4.2: nPOD identifying numbers (ID), corresponding symbols that are presented in the figures, and number of islets analysed per donor.

nPOD ID	Symbol	Number of islets analysed
6226	●	234
6257	N/A	301
6310	■	428
6363	▲	692
6383	◆	577
6082	✦	1009
6239	▼	1655
6405	★	522
6559	●	406
6479	■	413
6425	▲	441
6253	◆	747
6251	✦	822
6331	▼	1178
6401	★	1279

4.3.2 Overview of experimental workflow and image analysis pipeline

An unbiased, quantitative analysis of whole pancreatic tissue sections, labelled with multiple antibodies via IHC-IF, was performed using an automated image analysis pipeline to ensure robust quantification. The resulting data were subjected to statistical comparison and analysis. An illustration of the experimental workflow is shown in Figure 4.1. Figure 4.2 outlines the specific steps of the pipeline, including image acquisition, processing, segmentation, and quantitative analysis methods used for analysing the islet cell metrics.

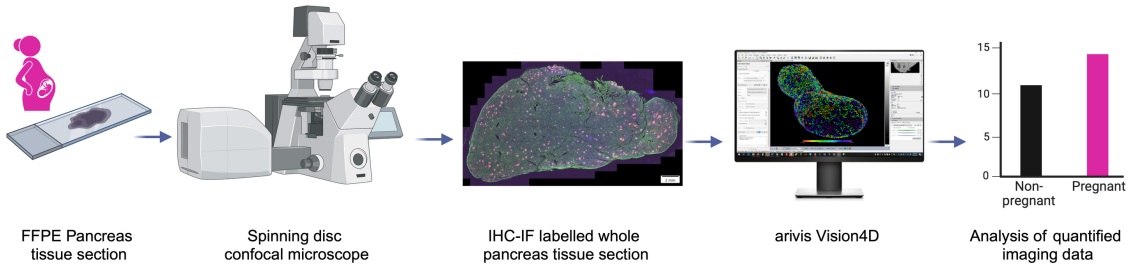

Figure 4.1. Schematic of the experimental workflow: formalin-fixed paraffin-embedded (FFPE) human pancreatic tissue sections were first labelled using immunofluorescence (IHC-IF). Images were acquired by confocal microscopy and subjected to quantitative analysis, concluding with data analysis comparing the pregnant and non-pregnant groups. Created with BioRender.com released under a Creative Commons Attribution-NonCommercial-NoDerivs 4.0 International license. Reproduced from a manuscript accepted for publication in *Nature Communications, Seedat et al.* (2025). This content is distributed under the Creative Commons Attribution License (CC BY 4.0).

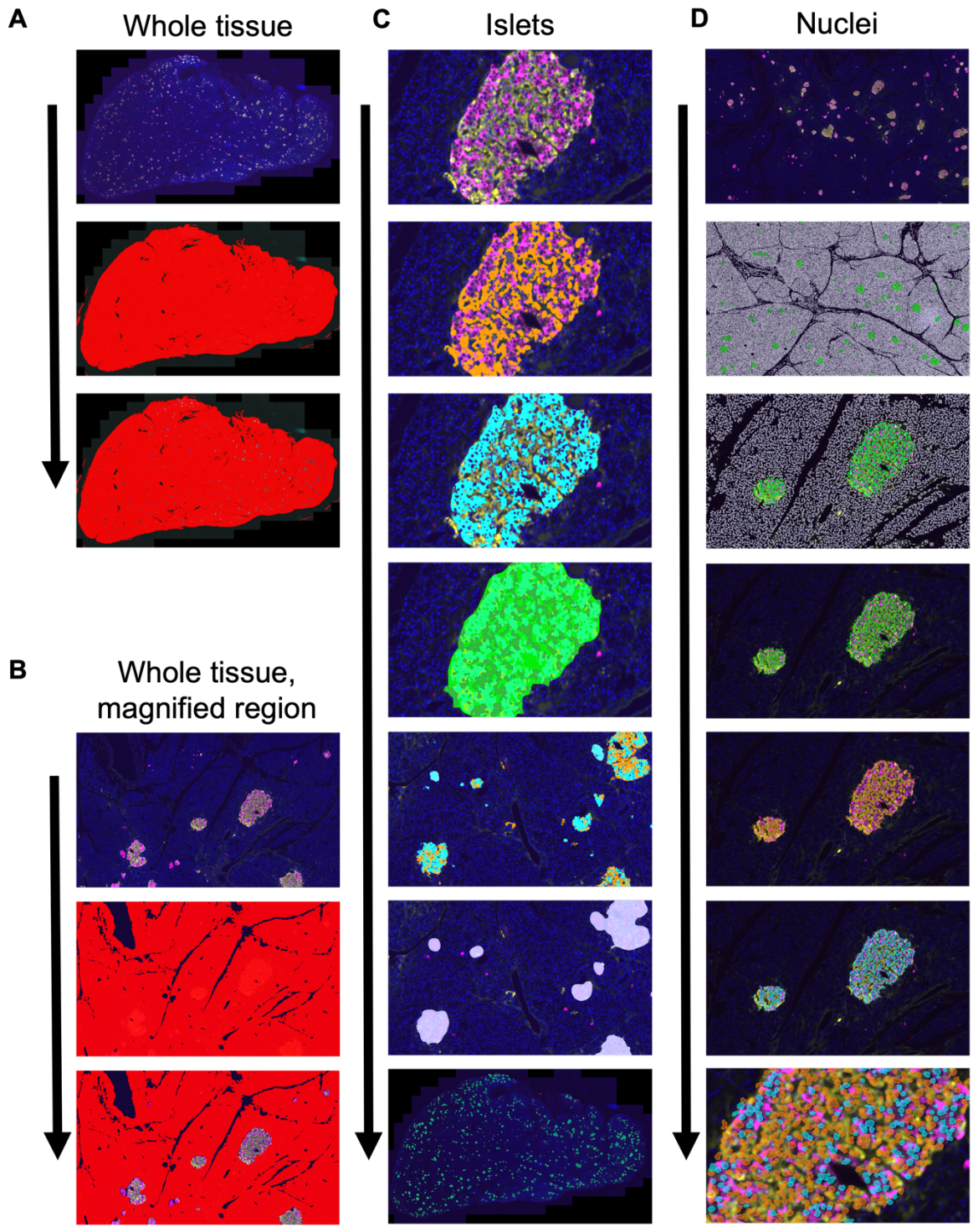

Figure 4.2. The images illustrate the key steps in the analysis pipeline used to evaluate immunofluorescence (IHC-IF) labelled pancreatic tissue sections. **A.** The full tissue section and **B.** a magnified area are shown, labelled with DAPI (nuclei in blue), anti-glucagon (α cells in yellow), and anti-insulin (β cells in magenta) antibodies. Thresholding was applied to the entire section (red), and exocrine tissue was identified by excluding islets from the

thresholded regions. **C.** Islets, labelled with anti-glucagon (yellow) and anti-insulin (magenta) antibodies, were analysed to mark α and β cells. Thresholding was used to identify α cells (orange) and β cells (blue), and these compartments were merged to define whole islets (green). α (orange) and β (blue) cell regions were marked across the entire tissue section. Size filtering was used to remove islets smaller than 1000 μm² from analysis. Whole islets were identified throughout the tissue section (green). **D.** Nuclei within islet tissue were examined. The image shows IHC-IF of labelled nuclei, α and β cells, and thresholded nuclei in exocrine tissue (white) and whole islets (green). Nuclei within whole islets (green), α cells (orange), and β cells (blue) were thresholded. A magnified view shows thresholded nuclei in α cells (orange) and β cells (blue). Reproduced from a manuscript accepted for publication in *Nature Communications, Seedat et al.* (2025).

4.3.3 Quantitative analysis of whole islet, α-cell, and β-cell area in pancreata from pregnant women

In tissue sections from each donor, islets (identified by markers for α and β cells) were distributed throughout the pancreatic tissue as expected (Figure 4.3). The relative areas (expressed as a percentage of total tissue area, termed fractional area) of whole islets, α cells, β cells, and bihormonal cells were increased in pregnant women compared to non-pregnant controls. Whole islet fractional area was increased by 1.9-fold (3 ± 0.46% vs. 1.6 ± 0.16%, $p = 0.0145$), α cell fractional area by 4.3-fold (0.44 ± 0.12% vs. 0.1 ± 0.02%, $p = 0.0206$), β cell fractional area by 1.9-fold (1.26 ± 0.23% vs. 0.65 ± 0.07%, $p = 0.0241$), and bihormonal cell fractional area by 5.4-fold (0.17 ± 0.05% vs. 0.03 ± 0.01%, $p = 0.0137$), respectively (Figure 4.4).

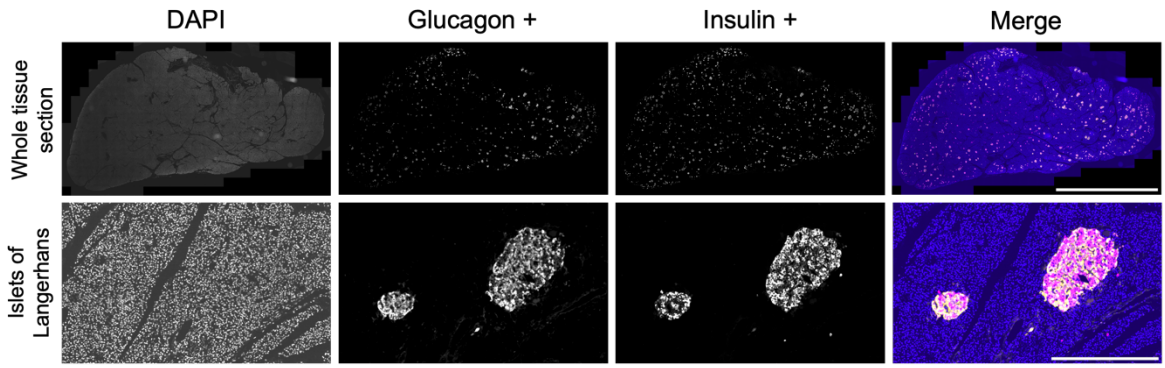

Figure 4.3. Immunofluorescence (IHC-IF) labelling of human pancreas tissue. Nuclei (DAPI, blue), glucagon-positive α cells (yellow), and insulin-positive β cells (magenta) are labelled in human pancreatic tissue. Individual channels are shown in grayscale and a merged composite image in colour. Both the entire tissue section and an individual islet a shown. Scale bars = 10 mm for the whole tissue section and 500 µm for the individual islet. Reproduced from a manuscript accepted for publication in *Nature Communications, Seedat et al.* (2025). This content is distributed under the Creative Commons Attribution License (CC BY 4.0).

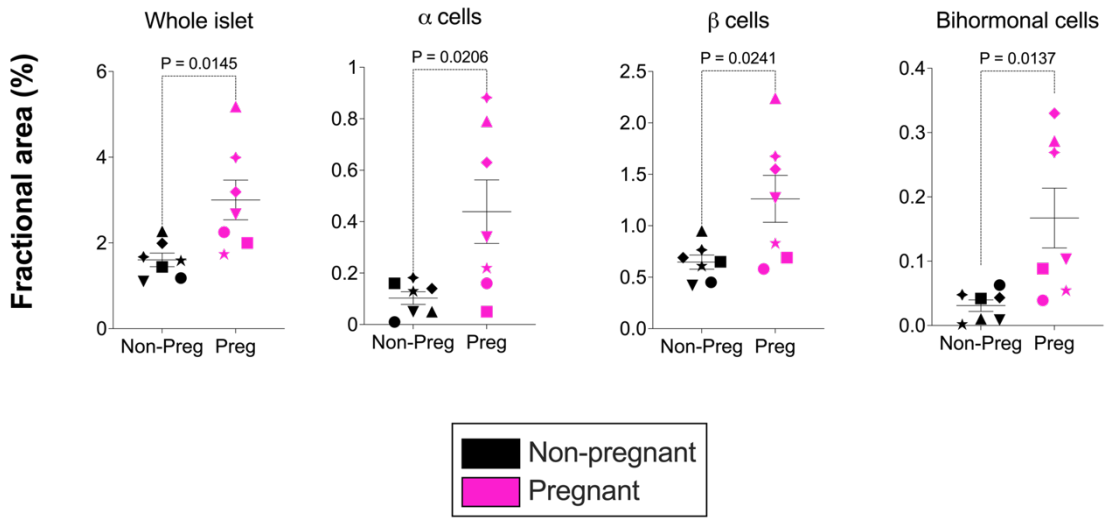

Figure 4.4. Quantitative comparisons between pregnant and non-pregnant women for fractional area (measured area as a percentage of total tissue area). Symbols in each figure correspond to individual donors as indicated in Table 4.2. Statistically significant differences are marked with p-values. Reproduced from a manuscript accepted for publication in *Nature Communications, Seedat et al.* (2025). This content is distributed under the Creative Commons Attribution License (CC BY 4.0).

Despite this increase in relative islet area, the density of islets (measured as the number of islets per mm² of tissue section) remained the same between pregnant and non-pregnant donors (Figure 4.5A), suggesting the changes observed may be driven by an increase in islet size rather than islet number. Supporting this, the longest axis of the islet diameter showed a 1.2-fold increase (92.73 ± 1.84 μm² vs. 109.28 ± 4.59 μm², p = 0.0058) (Figure 4.5B). However, due the irregular shapes of islets, islet area is a more reliable measure. Absolute measurements showed a 1.4-fold increase in the average islet area (8538.61 ± 551.65 μm² vs. 6253.80 ± 288.86 μm², p = 0.032) in samples from pregnant donors compared to controls (Figure 4.5C).

Further analysis revealed that the increased islet area in pregnant women was accompanied by a proportional increase in the average total areas of α cells, β cells, and bihormonal cells per islet. Specifically, α cells showed a 2.9-fold increase (1162.98 ± 180.99 μm² vs. 407.72 ± 87.05 μm², p = 0.0027), β cells a 1.3-fold increase (3469.66 ± 253.16 μm² vs. 2657.40 ± 156.02 μm², p = 0.0182), and bihormonal cells a 3.1-fold increase (408.43 ± 83.20 μm² vs. 132.83 ± 28.59 μm², p = 0.0087) (Figure 4.5C). These results indicate that the increase in islet size during pregnancy is driven by expansion of the α-cell, β-cell, and bihormonal cell populations.

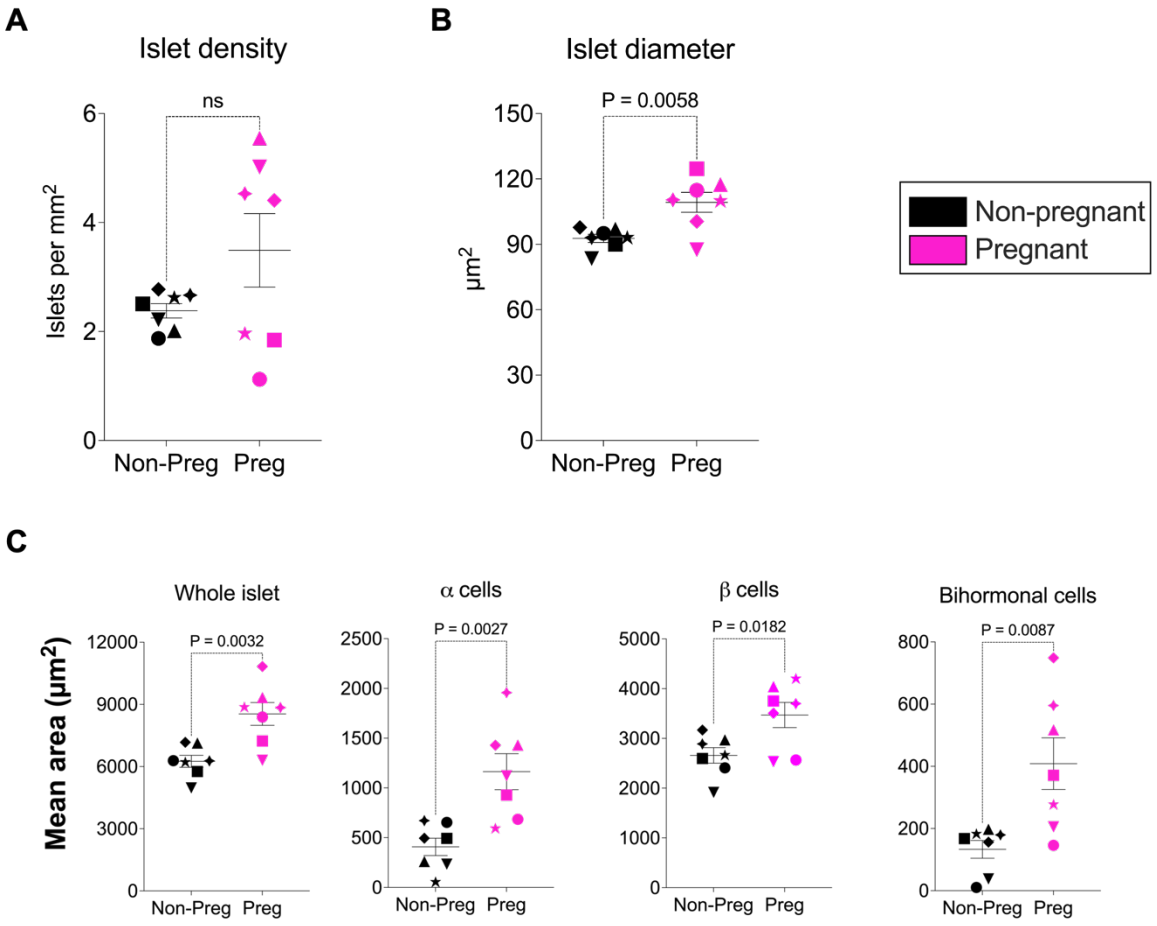

Figure 4.5. A. Islet density and **B.** whole islet diameter compared between non-pregnant and pregnant women. **C.** Quantitative comparisons between pregnant and non-pregnant women for mean area (measured area divided by number of islets per tissue section) of whole islets, α cells, β cells, and bihormonal cells. Symbols in each figure correspond to individual donors as indicated in Table 4.2. Statistically significant differences are marked with p-values, while "ns" indicates non-significant comparisons. Reproduced from a manuscript accepted for publication in *Nature Communications, Seedat et al.* (2025). This content is distributed under the Creative Commons Attribution License (CC BY 4.0).

Moreover, the relative cellular composition of the islets changed in pregnant women. The relative areas occupied by α cells and bihormonal cells increased by 2.3-fold (13.16 ± 2.60% vs. 5.83 ± 1.32%, p = 0.0273) and 2.6-fold (4.64 ± 1.21% vs. 1.76 ± 0.45%, p = 0.0452), respectively, while the proportion of β cells relative to total islet area remained unchanged (Figure 4.6). This suggests that in pregnancy, the mass of β cells grows proportionally with the entire islet, whereas the expansion of α and bihormonal cells outpaces overall islet growth.

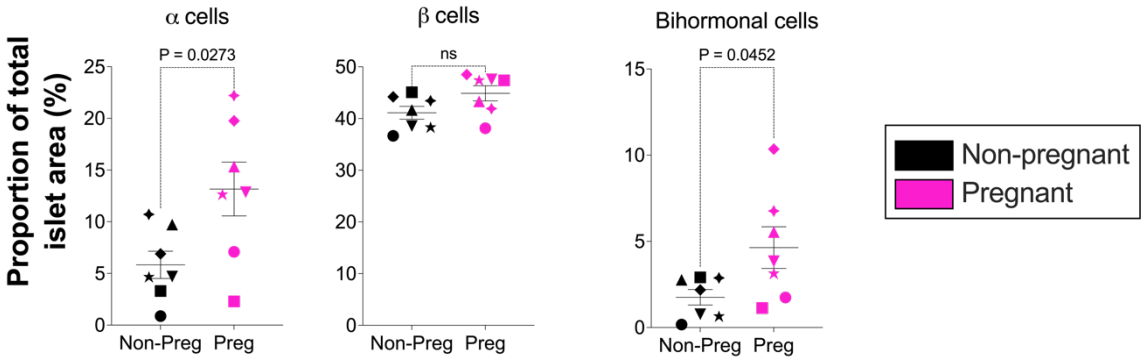

Figure 4.6. Quantitative comparisons between pregnant and non-pregnant women for comparisons of the proportions of α, β, and bihormonal cells relative to whole islets (measured area as a percentage of total whole islet area) are shown. Symbols in each figure correspond to individual donors as indicated in Table 4.2. Statistically significant differences are marked with p-values, while "ns" indicates non-significant comparisons. Reproduced from a manuscript accepted for publication in *Nature Communications, Seedat et al.* (2025). This content is distributed under the Creative Commons Attribution License (CC BY 4.0).

No differences were found in the size of individual α or β cells between pregnant and non-pregnant women (Figure 4.7), suggesting that the size of individual α and β cells remains constant. Additionally, the α-cell count increased by 3.3-fold (1.01 ± 0.28% vs. 0.3 ± 0.06%, $p = 0.0323$) and the β-cell count by 1.7-fold (2.11 ± 0.37% vs. 1.22 ± 0.12%, $p = 0.0384$) in pregnant donors compared to controls (Figure 4.7). Taken together this suggests that the increase in cellular area in pregnant women, compared to non-pregnant controls, is due to a rise in cell number rather than cell hypertrophy.

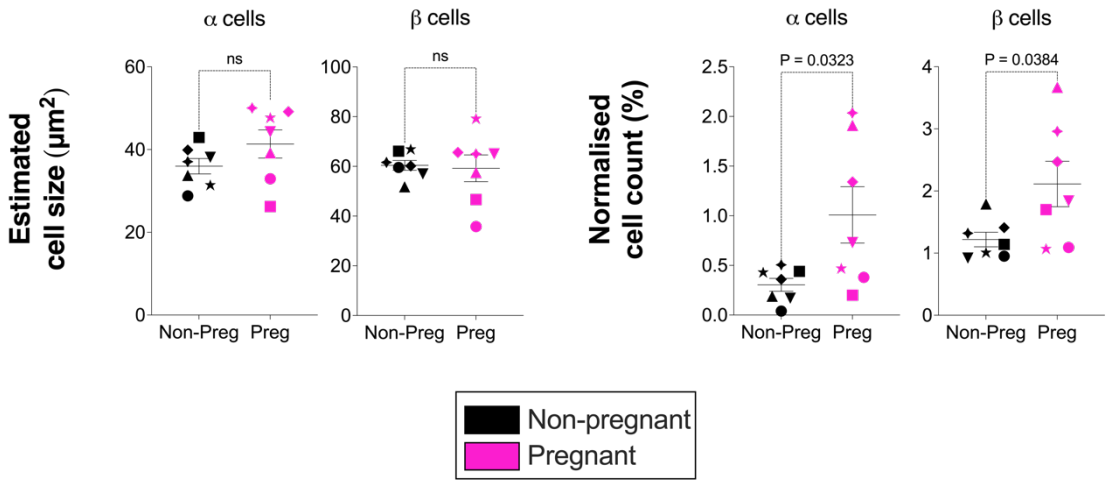

Figure 4.7. Measurements of estimated α-cell and β-cell sizes, as well as normalised α-cell and β-cell counts compared between pregnant and non-pregnant women. Symbols in each figure correspond to individual donors as indicated in Table 5.2. Statistically significant comparisons are indicated with p-values, while "ns" denotes non-significant differences. Reproduced from a manuscript accepted for publication in *Nature Communications, Seedat et al.* (2025). This content is distributed under the Creative Commons Attribution License (CC BY 4.0).

As I noted an increase in cell number as a possible explanation for the increase in α and β cell mass, I sought to investigate if evidence of islet cell proliferation could be observed during human pregnancy, by using an anti-Ki-67 antibody to detect proliferation. However, no Ki-67-positive islet cells were observed in tissue sections from pregnant women at 12, 32, or 34 weeks of gestation, nor in non-pregnant controls (Figure 4.8). The presence of Ki-67 in malignant tissues, which were labelled concurrently with the pancreas sections, and pancreatic exocrine cells served as a positive control, confirming that the anti-Ki-67 antibody was functional under the same experimental conditions (Figure 4.9).

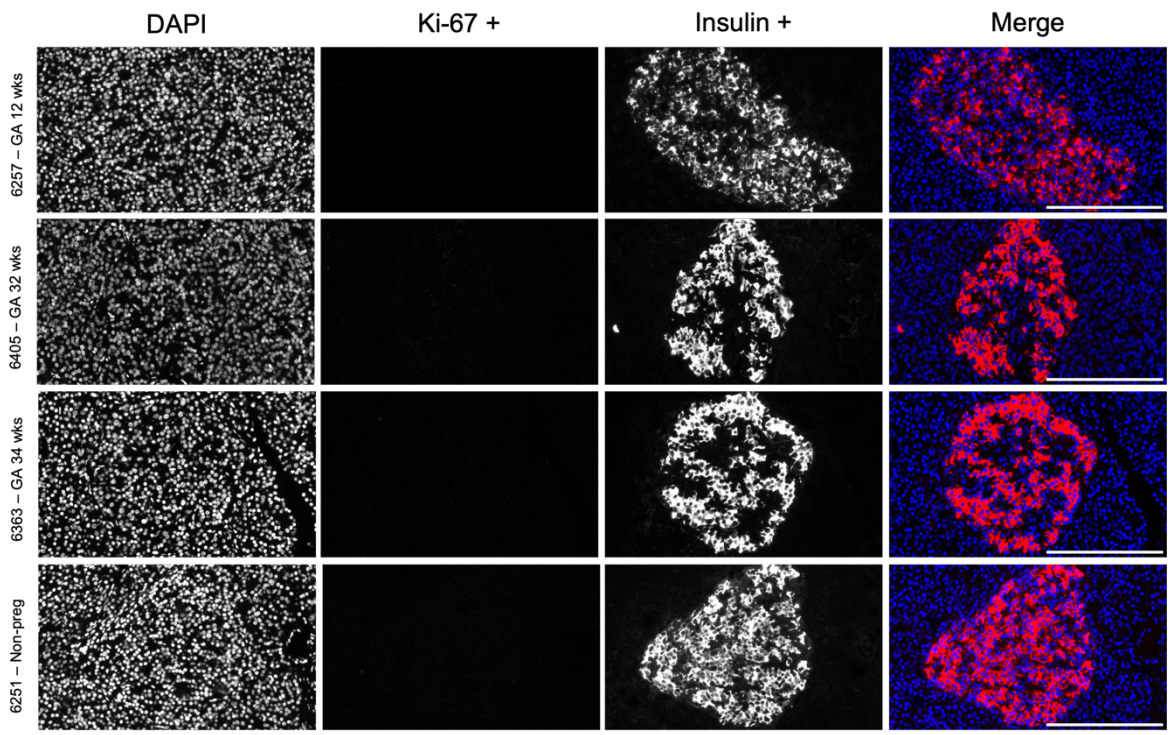

Figure 4.8. Anti-Ki-67 labelling of human pancreatic sections from pregnant women at different gestational ages and a non-pregnant control sample using immunofluorescence (IHC-IF). No Ki-67 signal is detected. Individual channels (nuclei (DAPI), Ki-67 +, and insulin + channels) are shown in grayscale and the merged image in colour (nuclei in blue, Ki-67 in cyan, and insulin in red). Scale bar = 200 μm. Reproduced from a manuscript accepted for publication in *Nature Communications, Seedat et al.* (2025). This content is distributed under the Creative Commons Attribution License (CC BY 4.0).

*GA – gestational age, wks – weeks, non-preg – non-pregnant.

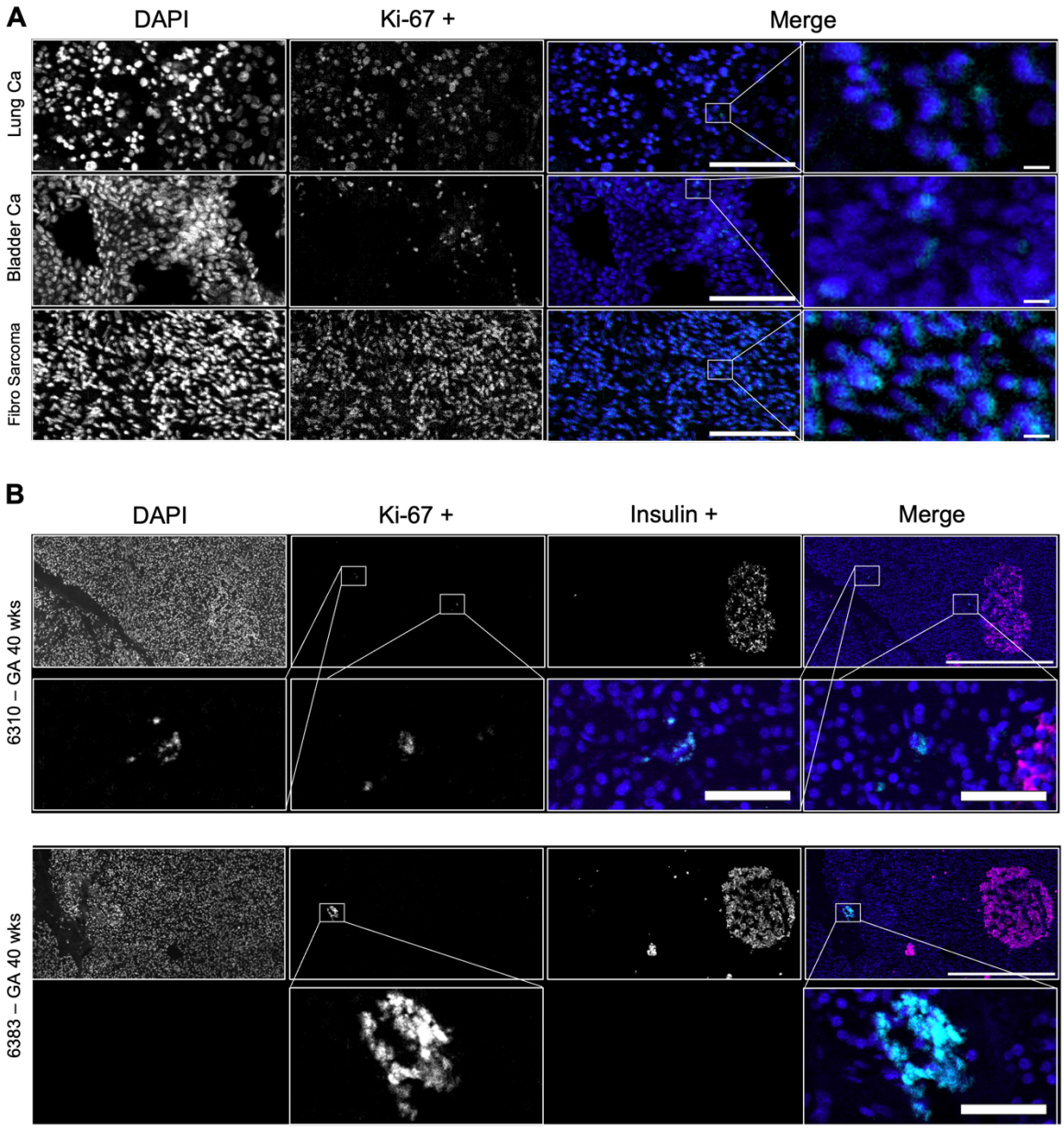

Figure 4.9. Positive controls for anti-Ki67 antibody used for immunofluorescence (IHC-IF) **A.** IHC-IF labelling of lung carcinoma (squamous cell carcinoma), bladder carcinoma (papillary transitional cell carcinoma), and fibrosynovial sarcoma for Ki-67 with the anti-Ki67 antibody (Table S2). Grayscale images of the nuclei (DAPI) and Ki-67 + channels are shown, and the composite merged image in colour shows the nuclei (DAPI, blue) and Ki-67 positive nuclei (cyan). Scale bar = 100 μm. A magnified inset image from the merged channel is also shown, Scale bar = 5 μm. **B.** Anti-Ki-67 labelling of human pancreatic sections from pregnant women at 40 weeks. Ki-67 + exocrine cells are identified in the

pancreatic sections in which islets were analysed for the presence of Ki67. Grayscale images of the nuclei (DAPI), Ki-67 +, and insulin + channels are shown, and the composite merged image in colour shows the nuclei (DAPI, blue), Ki-67 + nuclei (cyan), and insulin (magenta). Scale bar = 500 μm and a magnified inset image from the Ki-67+ grayscale channel and merged image is also shown, Scale bar = 50 μm. Reproduced from a manuscript accepted for publication in *Nature Communications, Seedat et al.* (2025). This content is distributed under the Creative Commons Attribution License (CC BY 4.0).

*GA – gestational age, wks – weeks, Ca - carcinoma.

Across all analyses, no significant differences were detected when comparing samples from women with gestational diabetes mellitus (GDM) and those with normal pregnancies (Figures 4.10 and 4.11).

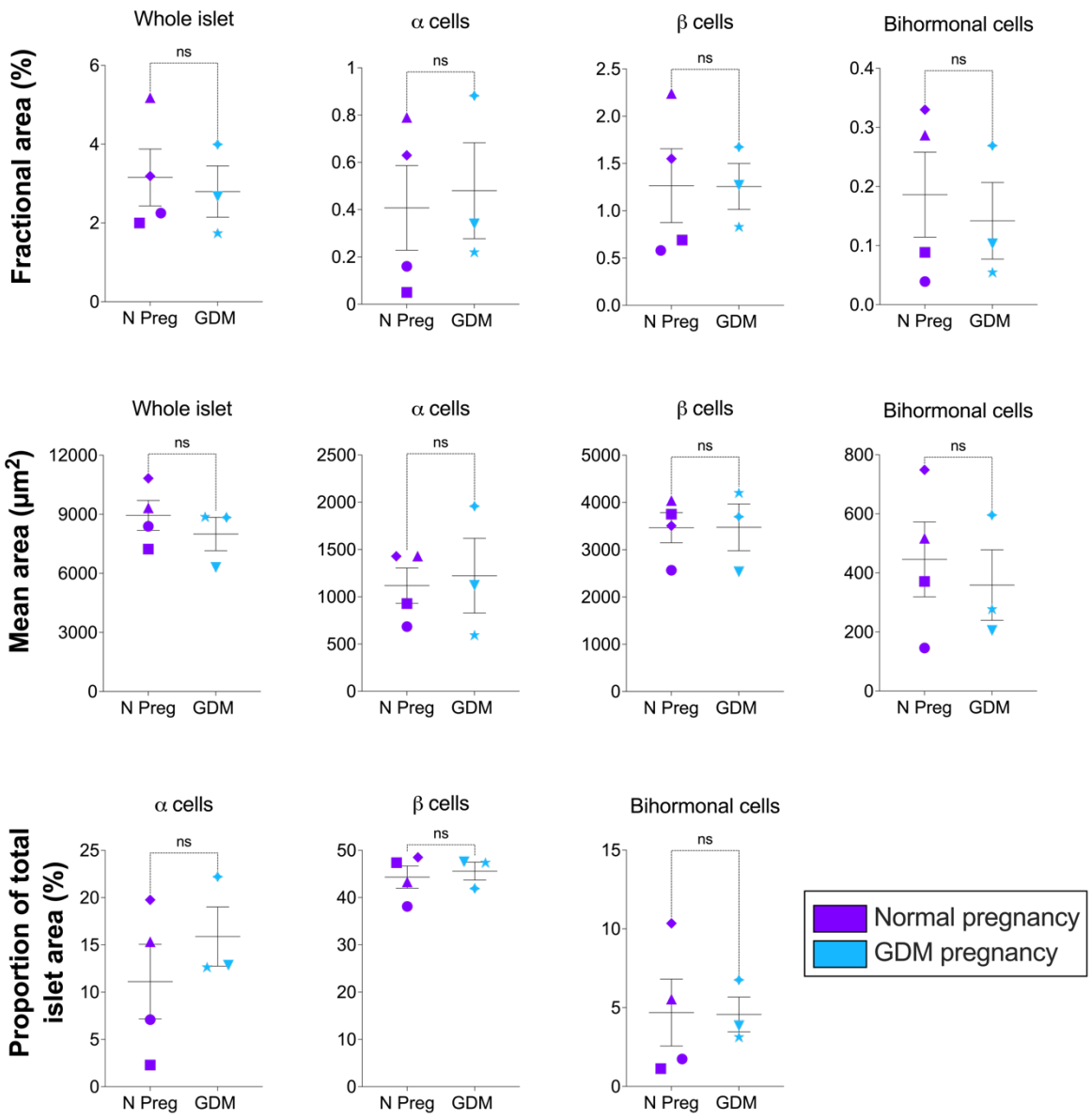

Figure 4.10. Quantitative comparisons of islet metrics between normal and gestational diabetes mellitus (GDM) pregnancy. The data includes comparisons for fractional and mean areas of whole islets, α cells, β cells, and bihormonal cells. Additionally, comparisons of the proportions of α, β, and bihormonal cells relative to whole islets are shown. Symbols in each figure correspond to individual donors as indicated in Table 5.2. "ns" indicates non-significant comparisons. Reproduced from a manuscript accepted for publication in *Nature Communications, Seedat et al.* (2025). This content is distributed under the Creative Commons Attribution License (CC BY 4.0).

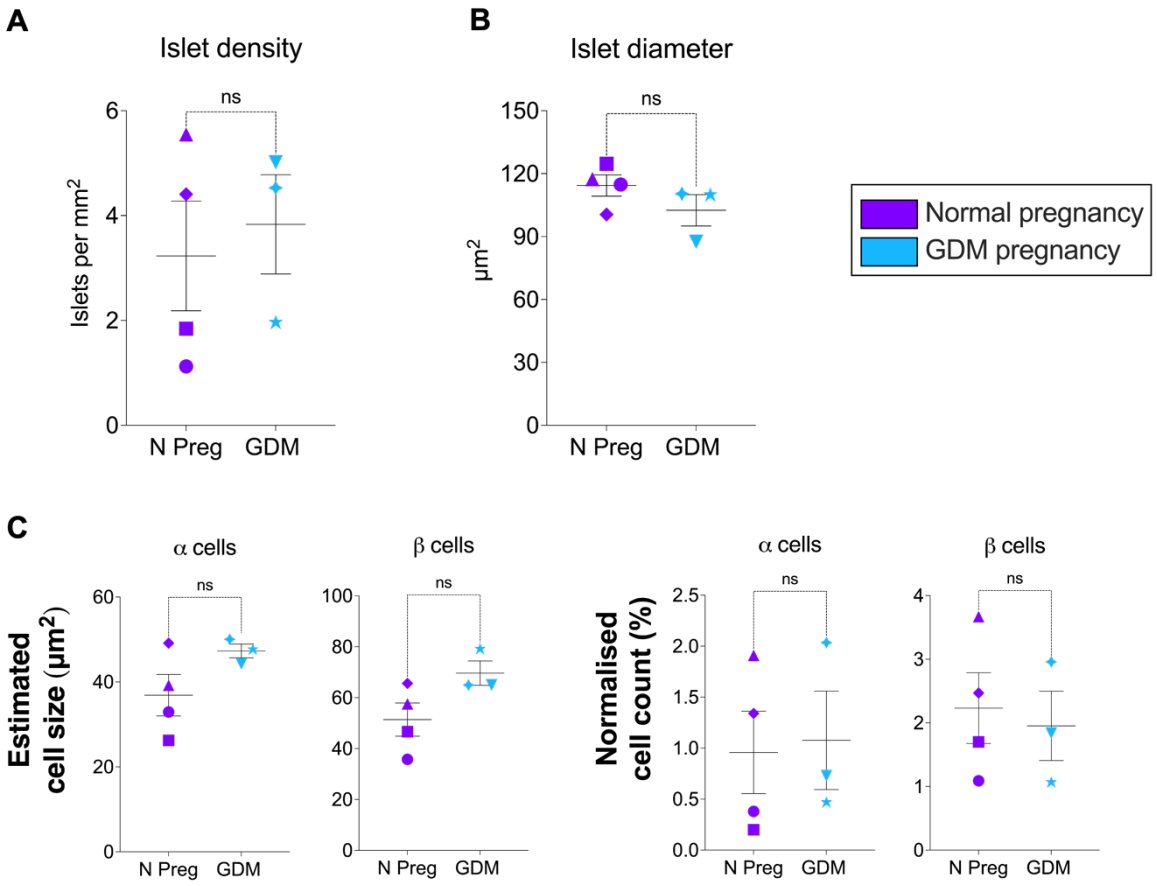

Figure 4.11. A. Islet density and **B.** whole islet diameter compared between normal and gestational diabetes mellitus (GDM) pregnancy. **C.** Quantitative comparisons of estimated α-cell and β-cell size and normalised α-cell and β-cell count between normal and GDM pregnancy. Symbols in each figure correspond to individual donors as indicated in Table 5.2. "ns" indicates non-significant comparisons. Reproduced from a manuscript accepted for publication in *Nature Communications, Seedat et al.* (2025). This content is distributed under the Creative Commons Attribution License (CC BY 4.0).

4.3.4 Validation of anti-PRLR and anti-5HT2B receptor antibodies

As neither the PRLR nor 5-HT2B receptor was identified by the proteomics analysis in Chapter 3, to thoroughly explore the expression and potential roles of PRLR and 5-HT2B receptors in pancreatic β cells during pregnancy, it was essential to analyse their expression patterns and quantify protein levels in specific islet cell types. Achieving these required techniques capable of single-cell resolution. However, given the limitations posed by the available sample types—donor FFPE pancreas tissue sections instead of fresh tissue or isolated islets—I chose to examine PRLR and 5-HT2B receptor expression during human pregnancy using a conventional approach. This involved high-resolution microscopy coupled with affinity reagents to label the target proteins via IHC-IF.

I first aimed to identify commercially available antibodies that can be used reliably to detect the PRLR and 5-HT2B receptor in FFPE human pancreas sections. I tested several commercially available antibodies and found that only the anti-PRLR (Cell Signaling Technology, cat. no. 13552) and anti-5-HT2B receptor (Santa Cruz Biotechnology, cat. no. sc-376878) antibodies showed high specificity and sensitivity, making them suitable for further analysis.

Immunoblotting confirmed that the anti-PRLR antibody successfully detected the PRLR in HEK293T cells overexpressing PRLR, as well as in parental WT HAP1 cell lysates. No signal was seen in *PRLR* knockout KO HAP1 cells (Figure 4.12A). The PRLR was also detected in FFPE T47D cell pellets, known for their high *PRLR* expression (Figure 4.12B), and in WT HAP1 FFPE pellets, but not in *PRLR* KO HAP1 FFPE cell pellets, confirming the antibody's specificity (Figure 4.12C). Furthermore, the PRLR was detected in human tissues with high *PRLR* expression but was absent in tissues with low *PRLR* levels (Figure

4.12D). By IHC-IF, the PRLR was detected in T47D FFPE cell pellets and placental tissue (Figure 4.12E and F).

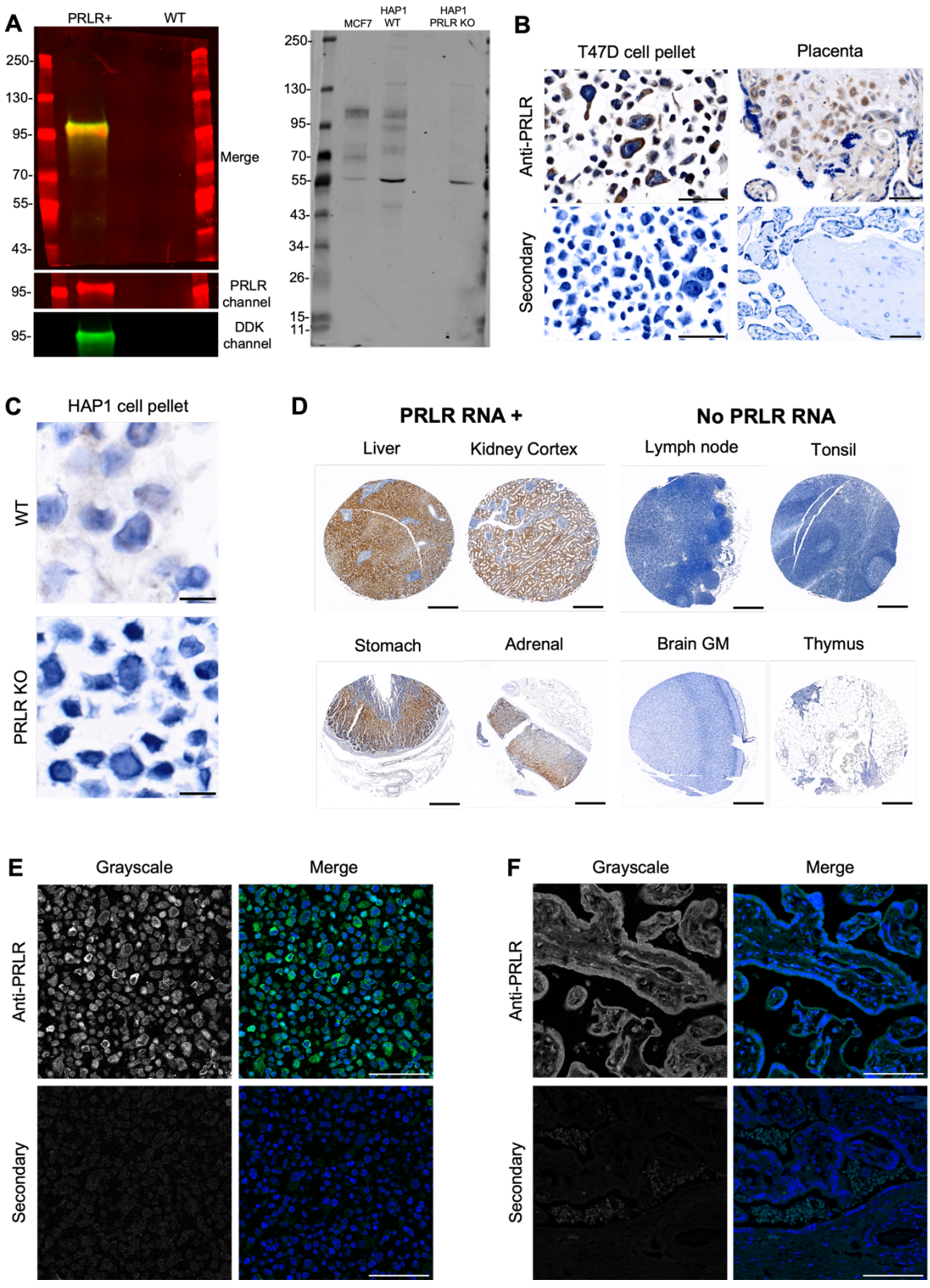

Figure 4.12. Validation of the anti-prolactin receptor (PRLR) antibody **A.** Immunoblot using the anti-PRLR antibody on PRLR overexpression in HEK293T cell lysate. Bands are observed in the PRLR overexpression cell lysate at the predicted molecular weight (PRLR

with DDK-tag) but not in the wild-type (WT) HEK293T cell lysate. A second immunoblot using the anti-PRLR antibody on MCF7 cells, HAP1 wild-type (WT), and HAP1 *PRLR* knockout (KO) cell lysate. Bands are observed at the predicted molecular weight for PRLR in MCF7 and HAP1 WT lysates but are absent in the HAP1 *PRLR* KO lysate. **B** Formalin-fixed paraffin-embedded (FFPE) T47D cell pellets and placental tissue labelled with the anti-PRLR antibody show a positive signal. No signal is observed in the secondary-only control. Scale bar = 50 µm. **C** Chromogenic immunohistochemistry (IHC) of HAP1 WT and *PRLR* KO Cells. FFPE HAP1 WT and *PRLR* KO cell pellets labelled with the anti-PRLR antibody show a positive signal in WT cells and no signal in *PRLR* KO cells. Scale bar = 20 µm. **D** IHC analysis using the anti-PRLR antibody on human tissues known to express *PRLR* RNA and tissues where the *PRLR* RNA is absent. Tissues with *PRLR* expression exhibit a positive signal, while those without *PRLR* RNA show no signal. Scale bar = 500 µm. **E** Immunofluorescence **(**IHC-IF) of FFPE T47D cell pellets and **F** placental tissue labelled with the anti-PRLR antibody showing a positive signal. No signal is observed in the secondary-only control. Scale bars: T47D cell pellets and placental tissue = 100 µm. Reproduced from a manuscript accepted for publication in *Nature Communications, Seedat et al.* (2025).

Non-specific binding by several other anti-PRLR antibodies tested in *PRLR* KO HAP1 cells is shown in Figure 4.13. These antibodies were not used in this study. The catalogue numbers and manufacturers of these antibodies used are provided in the figure legend.

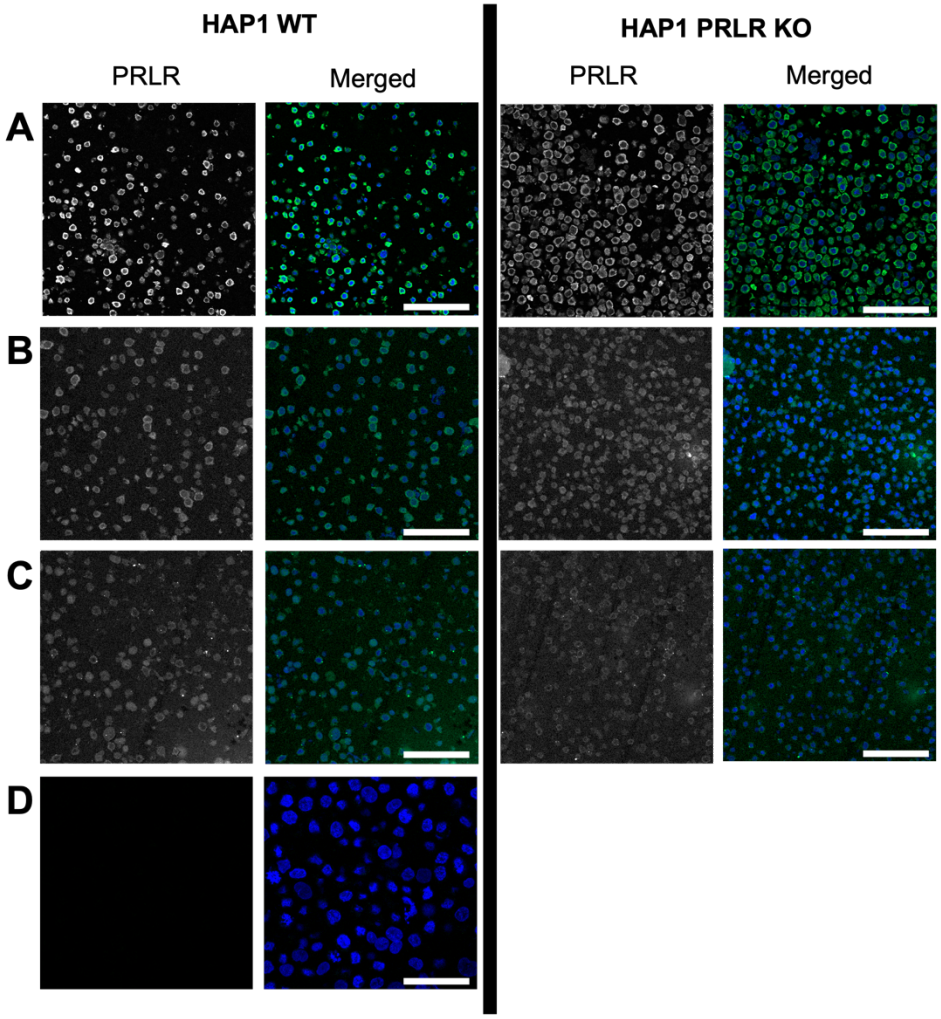

Figure 4.13. Assessment of specificity of anti-prolactin receptor (PRLR) antibodies by immunofluorescence (IHC-IF) of formalin-fixed paraffin-embedded FFPE HAP 1 wild-type (WT) and *PRLR* knockout (KO) cell pellets. Antibodies that were noted to label both HAP1 WT and *PRLR* KO cells are shown. These include **A.** PRLR monoclonal antibody (Proteintech, cat. no. 67292), **B.** Prolactin R antibody B6.2 + PRLR742 (Novus biologicals, cat. no. NBP2-34286), **C.** Human Prolactin R Antibody (R&D systems, cat. no. MAB1167), **D.** Secondary only control. Grayscale images of the PRLR channel is shown and the merged image shows the nuclei (DAPI, blue) and PRLR (green). Scale bar = 100 µm. Reproduced from a manuscript accepted for publication in *Nature Communications, Seedat et al.* (2025).

The anti-5-HT2B receptor antibody effectively detected the protein by immunoblotting in cell lysates with known 5-HT2B receptor expression, as well as in recombinant 5-HT2B protein (Figure 4.14A). No band was observed in cell lysates with low or absent 5-HT2B receptor expression. IHC-IF showed positive labelling in WT HAP1 FFPE pellets and cancerous tissues expressing high levels of the 5-HT2B receptor (Figure 4.14B and C).

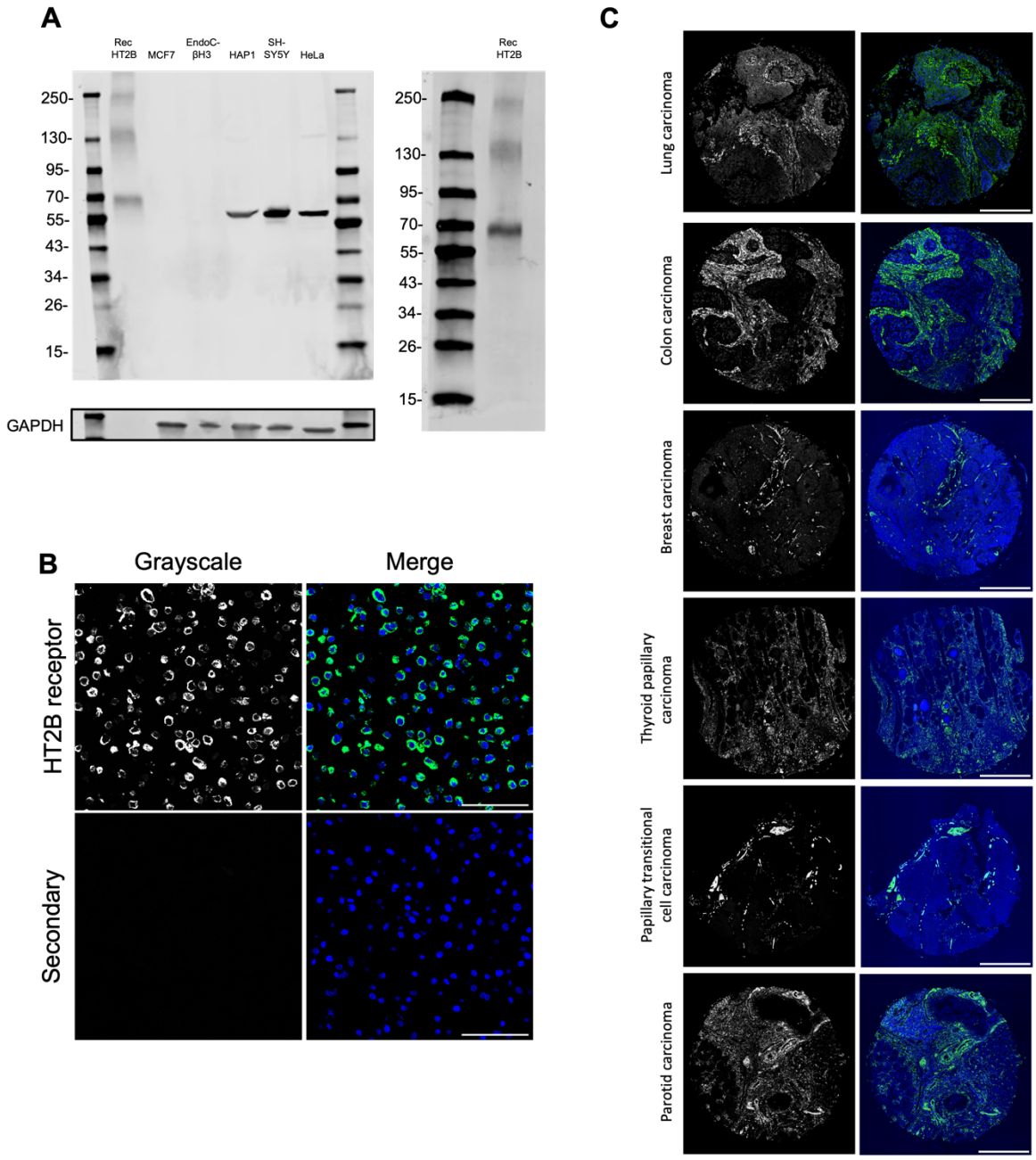

Figure 4.14. Anti-serotonin 2B (5-HT2B) receptor antibody validation **A.** Immunoblot using the anti-5-HT2B receptor antibody of full-length human 5-HT2B recombinant protein and whole cell lysates. Bands are observed in lanes containing full-length recombinant protein and whole cell lysates from cells known to express the *HTR2B* gene (HAP1, SH-SY5Y, and HeLa). No bands are seen in lysates where 5-HT2B receptor is absent (MCF7 and EndoC-βH3). GAPDH is used as a loading control. A second immunoblot of full-length human 5-HT2B recombinant protein using the anti-5-HT2B antibody. **B.** Formalin-fixed

paraffin-embedded (FFPE) HAP1 wild-type cell pellets labelled with the anti-5-HT2B receptor antibody show positive staining. No staining is observed in the secondary-only control. Images include grayscale of the 5-HT2B receptor channel and the merged image (5-HT2B and DAPI). Scale bar = 100 µm. **C.** Immunofluorescence analysis of human cancer tissues (IHC-IF) shows labelling by the anti-5-HT2B receptor antibody in malignancies known to express the 5-HT2B receptor. Grayscale images of the 5-HT2B receptor channel and merged images (DAPI and 5-HT2B) are shown. Scale bar = 500 µm. Reproduced from a manuscript accepted for publication in *Nature Communications, Seedat et al.* (2025).

4.3.5 PRLR receptor protein levels in α and β cells during human pregnancy

Immunolabelling with the anti-PRLR antibody revealed expression in both exocrine tissue and pancreatic islets from pregnant and non-pregnant women, demonstrating that PRLR is expressed at detectable levels in adult human pancreatic islets by IHC-IF (Figure 4.15A and B [secondary only control]) and IHC labelling (Figure 4.16). Quantification of PRLR labelling intensity showed increased expression in the α cells of pregnant women compared to non-pregnant controls (302.3 ± 10.12 AU/mm² vs. 267.7 ± 4.582 AU/mm²; $p = 0.0398$), but no significant difference was found in β cells (277.4 ± 3.002 AU/mm² vs. 270.3 ± 1.704 AU/mm²; $p = 0.0610$) (Figure 4.17). There were also no differences between GDM and normal pregnancy (Figure 4.18).

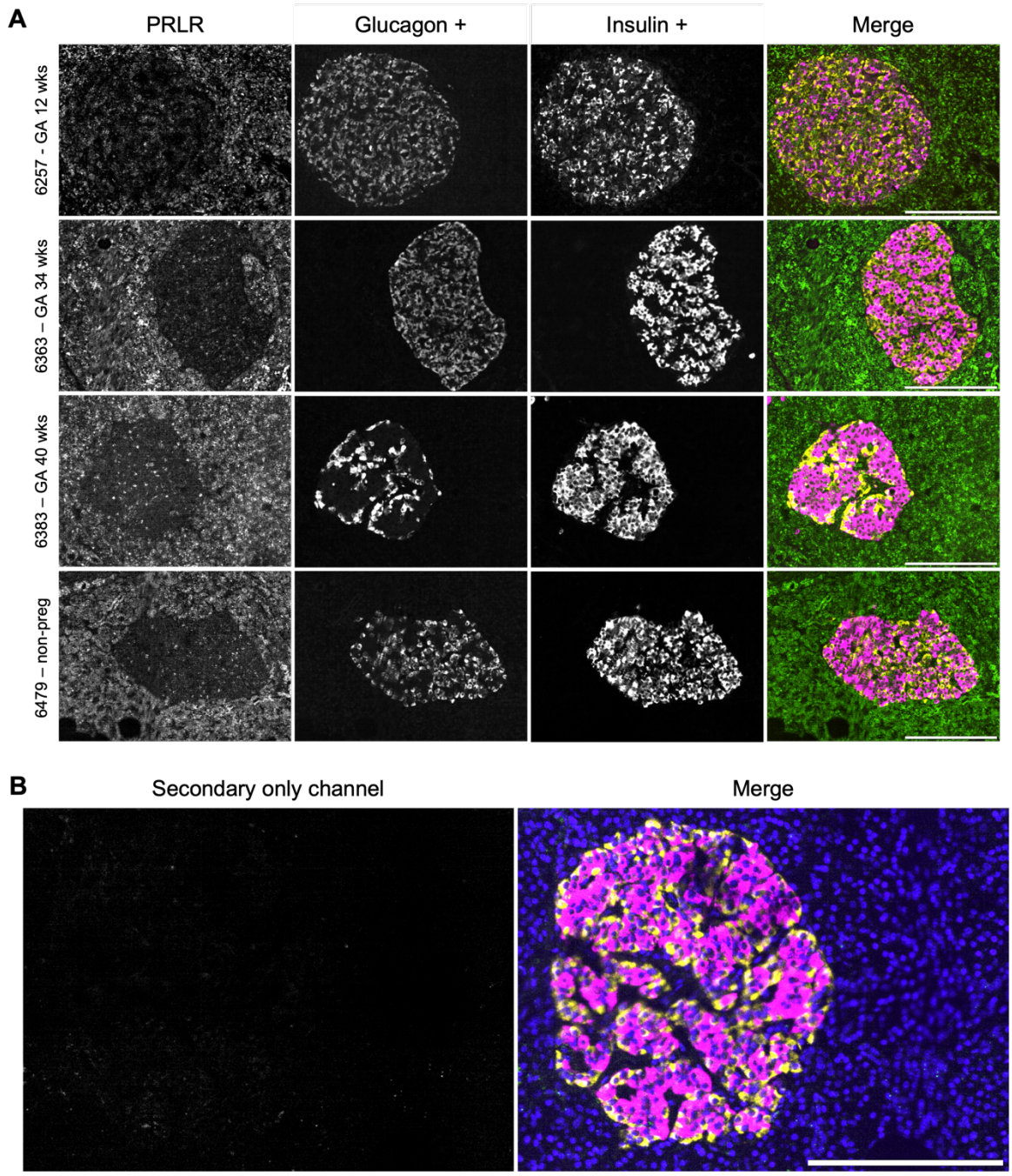

Figure 4.15. A. Detection of the prolactin receptor (PRLR) in human pancreatic islets and quantification of PRLR expression in pancreatic α and β cells during pregnancy by immunofluorescence (IHC-IF) analysis of human pancreatic sections from pregnant women at different gestational ages and a non-pregnant control sample. The PRLR signal is observed within α and β cells. The grayscale images represent the individual channels for PRLR, glucagon and insulin. PRLR (green), glucagon (yellow), insulin (magenta) are shown

in the merged channel. Scale bar = 200 µm. **B.** Secondary only controls of pancreatic tissue labelled by IHC-IF. The grayscale image represents the secondary control where only the VectaFluor™ Excel amplified anti-rabbit secondary antibody was applied to the tissue section, without the primary anti-PRLR antibody. The coloured image shows the merged channels. Scale bar = 200 µm. Reproduced from a manuscript accepted for publication in *Nature Communications, Seedat et al.* (2025). This content is distributed under the Creative Commons Attribution License (CC BY 4.0).

*GA – gestational age, wks – weeks, non-preg – non-pregnant.

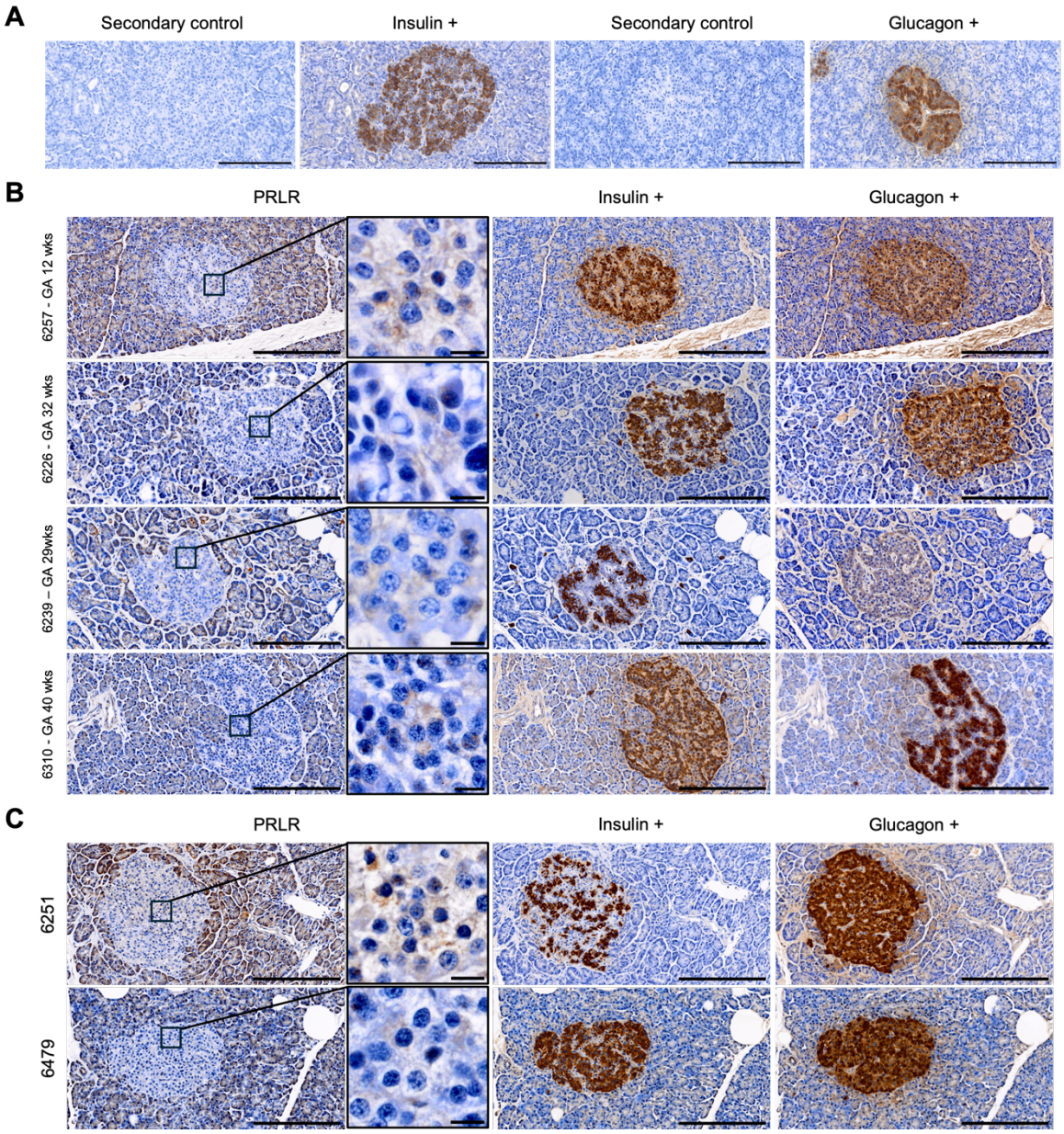

Figure 4.16. Chromogenic immunohistochemistry (IHC) labelling of the prolactin receptor (PRLR) in pancreatic islets in pregnancy and non-pregnant controls. **A.** Secondary only controls show no detectable signal in islets. Serial sections labelled with the secondary control followed by either insulin or glucagon are shown. **B.** PRLR signal is detected in islets from pregnant women. **C.** PRLR signal is detected in islets from non-pregnant controls. For **B.** and **C.** serial sections are shown labelled for PRLR, insulin and glucagon. Scale bar = 1000µm and 5µm for inset image. Reproduced from a manuscript accepted for

publication in *Nature Communications, Seedat et al.* (2025). This content is distributed under the Creative Commons Attribution License (CC BY 4.0).

*GA – gestational age, wks – weeks.

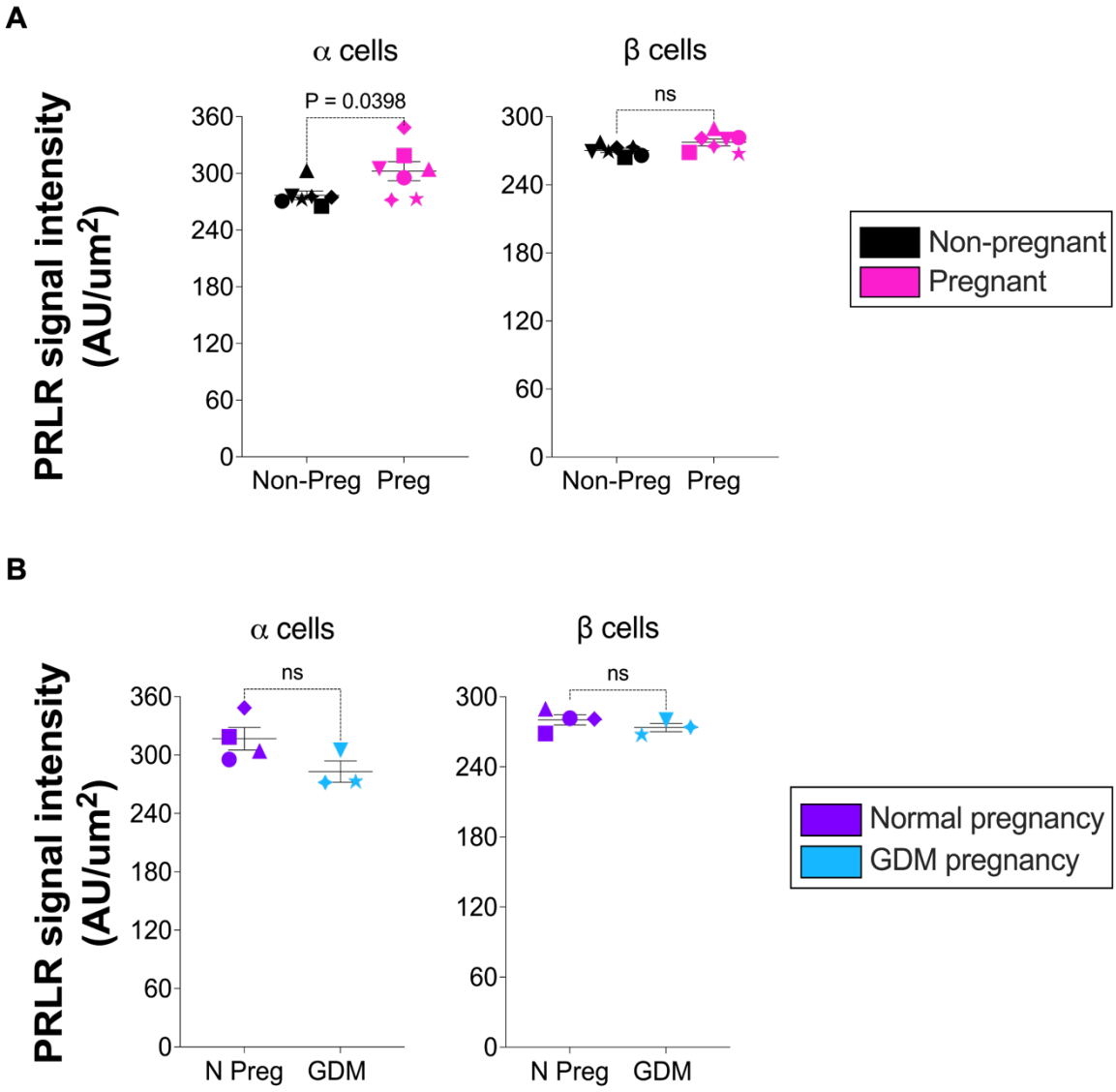

Figure 4.17. Quantification of prolactin receptor (PRLR) expression in pancreatic α and β cells during pregnancy. **A.** Signal intensity of PRLR detected in α and β cells of pregnant women compared to non-pregnant controls. **B.** Signal intensity of PRLR detected in α and β cells of normal compared to gestational diabetes mellitus (GDM) pregnancy. Symbols in each figure correspond to individual donors as indicated in Table 5.2. Statistically significant comparisons are indicated with p-values, while "ns" denotes non-significant differences. Reproduced from a manuscript accepted for publication in *Nature Communications, Seedat et al.* (2025). This content is distributed under the Creative Commons Attribution License (CC BY 4.0).

4.3.6 5-HT2B receptors in human α cells during pregnancy

The 5-HT2B receptor was detected in α cells within the islets and peri-ductal regions of both pregnant and non-pregnant donors (Figure 4.18A). The secondary only control is shown in Figure 4.18B. Quantification revealed that 5-HT2B receptor expression was significantly higher in the α cells of pregnant women compared to non-pregnant controls (387.4 ± 10.01 AU/mm² vs. 286.5 ± 13.46 AU/mm²; p=0.0359) (Figure 4.19A). No differences were found between GDM and normal pregnancy (Figure 4.19B).

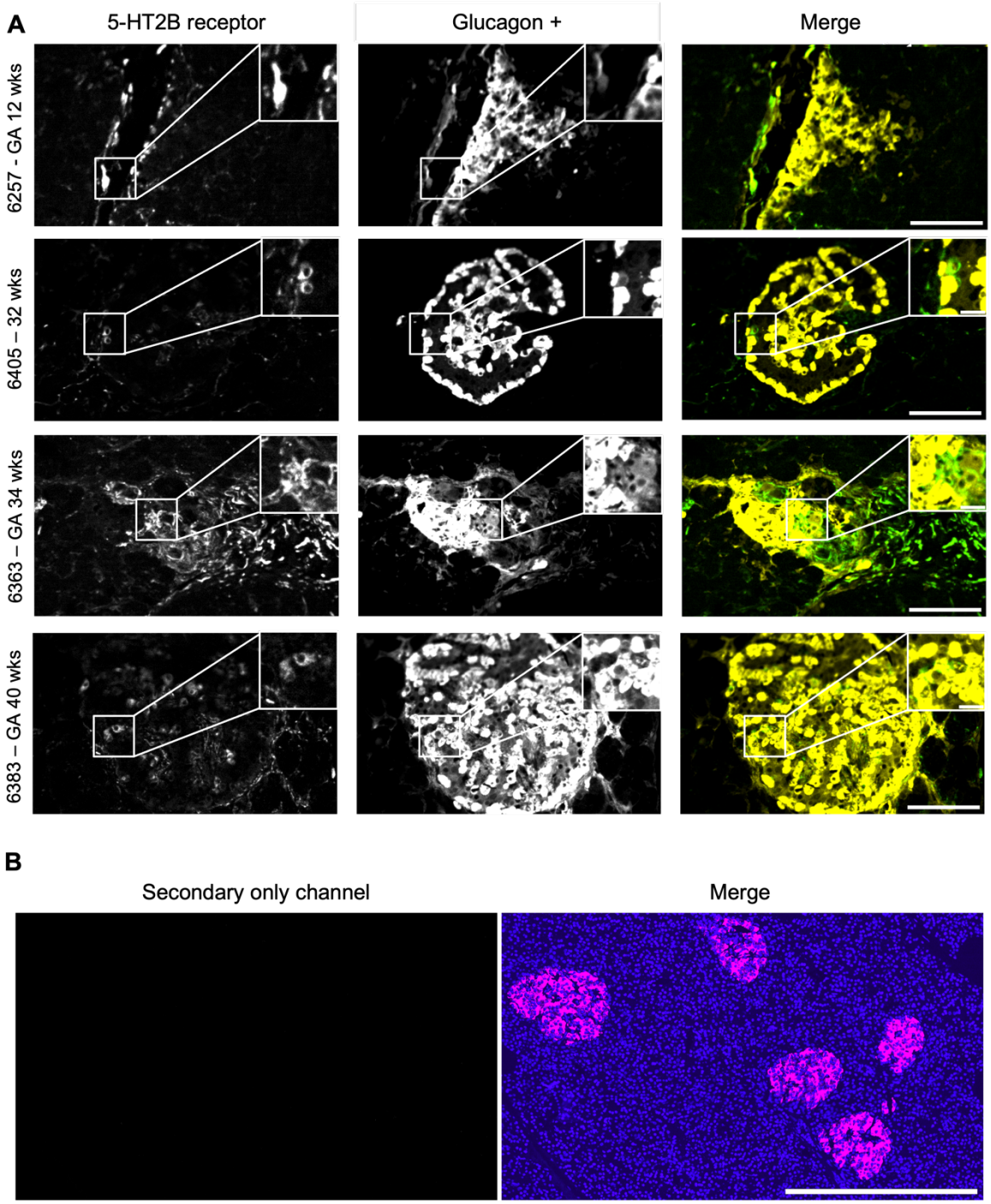

Figure 4.18. A. Immunofluorescence (IHC-IF) of human pancreatic sections from pregnant women at different gestational ages. The serotonin 2B (5-HT2B) receptor signal is observed in α cells, overlapping with glucagon. Both α cells surrounding pancreatic ducts and those within islets are shown. The grayscale images represent the individual channels for the 5-HT2B receptor and glucagon. The merged image displays the colocalisation of the 5-HT2B receptor (green) and glucagon (yellow). Scale bar = 200 µm for the image overview and 20

μm for the magnified area in the inset. Reproduced from a manuscript accepted for publication in *Nature Communications, Seedat et al.* (2025). This content is distributed under the Creative Commons Attribution License (CC BY 4.0).

* GA – gestational age, wks – weeks.

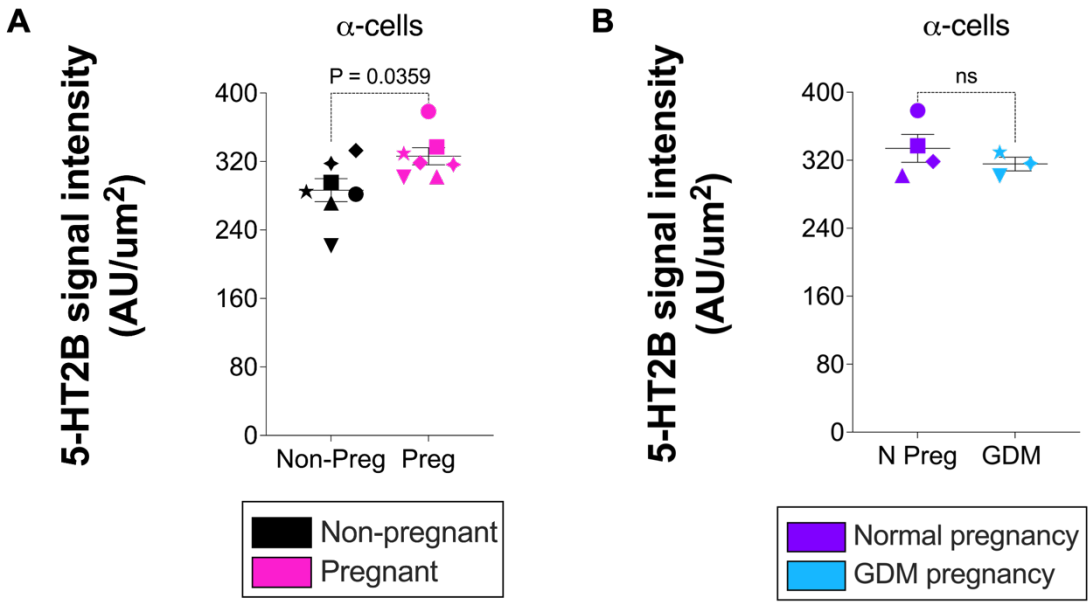

Figure 4.19. Serotonin 2B (5-HT2B) receptor in pancreatic α-cells during pregnancy **A.** Signal intensity of the 5-HT2B receptor detected in α cells of pregnant women compared to non-pregnant controls. **B.** Signal intensity of the 5-HT2B receptor detected in α cells of women with normal pregnancy compared to gestational diabetes mellitus (GDM) pregnancy. Symbols in each figure correspond to individual donors as indicated in Table 5.2. A statistically significant comparison is indicated a p-value shown. "ns" denotes non-significant. Reproduced from a manuscript accepted for publication in *Nature Communications, Seedat et al.* (2025). This content is distributed under the Creative Commons Attribution License (CC BY 4.0).

4.3.7 Absence of 5-HT2B receptors in human β cells during pregnancy

Unlike in mouse models, no 5-HT2B receptor expression was observed in human β cells in either pregnant or non-pregnant women (Figure 4.20A). Colocalisation analysis confirmed the absence of overlap between 5-HT2B receptor and insulin signals across whole tissue sections (Figure 4.20B). Importantly, 5-HT2B receptor expression in pancreatic ducts served as an internal positive control, confirming successful IHC-IF labelling of the 5-HT2B receptor human pancreatic tissue sections by this antibody during the experiment (Figure 4.20A).

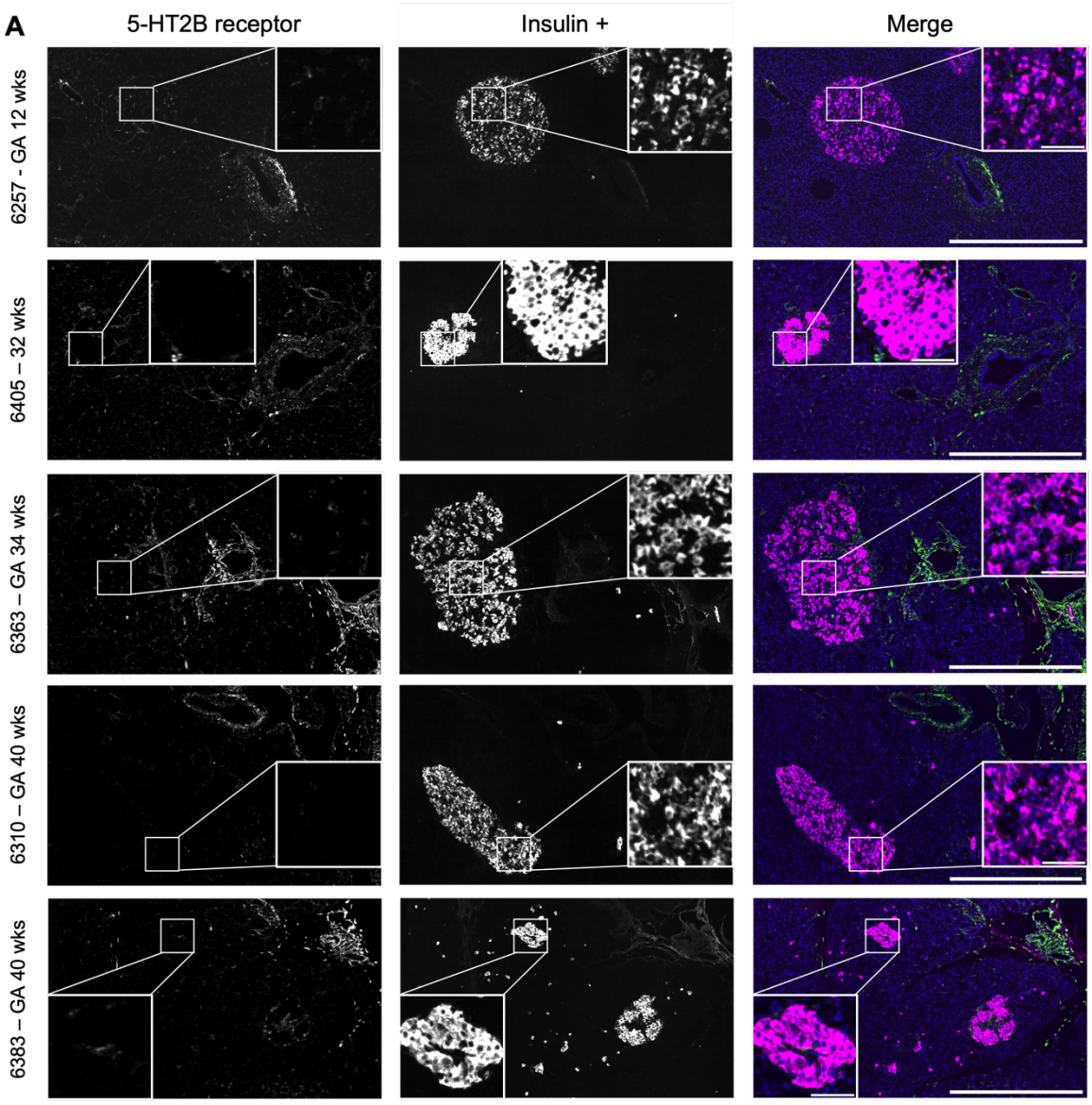

	6257–GA 12wks	6405–GA 32wks	6363–GA 34wks	6310–GA 40wks	6383–GA 40wks
M1	0.115	0.011	0.020	0.013	0.056
M2	0.037	0.015	0.019	0.020	0.032

Figure 4.20. Absence of serotonin 2B (5-HT2B) receptor in insulin-producing pancreatic β cells during pregnancy is demonstrated by **A.** immunofluorescence (IHC-IF) of human pancreatic sections from pregnant women at different gestational ages. No staining of the 5-

HT2B receptor is observed within β-islet cells; however, staining within pancreatic ducts is evident. The grayscale images represent the individual channels for the 5-HT2B receptor and insulin. The merged image displays the 5-HT2B receptor (green) and insulin (magenta) channels. Scale bar = 500 μm for the image overview and 50 μm for the magnified area in the inset. **B.** Colocalisation analysis demonstrating no colocalisation between the 5-HT2B receptor and insulin signals. Scatter plots showing pixel intensity from the 5-HT2B receptor and insulin channels plotted against each other are presented. Pixel intensity for each channel is plotted on the respective axes: the 5-HT2B receptor channel is represented in green on the y-axis, and the insulin channel is represented in magenta on the x-axis. Whole tissue sections from pregnant women at different gestational ages were analysed. Mander's overlap coefficients are shown in the table for each whole tissue section, where M1 represents the overlap of the insulin signal over the 5-HT2B receptor signal, and M2 represents the 5-HT2B receptor signal overlapping the insulin signal. Reproduced from a manuscript accepted for publication in *Nature Communications, Seedat et al.* (2025).

GA – gestational age, wks – weeks.

4.3.8 GLP-1 in human α cells during pregnancy

Alongside glucagon, α cells also produce the incretin GLP-1. GLP-1 enhances insulin secretion from human β-cells and promotes β-cell mass expansion in mice, with recent evidence suggesting a similar effect in humans (167, 168). Research indicates that GLP-1 produced by α cells is biologically active and works together with glucagon to enhance insulin secretion via intra-islet (paracrine) signalling (23). Given the notable increase in α-cell mass observed in the islets of pregnant women, we aimed to assess whether GLP-1 levels were greater in their α cells. For this, we used the anti-GLP-1 antibody (8G9) from Abcam (cat. no. ab26278), which has been validated for its sensitivity and specificity to GLP-1, without cross-reacting with glucagon (169).

IHC-IF revealed the presence of GLP-1 in α cells from both pregnant and non-pregnant women (Figure 4.21A). I once again employed the computational pipeline to successfully segment the GLP-1 signal and the quantify the area and intensity of GLP-1 signal within α cells (Fig. 4.21B).

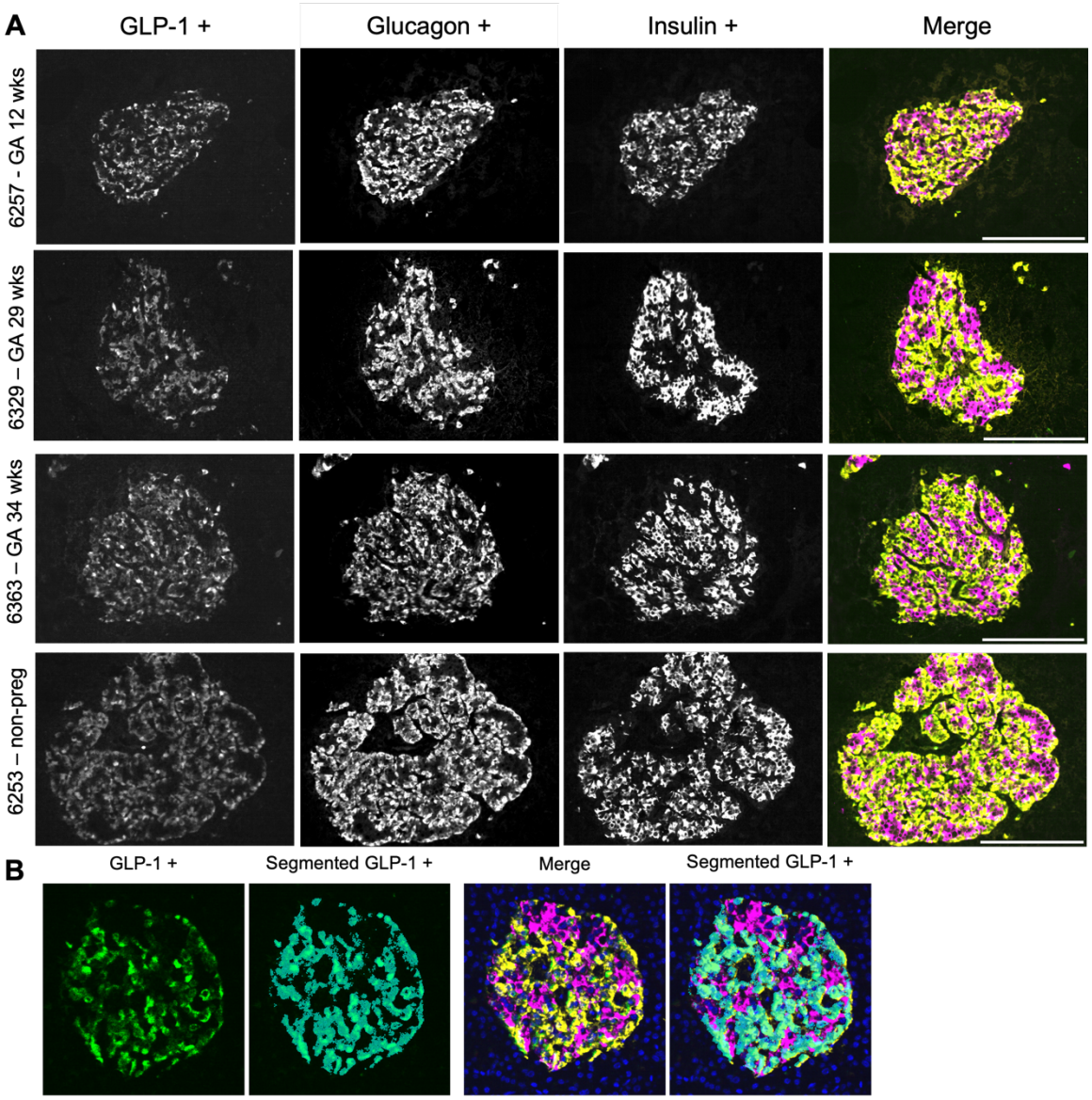

Figure 4.21. A. Immunofluorescence (IHC-IF) of human pancreatic sections from pregnant women at different gestational ages and a non-pregnant control sample. The glucagon-like peptide-1 (GLP-1) signal is observed in α cells, overlapping with glucagon. Both α cells surrounding pancreatic ducts and those within islets are shown. The grayscale images represent the individual channels for GLP-1, glucagon and insulin. GLP-1 (green), glucagon (yellow), and insulin (magenta) are shown in the merged channel. Scale bar = 200 μm. **B.** Images demonstrating the use of the imaging pipeline to quantify GLP-1 area and signal intensity. The labelling of GLP-1 labelled α cells by IHC-IF was followed by thresholding of the GLP-1 positive signal. An example of the thresholded region (cyan) identifying GLP-

1 positive signal is shown for the GLP-1 channel (green) and merged channel (GLP-1 [green], glucagon [yellow] and insulin [magenta]). Reproduced from a manuscript accepted for publication in *Nature Communications, Seedat et al.* (2025). This content is distributed under the Creative Commons Attribution License (CC BY 4.0).

* GA – gestational age, wks – weeks.

Quantification followed by comparisons between pregnant to non-pregnant controls showed a 2.9-fold increase in the relative area of GLP-1-positive α cells in pregnant women (0.6943 ± 0.1417% vs. 0.2386 ± 0.08854%, p = 0.0184) (Figure 4.22A) and a 3.1-fold increase in the average GLP-1-positive area per islet in pregnant women (1420 ± 244 μm² vs. 460.6 ± 147.8 μm², p = 0.0056) (Figure 4.22B). Moreover, the GLP-1-positive area increased by 2.78-fold relative to total islet area in pregnant women (15.55 ± 1.352% vs. 5.6 ± 1.484%, p = 0.0003) (Figure 4.22C). Even when normalised to α-cell area, GLP-1-positive area showed a 2.39-fold increase in pregnant women (52.69 ± 5.431% vs. 22.02 ± 2.546%, p = 0.0003) (Figure 4.22D). Additionally, GLP-1 signal intensity was 1.33-fold higher in pregnant women compared to non-pregnant controls (488.8 ± 26.42 AU/mm² vs. 366.6 ± 23.88 AU/mm², p = 0.005) (Figure 4.22E). These data suggest a disproportionate increase in GLP-1 abundance during pregnancy relative to the expansion of islet and α-cell size. No significant differences were observed between GDM and normal pregnancies (Figure 4.23).

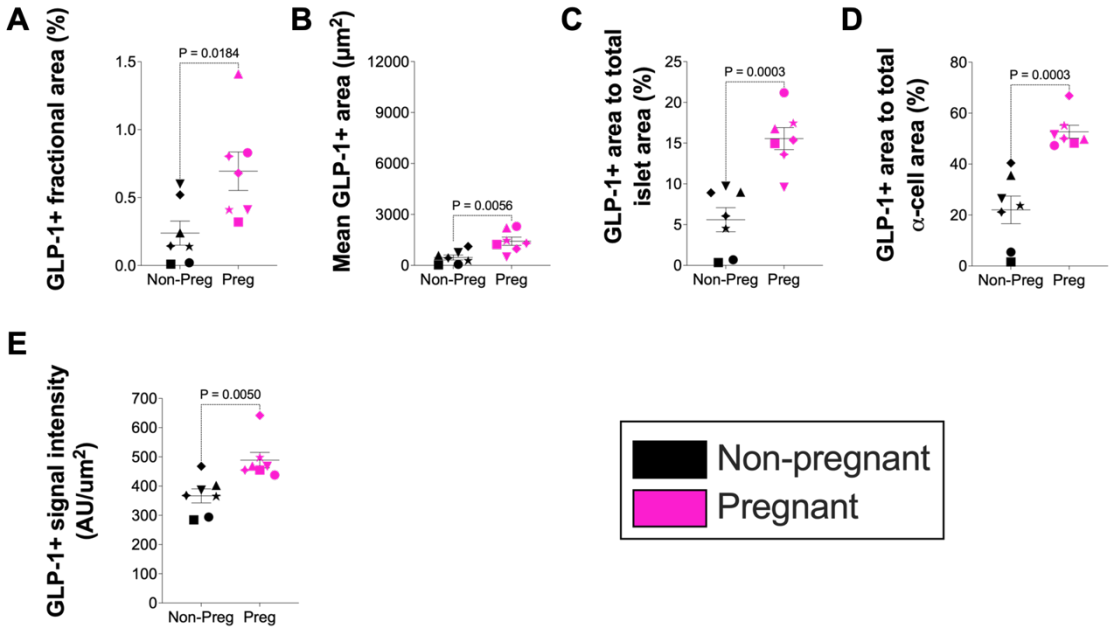

Figure 4.22. Quantitative comparisons of glucagon-like peptide-1 (GLP-1) between pregnant and non-pregnant women for several quantified islet measures. The data includes comparisons for **A.** fractional area (measured area as a percentage of total tissue area) and **B.** mean area (measured area divided by number of islets per tissue section). Additionally, comparisons of the proportions of GLP-1 positive area relative to **C.** whole islets (measured area as a percentage of total whole islet area) and **D.** relative to α-cell area (measured area as a percentage of α cell area) are shown. **E.** Signal intensity of GLP-1 detected in α cells of pregnant women compared to non-pregnant controls. Reproduced from a manuscript accepted for publication in *Nature Communications, Seedat et al.* (2025).

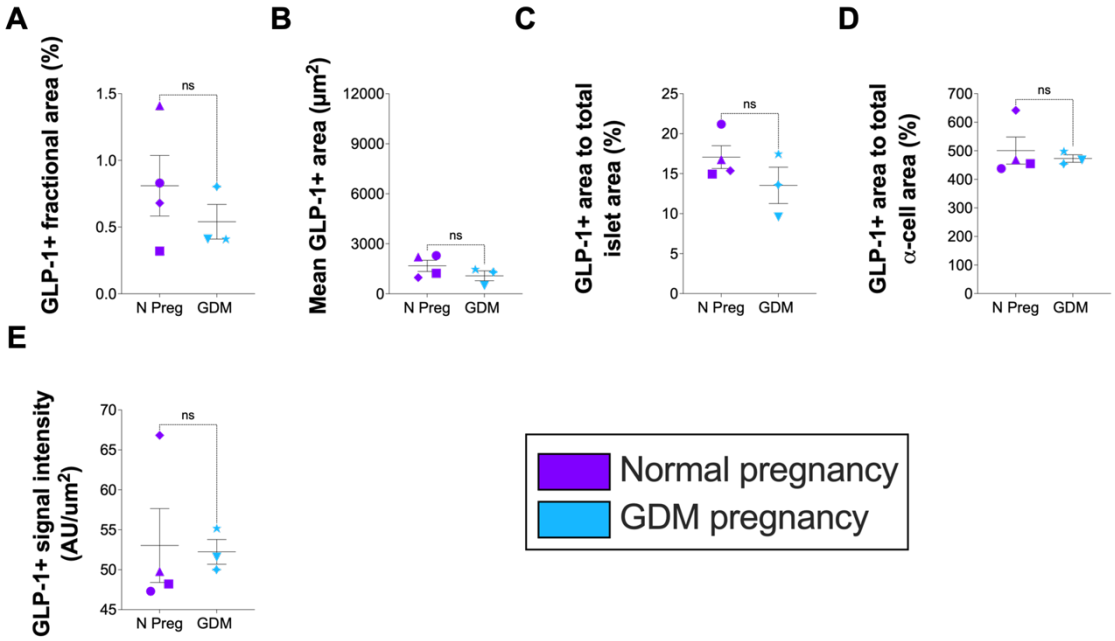

Figure 4.23. Quantitative comparisons of glucagon-like peptide-1 (GLP-1) area and signal intensity between normal and gestational diabetes mellitus (GDM) pregnancy. The data includes comparisons for **A.** fractional and **B.** mean area of whole islets, α cells, β cells, and bihormonal cells. Additionally, comparisons of the proportions of GLP-1 positive area relative to **C.** whole islets (measured area as a percentage of total whole islet area) and **D.** relative to α-cell area (measured area as a percentage of α cell area) are shown. **E.** Signal intensity of GLP-1 detected in α cells of GDM pregnancy compared to normal pregnancy controls. Symbols in each figure correspond to individual donors as indicated in Table 5.2. Statistically significant comparisons are indicated with p-values. "ns" indicates non-significant comparisons. Reproduced from a manuscript accepted for publication in *Nature Communications, Seedat et al.* (2025). This content is distributed under the Creative Commons Attribution License (CC BY 4.0).

4.4 Discussion

In this chapter, I performed a comprehensive, unbiased computational analysis of whole islet, α-cell, and β-cell metrics, and GLP-1 abundance in pregnant women using IHC-IF on FFPE pancreatic tissue sections. I also thoroughly validated antibodies against the PRLR and 5-HT2B receptors and analysed their expression in both α and β cells.

The observed increases in both fractional and mean β-cell areas during pregnancy are consistent with previous studies conducted on human samples (26, 27). While this is the first report of an increase in α-cell area in human pregnancy, murine studies have also shown a rise in α-cell area during pregnancy (23, 24). These increases in α- and β-cell areas appear to be driven by an increase in cell number rather than cell hypertrophy. Previous studies in mice have demonstrated that the expansion of β-cell mass during pregnancy occurs via three key mechanisms: proliferation, neogenesis (the formation of new β cells, often originating from pancreatic ducts), and transdifferentiation (conversion of α cells to β cells) (11, 13). In humans, the study by *Butler et al.* suggested that β-cell mass expansion during pregnancy is predominantly driven by islet neogenesis rather than proliferation (27). My findings in human pancreatic samples from women in the third trimester revealed an absence of Ki-67 expression in islets. This absence was consistent across both late gestation and a single early gestation sample, which suggests a lack of β-cell proliferation during late pregnancy despite the observed increase in cell number rather than cell size. However, these findings are limited by the gestational stage of the samples analysed, as prior studies indicate that β-cell proliferation is most active during early to mid-gestation (11, 13).

Regarding the contribution of β-cell neogenesis, my results differ from those of *Butler et al.*, as I did not observe a significant difference in islet density. This discrepancy could stem

from methodological differences; I applied more stringent criteria to exclude smaller islets to minimise the impact of staining artefacts, whereas *Butler et al.* defined islets more broadly as clusters of four or more insulin-positive cells. Additionally, I conducted an analysis of whole tissue sections, whereas *Butler et al.* focused solely on selected regions (27).

Transdifferentiation of α-cells into β-cells has been highlighted as a potential mechanism during pregnancy. My analysis noted bihormonal cells, which may represent cells that have undergone transdifferentiation, within islets and an increase in fractional and mean β-cell area. Nevertheless, limitations such as the absence of super-resolution microscopy to delineate cell borders precisely raise the possibility of misidentifying juxtaposed α- and β-cells as bihormonal. Furthermore, an expected greater increase in α-cell numbers compared to β-cells, which would support transdifferentiation, was not observed.

Taken together, the increase in β-cell mass during pregnancy driven primarily by an increase in cell numbers align with previous research. However, further investigation of pancreas samples from earlier stages of gestation is essential to dissect the contributions of proliferation, neogenesis, and transdifferentiation.

I identified an increase in α-cell area during human pregnancy, which is a novel finding in human pregnancy and aligns with observations in mouse pregnancy (23, 24). In contrast to mouse pregnancy, I observed a more pronounced increase in α-cell area relative to β-cell area due to an increase in α cell numbers (24). In mouse studies, this α-cell growth is attributed to proliferation, rather than neogenesis or transdifferentiation. However, in our investigation of late-gestation human pancreas tissue, evidence of α-cell proliferation was absent. Similar to β cells, this discrepancy may stem from the later gestational age of the

women from which the samples were obtained. Whether neogenesis or transdifferentiation contributes to the increase in α-cell area observed in human pregnancy requires further study.

The role of α-cells in glucose homeostasis during pregnancy is underscored by work from a mouse study examining the role of α cells in pregnancy (23). *Qiao et al.* determined that ablating α cells in pregnant mice impaired glucose-stimulated insulin secretion (GSIS), which lead to hypoinsulinemia and disruptions in maternal glucose regulation (23). Notably, treatment with GLP-1 restored GSIS, while antagonising the GLP-1 receptor significantly reduced GSIS, suggesting GLP-1 plays a more critical role than glucagon in modulating β-cell function during pregnancy (23). Notably, the authors demonstrated a marked increase in total pancreatic GLP-1 levels during mouse pregnancy. In humans, similar to mice, α cells also produce and secrete biologically active GLP-1, which by paracrine communication acts locally within islets to enhance GSIS (8, 9, 170).

Like *Qiao et al.*, we too observed an increase in α cell-derived GLP-1 in human pregnancy. GLP-1 plays a well-established role in enhancing insulin biosynthesis, secretion, and β-cell responsiveness (171). By optimising insulin utilisation and stimulating the machinery needed for increased insulin demand, GLP-1 facilitates metabolic adaptations. The structural organisation of human islets appears uniquely suited for paracrine communication. Unlike the segregated islet architecture in mice, where only 28% of β-cells are in direct contact with other endocrine cells, up to 80% of human β-cells maintain direct contact with α cells (113). Moreover, α cells constitute a larger proportion of human islets and secrete significantly higher amounts of GLP-1 compared to their murine counterparts (113, 118).

The metabolic demands of pregnancy require a robust increase in insulin production and secretion to maintain glucose homeostasis. Regulatory signals, including GLP-1, are likely essential for supporting this heightened β-cell activity. I propose that the increased α-cell mass in pregnancy serves to increase intra-islet GLP-1 levels, thereby enhancing GLP-1 mediated paracrine signalling within the islet microenvironment. This mechanism supports β cells in adapting to the increased metabolic demands of pregnancy. Further mechanistic studies are essential to validate this hypothesis.

An additional mechanism by which α cells may improve β cell function may be by improving parasympathetic intra-islet communication. Acetylcholine, the parasympathetic nervous system neurotransmitter, also plays a role in paracrine communication by priming β-cells to maintain their glucose responsiveness. Parasympathetic intra-islet communication has been corroborated using biosensor cells and in human islets transplanted into the anterior chamber of the eye, blood glucose control was retained when parasympathetic input was activated by ambient light (172). Human islets, unlike mice, exhibit weak parasympathetic innervation and human α cells, express markers of acetylcholine production - vesicular acetylcholine transporter (vAChT), choline transporter 1 (ChT1) and choline acetyltransferase (ChAT) -suggesting they secrete acetylcholine to support β-cell function (113, 118). This suggests that in humans, α-cells are the primary source of islet acetylcholine (113, 118). These data suggest that in humans that it is α cells, rather than the parasympathetic nervous system, that are the primary source of islet acetylcholine, providing another possible paracrine signal though which α cells may improve β-cell function. Nevertheless, further research is required to validate this hypothesis (113, 118).

It is unlikely that the observed increase in α cell mass is driven by a need to increase circulating glucagon, as plasma glucagon levels only rise intermittently during pregnancy (17, 23), whilst pregnancy-induced insulin resistance is primarily driven by placental hormones rather than elevated glucagon levels (173). Nevertheless, localised intra-islet elevations in glucagon may still exert significant effects on paracrine signalling, given that glucagon has been demonstrated to modulate intercellular communication within the islet microenvironment (113, 118).

PRLR is known to play a crucial role in enhancing β-cell adaptations and insulin secretion in mouse pregnancy (11, 31, 32, 34). However, we did not observe an increase in β-cell PRLR expression in islets from pregnant women, suggesting that PRLR is not upregulated in human pregnancy. However, in the context of higher circulating levels of lactogenic hormones, where receptor down regulation would be the expected physiological response, and the presence of unchanged PRLR expression may indicate a relative increase. In the mouse α cell line, α-TC1.9, lactogens stimulated cell proliferation and reduced glucagon secretion (24). The presence of elevated lactogenic hormones could imply a regulatory role for PRLR in α and β cells and requires further investigation.

Studies in mice have shown that 5-HT2B receptor signalling is critical for β-cell proliferation and increased insulin secretion (41, 42, 44), but we found no 5-HT2B receptor expression in human β-cells during early and late pregnancy or in non-pregnant women. The presence of 5-HT2B receptor signal in adjacent pancreatic ducts, which are known to express the 5-HT2B receptor (174), validated the functionality of the antibody under the experimental conditions we used, confirming the absence of this receptor in human β-cells. This suggests that, unlike in mice, the 5-HT2B receptor does not play a role in human

pregnancy-associated β-cell changes. A previous study has reported 5-HT2B receptor expression in human islets using a polyclonal antibody (42). However, as polyclonal antibodies target multiple epitopes, they are known to have limitations regarding antigen specificity (175). To address this issue, we utilised a monoclonal antibody clone, which provides enhanced specificity by targeting a single epitope. Moreover, we conducted extensive antibody validation by immunoblotting and IHC-IF, confirming that the antibody we used accurately detects the 5-HT2B receptor. Discrepancies in findings between studies may stem from differences in antibody specificity and validation protocols. Moreover, variations in tissue processing, staining methods, or experimental conditions could also influence the observed expression of the 5-HT2B receptor. By taking measures to minimise these factors, our study provides robust and reliable evidence for these findings.

In non-pregnant human islets, serotonin produced by β-cells in response to hyperglycaemia acts in a paracrine manner on α-cell 5-HT1F receptors to reduce glucagon secretion (176). I observed increased 5-HT2B receptor expression in α cells during pregnancy and *HTR2B* RNA has been detected in human α cells (176). The 5-HT1F receptor is coupled with the inhibitory G-protein (Gi), which inhibits adenyl cyclase and cAMP production. In contrast, the 5-HT2B receptor is coupled with the stimulatory G-protein (Gq) which activates phospholipase C, to increase intracellular calcium signalling and cell replication via the mitogen-activated protein kinase (MAPK) pathway (177). Although we did not detect markers of cell proliferation in α cells, calcium signalling is crucial for glucagon secretion (9, 178). Hence, it is possible that the paracrine signalling of 5-HT2B receptors on α cells, by serotonin, may stimulate glucagon release. I also found increased PRLR expression in α cells, and PRLR activation has been shown to decrease glucagon release under low glucose conditions in mice (24). Taken together, both the 5-HT2B receptor and PRLR can influence

glucagon release, further studies are needed to clarify the roles of these receptors in human α-cell function during pregnancy.

No differences in islet metrics, PRLR or 5-HT2B receptor expression, or GLP-1 abundance were observed between healthy pregnant women and those with GDM, consistent with the proteomics data from Chapter 3. As discussed in Chapter 3, the effects of GDM on islets may be subtle and could involve factors such as genetic variations, post-translational modifications, or external stressors like oxidative stress (40). Further research is required to explore these mechanisms in islet dysfunction during GDM.

Compared to mouse pregnancy, my findings show no significant increase in PRLR expression in human β cells, and 5-HT2B receptors were absent. However, 5-HT2B receptor expression was higher in α cells of pregnant women, suggesting that the adaptations in human β cells during pregnancy differ from those observed in mice. Although I noted an increase in β-cell area, it remains unclear whether this increase is sufficient to explain the heightened insulin secretion observed during pregnancy. It is well established that β-cells release only a small fraction of their stored insulin in response to hyperglycaemia (141, 179). I hypothesise that during human pregnancy, the insulin secretory capacity of β cells may be augmented by mechanisms originating from α cells. This could explain the relative increase in α-cell mass compared to β-cell mass observed during pregnancy as a greater number of α cells may be required to influence insulin secretion during pregnancy through various mechanisms. This may include paracrine communication through β-cell stimulation by glucagon or GLP-1 secreted from adjacent α cells, to increase insulin secretion from existing β cell stores. These changes, while significant, likely reflect the inherent plasticity of α and

β cells in human pregnancy to enhance insulin output through subtle intra-islet environmental changes, rather than the extensive remodelling seen in murine pregnancy.

The limitations related to sample size encountered in the proteomics analysis in Chapter 3, both for the entire cohort and specifically for the comparison between GDM and normal pregnancy, also apply to the data presented in this chapter. The sample size for this study was restricted due to the rarity and difficulty in obtaining high-quality pancreatic tissue from pregnant women. Just one sample from the first trimester was available but high-quality pancreas tissue from the second trimester was not available for this study. Increased collaboration between researchers and clinicians is essential to acquiring more samples, to reduce cohort heterogeneity, and enable the study of islets from women with GDM and those at earlier gestational stages of pregnancy, to advance research in this field.

In summary, using an unbiased computational approach, I quantified α-cell and β-cell areas via IHC-IF, showing that the increases in fractional and mean areas were driven by an increase in cell number. PRLR, 5-HT2B receptor expression, and GLP-1 abundance were elevated in α cells during pregnancy, while PRLR expression remained unchanged in β cells, and, in contrast to mouse models, the 5-HT2B receptor was absent. These results support the hypothesis that human islet adaptations during pregnancy are more subtle and nuanced than those observed in mouse models. The findings of marked increases in α cell area and GLP-1 abundance suggest that human β cells intra-islet paracrine signalling in pregnancy may play an important role; however, mechanistic studies are needed to confirm this. This study provides new insights into pancreatic islet changes during pregnancy and underscores the importance of using human-based models for islet research.

Chapter 5

Isolation and characterisation of placental small extracellular vesicles and their internalisation by EndoC-βH3 cells

5.1 Introduction

In Chapters 3 and 4, I studied the global changes in protein expression in human islets that occur *ex vivo* during pregnancy by conducting an unbiased liquid chromatography-mass spectrometry (LC-MS/MS) proteomic analysis of pancreatic islets that were isolated from pregnant women by laser capture microdissection. Additionally, I employed immunohistochemistry (IHC) to gain further insight into the expression of specific proteins of interest at the single-cell level within the different islet cell types in pancreatic tissue from pregnant women. Specifically, I investigated the abundance of the prolactin receptor (PRLR) and serotonin 2B (5-HT2B) receptor in β cells. In mice studies, prolactin is shown to be a key mediator of placental-islet communication in pregnancy (11, 34). The placenta secretes prolactin during pregnancy, which stimulates β-cell proliferation and insulin secretion via β cell PRLRs, whose expression in β cells is also upregulated during mouse pregnancy (11, 34). In pregnant mice, the 5-HT2B receptor is also upregulated in mouse pregnancy, to promote β-cell proliferation. PRLR activation increases the synthesis of serotonin in β cells to activate the 5-HT2B receptor (11). In contrast to what has been observed in mouse pregnancy, the LC-MS/MS and IHC analysis of islets from pregnant women did not show an increase in PRLR expression in human β cells during pregnancy. Furthermore, the 5-HT2B receptor was not detected in human β cells, either during pregnancy or in the non-pregnant state. Taken together, these data suggest that the mechanisms of placental-islet communication that increase insulin secretion during human pregnancy may differ from those observed in mouse pregnancy, indicating that other mechanisms are also involved.

In addition to hormones, the placenta also releases other mediators of cell-to-cell communication, such as placental small extracellular vesicles (psEVs) which can signal downstream tissues (57). To better understand the effects of placental communication on

pancreatic islets during human pregnancy and identify additional mechanisms of placental-islet communication, I aimed to explore the potential role of placental extracellular vesicles (psEVs) as mediators of this communication, particularly focusing on their effects on β cells. Additionally, I aimed to determine whether the effects of psEVs observed in mouse β cell models, as discussed in Chapter 1, also translated to human pregnancy. I chose to focus on psEVs, as after reviewing the literature, I found that studies on EV biodistribution report that medium/large EVs are not consistently detected in peripheral organs like the spleen or kidneys (63). In contrast, small extracellular vesicles (sEVs) are reliably identified in these organs as well as in the pancreas *in vivo* (63, 66). Research in the nano-signalling field also suggests that sEVs have greater cellular motility, facilitating their uptake and more efficient delivery of their cargo to distant tissues (65). Furthermore, published data describing pregnancy associated changes in insulin secretion observed in pancreatic islets has been linked specifically to psEVs (66, 85). Hence, I concluded that psEVs, rather than medium/large EVs, were more likely to reach pancreatic β cells *in vivo* and be internalised at a concentration sufficient enough to induce a biological effect.

I developed a human-based model system to investigate the impact of psEVs on β-cell biology by using the human β cell line, EndoC-βH3, and psEVs isolated from human placentae. In the subsequent chapters, I aim to examine the role played by psEVs in regulating insulin synthesis and secretion during human pregnancy using this model.

Before conducting detailed functional, transcriptomic, and proteomic analyses to explore the effects of psEVs on EndoC-βH3 cells, it was crucial to first isolate and successfully immunophenotypically characterise a population of psEVs using established methods commonly employed in extracellular vesicle (EV) research. (48). Additionally, since there

are no previous reports of EV internalisation by human β cells, it was essential to establish that differentiated EndoC-βH3 cells could internalise psEVs and understanding the dynamics of psEV internalisation was vital for optimally designing future experiments. This chapter focuses on these preliminary steps, which are foundational to the subsequent work in this thesis.

5.1.1 Aims

The aims of this chapter were to:

1. Isolate and characterise psEVs – the sEVs of interest.
2. Isolate and characterise red blood cell small extracellular vesicles (RBCsEVs) – the control sEVs.
3. Culture and differentiate EndoC-βH3 cells.
4. Confirm that psEVs and RBCsEVs are internalised by EndoC-βH3 cells.
5. Understand the dynamics of psEV uptake by EndoC-βH3 cells by quantifying the rate at which psEVs are internalised using a time-dose measurement.

5.2 Materials and methods

5.2.1 Ethics

This project was approved by the Central Oxfordshire Research Ethics Committee C (REFS: 07/H0607/74 and 07/H0606/148) and written informed consent was provided by all study participants.

5.2.2 Participants

Participants were recruited on the day of elective caesarean section, and all were at or beyond 37 weeks of gestation. Women with either normal pregnancies or gestational diabetes mellitus (GDM) were enrolled in the study. Using their clinical notes, a datasheet was completed detailing their age and clinical information, including body mass index, gestational age at delivery, maximum documented systolic and diastolic blood pressure, foetal gender, foetal birthweight, and for those with GDM, haemoglobin A1c and prescribed treatment. Their placentae were collected at the time of caesarean section. Normal pregnancy was defined as a healthy singleton pregnancy in a woman with no chronic, metabolic, or pregnancy related disease. GDM pregnancy was defined as per the International Association of the Diabetes and Pregnancy Study Groups (IADPSG) and World Health Organization (WHO) guideline recommendations for diabetes in pregnancy and was diagnosed when a participant had a fasting plasma glucose level that measured greater than 5.1 mmol/L or either a 1-hour plasma glucose greater than 10 mmol/L or a 2-hour plasma glucose that measured 8.5 mmol/L or higher following a 75 g oral glucose tolerance test (OGTT) performed at 24 – 28 weeks' gestation (14, 92). For participants with GDM, those with either a concomitant chronic disease or second pregnancy related disease were excluded. Peripheral blood was also collected from healthy pregnant women with no

chronic diseases, matched by chronological and gestational age to women whose placentae were collected.

5.2.3 Isolation of placental small extracellular vesicles

psEVs were isolated from the placentae of 8 women with normal pregnancy and 8 women with GDM using an *ex vivo* modified dual lobe placental perfusion system followed by differential ultracentrifugation (69). In principle, this system mimics *in utero* placental circulation. After a successful placental perfusion, the maternal perfusate that is collected contains the products shed by the placenta which, *in vivo*, would re-enter the maternal circulatory system. psEVs are then isolated from the maternal perfusate by density-based differential ultracentrifugation.

Medium 199 containing L-glutamine and Earle's salts (Sigma, cat. no. M4530), bovine serum albumin (BSA) (Sigma, cat. no. A3294), 500 units/L of sodium heparin was used as maternal media for the placental perfusion. For foetal media, media was prepared as above and 0.8% dextran (Sigma, cat. no. D1662) was also added. A fresh placenta was received immediately following delivery. The maternal facing surface of the placenta was inspected and a placental lobe/cotyledon without calcification or haemorrhage was selected. The artery and vein belonging to the selected lobe/cotyledon was cannulated on the foetal facing placental surface creating the foetal circuit. Foetal media was infused through the foetal circuit at a rate of 9 rpm and the outflow to the foetal circuit cylinder maintained at 80-100 mL per 20 minutes for the duration of the perfusion. The maternal circuit was created by inserting multiple cannulae into the selected placental cotyledon/lobe on the maternal facing placental surface. Maternal media, supplemented with 95% oxygen, was infused at a rate of 30 rpm through the maternal circuit. Maternal perfusate that collected within the reservoir

was recirculated through the circuit. The perfusion was continued for 3 hours after which the maternal perfusate was collected for ultracentrifugation. An illustration of the perfusion circuit is shown in Figure 5.1.

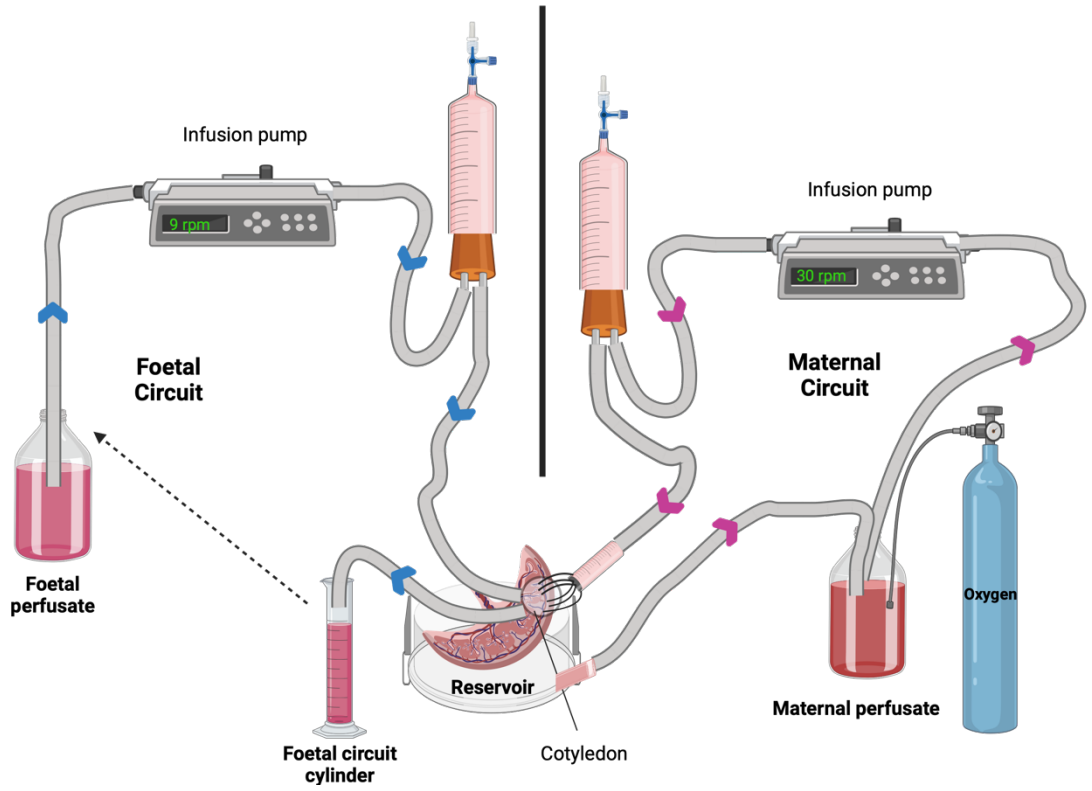

Figure 5.1. Illustration of the circuit used for placental perfusion. The arrows represent the direction of flow of foetal (blue arrows) and maternal (pink arrows) perfusate. Created with BioRender.com released under a Creative Commons Attribution-NonCommercial-NoDerivs 4.0 International license.

Maternal perfusate was first centrifuged (Beckman Coulter Avanti J-20XP centrifuge and Beckman Coulter Js-5.3 swing out rotor) twice at 1,500 *g* for 10 minutes at 4°C to remove cell debris. psEVs were then separated sequentially using ultracentrifugation (Beckman L80 ultracentrifuge and Sorvall TST28.39 swing out rotor). Maternal perfusate was first ultracentrifuged at 10,000 *g* for 35 minutes to pellet medium/large placental EVs (200-1000 μm). The supernatant was collected and filtered through a 0.22 μm stericup filter (Merck Millipore, cat. no. SCGPU02RE) and then spun at 150,000 *g* for 120 minutes at 4°C to pellet psEVs (50-200 μm) (Figure 5.2). The pellet was resuspended in filtered phosphate buffered saline (fPBS). fPBS was prepared by filtering PBS (Gibco, cat. no. 10010023) using a 0.1 μm Thermo Scientific™ Nalgene™ Rapid-Flow™ Sterile Disposable Filter Unit with PES, CN, SFCA or Nylon Membrane (Thermo Fisher Scientific cat. no. 565-0010). The resuspended pellet was quantified using the Pierce™ bicinchoninic acid (BCA) protein assay, as described in Chapter 2, aliquoted and stored at -80°C.

After a successful placental perfusion and following differential ultracentrifugation, the final preparation contained sEVs and the medium in which they were carried - the sEV carrier medium. To accurately control for the effects of the sEV carrier medium in experiments, an sEV carrier control was created. To do so, the initial maternal perfusion media, after excluding the placental perfusion step, was processed by differential ultracentrifugation and resuspended in fPBS, quantified, aliquoted and stored as described above for psEVs.

5.2.4 Isolation of red blood cell small extracellular vesicles

RBCsEVs were isolated from the peripheral blood collected from chronological and gestational age matched healthy pregnant women. Blood was collected in a citrate-coated tube (BD diagnostics, cat. no. 363080). Tubes were centrifuged within 10 minutes of

collection at 2,000 *g* for 5 minutes at 21°C and the plasma and buffy coat removed leaving behind just the red blood cells (RBCs). To stimulate RBCsEV formation, 2 mM of calcium chloride (Sigma, cat. no. C1016) and 5 μM calcium ionophore A23187 (Sigma, cat. no. C7522) were added to the RBCs then incubated overnight at 37°C. The following morning 5 mM of EDTA (Thermo Fisher Scientific, cat. no. 15575020) was added to stop the reaction. The RBC solution was ultracentrifuged (Figure 5.2), quantified, aliquoted, and stored as described above for psEVs.

RBCsEVs were used as a control against psEVs to account for the effects of general EV components, such as the lipid membrane, as well as to control for possibility that RBCsEVs may be co-isolated with psEVs following placental perfusion due to the unavoidable presence of maternal blood in placental vessels (72). This allowed the effects observed from psEVs to be attributed specifically to placental-derived contents.

Figure 5.2. Flow chart showing the details of the ultracentrifugation performed on maternal perfusate and the red blood cell (RBC) solution to enrich placental small extracellular vesicles (psEVs) and red blood cell small extracellular vesicles (RBCsEVs).

5.2.5 Characterisation of placental and red blood cell small extracellular vesicles

5.2.5.1 Immunoblotting

Immunoblotting was performed to immunophenotype normal pregnancy psEVs, GDM psEVs, and RBCsEVs. Methods for immunoblotting are previously described in Chapter 2 and the primary and secondary antibodies used are listed in Table 5.1.

Table 5.1: Antibodies and dyes used for immunoblotting and immunocytochemistry.

Antibody/Dye	Concentration	Manufacturer	Catalog Number	Species	Clonality	Dilution
Immunoblotting						
Primary antibodies						
Alix 3A9	200 µg/mL	Santa Cruz Biotechnology	sc-53538	Mouse	Monoclonal	1 in 200
CD81	200 µg/mL	Santa Cruz Biotechnology	sc-166029	Mouse	Monoclonal	1 in 200
CD63	200 µg/mL	Santa Cruz Biotechnology	sc-5275	Mouse	Monoclonal	1 in 1000
CD9	100 µg/mL	Santa Cruz Biotechnology	sc-59140	Mouse	Monoclonal	1 in 200
Cytochrome C	100 µg/mL	Cell Signalling Technology	11940	Rabbit	Monoclonal	1 in 1000
GAPDH	1 mg/mL	Abcam	Ab 9485	Rabbit	Polyclonal	1 in 1000
Glycophorin A	200 µg/mL	Santa Cruz Biotechnology	sc-53905	Mouse	Monoclonal	1 in 200
Placental alkaline phosphatase (PLAP)	0.1 mg/mL	Abcam	Ab 243731	Rabbit	Polyclonal	1 in 1000
TSG 101	200 µg/mL	Santa Cruz Biotechnology	sc-7964	Mouse	Monoclonal	1 in 200
Syntenin	0.54 mg/mL	Abcam	Ab 133267	Rabbit	Monoclonal	1 in 1000
SV40 Large T-antigen	0.2 mg/mL	Abcam	Ab16879	Mouse	Monoclonal	1 in 1000
Secondary antibodies						
IRDye 680 anti-Mouse IgG	10 mg/mL	LI-COR Biosciences	926-68072	Donkey	-	1in 10000
IRDye 800 anti-Rabbit IgG	10 mg/mL	LI-COR Biosciences	926-32213	Donkey	-	1in 10000
Immunocytochemistry						
Fluorescent Dyes					-	
PKH 26	1 mM	Sigma	PKH26GL-1KT	-	-	
SytoRNA Select	5 mM	Thermo Fisher Scientific	S32703	-	-	
WGA 488	1 mg/mL	Thermo Fisher Scientific	W11261	-	-	1 in 200
WGA 555	1 mg/mL	Thermo Fisher Scientific	W32464	-	-	1 in 200
WGA 647	1 mg/mL	Thermo Fisher Scientific	W32466	-	-	1 in 200
Hoechst 33342	10 mg/mL	Life Technologies	H3570	-	-	1 in 2000
DAPI	1 mg/mL	Thermo Fisher Scientific	62248	-	-	1 in 1000
Live Cell Fluorescent Dyes						
MemGlow™ 488	20 uM	Cytoskeleton, Inc	MG01-02	-	-	1 in 200
SiR-DNA 647	1 mM	Spirochrome	CY-SC007	-	-	1 in 1000
CellTrace™ CFSE 488	5 mM	Thermo Fisher Scientific	C34570	-	-	1 in 1000
NucBlue™ LiveReadyProbes™ Reagent		Thermo Fisher Scientific	R37605	-	-	
Primary antibodies						
PLAP	0.1 mg/mL	Abcam	Ab 243731	Rabbit	Polyclonal	1 in 250
SV40 Large T-antigen	0.2 mg/mL	Abcam	Ab16879	Mouse	Monoclonal	1 in 250
Insulin	0.041 mg/mL	Abcam	Ab108326	Rabbit	Monoclonal	1 in 250
Secondary antibodies						
Goat anti-Mouse IgG (H+L) Highly Cross-Adsorbed Secondary Antibody, Alexa Fluor™ Plus 488	2 mg/mL	Invitrogen	A32723	Goat	Polyclonal	1 in 400
Goat anti-Mouse IgG (H+L) Highly Cross-Adsorbed Secondary Antibody, Alexa Fluor™ Plus 555	2 mg/mL	Invitrogen	A32727	Goat	Polyclonal	1 in 400
Goat anti-Mouse IgG (H+L) Highly Cross-Adsorbed Secondary Antibody, Alexa Fluor™ Plus 647	2 mg/mL	Invitrogen	A32728	Goat	Polyclonal	1 in 400
Goat anti-Rabbit IgG (H+L) Highly Cross-Adsorbed Secondary Antibody, Alexa Fluor™ Plus 488	2 mg/mL	Invitrogen	A32731	Goat	Polyclonal	1 in 400
Goat anti-Rabbit IgG (H+L) Highly Cross-Adsorbed Secondary Antibody, Alexa Fluor™ Plus 555	2 mg/mL	Invitrogen	A32732	Goat	Polyclonal	1 in 400
Goat anti-Rabbit IgG (H+L) Highly Cross-Adsorbed Secondary Antibody, Alexa Fluor™ Plus 647	2 mg/mL	Invitrogen	A32733	Goat	Polyclonal	1 in 400

5.2.5.2 Nanoparticle tracking analysis

Nanoparticle tracking analysis (NTA) was used to evaluate the size versus distribution of normal pregnancy psEVs, GDM psEVs, and RBCsEVs. The Nanosight NS500 instrument equipped with a 405 nm laser and sCMOS camera (Malvern) was used. Instrument performance was assessed with silica 100 nm latex transfer standards (Malvern, cat. no. NTA4088). Samples were diluted in fPBS to achieve a particle concentration of $2x10^8$ to $1x10^9$ and introduced by an automated syringe pump. A camera level was set to 12 and settings unchanged between samples. Five recordings, 60 seconds each, were captured and a minimum of 500 valid tracks required for analysis using NTA software (v2.3, Build 033) (Malvern). Size versus distribution profiles of psEVs and RBCsEVs were acquired.

5.2.5.3 Transmission electron microscopy

Normal pregnancy psEVs, GDM psEVs, and RBCsEVs were visualised by transmission electron microscopy to characterise their morphology. TEM was performed by Dr Errin Johnson (Sir William Dunn School of Pathology). To achieve a concentration between 0.1-0.3 μg/μL, samples were diluted with fPBS. 10 μL of sEV solution was applied to freshly glow-discharged carbon formvar 300 mesh copper grids for 2 minutes, blotted with filter paper, and stained with 2% uranyl acetate for 10 seconds, then blotted and air-dried. sEVs on the grid were negatively stained to enhance the contrast between sEVs and the background. A FEI Tecnai 12 transmission electron microscope at 120 kV with a Gatan OneView CMOS camera was used to image the grids.

5.2.6 Cell culture and differentiation of EndoC-βH3 cells

EndoC-βH3 cells, a human β cell line, (Human Cell Design, France) were cultured in Dulbecco's modified Eagle medium (DMEM), low glucose, glutaMAX supplement,

pyruvate media (Gibco, cat. no. 21885-108) containing 2% BSA (Roche, cat. no. 10775835001), 10 mM nicotinamide (Sigma, cat. no. N3376), 50 μM β-2 mercaptoethanol (Gibco, cat. no. 31350010), 5.5 μg/mL transferrin (Sigma, cat. no. T8158), 6.6 ng/mL sodium selenite (Sigma, cat. no. T8158), 100 units/mL penicillin, and 100 μg/mL streptomycin (Gibco, cat. no. 15070063). Cells were cultured at 37°C in a humidified incubator supplying air and 5% carbon dioxide (CO_2). Cells were passaged approximately every 7 days when they reached a 90-95% confluence.

Excision of immortalising genes for the proteins SV40 Large T cell antigen (SV40LT) and human telomerase reverse transcriptase by cyclisation recombination-estrogen receptor T (Cre-ERT2) was required to differentiate EndoC-βH3 cells (126). Cre-ERT2 activity is induced by 4-hydroxytamoxifen, leading to excision of immortalising genes and β-cell differentiation. Cells were differentiated by adding 4-hydroxitamoxifen (1 μL/10 mL) to culture media for 21 days. A reduction in SV40LT signal was used to confirm successful cell differentiation. Differentiated cells were used at a confluence of 90-95% for experiments.

5.2.6.1 Brightfield imaging

Brightfield images were acquired using the Leica SP8 X-SMD FLIM confocal microscope at high power (63X).

5.2.6.2 Detection and quantification of SV40 Large T cell antigen signal

Loss of SV40LT signal in differentiated EndoC-βH3 cells was quantified by immunoblotting and immunocytochemistry to validate cell differentiation of EndoC-BH3 cells.

Undifferentiated and differentiated whole cell lysates were prepared, and immunoblotting performed as described in Chapter 2. Membranes were probed with anti-SV40LT and anti-GAPDH primary antibodies (Table 5.1). Differences in band intensity between undifferentiated and differentiated EndoC-βH3 cells were quantified using the analysis tool in Image Studio™ software v5.5.4. Band intensity measures for SV40LT were normalised to the loading control (GAPDH) and comparisons between undifferentiated and differentiated EndoC-βH3 cells analysed by the Mann-Whitney test.

For immunocytochemistry, undifferentiated and differentiated EndoC-βH3 cells were immunolabelled for SV40LT. DAPI was used as a nuclear marker, and the cells were labelled with an anti-insulin antibody (Table 5.1). Images were acquired using the Leica SP8 X-SMD FLIM confocal microscope using a 63x 1.4 numerical aperture objective to acquire images, using LASX acquisition software. 30 μm^2 sized images were acquired, laser excitation wavelengths were set to 410 nm, 504 nm and 558 nm, and HyD and PMT detectors used. Image acquisition settings were consistent for each comparative condition within each experiment. ImageJ (Fiji; https://imagej.net/ij/) (v2.3) was used for image processing. The Fiji plugin JACOP BIOP (180) was used for image colocalisation analysis of the nuclear SV40LT signal and nuclear signal labelled with DAPI. Auto-thresholding using Otsu's thresholding (181) was applied to segment the nuclei and SV40LT signal. The percentage of overlap, Pearson's correlation, and Mander's coefficient for the colocalisation of nuclear SV40LT and DAPI nuclear signal were measured and compared between undifferentiated and differentiated EndoC-βH3 cells using the Mann-Whitney test.

5.2.7 Internalisation of small extracellular vesicles by EndoC-βH3 cells

Confocal microscopy was used to demonstrate the internalisation of normal pregnancy psEVs, GDM psEVs, and RBCsEVs by EndoC-βH3 cells. The membrane and intravesicular RNA of psEVs and RBCsEVs were pre-labelled with fluorescent dyes (PKH26 and SytoRNA Select). The labelled psEVs were then added to EndoC-βH3 cells. Additionally, EndoC-βH3 cells were also treated with unlabelled psEVs. Intracellular signal of the pre-labelled sEVs and the psEV specific marker placental alkaline phosphatase (PLAP), in unlabelled psEV treated cells, were visualised.

5.2.7.1 Labelling of small extracellular vesicles with fluorescent dyes

PKH26 dye (Table 5.1) was used to label the sEV membrane. Diluent C (Sigma, cat. no. PKH26GL) was added to normal pregnancy psEVs, GDM psEVs, RBCsEVs, and the sEV control followed by PKH26 dye and incubated at room temperature for 5 minutes. The staining reaction was quenched using 10% BSA and serum-free media. Following creation of a continuous 30% sucrose cushion (Sigma, cat. no. S0389), samples were ultracentrifuged at 150,000 *g* for 120 minutes at 4°C. Each pellet was resuspended in fPBS and transferred to an Amicon 4 mL Ultra Centrifugal Filter 100 kDa column (Merck Millipore, cat. no. UFC8100), to re-concentrate the sEVs, and centrifuged at 4,000 *g* until the sample volume measured less than 500 µL. sEVs were then further purified using the qEV1/35 nm size exclusion column (Izon Science). The qEV1/35 nm column was pre-flushed twice with two column volumes of cold fPBS. The sample was resuspended in 500 µL of fPBS and loaded onto the column. fPBS was then added, and the void volume (1.5 mL) was collected. This process was repeated. After the third addition of fPBS, the purified sEVs were collected in the elution fraction (1.5 mL). The elution volumes were combined and re-concentrated using

the Amicon 4 mL Ultra Centrifugal Filter 100 kDa column as described above. Protein concentration was measured using a BCA protein assay.

SytoRNA Select dye (Table 5.1) was used to label the sEV RNA. SytoRNA Select dye (1 mM) was added to normal pregnancy psEVs, GDM psEVs, and RBCsEVs, respectively, and incubated for 20 minutes at 37°C. sEVs were re-isolated using the qEV1/35 nm size exclusion column as described above and a BCA protein assay performed to quantify the protein concentration.

To control for the visualisation of free dye aggregates, for both dyes, the sEV carrier control was processed alongside the psEVs and RBCsEVs and used as dye controls in experiments. PKH26- and SytoRNA Select-labelled psEVs, RBCsEVs, and dye controls were analysed by NTA to determine if any changes in particle size profiles had occurred following labelling and to determine if sEV sized dye aggregates, that may mimic sEVs, could be detected in the dye controls.

5.2.7.2 Confocal imaging following cell treatments with labelled small extracellular vesicles

EndoC-βH3 cells were seeded at 1 x 10^6 in each well of a chambered glass bottom coverslip 8 well µ-slide (Ibidi, cat. no. 80827). Cells were treated for 6 hours with 40 µg/mL of labelled normal pregnancy psEVs, GDM psEVs or RBCsEVs (PKH26 and SytoRNA Select) and matched with the appropriate dye control. After 6 hours, slides were washed with PBS, fixed and permeabilised with 4% paraformaldehyde (Thermo Fisher Scientific, cat. no. 043368.9M), and nuclei (Hoechst 33342) and cell labelling dyes were then added as described in Chapter 2. The cells were labelled with wheat germ agglutinin (WGA) 488

when EndoC-βH3 cells were treated with PKH26-labelled sEVs and WGA 555 when SytoRNA Select-labelled sEVs were used, respectively (Table 5.1).

5.2.7.3 Immunocytochemistry to detect intracellular placental alkaline phosphatase signal

EndoC-βH3 cells, seeded in a chambered coverslip 8 well µ-slide as described above, were treated for 6 hours with 40 µg/mL of unlabelled normal pregnancy and GDM psEVs, and sEV carrier control. After 6 hours, slides were washed with PBS and psEVs labelled using immunocytochemistry, as described in Chapter 2, with an anti-PLAP antibody (Table 5.1). DAPI was used to label the nuclei and WGA 488 to label the cells (Table 5.1). Figure 5.3 provides an illustrative representation of the methodology used for detecting psEVs in EndoC-βH3 cells using fluorescent dyes and PLAP labelling.

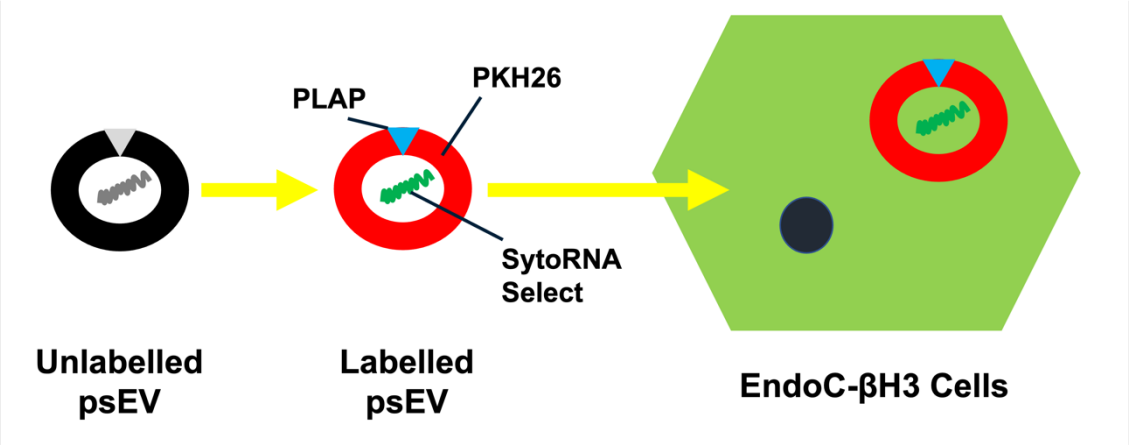

Figure 5.3. Schematic illustrating how placental small extracellular vesicle (psEV) labelling with fluorescent dyes and placental alkaline phosphatase (PLAP) were used to detect psEVs internalised by EndoC-βH3 cells

5.2.7.4 Image acquisition following small extracellular vesicle cell treatments

The Leica SP8 X-SMD FLIM confocal microscope, previously described, was used to acquire images at high power (63x). Image acquisition settings were consistent for each comparative condition within each experiment.

5.2.7.5 Colocalisation of intracellular placental alkaline phosphatase and SytoRNA Select dye signal

EndoC-βH3 cells previously treated with SytoRNA Select stained normal pregnancy psEVs were labelled with the anti-PLAP primary antibody by immunocytochemistry, as described in Chapter 2.

Colocalisation of the PLAP and SytoRNA Select signal was then quantified. Auto-thresholding using Otsu's thresholding was applied to segment the PLAP and SytoRNA Select signal. The colocalisation of PLAP and SytoRNA Select signal, using the percentage overlap, Pearson's correlation and Mander's coefficient (PLAP signal overlapping SytoRNA Select signal and vica versa) was measured using the Fiji plugin JACOP BIOP (180). The scatterplot was plotted in R studio (v2022.12.0) using the ggplot2 package (182).

5.2.7.6 Reverse transcription quantitative polymerase chain reaction for detection of chromosome 19 miRNA expression

To confirm the internalisation of normal pregnancy psEVs by EndoC-βH3 cells using an alternate methodology, reverse transcription quantitative polymerase chain reaction (RT-qPCR) was used to detect the presence of placental specific miRNAs (C19 microcluster (59, 183)) in EndoC-βH3 cells following treatment with psEVs.

EndoC-βH3 cells were seeded into 6 well plates (TPP, cat. no. 92006) at 1.2 x 10^6 cells per well and treated with psEVs (n=3), RBCsEVs (n=3) and the sEV carrier control (n=3) at 40 μg/mL for 6 hours. After 6 hours RNA was extracted as described in Chapter 2.

10 ng of cDNA was transcribed from RNA using the TaqMan Advanced miRNA cDNA Synthesis Kit (Thermo Fisher Scientific, cat. no. A28007). In contrast to traditional cDNA synthesis of polyA RNA, this is a multistep process requiring the addition of a polyA tail to the miRNA since miRNAs are comprised of shorter sequences without a polyA tail. Four steps were performed: 1) polyA tailing, 2) adaptor ligation, 3) reverse transcription and 4) miR-Amp reaction. For each step reagents were added in quantities as per the manufacturer's instructions and the reactions performed in the thermal cycler using the manufacturer-recommended settings. The following TaqMan miRNA assays were chosen for analysis: homo-sapiens-miRNA 517a (hsa-miR-517a), hsa-miR-517c, hsa-miR-518b, and hsa-miR-519a (Table 5.2). These belong to the placental specific C19 miRNA cluster and are highly expressed in psEVs (59, 183). U6 snRNA was used as the endogenous control/housekeeping gene (Table 5.2). RT-qPCR was performed, and raw data analysed as described in Chapter 2. Statistical differences between groups were analysed by a one-way ANOVA for multiple comparisons.

Table 5.2: List of assays used for RNA detection.

Assay type	Manufacturer	Target	Identifier
TaqMan™ MicroRNA Assay	Applied Biosystems	miR 517a	002402
		miR 517c	001153
		miR 518b	001156
		miR 519a	002415
		U6	001973

5.2.7.7 Live-cell imaging to quantify internalisation of placental small extracellular vesicles

To understand the time and dose relationship of psEV internalisation by EndoC-βH3 cells a live-cell imaging experiment was performed using the Olympus SpinSR SoRa spinning disc confocal microscope, utilising a 60x 1.3 numerical aperture Silicone objective and the 50 µm pinhole disc of a Yokogawa CSU-W1 spinning disc unit. The system was equipped with a Hammamatsu ORCA Fusion BT camera and excitation lasers at 405 nm, 488 nm, 561 nm and 640 nm. The system was controlled using the CellSense software package and was equipped with full CO_2, humidity, and temperature control. During this assay EndoC-βH3 cells were treated with different doses of PKH26-labelled normal pregnancy psEVs and imaged for 12 hours. The uptake of PKH26-labelled psEVs by EndoC-βH3 cells was visualised by confocal microscopy and images analysed using Arivis Vision 4D Image Analysis software (v4.1.2) to quantify cellular psEV internalisation. However, as the cells were exposed to high laser intensity for a long duration of time it was necessary to first optimise the labelling of cells and nuclei to minimise signal bleaching. Maintaining high-quality cell and nuclei signals throughout the assay was essential, as good quality signal was necessary for the image analysis software to accurately delineate cell borders and measure psEV volume. Image acquisition was performed in collaboration with Dr James Bancroft and Edward Drydale (Cellular Imaging Core Facility, CHG, Oxford UK).

5.2.7.7.1 Optimisation of cell efflux pump inhibitor dose

To ensure that the live imaging dyes remained within the cells, to improve their labelling efficacy and maintain a high signal intensity, it is recommended to add verapamil, a calcium efflux pump inhibitor, along with the live imaging dye to prevent dye extrusion (184). As I was unsure of the effect verapamil would have on EndoC-βH3 cell viability over 24 hours, I first tested different doses of verapamil co-cultured with EndoC-βH3 cells for 24 hours.

Verapamil was provided by Dr James Bancroft and Edward Drydale (Cellular Imaging Core Facility, CHG, Oxford UK). EndoC-βH3 cells were seeded at 1 x 10^6 in each well of a chambered coverslip 8-well µ-slide and three doses of verapamil (5 µM, 10 µM and 20 µM) and control (no verapamil) was added. Cells were visualised by brightfield using the EVOS cell imaging system (Thermo Fisher Scientific) 24 hours later to determine cell viability.

5.2.7.7.2 Optimisation of cell and nuclei labelling dyes

To determine which of the live imaging dyes would retain a high signal over the course of the assay I performed a test experiment comparing different nuclei and cell content labelling dyes. Four dyes were used that labelled either the whole cell or the nuclei: 1) CellTrace™ CFSE 488 (whole cell), 2) MemGlow™ 488 (whole cell) 3) SiR-DNA 647 (nuclei), and 4) NucBlue™ 405 (nuclei) (Table 5.1). Aliquots of SiR-DNA 647, NucBlue™ 405, MemGlow™ 488, and verapamil were provided by Dr James Bancroft and Edward Drydale (Cellular Imaging Core Facility, CHG, Oxford UK). Four different dye combinations were tested which included the addition of 10 µM of verapamil in two wells. The different combinations that were used are detailed in Figure 5.4.

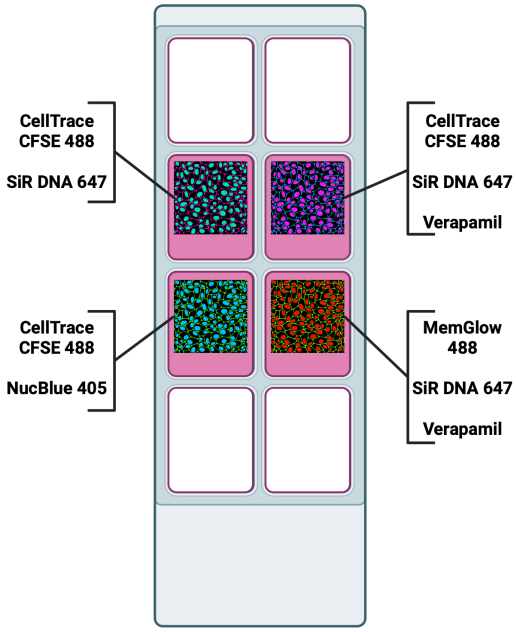

Figure 5.4. Illustration of the chambered coverslip 8 well µ-slide seeded with EndoC-βH3 cells labelled with the four dye combinations tested, including the addition of verapamil to two of the wells. Created with BioRender.com released under a Creative Commons Attribution-NonCommercial-NoDerivs 4.0 International license.

Each dye combination was added to a well containing EndoC-βH3 cells. CellTrace™ CFSE 488 was diluted to 5 µM and added to the cells for 20 minutes at 37°C followed by two washes with media. One microlitre of 1 mM of SiR-DNA stock per 1 mL of media was added to the cells. For NucBlue™ 405 a single drop was added to the cells 20 minutes before imaging. Five microlitres of 20 µM of MemGlow™ 488 stock was diluted in 1 mL of media and added to the cells. When SiR-DNA 647 and MemGlow™ 488 were used the media containing the dyes was not removed. In wells in which verapamil was used 10 µM was added to the cells.

Following labelling, the cells were then imaged. Four points per well were marked at the start of the assay and Z-stacks acquired at each of these points throughout the assay. The microscope was programmed to move from the first point in the first well through all the marked points to the last point in the final well and to continually repeat this circuit throughout the assay. The assay was run over 12 hours during which the cells were housed in an imaging box in which air with 5% CO_2 was supplied and the ambient temperature maintained at 37°C.

5.2.7.7.3 Live-cell assay and image analysis to quantify internalisation of placental small extracellular vesicles

Cells and nuclei were labelled using MemGlow™ 488 and SiR-DNA 647 as described above and 10 µM of verapamil was also added to the cells. PKH26-labelled normal pregnancy psEVs were then added at 3 different doses: 10 µg/mL, 20 µg/mL, and 40 µg/mL to three wells. The PKH26-labelled sEV carrier control was also added as the fourth condition. Before beginning the assay, nine points per well were marked where Z-stacks were to be acquired (Figure 5.5). The microscope cycled through all points acquiring Z-stacks

continuously over the course of the assay. The assay was run over 12 hours generating 180 time points. At each time point, nine Z-stacks were captured per well. This ensured that from each of the wells, per timepoint, nine replicate images were available for analysis.

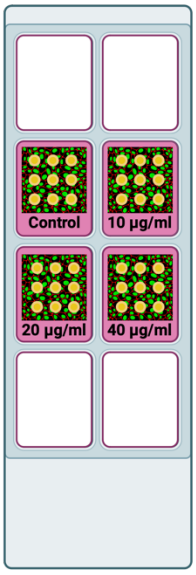

Figure 5.5. Illustration of the chambered coverslip 8 well µ-slide used during the live-cell assay to quantify placental small extracellular vesicle (psEV) uptake by EndoC-βH3 cells. The nine imaging points marked per well (yellow) were Z-stacks were continually acquired and dose of PKH26-labelled psEVs added per well are shown. Created with BioRender.com released under a Creative Commons Attribution-NonCommercial-NoDerivs 4.0 International license.

Acquired images were converted and loaded onto the Arivis Vision 4D image analysis software. An analysis pipeline was constructed which was applied to all acquired images. A Gaussian blur was applied to the cell and nuclei channels. The Blob Finder operation was used to segment nuclei. An intensity threshold was used to segment the cells and PKH26-labelled psEV volume, respectively. Nuclei counts, the total cell volume, and the psEV volume detected within the segmented total cell volume for each Z-stack was measured. Total cell volume and internalised psEV volume for each data point were exported to and processed in Microsoft Excel. Internalised psEV volume was normalised to the total cell volume per time point for each dose. The normalised nine values per time point were averaged and mean values plotted in Prism 10. Non-linear regression was performed to determine the best fit for each dose curve. Statistical comparisons between the curves were made comparing the EC50 for each by an extra sum-of-squares F-test.

5.3 Results

5.3.1 Patient demographics and clinical characteristics

Table 5.3 provides a comparative overview of the demographic and clinical characteristics between the normal pregnancy and GDM participant groups. Participant age and body mass index were similar across the groups. Both groups had the same median gestational age of 39.2 weeks. All women were normotensive with no differences between groups. Haemoglobin A1c levels were recorded only for the GDM group, the median value measured 5% (interquartile range (IQR) 4.8-5.6). Treatment for GDM varied, with two participants managed with diet alone, four with metformin, and two requiring both metformin and insulin. The proportion of male foetuses was identical in both pregnancy groups (50%), with a slightly higher average foetal birthweight in the GDM group (3657.5 g, interquartile range [IQR] 3455-4357.5) compared to the normal pregnancy group (3507.5 g, IQR 3255-4340) but this was not significant ($p = 0.81$) (Table 5.3).

Table 5.3: Characteristics of study participants.

	Norm Preg (n=8)	GDM (n=8)	p-value
Age (years)	33.5 (32.3-39)	29.5 (23.8-34.3)	0.85
Body mass index (kg/m^2)	25.5 (23-31)	27.8 (25.1-32.6)	0.28
Gestational age at delivery (weeks)	39.2 (39.1-39.6)	39.2 (38.1-39.4)	0.23
Maximum systolic blood pressure (mmHg)	126 (118-134)	131 (128-139)	0.26
Maximum diastolic blood pressure (mmHg)	80 (77-84)	82 (79-85)	0.68
Haemoglobin A1c (%)	-	5 (4.8-5.6)	-
GDM treatment Diet no. (%) Metformin no. (%) Metformin and insulin no. (%)	N/A	 2 (25) 4 (50) 2 (25)	-
Male foetus no. (%)	5 (50)	4 (50)	> 0.99
Foetal birthweight (g)	3507.5 (3255-4340)	3657.5 (3455-4357.5)	0.81

*Continuous data are described using median/interquartile range (IQR) and categorical data are described using counts and percentages.

**Norm Preg - normal pregnancy, GDM - gestational diabetes mellitus, no – number.

5.3.2 Immunophenotypic characterisation of placental and red blood cell small extracellular vesicles

To confirm successful isolation of normal pregnancy and GDM psEVs, as well as RBCsEVs, respectively, I verified their characteristic immunophenotypic features. Immunoblotting shown in Figure 5.6 confirmed that isolated normal pregnancy psEVs, GDM psEVs, and RBCsEVs were enriched for traditional EV markers: transmembrane tetraspanins, CD63 and CD9, and the cytosolic proteins, Alix and TSG101, which are also endosome sorting complex required for transport (ESCRT) machinery proteins. Another cytosolic protein, syntenin, was also present in both sets of sEVs. Normal pregnancy and GDM psEVs expressed PLAP confirming their placental origin, and RBCsEVs were enriched for CD235a confirming their RBC origin. The absence of cytochrome C in normal pregnancy psEVs, GDM psEVs, and RBCsEVs confirmed the purity of the sEV isolation, as cytochrome C is an intracellular protein known to be absent in sEVs. NTA analysis in Figure 5.7 detected a homogenous population of particles in line with the expected size distribution of sEVs (< 200 nm) for each sEV type. Mean and modal sizes are shown in Table 5.4. Particles consistent with the morphological appearance of normal pregnancy psEVs, GDM psEVs, and RBCsEVs were visualised by transmission electron microscopy (Figure 5.8).

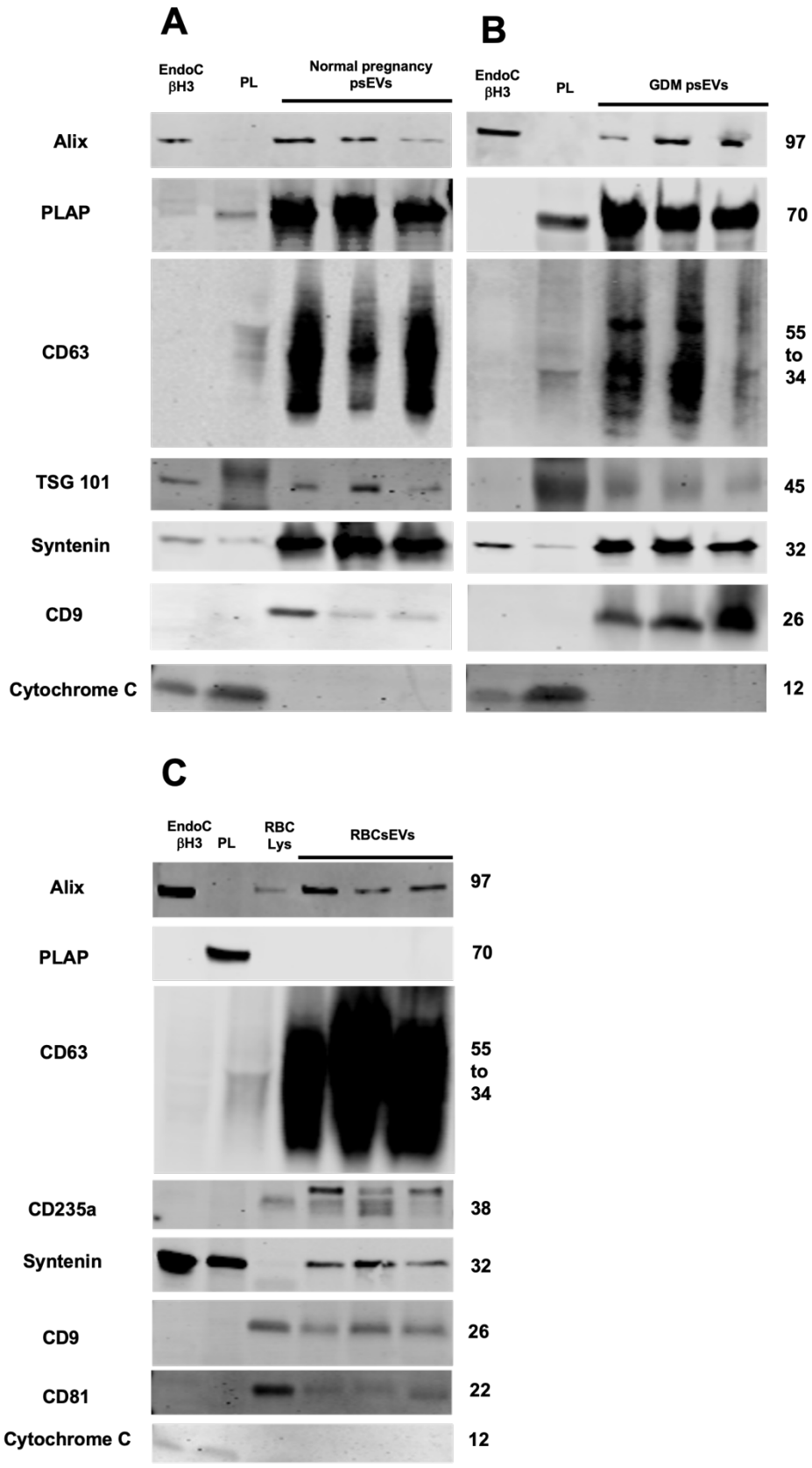
A
EndoC βH3
PL
Normal pregnancy psEVs
B
EndoC βH3
PL
GDM psEVs
Alix
PLAP
CD63
TSG 101
Syntenin
CD9
Cytochrome C
97
70
55 to 34
45
32
26
12
C
EndoC βH3
PL
RBC Lys
RBCsEVs
Alix
PLAP
CD63
CD235a
Syntenin
CD9
CD81
Cytochrome C
97
70
55 to 34
38
32
26
22
12

Figure 5.6. Immunoblot showing that isolated **A.** normal pregnancy and **B.** gestational diabetes mellitus (GDM) placental small extracellular vesicles (psEVs) as well as **C.** red blood cell small extracellular vesicles (RBCsEVs) are enriched for classic small extracellular vesicle markers and organ-specific markers, including the placental marker placental alkaline phosphatase (PLAP) and red blood cell marker CD235a. The observed molecular weight is indicated for each protein. Reproduced from *Seedat et al.*, *Clinical Science* (2024), with permission from Portland Press. This content is distributed under the Creative Commons Attribution License (CC BY 4.0).

*Lys – lysate, PL – placental lysate.

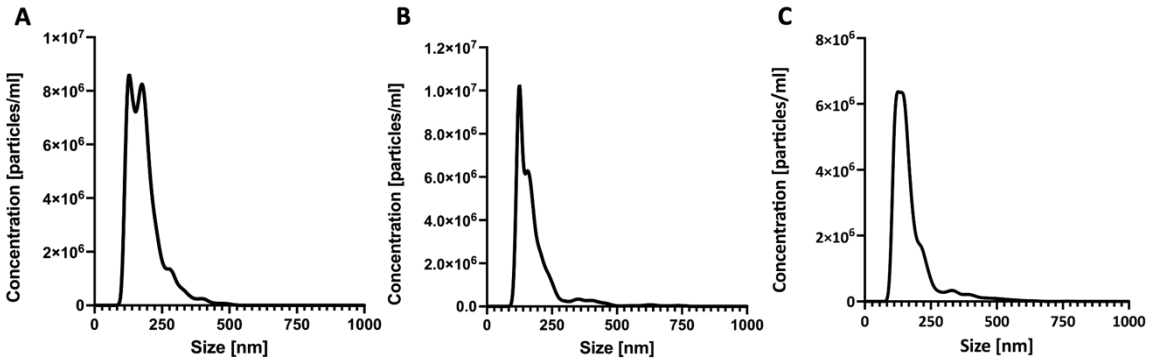

Figure 5.7. Nanoparticle tracking analysis for **A.** normal pregnancy placental small extracellular vesicles (psEVs), **B.** Gestational diabetes mellitus (GDM) psEVs, and **C.** Red blood cell small extracellular vesicles (RBCsEVs). Size versus distribution profiles are shown. Reproduced from *Seedat et al.*, *Clinical Science* (2024), with permission from Portland Press. This content is distributed under the Creative Commons Attribution License (CC BY 4.0).

Table 5.4: Nanoparticle tracking analysis of mean and mode particle size of placental and red blood cell small extracellular vesicles.

	NP psEVs		GDM psEVs		RBCsEVs	
	Average (nm)	Standard Error	Average (nm)	Standard Error	Average (nm)	Standard Error
Mean	184.5	0.3	180.7	3.8	166.4	2
Mode	155.3	10.8	125.2	2.1	120.7	2.5
SD	62.2	0.8	86.9	4.9	72.7	2.9

*GDM – gestational diabetes mellitus, NP – normal pregnancy, psEVs – placental small extracellular vesicles, RBCsEVs – red blood cell small extracellular vesicles.

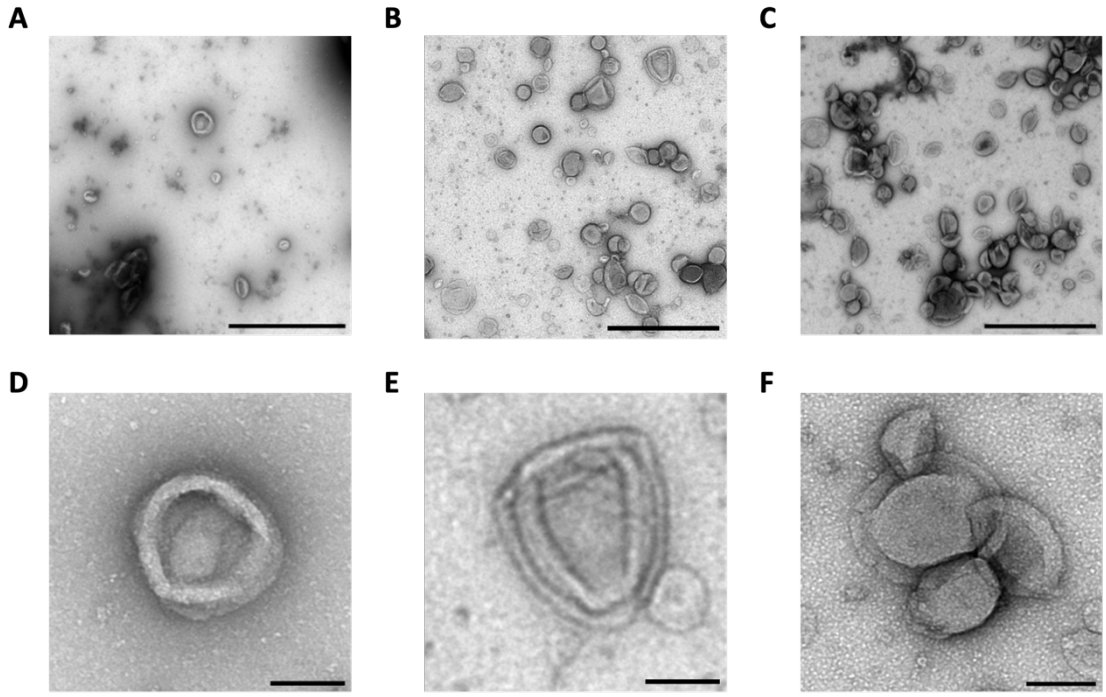

Figure 5.8. Transmission electron microscopy showing the typical cup shaped appearance of an extracellular vesicle seen for **A.** and **C.** Normal pregnancy placental small extracellular vesicles (psEVs), **B.** and **D.** Gestational diabetes mellitus (GDM) psEVs, and E. and F. Red blood cell small extracellular vesicles (RBCsEVs). **A.**, **B.**, and **C.** Scale bar = 1000 nm. **D.**, **E.**, and **F.** Scale bar = 100 nm. Reproduced from *Seedat et al.*, *Clinical Science* (2024), with permission from Portland Press. This content is distributed under the Creative Commons Attribution License (CC BY 4.0).

5.3.3 Differentiation of EndoC-βH3 cells

Following 4-hydroxitamoxifen treatment I sought to confirm that the EndoC-βH3 cells had indeed undergone differentiation. Successful differentiation of EndoC-βH3 cells was first demonstrated by the observed changes in cellular morphology and an increase in the number of insulin-containing vesicles (Figure 5.9).

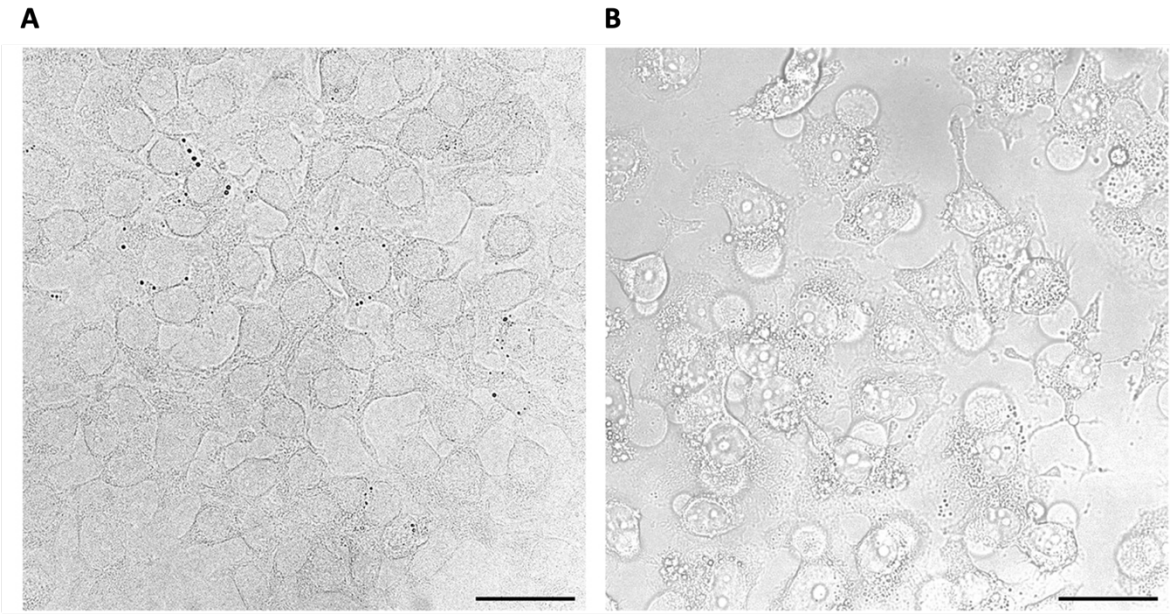

Figure 5.9. Brightfield images of **A.** undifferentiated and **B.** differentiated EndoC-βH3 cells. A greater number of cell projections and insulin containing vesicles are evident in the differentiated cells. Images were acquired at 63x magnification. Scale bar = 20 μm.

A decrease in SV40LT signal, indicative of cellular differentiation, was illustrated using immunocytochemistry (Figure 5.10A(i) – (vi)). It was visually apparent that SV40LT signal was reduced in differentiated compared to undifferentiated cells. Differences were also objectively quantified by colocalising detected SV40LT signal to the nuclear signal, with a reduction representing a loss of SV40LT signal intensity. A decrease in SV40LT and DAPI nuclear colocalisation was noted in differentiated cells compared to undifferentiated cells when analysed by percentage signal overlap ($p < 0.005$), Pearson's correlation coefficient ($p < 0.005$), and Mander's coefficient for colocalisation ($p < 0.005$) (Figure 5.10A(vii) - (ix)). A reduction of SV40LT signal in differentiated cells was further confirmed by immunoblotting (Figure 5.10B(i)), with a decrease in signal band intensity in the differentiated cells ($p < 0.005$) (Figure 5.10 (ii) and B(iii)).

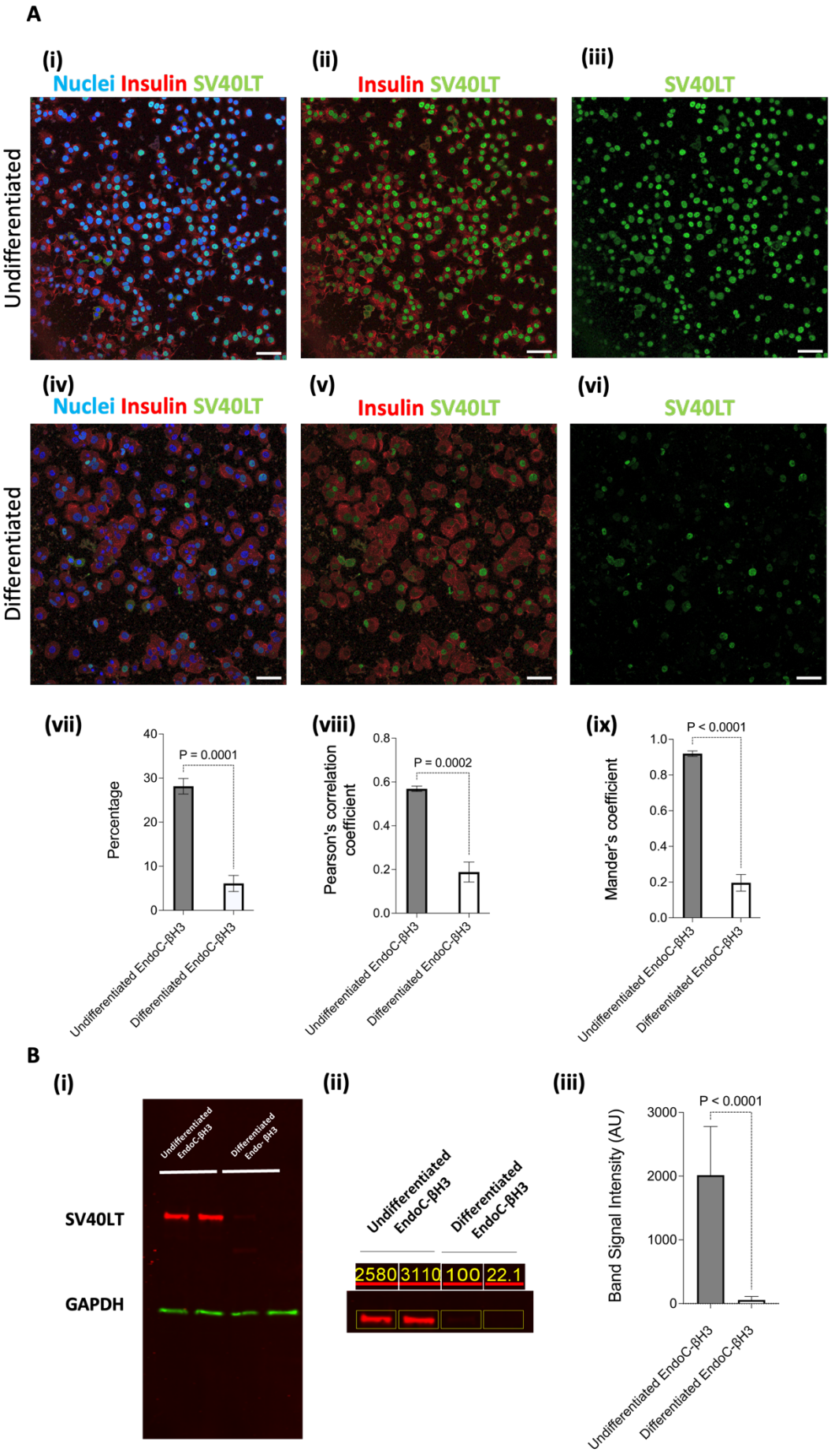
A
(i)
Nuclei Insulin SV40LT
(ii)
Insulin SV40LT
(iii)
SV40LT
Undifferentiated
(iv)
Nuclei Insulin SV40LT
(v)
Insulin SV40LT
(vi)
SV40LT
Differentiated
(vii)
Percentage
P = 0.0001
Undifferentiated EndoC-βH3
Differentiated EndoC-βH3
(viii)
Pearson's correlation coefficient
P = 0.0002
Undifferentiated EndoC-βH3
Differentiated EndoC-βH3
(ix)
Mander's coefficient
P < 0.0001
Undifferentiated EndoC-βH3
Differentiated EndoC-βH3
B
(i)
Undifferentiated EndoC-βH3
Differentiated Endo-βH3
SV40LT
GAPDH
(ii)
Undifferentiated EndoC-βH3
Differentiated EndoC-βH3
2580 3110 100 22.1
(iii)
Band Signal Intensity (AU)
P < 0.0001
Undifferentiated EndoC-βH3
Differentiated EndoC-βH3

Figure 5.10. A. Immunocytochemistry of EndoC-βH3 cells demonstrating reduced SV40 Large T cell (SV40LT) signal in differentiated cells after 21 days of 4-hydroxitamoxifen treatment **(i)-(vi)**. Cells were stained as follows: nuclei (DAPI in blue), insulin (red) and SV40LT (green). The merged channel, insulin and SV40LT signals combined and SV40LT alone is shown. Scale bar = 50 μm. SV40LT signal in undifferentiated and differentiated cells was compared and represented as follows: **(vii)** Percentage overlap of SV40LT over nuclear signal. **(viii)** Pearson's correlation of SV40LT and nuclear signal. **(ix)** Mander's coefficient for the colocalisation of SV40LT and nuclear signal. Differences were analysed by the Mann-Whitney test and significant p-values are shown. **B.** Immunoblot and quantification of SV40LT signal demonstrating reduced SV40LT signal in differentiated cells. **(i)** Immunoblot showing the presence of SV40LT signal in undifferentiated cells but its near absence in differentiated cells. GAPDH (loading control) was present in all lanes **(ii)** Quantification of SV40LT signal in differentiated and undifferentiated cells **(iii)** Graphical representation of band signal intensity of SV40LT signal in undifferentiated and differentiated EndoC-βH3 cells. Differences were analysed by the Mann-Whitney test and the significant p-value is shown.

5.3.4 Nanoparticle tracking analysis of placental small extracellular vesicles labelled with fluorescent dyes

Following PKH26 and SytoRNA Select labelling of psEVs, labelled normal pregnancy psEVs and the psEV carrier control were re-analysed by NTA to determine if labelling had altered the sEV size and if sEV dye aggregates, that may mimic sEVs, could be detected in the labelled sEV carrier dye control. The size of PKH26-labelled psEVs were expectedly slightly smaller, due to the addition of the size exclusion step on re-isolation, compared to unlabelled sEVs (Figure 5.11). Notably, the mean and modal size of labelled psEVs remained under 200 nm post labelling using PKH26 and SytoRNA Select dyes, respectively (Table 5.5). No sEV sized particles were detected by NTA in the sEV carrier dye control samples labelled with either PKH26 or SytoRNA Select (insufficient number of valid tracks <100) suggesting the absence of dye aggregates that may mimic sEVs.

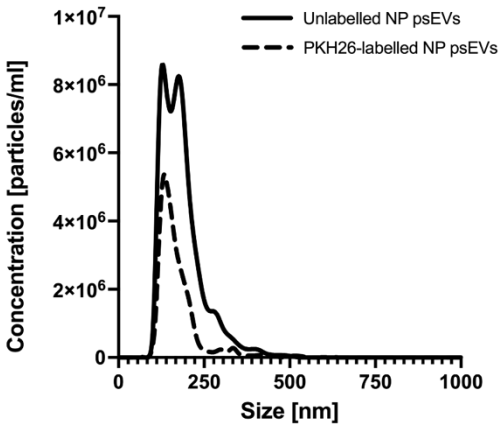

Figure 5.11. Nanoparticle tracking analysis following PKH26 labelling of normal pregnancy (NP) placental small extracellular vesicles (psEVs). Size versus distribution profiles of unlabelled psEVs compared to PKH26-labelled psEVs are shown.

Table 5.5: Nanoparticle tracking analysis of mean and mode particle size of PKH26- and SytoRNA Select-labelled normal pregnancy placental small extracellular vesicles.

	PKH26-labelled NP psEVs		**SytoRNA Select-labelled NP psEVs**	
	Average (nm)	Standard Error	Average (nm)	Standard Error
Mean	171.5	1.2	161.7	1.4
Mode	143	4.5	127.4	5.7
SD	65	2.1	57.7	1.1

*NP – normal pregnancy, psEVs – placental small extracellular vesicles.

5.3.5 Demonstration of internalisation of small extracellular vesicles by EndoC-βH3 cells

It was crucial to confirm the internalisation of normal pregnancy psEVs, GDM psEVs, and RBCsEVs by EndoC-βH3 cells before proceeding with further experiments. The following data demonstrate psEV and RBCsEV cellular internalisation.

5.3.5.1 Confocal microscopy

EndoC-βH3 internalisation of PKH26- and SytoRNA Select-labelled normal pregnancy psEVs, GDM psEVs, and RBCsEVs was confirmed by confocal microscopy (Figure 5.12 and Figure 5.13). Intracellular PLAP signal also was detected in cells treated with unlabelled normal pregnancy and GDM psEVs (Figure 5.12).

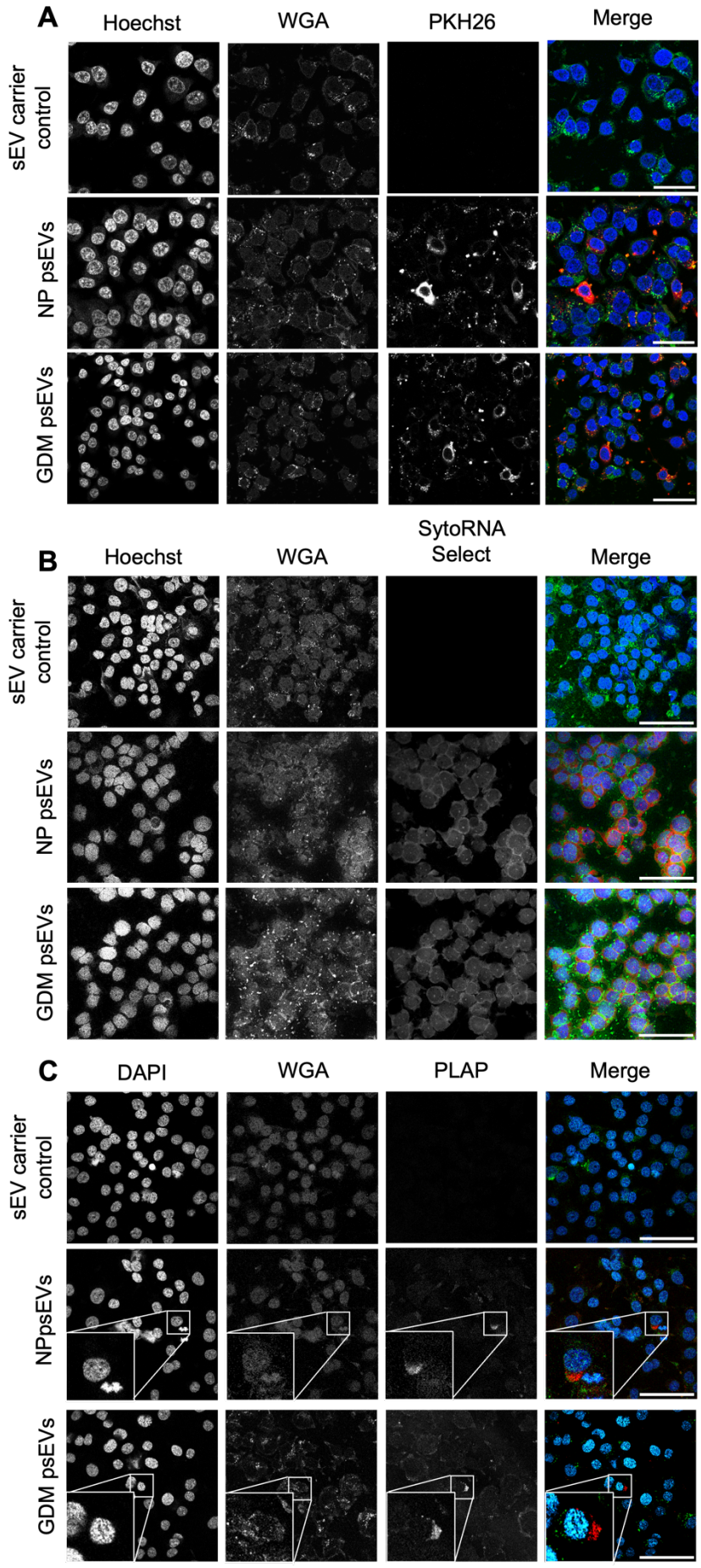
A
Hoechst
WGA
PKH26
Merge
sEV carrier control
NP psEVs
GDM psEVs
B
Hoechst
WGA
SytoRNA Select
Merge
sEV carrier control
NP psEVs
GDM psEVs
C
DAPI
WGA
PLAP
Merge
sEV carrier control
NPpsEVs
GDM psEVs

Figure 5.12. Normal pregnancy (NP) and gestational diabetes mellitus (GDM) placental small extracellular vesicle (psEV) internalisation by EndoC-βH3 cells visualised by confocal microscopy. **A.** Confocal microscopy reveals the presence of internalised PKH26-labelled placental extracellular vesicles, shown in red, within EndoC-βH3 cells. Scale bar = 10 μm. **B.** Following treatment with SytoRNA-Select labelled psEVs, intracellular detection of SytoRNA Select dye, in red, is observed. Scale bar = 20 μm. **C.** Immunocytochemistry indicates the presence of placental alkaline phosphatase (PLAP), in red, within EndoC-βH3 cells after exposure to psEVs. Scale bar = 20 μm. Panels are shown for the small extracellular vesicle (sEV) carrier control, normal pregnancy psEVs, and GDM psEVs for PKH26 and Syto RNA Select labelling dyes as well as for immunolabelling with the anti-PLAP antibody. For all images each channel is shown as a grayscale image and the merged channel is shown in colour (nuclei in blue, EndoC-βH3 cells in green and labelled psEVs [PKH26 and SytoRNA Select] or PLAP in red). Reproduced from *Seedat et al.*, *Clinical Science* (2024), with permission from Portland Press. This content is distributed under the Creative Commons Attribution License (CC BY 4.0).

*WGA – wheat germ agglutinin.

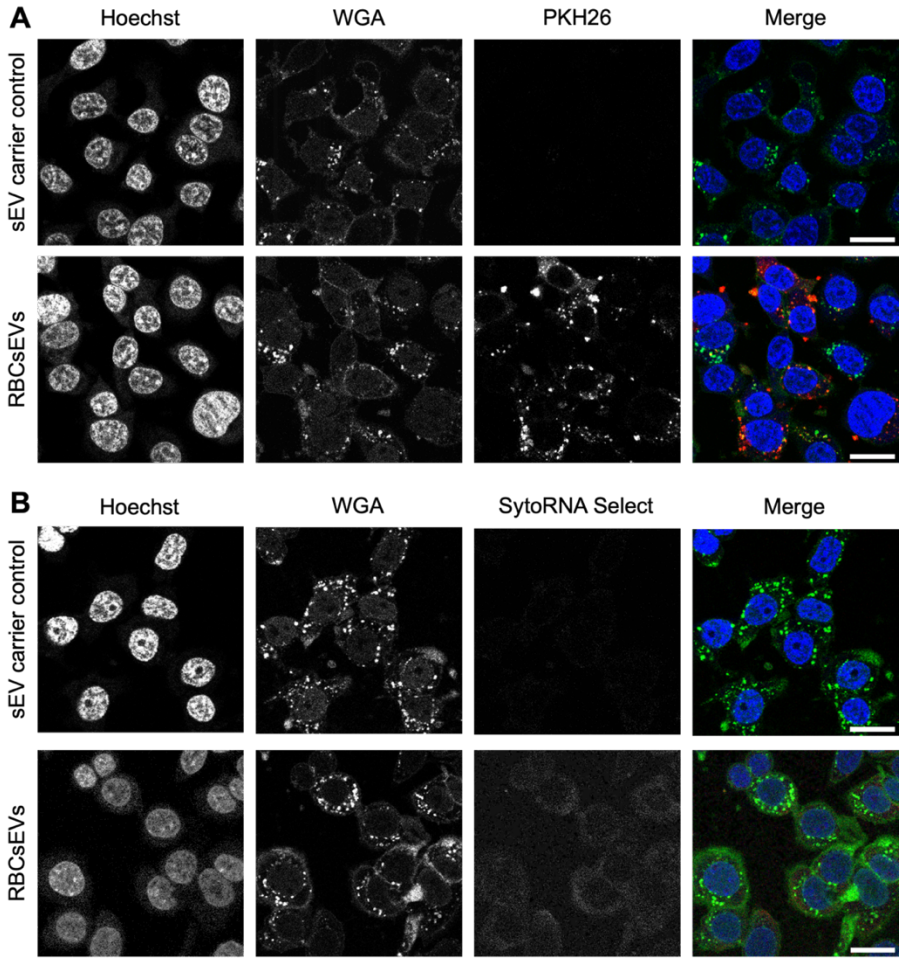

Figure 5.13. Confocal microscopy demonstrating internalisation of red blood cell small extracellular vesicles (RBCsEVs) by EndoC-βH3 cells. **A.** Internalised PKH26-labelled RBCsEVs (red) within EndoC-βH3 cells. **B.** Intracellular detection of SytoRNA Select dye following treatment with SytoRNA Select-labelled RBCsEVs. Panels are shown for the small extracellular vesicle (sEV) carrier control and RBCsEVs for both the PKH26 and Syto RNA Select labelling dyes. For all images, each channel is shown in grayscale and the merged channel is shown in colour (nuclei in blue, EndoC-βH3 cells in green and labelled RBCsEVs in red). Scale bar = 10 µm. Reproduced from *Seedat et al.*, *Clinical Science* (2024), with permission from Portland Press. This content is distributed under the Creative Commons Attribution License (CC BY 4.0).

*WGA – wheat germ agglutinin.

The detected intracellular SytoRNA Select signal can be attributed to psEVs, rather than dye aggregates, as this was colocalised with PLAP (Figure 5.14). A cytofluorogram and signal intensity plot illustrate the correlation between these two signals (Figure 5.14 B(i) and (ii)). The colocalisation of PLAP and SytoRNA Select signal was further quantified showing an 85% percentage overlap, Pearson's correlation coefficient of 0.84, and Mander's colocalisation coefficient of 0.47 for SytoRNA Select signal overlapping PLAP signal (M1) and 0.96 PLAP signal overlapping SytoRNA Select signal (M2) (Figure 5.14 B(iii) and (iv)).

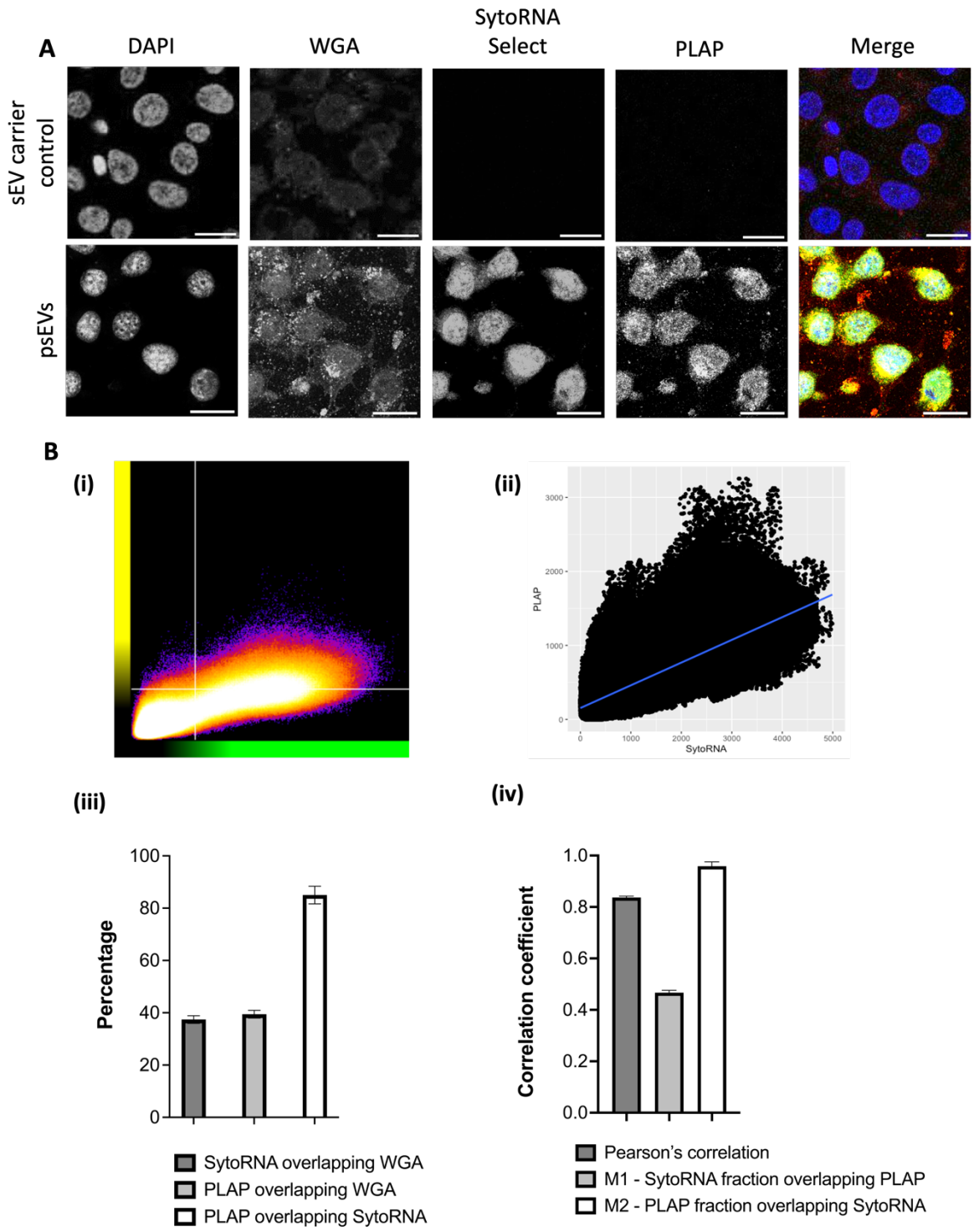
A
DAPI
WGA
SytoRNA Select
PLAP
Merge
sEV carrier control
psEVs
B
(i)
(ii)
PLAP
SytoRNA
(iii)
Percentage
SytoRNA overlapping WGA
PLAP overlapping WGA
PLAP overlapping SytoRNA
(iv)
Correlation coefficient
Pearson's correlation
M1 - SytoRNA fraction overlapping PLAP
M2 - PLAP fraction overlapping SytoRNA

Figure 5.14. A. Immunocytochemistry shows the colocalisation of SytoRNA Select and placental alkaline phosphatase (PLAP) signals within EndoC-βH3 cells after treatment with SytoRNA Select-labelled normal pregnancy placental small extracellular vesicles (psEVs). Each channel is depicted in grayscale, with the merged image in colour (nuclei in blue, wheat germ agglutinin (WGA) in red, SytoRNA Select in green, and PLAP in yellow). Scale bar = 20 μm. **B(i)** Cytofluorogram showing SytoRNA Select-labelled psEV signal plotted on the x-axis (green) and PLAP signal plotted on the y-axis (yellow) and **B(ii)** pixel intensity scatter plot display the colocalisation of light spectra and pixels, respectively, for the PLAP and SytoRNA Select signals, respectively. The blue line indicates the linear correlation between the PLAP and SytoRNA Select signals. **B(iii)** Quantification of the percentage overlap of SytoRNA Select overlapping WGA marking the EndoC-βH3 cells, PLAP signal overlapping WGA marking the EndoC-βH3 cells, and PLAP signal overlapping SytoRNA Select. **B(iv)** Pearson's correlation and Mander's coefficients (M1, SytoRNA Select overlapping PLAP and M2, PLAP overlapping SytoRNA Select) are provided for the colocalisation of PLAP and SytoRNA Select signals.

3.3.5.2 C19 mIRNA

Internalisation of psEVs by EndoC-βH3 cells was further validated by RT-qPCR that confirmed the presence of placental specific C19 micro cluster miRNA in cells treated with normal pregnancy psEVs ($p < 0.005$) (Figure 5.15).

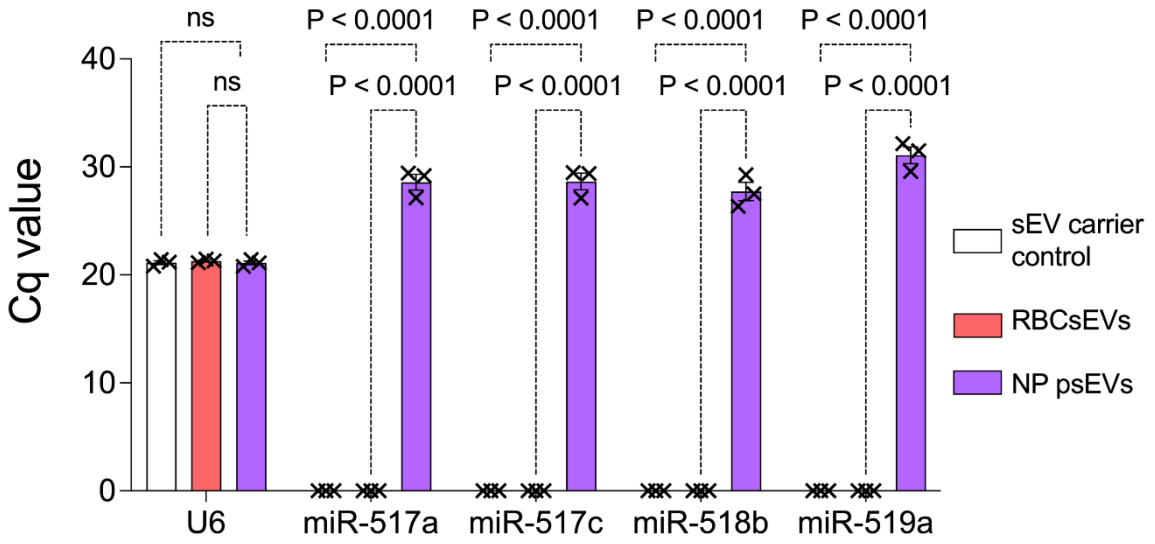

Figure 5.15. Placental small extracellular vesicle (psEV) internalisation is demonstrated using reverse transcription-quantitative polymerase chain reaction (RT-qPCR). Placental specific C19 miRNA was only detected within EndoC-βH3 cells treated with normal pregnancy psEVs and not in those treated with red blood cell small extracellular vesicles (RBCsEVs) nor in those treated with the small extracellular vesicle (sEV) carrier control. U6 was used as the housekeeping gene. The C19 specific miRNAs analysed are represented on the x-axis. Differences were analysed by a one-way ANOVA for multiple comparisons. Only significant p-values are shown. ns = non-significant, $p > 0.05$. Reproduced from *Seedat et al.*, *Clinical Science* (2024), with permission from Portland Press. This content is distributed under the Creative Commons Attribution License (CC BY 4.0).

5.3.6 Effect of dose and duration of treatment on internalisation of placental small extracellular vesicles by EndoC-βH3 cells

I aimed to investigate the uptake dynamics of psEVs by EndoC-βH3 cells using live-cell imaging. However, prior to this, initial optimisation work was necessary. First, I needed to determine the dose of the efflux pump inhibitor to use in to maintain cell viability throughout the experiment. The inhibitor was used to prevent premature extrusion of cell labelling dyes and improve dye labelling efficacy, ensuring a consistent image signal during the live-cell imaging.

The viability of EndoC-βH3 cells was confirmed for each of the three doses tested (5 μM, 10 μM, and 20 μM) of the efflux pump inhibitor verapamil over 24 hours. Minimal to no cell death occurred at all doses, and the treated cells appeared similar to the control group after 24 hours (Figure 5.16). Although cell viability was maintained at a verapamil dose of 20 μM, I chose to use a dose of 10 μM. This decision was influenced by the positive results achieved by other users of the cellular imaging core at this concentration. Additionally, I was uncertain about the potential impact of extensive dye retention on cell viability and decided that 10 μM was a prudent starting point before considering the higher 20 μM dose.

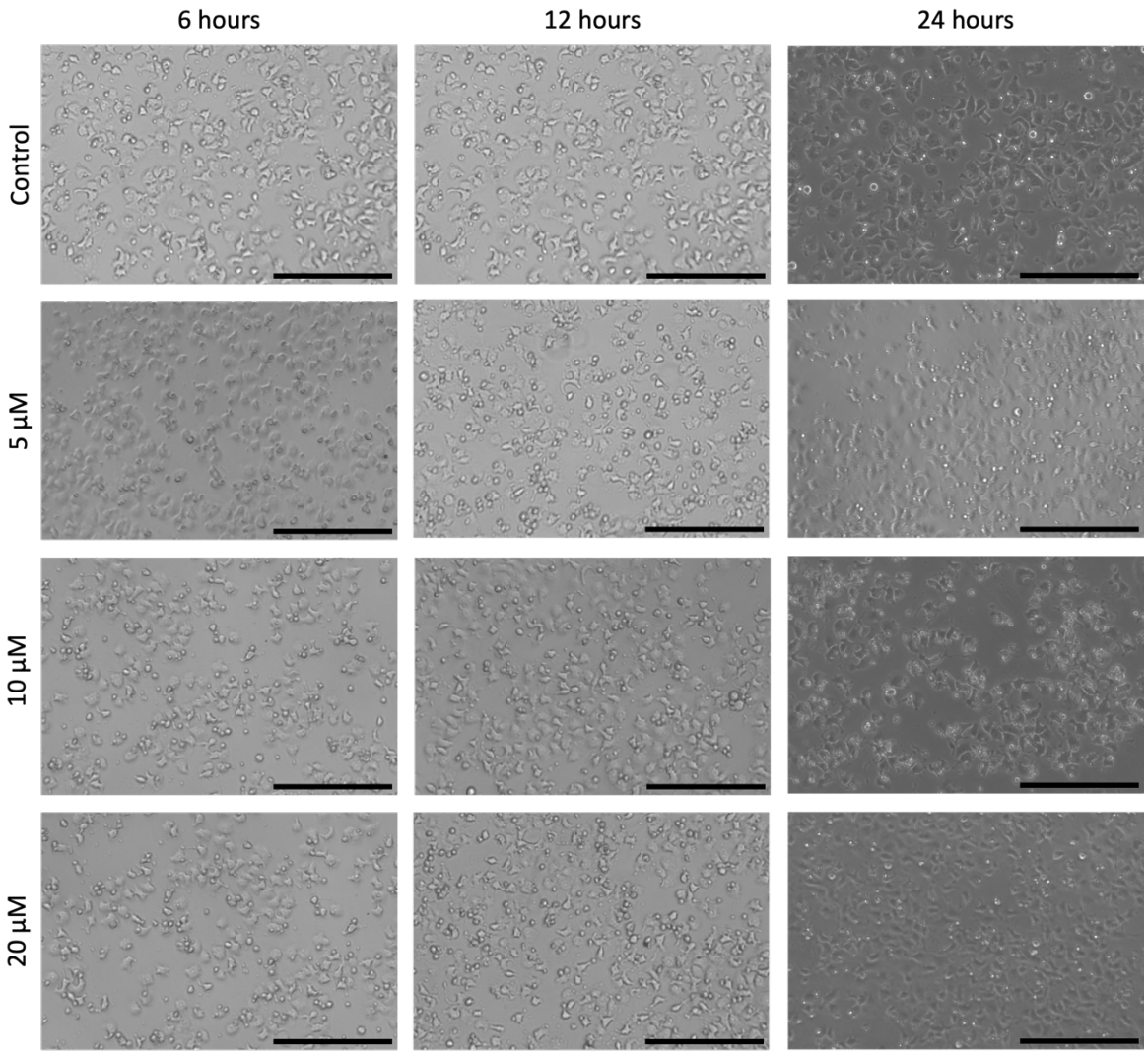

Figure 5.16. Dose titration test of the cell efflux pump inhibitor (verapamil) to assess cell viability over 24 hours. Brightfield images of EndoC-βH3 cells treated with verapamil at concentrations of 5 µM, 10 µM, and 20 µM, compared to the control. Images were captured at 6-, 12-, and 24-hours post-treatment. Scale bar = 200 µm.

After optimising the efflux pump inhibitor dose, I then investigated different cell labelling dye combinations to identify the best combination that would provide a consistent signal throughout the experiment. Given the length of the experiment, there was a risk of signal loss due to bleaching. It was vital to ensure sufficient signal was present throughout the duration of the experiment so the images could be accurately analysed using the image analysis software. I observed that while the combination of CellTrace™ CFSE 488 used to label the cell contents with either SiR-DNA 647 or NucBlue™ 405 to label the nuclei did indeed label the respective structures, the signal intensity faded significantly after 12 hours of imaging (Figure 5.17). This loss of signal would prevent reliable segmentation of cells for quantifying psEV internalisation by EndoC-βH3 cells. When verapamil was added to the CellTrace™ CFSE 488 and SiR-DNA 647 combination, the nuclear signal was retained at 12 hours (Figure 5.17). However, the signal marking the cell contents faded once again, making it inadequate for computational cell segmentation. The MemGlow™ 488 and SiR-DNA 647 combination with verapamil provided the clearest and most detailed marking of cell contents and nuclei at the start of the assay (time point 0), and good signal intensity was retained at 12 hours (Figure 5.17). This combination would allow for effective segmentation of cell areas and reliable quantification of PKH26-labeled psEV uptake and was, therefore, used for the live-cell psEV uptake assay to quantify psEV internalisation by EndoC-βH3 cells.

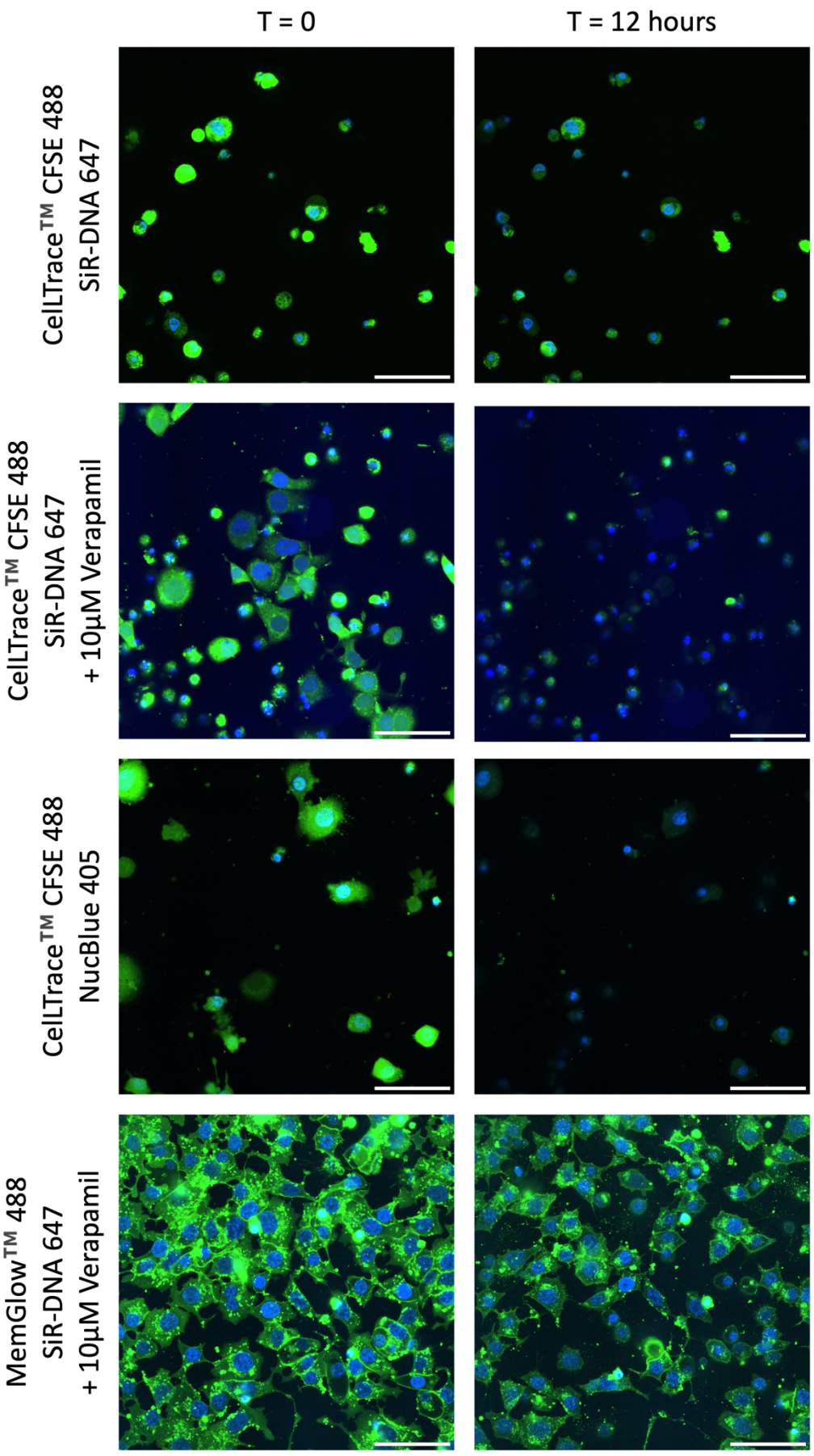
T = 0
T = 12 hours
CellTrace™ CFSE 488
SiR-DNA 647
CellTrace™ CFSE 488
SiR-DNA 647
+ 10µM Verapamil
CellTrace™ CFSE 488
NucBlue 405
MemGlow™ 488
SiR-DNA 647
+ 10µM Verapamil

Figure 5.17. Live-cell imaging of EndoC-βH3 cells to test efficacy of nucleus and cell content labelling dyes and the retention of signal intensity following 12 hours of imaging with and without the use of efflux pump inhibitor, verapamil. Merged images for each condition at timepoint (T) 0 (left), the start of the assay, and 12 hours (right) are shown. The nuclei are in represented in blue and cells in green. Scale bar = 50 μm.

The live-cell psEV uptake assay was performed over 12 hours, and representative images illustrating uptake of PKH26-labelled psEVs are presented in Figure 5.18. The image analysis pipeline that was created was then used to analyse all the acquired images. Applying the same computational analysis to all images ensured unbiased quantitative data was acquired. The details of the segmentation and steps applied in the image analysis pipeline is shown in Figure 5.19. The live-cell psEV uptake assay demonstrated that psEVs are internalised in a dose- and time-dependent manner (Figure 5.20). Maximal uptake occurred before 3 hours for the 10 µg dose, at 4-6 hours for the 20 µg dose but uptake for up to 12 hours was seen when a treatment dose of 40 µg was administered.

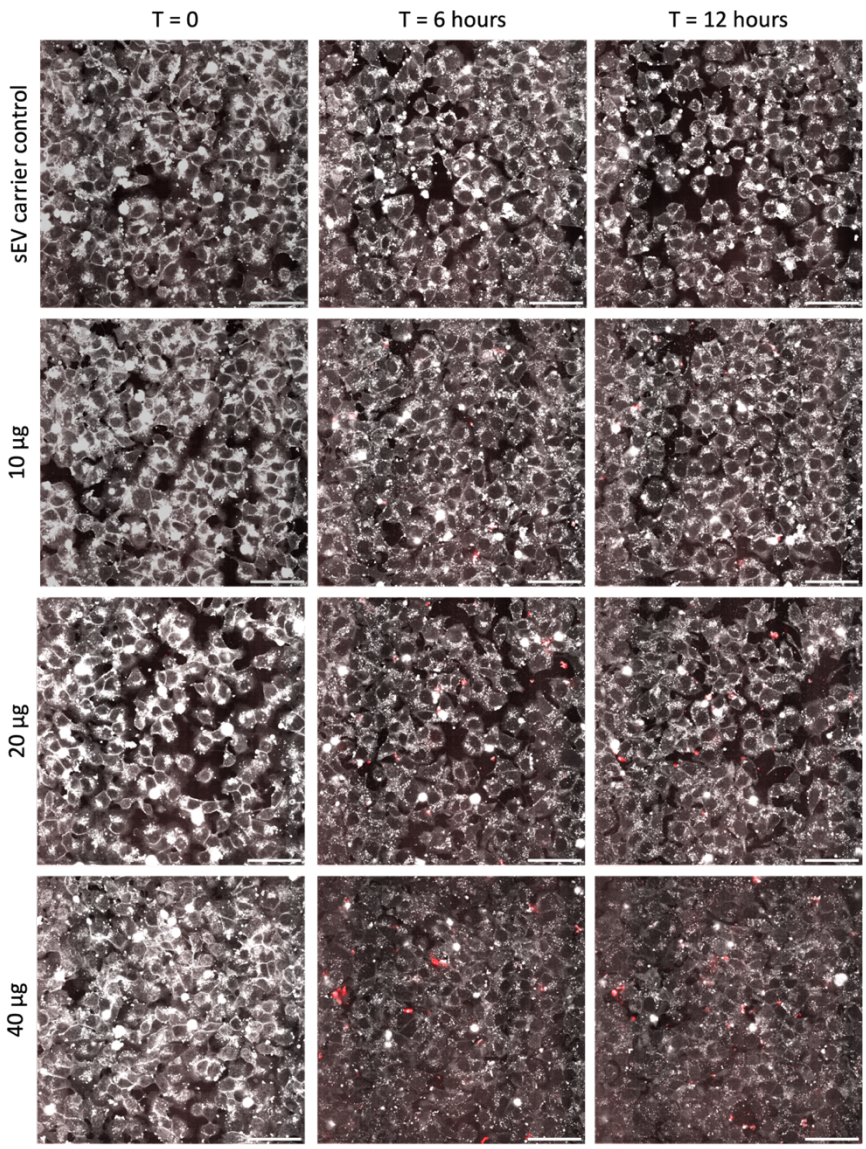

Figure 5.18. Live-cell imaging of PKH26-labeled normal pregnancy placental small extracellular vesicle (psEV) internalisation at various time points. Images are presented for 0, 6, and 12 hours for cells treated with the small extracellular vesicle (sEV) carrier control and different concentrations of PKH26-labeled psEVs (10 µg, 20 µg, and 40 µg). The merged images display nuclei and cells in grayscale, while PKH26-labeled psEVs appear in red. Scale bar = 50 µm. Reproduced from *Seedat et al.*, *Clinical Science* (2024), with permission from Portland Press. This content is distributed under the Creative Commons Attribution License (CC BY 4.0).

i)

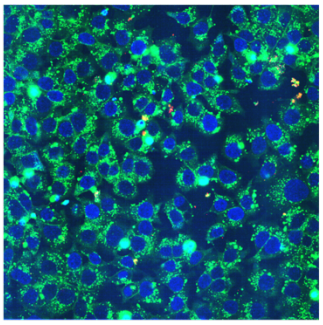

ii)

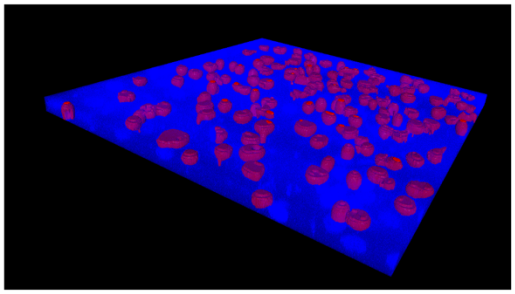

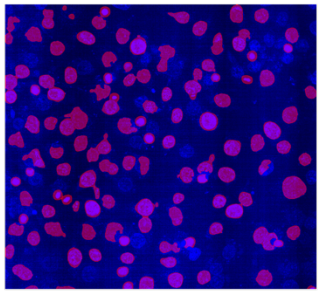

iii)

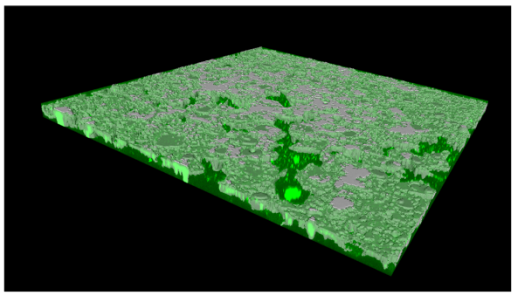

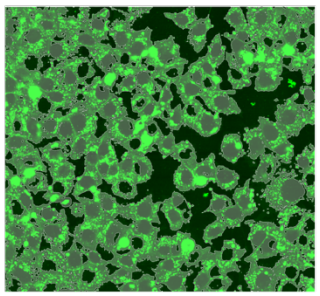

iv)

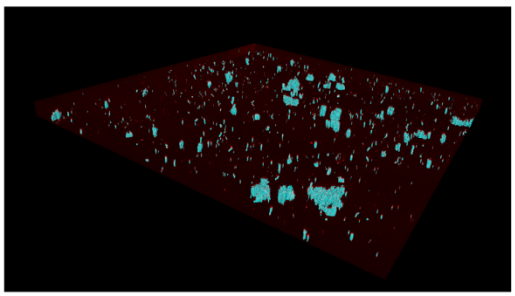

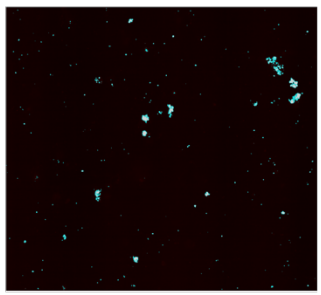

v)

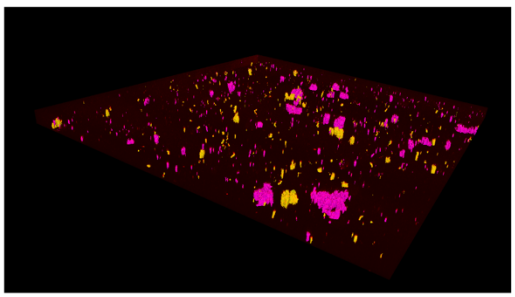

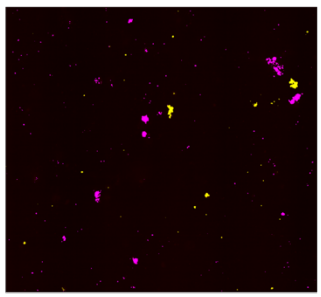

vi)

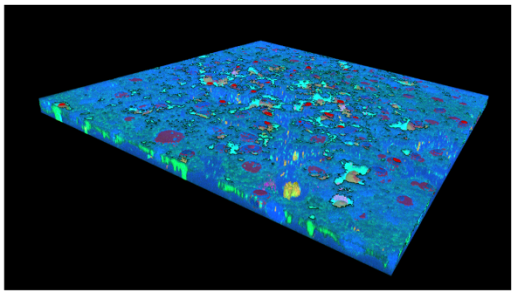

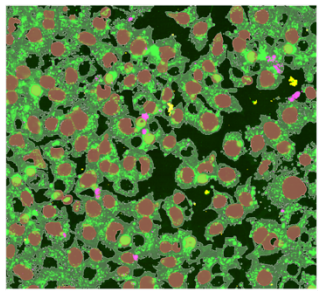

Figure 5.19. Image analysis pipeline used to quantify placental small extracellular vesicle (psEV) uptake by EndoC-βH3 cells using Arivis Vision 4D Image Analysis software. Images at different stages of the analysis are shown to illustrate the methodological steps used to segment the cells, identify PKH26-labelled psEVs, and quantify the volume of internalised psEV within the cells. Left: 3D images; Right: 2D images. (i) Single Z-position from converted image at timepoint 120 treated with 20 μg of PKH26-labelled psEVs. (ii) Nuclei (red) segmented using the blob finder tool. (iii) EndoC-βH3 cells segmented (green) using intensity thresholding. (iv) PKH26-labelled psEVs segmented using intensity thresholding. (v) Internalised (pink) and extracellular (yellow) PKH26-labelled psEVs. (vi) Composite image showing segmentation of nuclei (red), cells (green), internalised psEVs (pink), and extracellular psEVs (yellow). Reproduced from *Seedat et al.*, *Clinical Science* (2024), with permission from Portland Press. This content is distributed under the Creative Commons Attribution License (CC BY 4.0).

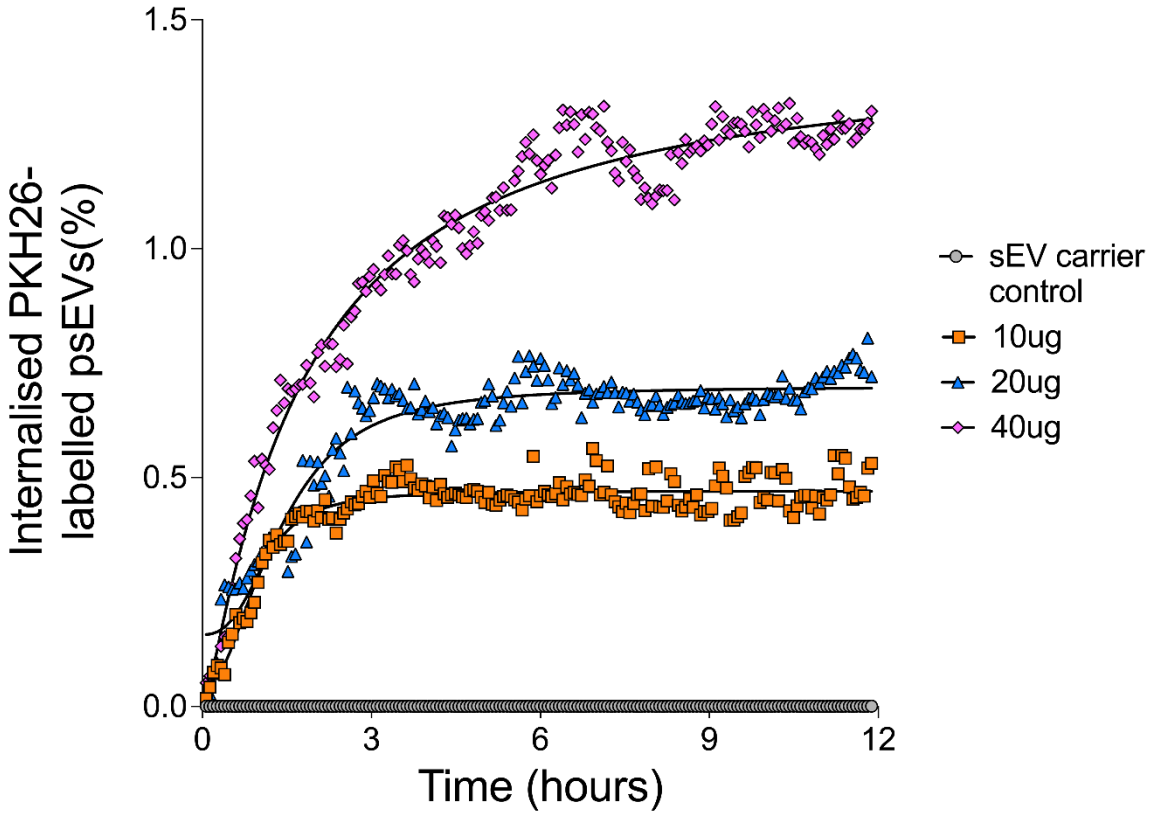

Figure 5.20. Time course of the internalisation of PKH26-labelled placental small extracellular vesicles (psEVs) by EndoC-βH3 cells. The volume of internalised PKH26-labelled normal pregnancy psEVs within EndoC-βH3 cells was quantified and expressed as a percentage of the total cell volume. The mean volume (n=9) at each time point for each dose is plotted. Non-linear regression was used to create the best-fit line, and there was a difference when comparing EC50 values by an F-test (p=0.002). Reproduced from *Seedat et al.*, *Clinical Science* (2024), with permission from Portland Press. This content is distributed under the Creative Commons Attribution License (CC BY 4.0).

5.4 Discussion

I successfully isolated normal pregnancy psEVs, GDM psEVs, and RBCsEVs using established techniques consistently employed by our research group with reproducible results (87, 185-187). I then characterised the isolated sEVs using well-documented methods, aligning with the recommendations of the International Society for Extracellular Vesicles (ISEV) (48, 49). The immunophenotypic features of the sEVs were consistent with classic sEV characteristics routinely detected by our group and widely reported in the EV literature, as endorsed by the ISEV (48, 49, 59, 87, 185-187).

EndoC-βH3 cells were successfully cultured and differentiated. Loss of SV40-LT signal was demonstrated by confocal microscopy in differentiated EndoC-βH3 cells, replicating the phenotypic features that have been previously published to illustrate successful EndoC-βH3 differentiation (126). I also validated this finding using an alternate technique, as loss of SV40LT signal in differentiated cells was demonstrated using immunoblotting. Maintaining the EndoC-βH3 human β cells is technically challenging. Unlike cancer cell lines, their growth is slow, they are passaged weekly and replicate at a rate of 1.1 – 1.4x per week (126). This necessitates culturing a large volume of cells over several weeks to establish the cell cultures and achieve a sufficient cell number prior to cell differentiation. During the differentiation process, cell death rates are high and the process is itself prolonged. Given these challenges, it was essential in this project to successfully culture and demonstrate robust differentiation of these cells to ensure that an adequate and consistent supply of cells would be available for use in future experiments.

These data demonstrate the first example of psEV uptake by human β cells. Internalisation was confirmed using confocal microscopy by detecting pre-labelled sEVs within EndoC-

βH3 cells. The utilisation of lipophilic dyes for labelling EVs, followed by employing the labelled EVs in subsequent experiments to demonstrate sEV internalisation, is a well-established technique within the EV research field (59, 185). However, increasingly the limitations EV of labelling by lipophilic fluorescent dyes are reported: lipophilic dyes have been shown to self-aggregate to mimic sEVs and an increase in size (a "size shift") may also occur following labelling (188-190). To overcome these limitations, I purified the labelled sEVs using a 2-step purification process: first, using a continuous sucrose cushion when isolating sEVs by ultracentrifugation, and second, by size exclusion (189). I also prepared appropriate labelling dye controls using the sEV carrier control alongside labelled sEVs. Labelled sEVs and the labelled sEV dye controls were then evaluated using NTA and I did not detect nanosized particles mimicking dye aggregates in the labelled sEV carrier controls whilst the mean and mode measures of labelled sEVs remained in the sEVs size range measuring under 200 nm, and no increased size shift was noted. By incorporating size exclusion following ultracentrifugation, as an additional purification step, I ensured that no dye aggregates remained in the labelled psEV and RBCsEV preparations. Consequently, the nanosized particles visualised within cells were likely labelled psEVs and RBCsEVs, rather than dye aggregates. Although these data were reassuring the use of a lipophilic dye to label sEVs remains a limitation and alternative dyes have been shown to more reliably label EVs (190, 191). Future experiments may benefit from optimisation and utilisation of these alternative dyes.

Given the lack of previous descriptions of EV internalisation by EndoC-βH3 cells, I aimed to confirm the reproducibility of our initial findings when using EV labelling dyes by using alternative methods. To achieve this, I used immunocytochemistry to detect PLAP protein and RT-qPCR to detect the C19 miRNA cluster within psEV treated EndoC-βH3 cells, both

of which are psEV-specific markers. Both methods have been previously validated in the literature, reinforcing their credibility and reliability (59, 185). By using these psEV-specific markers to demonstrate internalisation, I leveraged inherent features of psEVs, thereby avoiding limitations associated with labelling or tagging them. Utilising these additional techniques to corroborate the confocal microscopy data with labelled sEVs provided more robust evidence of sEV internalisation by EndoC-βH3 cells.

Live-cell imaging using confocal microscopy was utilised to visualise and quantify sEV internalisation by EndoC-βH3 cells. To our knowledge, this is the first description of live-cell high-resolution microscopic imaging to both visualise and quantify intracellular sEV internalisation. While traditional flow cytometry has been extensively used in the literature by measuring and quantifying the fluorescence of the EV labelling dye to infer EV internalisation, it is typically conducted on fixed cells at different time points and does not allow for direct visualisation of EV internalisation (59). This process necessitates the effective removal of EVs from the cell surface through washing steps prior to fixation. This can be challenging because EVs may adhere to the cell surface, and without directly visualising EV uptake, there is a risk of incorrectly inferring internalisation. Our method is an advance in that it allows direct visualisation of EVs within cells, providing certainty of internalisation, followed by reliable quantification of uptake. Despite the limitations of flow cytometry, it is interesting and reassuring that the data on psEV internalisation aligns with previously published data in other cell lines (59, 192). The live-cell imaging assay I used is limited by the use of a lipophilic dye to label the psEVs, which may present challenges as discussed above. Despite this, our optimised assay ensures reliable cell labelling with minimal signal loss, employs high-resolution microscopic imaging to identify and directly visualise EV internalisation, and uses a computational image analysis pipeline to eliminate

observer bias. This assay provides a valuable platform for further research of EV uptake and improved assessments in this area. Future work should focus on employing more reliable sEV labelling dyes or enhancing this technique by using a native psEV constituent such as PLAP.

A further limitation of the live-cell psEV uptake assay is the exclusive use of psEVs from normal pregnancies for live-cell quantification of sEV uptake, without incorporating psEVs from GDM pregnancies or RBCsEVs. The logistical constraints and cost associated with performing the live-cell assay multiple times for each EV subtype, along with the computational challenges—requiring five days of continuous uninterrupted processing on a high-performance computing system to produce quantifiable data from a single assay—rendered it impractical to extend this analysis to all EV subtypes. However, I was reassured by the fact that the different sEV subtypes shared similar immunophenotypic characteristics and exhibited comparable patterns of internalisation in fixed cells. Additionally, the psEV live-cell imaging data were consistent with previously published internalisation data, all of which suggest that the other sEV types were likely to follow a similar, if not identical, time-dose relationship to that observed with normal pregnancy psEVs. This is particularly relevant for GDM psEVs, given their origin from the same biological source.

In this chapter, normal pregnancy psEVs, GDM psEVs, and RBCsEVs were successfully isolated and immunophenotypically characterised. The human β cell line, EndoC-βH3, was cultured and differentiated. Using confocal imaging and RT-qPCR for placental-specific miRNAs, it was demonstrated that normal pregnancy psEVs, GDM psEVs, and RBCsEVs are internalised by EndoC-βH3 cells. Additionally, live-cell high resolution confocal microscopic imaging combined with computational quantitative analysis revealed that psEV

uptake by EndoC-βH3 cells is dose- and time-dependent. With confirmation of psEV internalisation and a clear understanding of the uptake dynamics, I proceeded to investigate the effects of psEVs on the transcriptome, proteome, and function of EndoC-βH3 cells.

Chapter 6

Gene expression in EndoC-βH3 cells following treatment with placental small extracellular vesicles

6.1 Introduction

In Chapter 5, I isolated placental extracellular vesicles (psEVs) from human placentae of women with normal pregnancy and gestational diabetes mellitus (GDM). I then immunophenotypically characterised isolated psEVs to confirm that the isolated vesicles exhibited features consistent with psEVs. I further demonstrated that psEVs were internalised by EndoC-βH3 cells, a human pancreatic β-cell line. Having established this, I explored whether psEVs could induce genetic changes in EndoC-βH3 cells by assessing their impact on the transcriptome.

Previous studies have provided evidence that psEVs can influence the function of recipient cells by delivering bioactive cargo (187, 193, 194). These studies suggest that psEVs play an active role in cellular communication during pregnancy by delivering miRNAs and proteins that regulate gene expression in target cells. psEVs have also been reported to modulate gene expression in specific cell types, including endothelial and endometrial cells (59, 195). A recent study demonstrated that miR-320b, which is upregulated in human GDM psEVs compared to normal pregnancy psEVs, decreased glucose-stimulated insulin secretion (GSIS) and increased apoptosis when miR-320b was overexpressed in mouse islets (66). Given these findings, I hypothesised that psEVs might similarly affect the transcriptome of EndoC-βH3 cells, potentially influencing their function during pregnancy.

I aimed to treat EndoC-βH3 cells with psEVs and then analyse the transcriptomic changes by performing RNA sequencing (RNA-seq). This approach would allow me to comprehensively assess the extent to which psEVs influence gene expression in these cells, potentially revealing novel insights into pancreatic-placental psEV-mediated signalling pathways in pregnancy.

Initially, I treated EndoC-βH3 cells with normal pregnancy psEVs only and appropriate controls. This first RNA-seq experiment was designed as a pilot study to inform future sequencing experiments in several key aspects. Firstly, it would allow me to determine the effect size of psEVs on gene expression, enabling accurate sample size calculations for subsequent experiments. Additionally, I aimed to identify a subset of differentially expressed genes (DEGs) with the most significant positive and negative fold changes. Utilising reverse transcription-quantitative polymerase chain reaction (RT-qPCR), this subset of genes would be used to optimise the dose of psEV treatments, and the time point to isolate RNA following psEV treatments. This would provide the optimised conditions for capturing the maximal effects of psEVs on gene expression in EndoC-βH3 cells. Once these parameters were optimised, I planned to repeat the RNA-seq experiment, incorporating GDM-derived psEVs and increasing the sample size, to fully characterise the impact of psEVs on the EndoC-βH3 transcriptome.

6.1.1 Aims

The aims of this chapter were to:

1. Extract high-quality RNA for sequencing from EndoC-βH3 cells treated with normal pregnancy psEVs.
2. Assess whether normal pregnancy psEVs alter the transcriptome of EndoC-βH3 cells.
3. Identify key genes that are differentially expressed in EndoC-βH3 cells following treatment with normal pregnancy psEVs.
4. Determine the pathways significantly enriched in EndoC-βH3 cells after treatment with normal pregnancy psEVs.
5. Optimise the time point at which to isolate RNA following psEV treatments and the dose of psEVs to maximise their effects on gene expression in EndoC-βH3 cells.

6.2 Materials and methods

6.2.1 Treatments of EndoC-βH3 cells with placental small extracellular vesicles

I used an initial small extracellular vesicle (sEV) treatment dose of 40 μg/mL, based the findings from the live-cell psEV uptake assay (Chapter 5) that showed that this dose of psEVs provided the greatest psEV volume internalised by EndoC-βH3 cells at the final timepoint in the experiment. I postulated that using the dose, which exhibited the greatest psEV uptake by EndoC-βH3 cells, would provide the likeliest chance to view a large treatment effect with psEVs.

For RNA collection following psEV cell treatments, I chose a time point of 18 hours, which differs from the more common collection time of within 6 hours, typically used to capture RNA effects seen in cells following an intervention or treatment (196). My rationale was that psEVs contain substantial amounts of RNA, and collecting cells too early might lead to the detection of RNA delivered by the psEVs rather than observing changes conferred by psEVs on the native transcriptome of EndoC-βH3 cells. From the live-cell uptake assay, I observed that it was only by 12 hours that the internalisation of normal pregnancy psEVs at the 40 μg/mL dose began to plateau. Therefore, I chose the 18-hour time point to allow for an additional 6 hours post-maximal psEV internalisation. This would allow for RNA from psEVs to be degraded by the cell and ensure that the genetic changes I would sequence were a result of psEV-mediated effects on the endogenous transcriptome of the cells, rather than passive RNA transfer from psEVs.

I acknowledged that this extended time frame could result in observing smaller fold changes in gene expression; however, I planned to optimise these outcomes through future dose-response and time-course experiments. In addition, in future RNA-seq experiments, I would

also consider sequencing the psEVs themselves, alongside psEV-treated cells, as an additional control. This would help to ensure that the DEGs identified in psEV-treated cells were due to the effect of psEVs on the cell transcriptome, and not simply a reflection of high levels of RNA delivered by the psEVs.

Differentiated EndoC-βH3 cells were seeded into 6 cm culture dishes at 3 x 10^6 cells per dish and treated with 40 µg/mL of normal pregnancy psEVs, red blood cell small extracellular vesicles (RBCsEVs), and the sEV carrier control (n = 4 per treatment group). RBCsEVs and the sEV carrier were included to control for the effects of general EV constituents (RBCsEVs) and the sEV carrier medium (sEV carrier control) as described in Chapter 5. After 18 hours cells were collected for RNA isolation as described in Chapter 2.

6.2.2 RNA isolation from EndoC-βH3 cells, quantification, and quality assessment

The methods for isolating RNA from EndoC-βH3 cells, along with the use of the NanoDrop™ 8000 spectrophotometer (Thermo Fisher Scientific, cat. no. ND-8000-GL) to assess RNA purity ratios and the Qubit® 2.0 fluorometer (Thermo Fisher Scientific, cat. no. Q32866) with the Qubit™ RNA HS Assay Kit (Thermo Fisher Scientific, cat. no. Q32852) to measure RNA concentration, have been previously detailed in Chapter 2.

6.2.3 Measurement of RNA integrity number values

RNA integrity number (RIN) values were measured using the Agilent Technologies 4200 TapeStation System (Agilent, cat. no. G2991BA) which included use of High Sensitivity RNA ScreenTape (Agilent, cat. no. 5067-5579), sample buffer (Agilent, cat. no. 5067-5580), and ladder (Agilent, cat. no. 5067-5581). One µL of sample buffer was added to 2 µL of RNA for each sample. In addition, 1 µL of sample buffer was added to 2 µL of the High

Sensitivity RNA ladder. The RNA samples and ladder were vortexed for 1 minute using the IKA MS3 vortexer (IKA, cat. no. 0003617000) at 2000 rpm and centrifuged using a Prism™ Mini Centrifuge (Prism, cat. no. AA9760) for 1 minute. The samples and ladder were heated to 72°C for 3 minutes, cooled on ice for 2 minutes, and centrifuged for 1 minute. The processed samples, ladder and a High Sensitivity RNA ScreenTape were loaded into the TapeStation instrument and RIN values measured. The TapeStation Analysis Software v3.2 was used for sample analysis.

6.2.4 RNA sequencing of EndoC-βH3 cell treated with placental small extracellular vesicles

Isolated RNA from EndoC-βH3 cells treated with normal pregnancy psEVs (n = 4), RBCsEVs (n = 4), and the sEV carrier controls (n = 4), were submitted to the Oxford Genomics Centre (OGC) at the Centre for Human Genetics (CHG) for high-throughput sequencing. Polyadenylated (polyA) enriched RNA was sequenced using the Illumina NovaSeq 6000 platform, employing 150 base pairs (bp) paired-end reads. Library preparation was performed by the OGC, with an output of 25 million reads per sample, ensuring comprehensive coverage and high sensitivity for transcript detection. This platform enables robust analysis of gene expression by providing deep sequencing data with minimal biases.

6.2.5 Bioinformatic analysis of RNA sequencing data

Bioinformatics analysis was performed in collaboration with Dr Avigail Taylor from the Bioinformatics Core at the CHG.

The analysis was conducted using Python (v3.10), following a standard pipeline for RNA-seq data processing. This included quality control checks, alignment of reads to the reference genome, quantification of gene expression, and differential expression analysis. Specific tools used in the pipeline included FastQC for quality control, HISAT2 for alignment, featureCounts for quantification, and DESeq2 for differential expression analysis. Identified genes were mapped to the Ensembl database for accurate gene annotation. Dr Avigail Taylor performed all coding and data processing operations, ensuring the integrity and accuracy of the bioinformatics workflow.

Principal Component Analysis (PCA) was performed to explore the variance across samples. To determine DEGs, gene expression in EndoC-βH3 cells treated with normal pregnancy EVs were compared to those in cells treated with the controls (RBCsEVs and the sEV carrier control). A false discovery rate (FDR) threshold less than 0.05 was used to determine significance and the Benjamini-Hochberg method was used to correct for multiple comparisons. Genes in the normal pregnancy-treated cells that were differentially expressed relative to both the sEV carrier control and RBCsEVs were deemed significant and subsequently selected for detailed functional and pathway analysis. A volcano plot of log2 fold changes against negative log10 FDR values was generated to visualise differential expression (an FDR < 0.05 = -log 10 FDR). Hierarchical clustering was conducted using the SciPy library in Python to group samples based on gene expression patterns. Data generated was plotted in Prism 10 to generate the PCA plot, volcano plot, and heatmaps.

6.2.6 Pathway analysis

I performed a pathway analysis of psEV induced DEGs, identified from the RNA-seq experiment, to detect enriched biological pathways. This analysis focused on determining

which pathways were overrepresented in the DEGs, providing insight into the functional implications of the observed gene expression changes. The group of genes identified as significant (differentially expressed in the normal pregnancy psEV group relative to both controls) were analysed using the PANTHER Classification System (version 17.0) (197) to identify enriched pathways for enriched pathways using overrepresentation analysis in the Gene Ontology (GO) Biological Process and Reactome databases. A Fisher's Exact Test was performed, and the Benjamini-Hochberg method was applied to correct for multiple comparisons, with an FDR threshold of < 0.05 used to define statistical significance.

6.2.7 Reverse transcription-quantitative polymerase chain reaction to validate RNA sequencing and optimise conditions for future experiments

For all repeat cell treatment experiments, including the validation, time to RNA isolation, and dose optimisation, cells were collected, RNA was extracted, quantified, and then converted to cDNA as described in Chapter 2. The RT-qPCR protocol and methods for data analysis are also included in Chapter 2.

Six genes were chosen for the validation and optimisation experiments. Table 6.1 details the primers used for RT-qPCR to validate the sequencing data and optimise the psEV dose and time to RNA isolation. For all RT-qPCR data analysis, fold changes of the genes of interest were calculated using TATA-Box Binding Protein (*TBP*) as the endogenous control/housekeeping gene. *TBP* was validated as a stable housekeeping gene in the original study that characterised EndoC-βH3 cells. The genes of interest included Cholinergic Receptor Nicotinic Alpha 3 Subunit (*CHRNA3*), Claudin 15 (*CLDN15*), Crystallin Beta A2 (*CRYBA2*), GLI Family Zinc Finger 3 (*GLI3*), Insulin-Like Growth Factor 1 Receptor (*IGF1R*), and Insulin Receptor (*INSR*).

Prior to initiating the validation and optimisation RT-qPCR experiments, a dilution series was performed for each primer using RT-qPCR on RNA isolated from untreated, differentiated EndoC-βH3 cells. This experiment was conducted to determine the optimal RNA concentration required to achieve a Cq value within the 20–30 range for each primer. The identified RNA concentration for each primer was then applied in subsequent RT-qPCR studies.

Table 6.1: Primers used in reverse transcription-quantitative polymerase chain reaction studies for RNA detection.

Assay type	Manufacturer	Target	Identifier
TaqMan™ gene expression assay	Applied Biosystems	*CHRNA3*	Hs01088199_m1
		CLDN15	Hs00204982_m1
		CRYBA2	Hs00193234_m1
		GLI3	Hs00609233_m1
		IGF1R	Hs00609566_m1
		INSR	Hs00961557_m1
		TBP	Hs00427620_m1

6.2.7.1 Validation of RNA sequencing

Validation RT-qPCR studies were performed on three sample sets. The first set consisted of the same samples submitted for RNA-seq (n=4 per treatment condition). The second and third sets were from two independent replicate experiments. In these experiments, the cell treatments were repeated using the same psEV dose and treatment duration as in the original experiment, but with different biological samples (n = 8 per treatment condition in each experiment).

6.2.7.2 Optimisation of placental small extracellular vesicles dose and time-point for RNA isolation

To optimise the ideal time point for RNA isolation, cells were treated with 40 µg/mL of normal pregnancy psEVs, RBCsEVs, and the sEV carrier control (n = 8 per condition), with samples collected at 4, 8, and 18 hours.

For dose optimisation, cells were treated with 5 µg/mL, 10 µg/mL, 20 µg/mL, or 40 µg/mL of psEVs and RBCsEVs, along with the sEV carrier control (n = 8 per condition), and samples were collected after 8 hours of treatment.

6.3 Results

6.3.1 RNA ratios, RNA quantification, and RNA integrity number values of extracted RNA submitted for sequencing

Analysis of RNA concentration, purity ratios, and RIN values demonstrated that the isolated RNA had a high concentration and excellent purity, with 260/280 and 260/230 ratios approximating to two for all samples. The RNA was also of high quality, as RIN values exceeded nine, indicating its suitability for reliable downstream applications such as RNA sequencing (Table 6.2 and Figure 6.1).

Table 6.2: RNA concentration and purity ratios (260/280 and 260/230) isolated from EndoC-βH3 cells following cell treatments.

	RNA Concentration (ng/µL)	260/280	260/230
NP psEVs 1	76	2.04	2.09
NP psEVs 2	111	2.06	1.91
NP psEVs 3	86.4	2.08	2.08
NP psEVs 4	80	2.07	2.02
RBCsEV 1	64	2.07	2.12
RBCsEV 2	71.8	2.08	1.94
RBCsEV 3	50.8	2.08	2.04
RBCsEV 4	88.6	2.08	2.07
sEV Carrier 1	59.4	2.07	1.94
sEV Carrier 2	65.4	2.07	2.1
sEV Carrier 3	75.4	2.1	2.08
sEV Carrier 4	46.6	2.14	1.92

*psEV – normal pregnancy placental small extracellular vesicle, RBCsEV – red blood cell small extracellular vesicle, sEV – small extracellular vesicle.

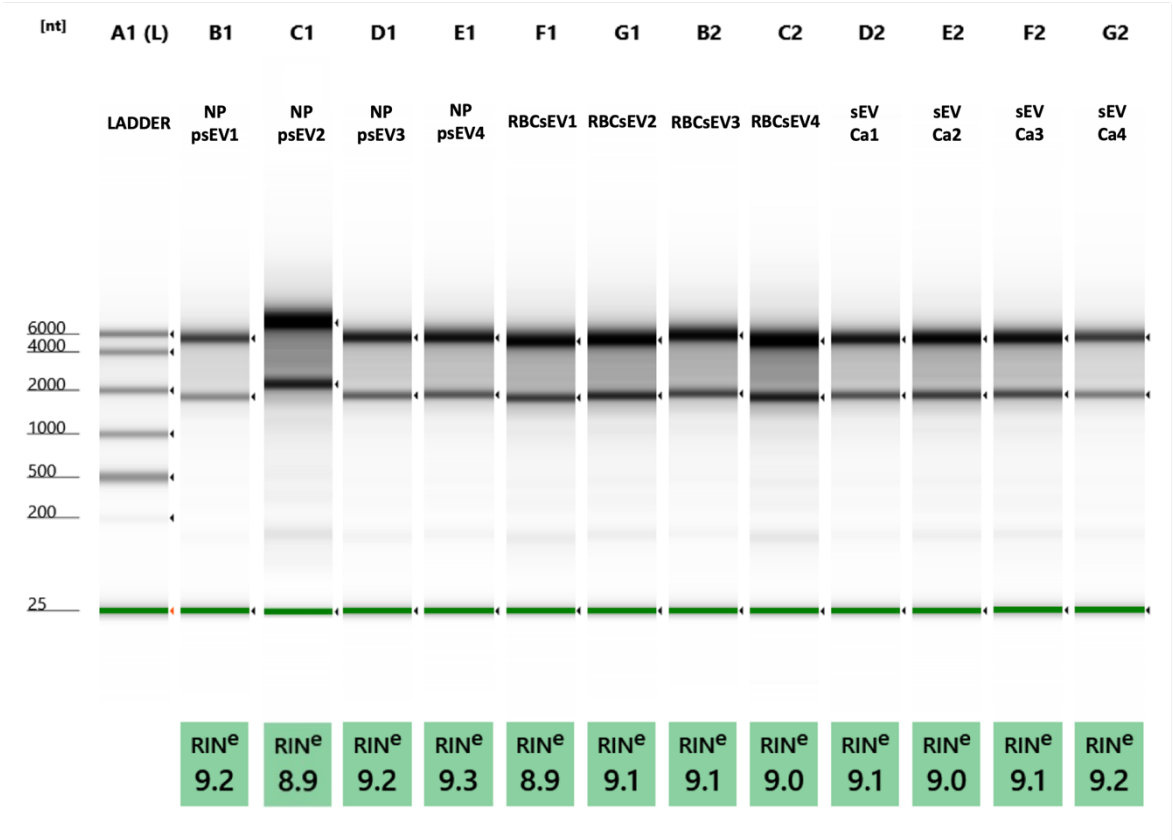

Figure 6.1. RNA integrity numbers (RIN) of RNA isolated from EndoC-βH3 cells following cell treatments.

*NP psEV – normal pregnancy placental small extracellular vesicle, RBCsEV – red blood cell small extracellular vesicle, sEV Ca– small extracellular vesicle carrier control.

6.3.2 RNA sequencing of EndoC-βH3 cells treated with placental small extracellular vesicles

6.3.2.1 Principal component analysis

Principal component analysis of the treatment groups revealed that samples within each group (normal pregnancy psEVs, RBCsEVs, and sEV carrier control) clustered closely together, demonstrating consistency within the groups. Additionally, there were distinct separations between the clusters of each respective group, indicating clear differences in their underlying genetic profiles (Figure 6.2).

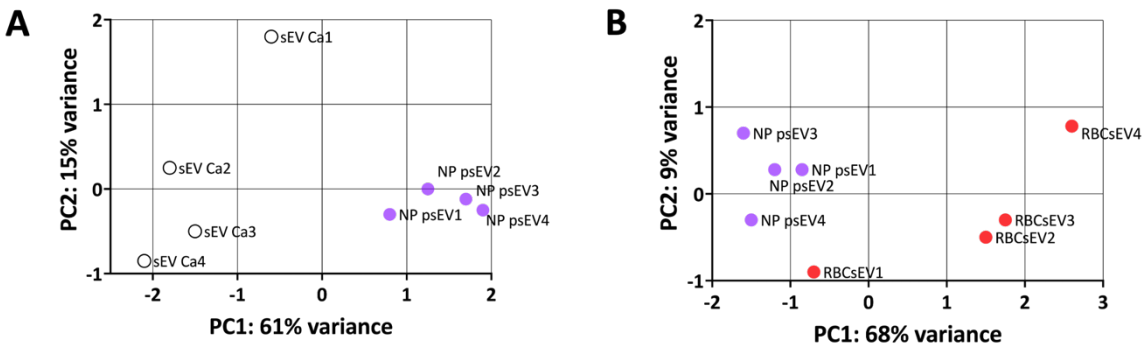

Figure 6.2. A. Principal component analysis comparing normal pregnancy placental small extracellular vesicles (NP psEVs) to the **A.** small extracellular vesicle carrier control (sEV Ca) and **B.** red blood cell small extracellular vesicles (RBCsEVs).

6.3.2.2 Differentially-expressed genes

Gene expression in normal pregnancy psEV-treated cells was compared to gene expression in both sEV carrier control-treated cells and RBCsEV-treated cells. The comparison between normal pregnancy psEV-treated cells and sEV carrier control-treated cells revealed 1,511 DEGs, while the comparison between psEV-treated cells and RBCsEV-treated cells identified 557 DEGs. To isolate DEGs specifically associated with psEVs, only genes differentially expressed relative to both controls (RBCsEVs and sEV carrier control) were considered significant, resulting in 348 DEGs (FDR < 0.05). This is illustrated in Figure 6.3.

Of these 348 DEGs, 138 genes exhibited a log2 fold change (FC) more than ± 0.2. Among these, *CLDN15* (log2 FC = 0.44, FDR = 0.015) , *LMO3* (log2 FC = 0.41, FDR = 0.003), and *GLI3* (log2 FC = 0.4, FDR = 0.014) showed the largest upregulation, while *PERCC1* (log2 FC = -0.58, FDR = 0.001), *CRYBA2* (log2 FC = -0.51, FDR = 0.000002), and *CHRNA3* (log2 FC = -0.5, FDR = 0.005) exhibited the greatest downregulation.

To understand the magnitude of difference in gene expression between normal pregnancy psEVs compared to both controls, a volcano plot was created to illustrate the results of the DEG analysis (Figure 6.4). Hierarchical clustering analysis of the 20 most upregulated and downregulated genes was also performed and is presented in Figure 6.5.

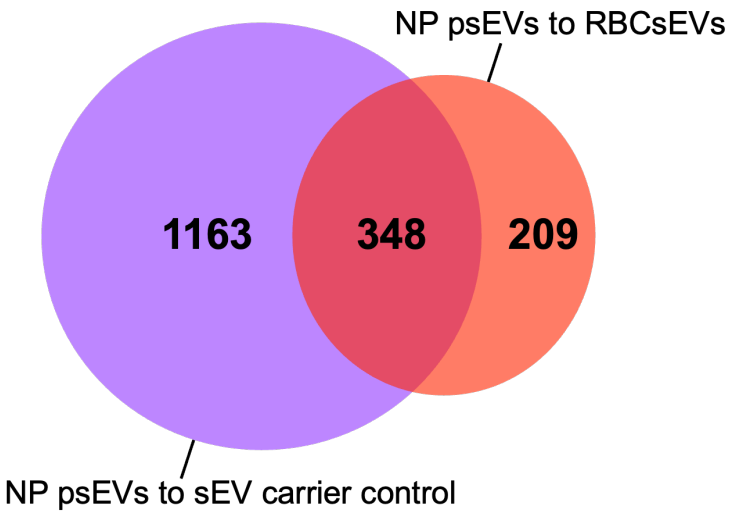

Figure 6.3. Venn diagram illustrating the number of differentially expressed genes when comparing normal pregnancy placental small extracellular vesicles (NP psEVs) to cells treated with either the small extracellular vesicle (sEV) carrier control or red blood cell extracellular vesicles (RBCsEVs). The intersection, where genes were differentially expressed relative to both controls (n = 348), was considered significant and prioritised for detailed downstream analysis, including functional annotation and pathway enrichment.

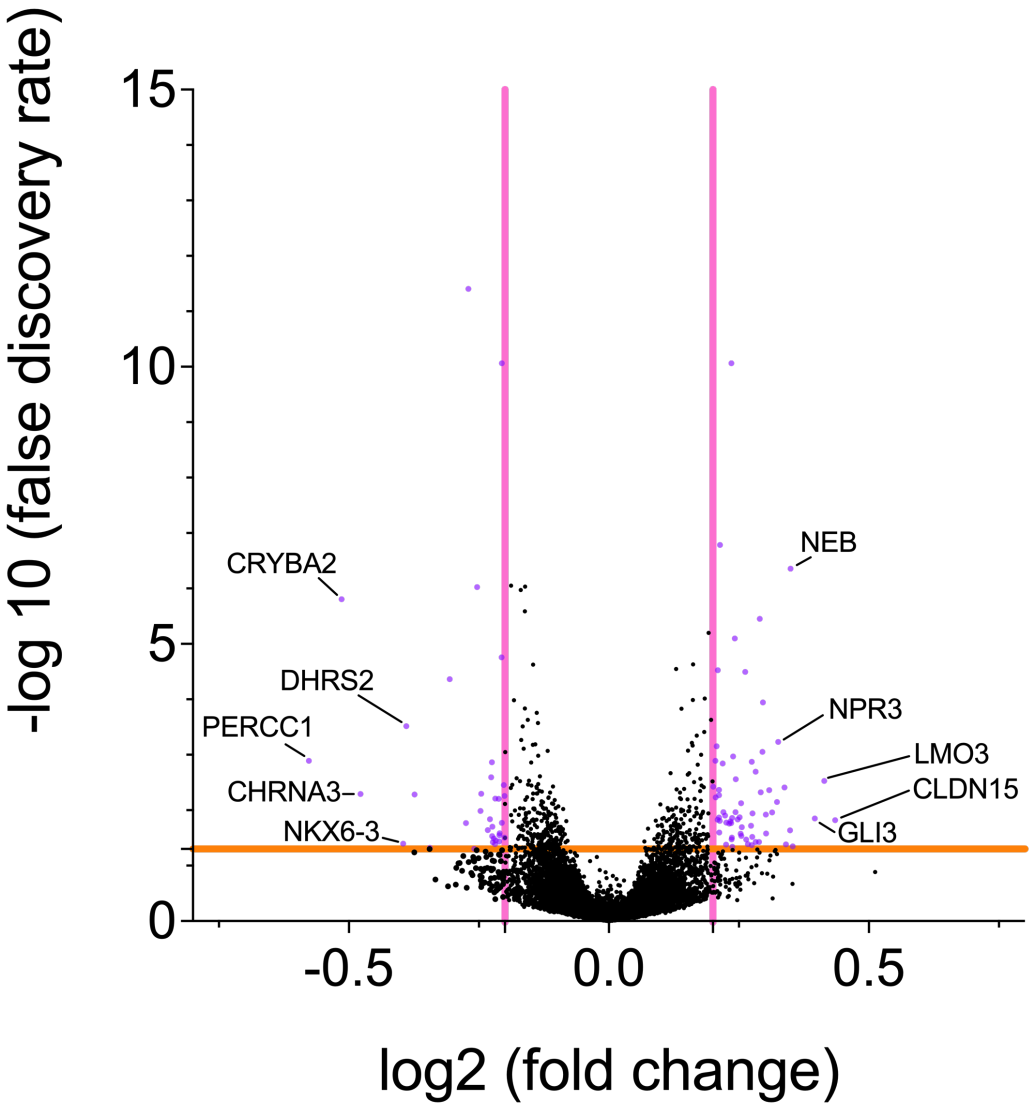

Figure 6.4. Volcano plot showing differentially-expressed genes when comparing EndoC-βH3 cells treated with normal pregnancy placental small extracellular vesicles to cells treated with treated with controls (small extracellular vesicle carrier control and red blood cell extracellular vesicles). The vertical axis displays statistical significance (−log10 FDR), while the horizontal axis represents the magnitude of change (log2 fold change) for each gene. Significance was determined using an FDR < 0.05, where FDR < 0.05 = -log 10 FDR > 1.3 (marked by the horizontal line coloured in orange). Genes that met both the FDR threshold and a log2 fold change ± 0.2 (marked by the vertical lines coloured pink) are highlighted (purple) and significant differentially expressed genes with the largest positive and negative log2 fold changes are labelled.

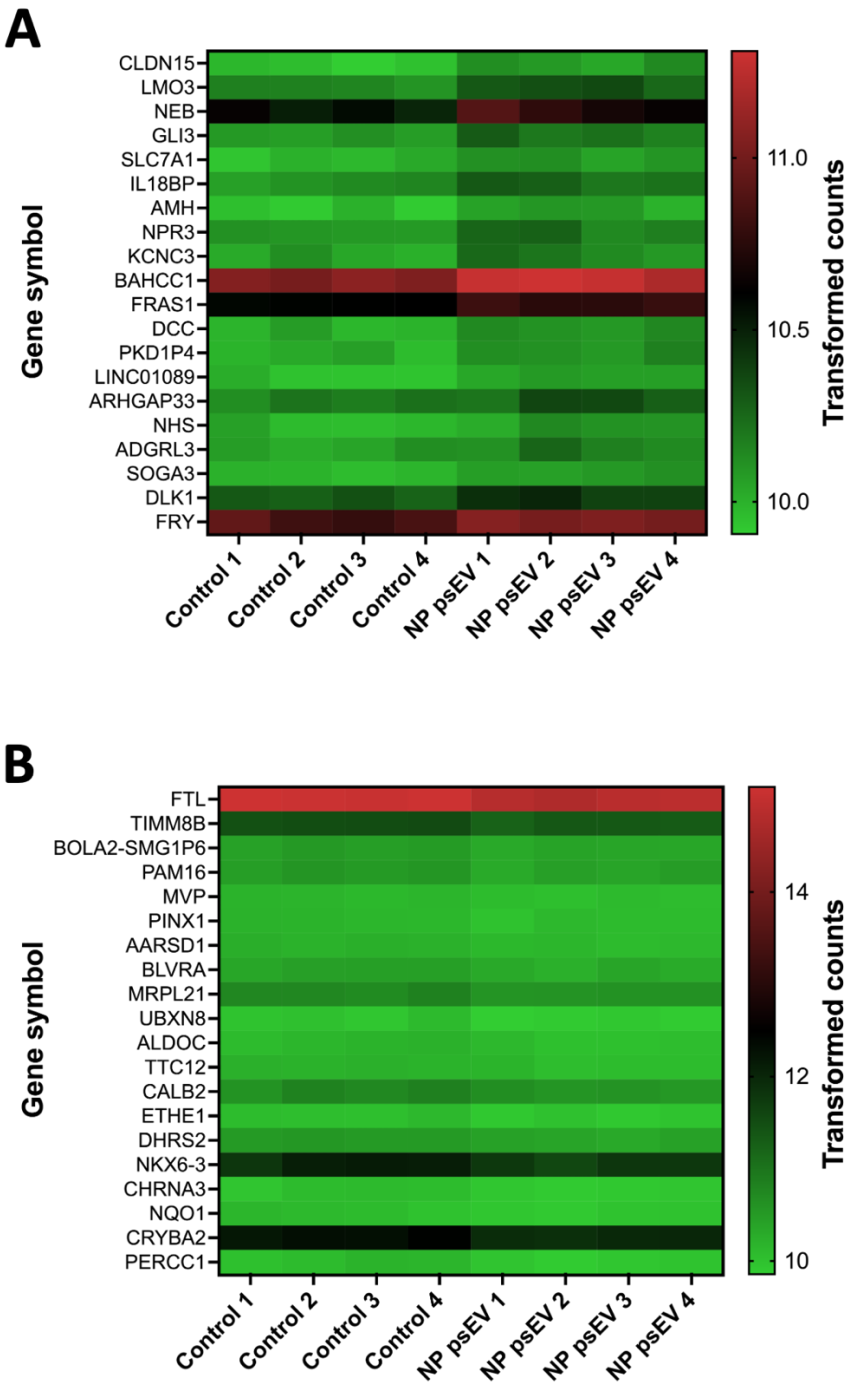

Figure 6.5. Hierarchical clustering of differentially expressed genes (DEGs) in cells treated with normal pregnancy placental small extracellular vesicles compared to controls (small extracellular vesicle carrier control and red blood cell small extracellular vesicles). Two heat maps are presented, showing the top 20 most DEGs. **A.** Heat map of the 20 most upregulated genes and **B.** heat map of the 20 most downregulated genes. Gene expression is

visualised as relative fold changes, with hierarchical clustering applied to highlight patterns of gene expression across treatment groups. Warmer colours (red) represent higher expression, while cooler colours (green) indicate lower expression.

6.3.3 Pathway analysis of differentially expressed genes

An overrepresentation analysis was performed on the 348 DEGs to identify enriched pathways in the GO Biological Processes and Reactome databases. The analysis identified key pathways that were significantly enriched, highlighting molecular pathways altered by normal pregnancy psEVs.

The results indicate enrichment in pathways related to metabolism and cellular processes. Specifically, within the GO Biological Processes, prominent pathways included those involved in protein processing, cellular metabolism, and both cell and anatomical development, highlighting the potential influence of normal pregnancy psEVs on these critical biological functions. Similarly, Reactome analysis revealed enrichment in pathways associated with the cell cycle and mitosis, as well as metabolic and developmental processes, aligning with the GO results (Figure 6.6). Collectively, these findings indicate that psEVs modulate gene expression to regulate key intracellular processes, potentially impacting β-cell function and biology.

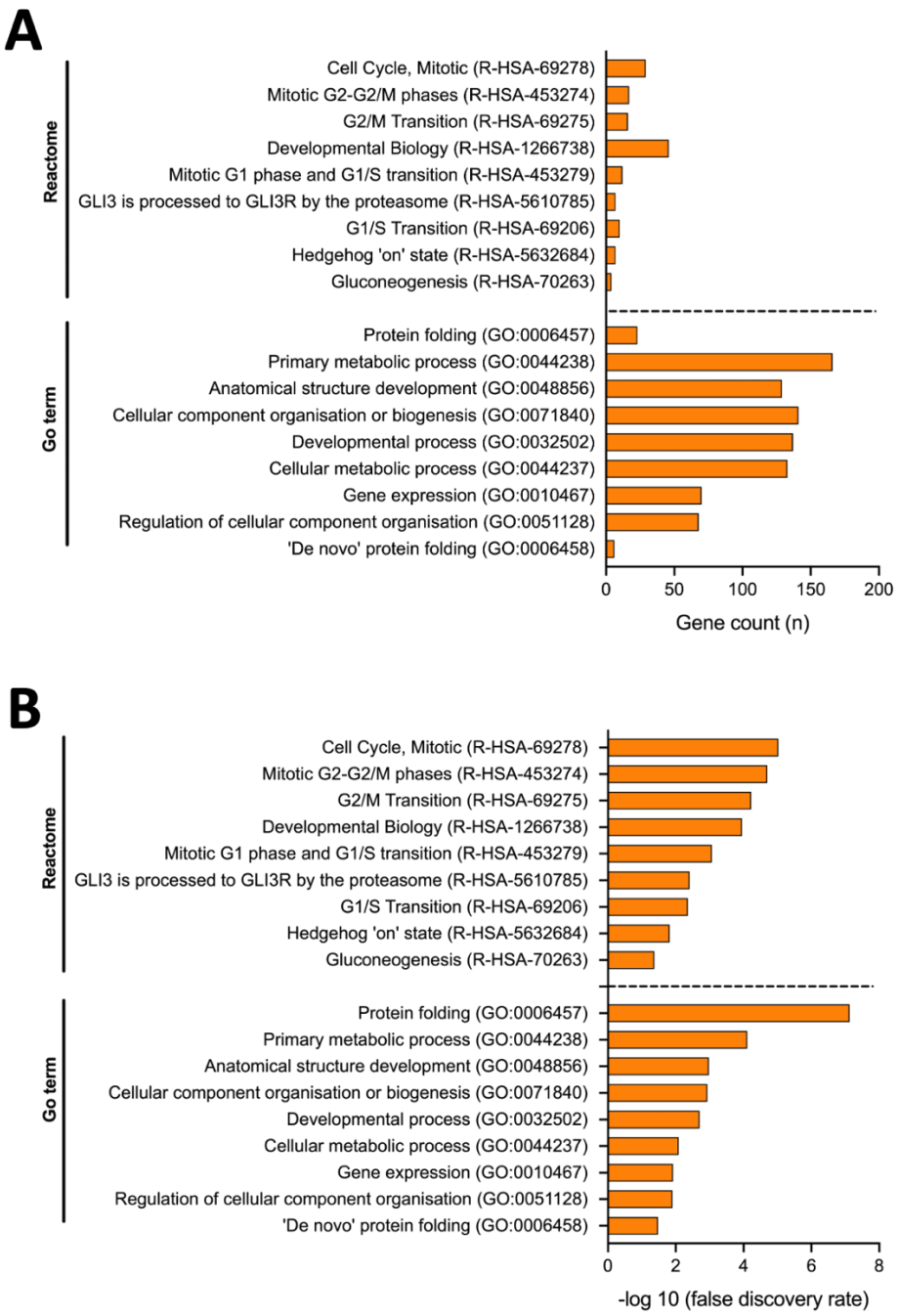

Figure 6.6. Pathway analysis of 348 differentially expressed genes (DEGs) was performed using the Gene Ontology (GO) Biological Processes and Reactome databases. Pathways of interest from each database are presented. **A.** The -log10 false discovery rate (FDR) for each enriched pathway is displayed and **B.** the number of genes (n) involved in each enriched pathway is shown. FDR < 0.05.

6.3.4 Validation of key differentially expressed genes by reverse transcription-quantitative polymerase chain reaction

I selected six genes to validate the results of the RNA-seq experiment. This included two genes with the highest upregulation (*CLDN15* and *GLI3*), two with the highest downregulation (*CHRNA3* and *CRYBA2*), and two with minimal upregulation: *IGF1R* (log2 FC = 0.21, FDR = 0.0000002) and *INSR* (log2 FC = 0.18, FDR = 0.0004).

6.3.4.1 Dilution series to optimise RNA concentration required for each primer

Prior to performing the validation RT-qPCR studies, I conducted an RNA dilution study to determine the optimal RNA concentration for each primer using RNA isolated from untreated, differentiated EndoC-βH3 cells.

Starting with an initial RNA concentration of 3.5 ng/µL, I tested undiluted RNA alongside serial dilutions of 1:2, 1:4, 1:5, 1:8, 1:10, and 1:100 for all primers. For *TBP*, *CRYBA2*, *GLI3*, *IGF1R*, and *INSR* a 1:2 dilution (1.75 ng/µL) produced a Cq value between 20 – 30 (Figure 6.7A). However, this was not the case for *CHRNA3* or *CLDN15*, where undiluted RNA resulted in Cq values approaching 30, and the 1:2 dilution produced Cq values above 30 (Figure 6.7A). To optimise these two primers, I repeated the experiment with a starting RNA concentration of 12.25 ng/µL, using the same serial dilutions. Both the undiluted RNA and the 1:2 dilution (6.125 ng/µL) yielded Cq values between 20 and 30 (Figure 6.7B).

Based on these results, for all subsequent RT-qPCR experiments, I used 1.75 ng/µL of RNA per well for the *CRYBA2*, *GLI3*, *IGF1R* and *INSR* primers, and 12.25 ng/µL of RNA per well for the *CHRNA3* and *CLDN15* primers. Since *TBP* was measured in the same well as

the primers of interest, the concentration used to measure *TBP* depended on the amount of RNA used for the primers of interest.

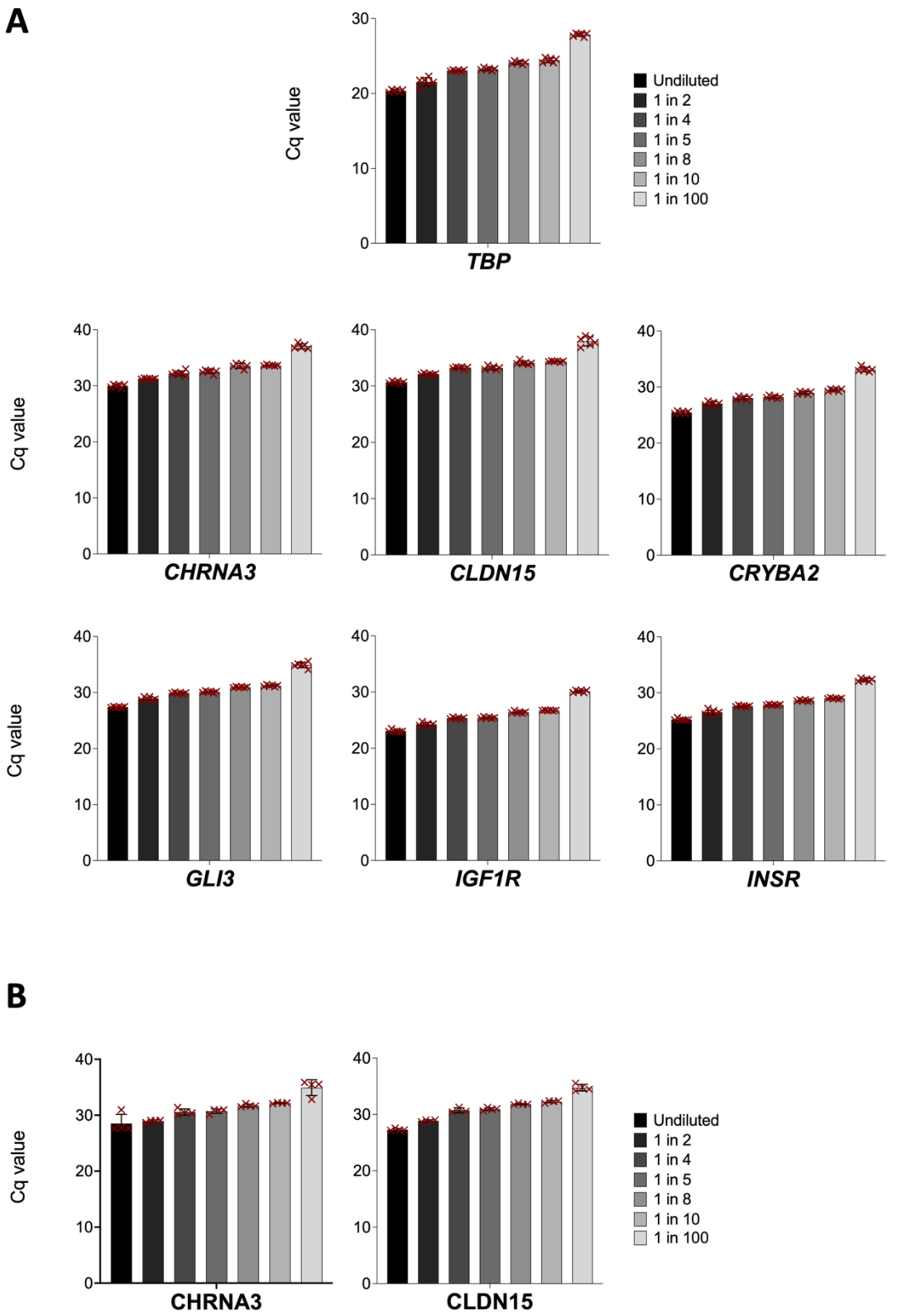

Figure 6.7. Dilution experiment to determine the optimal RNA concentration for each primer, aiming to achieve a Cq value between 20 and 30. Undiluted RNA samples were serially diluted as detailed in the legend. The colours in the legend correspond to the bars in

the figure representing each respective dilution. Individual Cq values for each dilution are displayed. A. RNA concentration of 3.5 ng/µL was tested for all primers. B. RNA concentration of 12.25 ng/µL was tested for primers to *CHRNA3* and *CLDN15*.

6.3.4.1 RNA sequencing validation

Validation of the RNA sequencing results was performed using RT-qPCR on the same samples submitted for RNA sequencing, as well as on new samples generated from two independent experiments. These new experiments followed the same experimental design as the original experiment, including the time of RNA isolation and psEV dose, but were conducted using a separate batch of differentiated EndoC-βH3 cells and biological samples.

For the six selected genes, the direction of gene expression regulation (up or down) was consistent with the RNA sequencing data. For each gene, the log2 fold changes and standard error of the mean are presented in Figure 6.8. These data validated the RNA sequencing results by demonstrating that the changes in gene expression was consistent when using a different technique on the original sample set, as well as in two further replicate independent experiments (Figure 6.8).

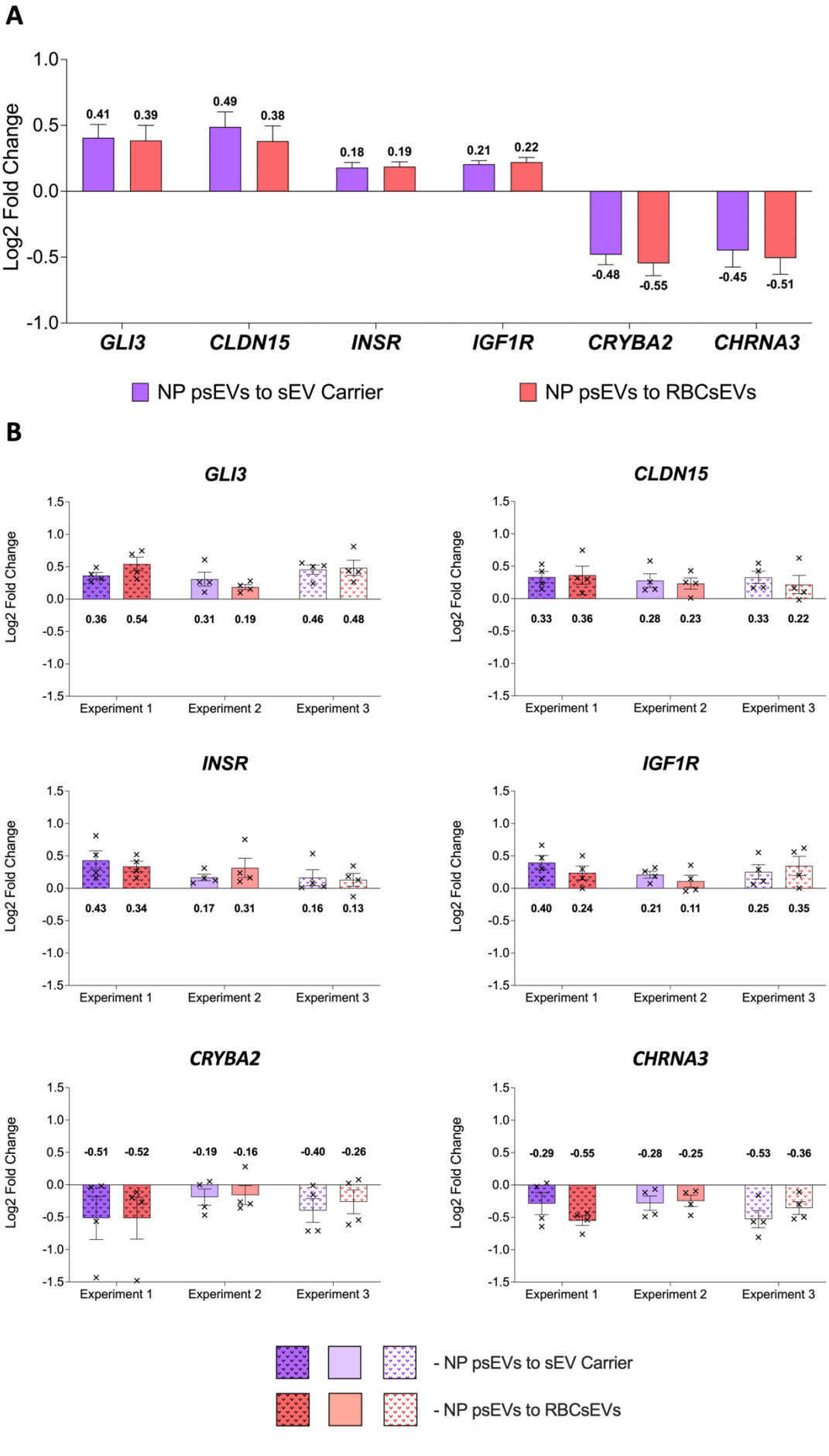
A
Log2 Fold Change
1.0
0.5
0.0
-0.5
-1.0
0.41
0.39
0.49
0.38
0.18
0.19
0.21
0.22
-0.48
-0.55
-0.45
-0.51
GLI3
CLDN15
INSR
IGF1R
CRYBA2
CHRNA3
NP psEVs to sEV Carrier
NP psEVs to RBCsEVs
B
GLI3
0.36 0.54 0.31 0.19 0.46 0.48
CLDN15
0.33 0.36 0.28 0.23 0.33 0.22
INSR
0.43 0.34 0.17 0.31 0.16 0.13
IGF1R
0.40 0.24 0.21 0.11 0.25 0.35
CRYBA2
-0.51 -0.52 -0.19 -0.16 -0.40 -0.26
CHRNA3
-0.29 -0.55 -0.28 -0.25 -0.53 -0.36
Experiment 1
Experiment 2
Experiment 3
- NP psEVs to sEV Carrier
- NP psEVs to RBCsEVs

Figure 6.8. A. RNA sequencing results for the six genes chosen for validation. B. Reverse transcription-quantitative polymerase chain reaction (RT-qPCR) studies validating the RNA sequencing experiment. Experiment 1 shows the RT-qPCR results from the same set of samples submitted for RNA sequencing. Experiments 2 and 3 display RT-qPCR results from two independent experiments, each conducted using a separate batch of differentiated EndoC-βH3 cells and different biological replicates. For each gene assayed, normal pregnancy placental small extracellular vesicles (NP psEVs) were compared to both the small extracellular vesicle (sEV) carrier and the red blood cell small extracellular vesicle (RBCsEV) control. The calculated mean log2 fold changes and the individual data points are displayed.

6.3.5 Optimisation of the dose of placental small extracellular vesicle treatments and time point for RNA isolation

RNA was isolated at three time points: 4 hours, 8 hours, and 18 hours, and gene expression was analysed. The 8-hour time point produced the greatest fold changes in gene expression, making it the optimal time for RNA isolation to capture the most significant changes in gene expression. Notably, at the 8-hour time point, the direction of gene expression changes for *CLDN15*, *CHRNA3*, and *CRYBA2* was opposite to the results observed at the 18-hour time point or the RNA-seq data, where RNA was also isolated at 18 hours (Figure 6.9). For each gene, the log2 fold changes and standard error of the mean are presented in Figure 6.9.

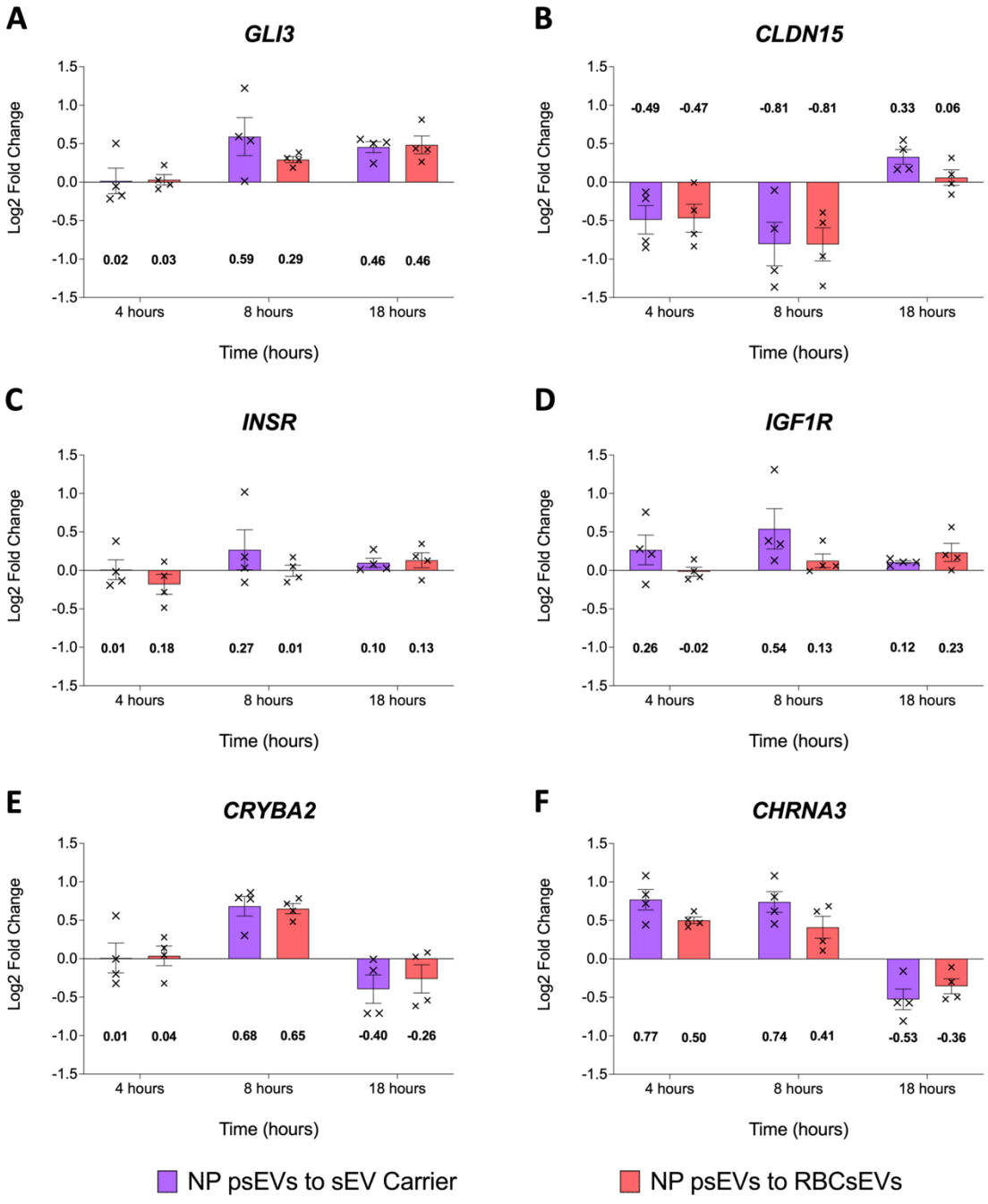

Figure 6.9. Reverse transcription-quantitative polymerase chain reaction (RT-qPCR) was used to optimise RNA isolation time points following the treatment of EndoC-βH3 cells with placental small extracellular vesicles (psEV). Six genes that were upregulated or downregulated in the RNA sequencing experiment were analysed. For each gene assayed, normal pregnancy placental small extracellular vesicles (NP psEVs) were compared to both the small extracellular vesicle (sEV) carrier and the red blood cell small extracellular vesicle

(RBCsEV) control. Calculated mean log2 fold changes and the individual data points are displayed.

6.3.6 Optimisation of the dose of placental small extracellular vesicle treatments

With the 8-hour time point established as optimal for RNA isolation, I proceeded to dose optimisation experiments. A range of psEV concentrations were tested (5 µg/mL, 10µg/mL, 20 µg/mL, and 40µg/mL), and I found that 40 µg/mL produced the greatest fold changes in gene expression across almost all of the six genes analysed, establishing it as the most effective dose for further experiments (Figure 6.10). For each gene, the log2 fold changes and standard error of the mean are presented in Figure 6.10.

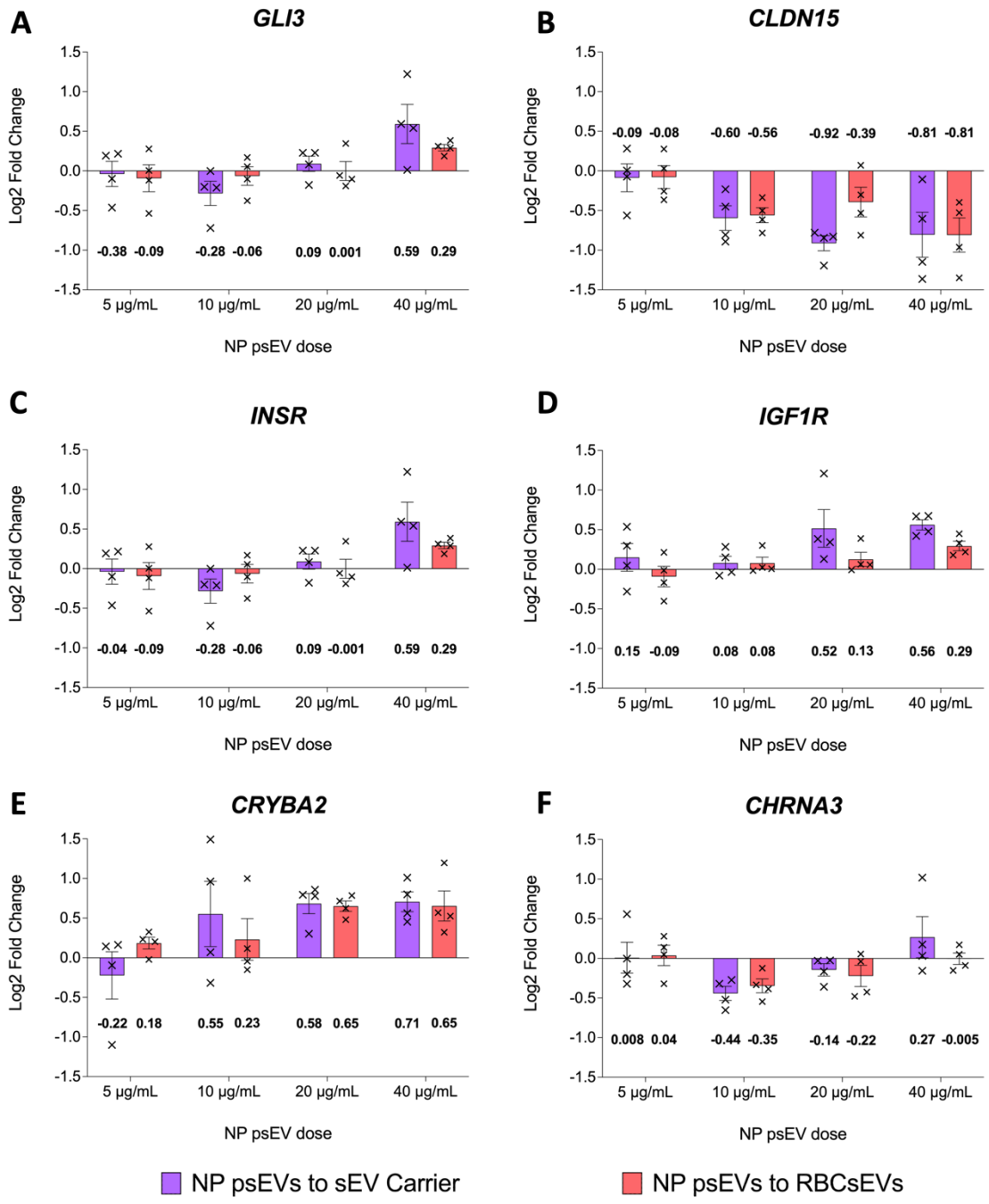

Figure 6.10. Reverse transcription-quantitative polymerase chain reaction (RT-qPCR) was used to optimise the dose of normal pregnancy placental small extracellular vesicles (NP psEVs) to use when treating EndoC-βH3 cells. Six genes that were upregulated or downregulated in the RNA sequencing experiment were analysed. For each gene assayed, normal pregnancy placental small extracellular vesicles (NP psEVs) were compared to both the small extracellular vesicle (sEV) carrier and the red blood cell small extracellular vesicle

(RBCsEV) control. Calculated mean log2 fold changes and the individual data points are displayed.

6.4 Discussion

In this chapter I demonstrated that psEVs induce transcriptomic changes in EndoC-βH3 cells, enriching biological pathways related to the cell cycle, mitosis, development, and metabolism. These transcriptomic alterations were confirmed through RNA sequencing and validated by RT-qPCR. Furthermore, I optimised the psEV dose and determined the optimal time point for RNA isolation, ensuring that future experiments could capture the largest and most consistent fold changes in gene expression following psEV treatments.

The work presented in this chapter is the first study, to my knowledge, to show that psEVs can alter the transcriptome of pancreatic β cells. Previous research has primarily focused on the role of psEVs in regulating insulin secretion (85), but no prior studies have explored how psEVs directly modulate gene expression in human pancreatic β cells. I identified several enriched pathways, suggesting that the altered genes were acting together to perform distinct biological functions. Given the increased demand for β-cell functional capacity during pregnancy, it was notable that the enriched pathways related to the cell cycle, mitosis, development, and metabolism. While these findings were compelling, it was essential to further characterise the specific functional effects of the DEGs altered by psEVs in β cells. This would require first pinpointing key genetic targets within the enriched pathways to investigate their direct impact on cell proliferation, insulin synthesis, and secretion, with the aim of exploring their specific mechanisms in EndoC-βH3 cells using gene overexpression or knockdown models.

An important outcome was the robust validation of the transcriptomic changes via RT-qPCR. I not only validated the RNA-seq findings using the same samples submitted for sequencing but also repeated the RT-qPCR in two independent experiments using a separate

batch of differentiated EndoC-βH3 cells and biological replicates. This thorough validation supports the reliability and accuracy of the observed transcriptomic changes, by RNA-seq adding weight to the findings.

By optimising the psEV dose and the time point for RNA isolation I determined that 40 µg/mL of psEVs and an 8-hour time point for RNA isolation were optimal for capturing the most robust transcriptomic effects of psEV treatments. This optimisation would be crucial to maximise the detection of gene expression changes and ensuring that the experimental conditions were ideal for capturing biologically relevant results in future experiments.

A limitation of the data presented in this chapter was the small fold changes observed in gene expression in both the RNA-seq and RT-qPCR experiments, even at the optimised 8-hour time point using a psEV dose of 40 µg/mL. Although the log2 fold changes increased at this earlier time point, they were still not substantial (less than ± 1). Additionally, increasing the psEV dose beyond 40 µg/mL was deemed impractical, as this dose had already been established in both the literature and previous work within the Vatish group as approaching the upper limit of the optimal psEV concentration range (59, 185). Doses exceeding this threshold would be considered supraphysiological and may not accurately reflect the *in vivo* biological effects of psEVs. This raised concerns regarding the potential biological significance of these small changes observed in gene expression.

Given the small changes in gene expression observed, even when RNA was isolated 8 hours post-treatment at the maximal psEV dose, I reconsidered the merit of repeating the RNA-seq experiment. I was concerned that repeat RNA-seq results would not reveal biologically impactful changes in gene expression, a concern further reinforced by the observation of

distinct gene expression patterns for some of the genes selected for validation and optimisation in RT-qPCR studies between the 8-hour and 18-hour time points. Additionally, I was concerned that performing sequencing at an earlier time point could predominantly capture transferred psEV RNA, rather than the changes in cellular mRNA expression conferred by psEVs, limiting the interpretation of the data. Taken together, this would make it difficult to reliably identify potential target genes of interest altered by psEVs for detailed analysis in future experiments. Therefore, I decided against repeating the RNA sequencing experiment. This decision meant that I did not investigate the effects of GDM-derived psEVs on the transcriptome of EndoC-βH3 cells, which is a limitation of this work. However, I felt it was more sensible to adopt a different approach moving forward.

Rather than additional transcriptomic experiments, I decided to investigate the functional effects of psEVs on β cells in a human-based model system, focusing on their impact on insulin content and secretion. Only if functional effects in response to psEV treatments were present, would a follow-up omics experiment be justified to characterise the underlying biological mechanisms contributing to these effects. Given the challenges I encountered using sequencing to study the effects of psEVs, I postulated that that post-transcriptional or post-translational mechanisms play a greater role in psEV-mediated effects. Therefore, I considered proteomics to be a better option than transcriptomics for future omics studies, as this approach would enable the study of protein expression while addressing concerns about sequencing transferred genetic material. Moreover, changes in gene expression may not always correspond to changes in protein abundance (198-200). Studying protein alterations directly would provide clearer insights into the mechanistic changes driving cellular processes influenced by psEVs, as changes in protein abundance or modifications have an immediate and significant impact on cellular function (201).

By prioritising functional studies of insulin synthesis and secretion in the next phase of experiments, I aimed to establish whether psEVs have a biologically meaningful impact on β-cell function. If functional effects were confirmed, proteomics could offer insights into the molecular pathways modulated by psEVs, ultimately providing a more comprehensive understanding of their role in β-cell biology during pregnancy. The results of this approach are shown in Chapter 7.

Chapter 7

Changes in insulin gene, insulin content, and protein abundance in EndoC-βH3 cells following treatment with placental small extracellular vesicles

7.1 Introduction

In Chapter 6, I demonstrated that normal pregnancy placental small extracellular vesicles (psEVs) induced transcriptomic changes in EndoC-βH3 cells, highlighting their influence on gene expression. Despite the large number of differentially expressed genes observed, the fold changes (FCs) in gene expression were small (log2 FC ≈ -0.5 to 0.5). As such, interpreting the biological relevance of the genetic changes induced by psEVs in EndoC-βH3 cells was challenging, as was identifying which genes warranted further investigation as significant targets. I proposed that to determine whether psEVs exert biologically significant effects on EndoC-βH3 cells, it was essential to first assess their impact on β-cell function. Detecting functional changes would then justify conducting an additional omics-based experiment to identify potential biological mechanisms underlying these effects. Given that proteomic changes tend to be fewer but more closely aligned with functional outcomes compared to transcriptomic changes, and considering the often poor correlation between RNA and protein levels (198-201), I determined that a proteomics approach would be the most appropriate omics-based experiment in this context. By identifying differentially expressed proteins following psEV treatment, key targets or pathways responsible for the observed biological effects could be elucidated, thereby shedding light on the cellular mechanisms driving these functional changes.

My hypothesis was that psEVs from normal and gestational diabetes mellitus (GDM) pregnancies modulate the function of pancreatic β cells, potentially enhancing their activity during pregnancy. Specifically, I was interested in whether psEVs affect insulin synthesis and secretion. This required designing experiments using insulin ELISA assays to measure intracellular and secreted insulin levels following psEV treatments. However, owing to the substantial expense of insulin ELISA assays, I decided to first investigate changes in insulin

gene (*INS)* expression. This approach would allow me to first determine whether changes in insulin content and secretion were likely to occur following psEV treatments. More importantly, identifying when changes in *INS* expression take place would guide the selection of the optimal time point for conducting ELISA assays.

In addition, I used pancreatic tissue from pregnant women that was obtained from the Network for Pancreatic Organ Donors with Diabetes (nPOD), as an *ex vivo* model to study psEV-associated islet changes during human pregnancy. The same samples used in Chapters 3 and 4 were now analysed to identify psEV-specific markers in pregnant islets, aiming to determine whether evidence of psEVs could be detected. Demonstrating the presence of psEVs within pancreatic islets from pregnant women would confirm their role as signalling molecules to the pancreas *in vivo*, further validating the *in vitro* model I utilised. Additionally, if changes in protein abundance were observed in EndoC-βH3 cells following treatment with psEVs, I aimed to determine whether similar changes were observed in the islets from pregnant women, analysed by LC-MS/MS, which is presented in Chapter 3.

7.1.1 Aims

The aims of this chapter were to:

1. Assess whether psEVs induce changes in *INS* expression in EndoC-βH3 cells, and to use these findings to inform the design of insulin ELISA assays.
2. Determine if psEVs change insulin content in EndoC-βH3 cells.
3. Investigate whether psEVs alter insulin secretion from EndoC-βH3 cells.
4. To investigate the cellular mechanisms underlying any observed changes in insulin content and/or secretion by identifying alterations in protein abundance in EndoC-βH3 cells induced by psEVs.

5. Assess whether psEVs can be detected in islets from pregnant women *ex vivo*.
6. If psEVs alter protein abundance in EndoC-βH3 cells, determine if similar changes in protein abundance are also observed in islets from pregnant women *ex vivo*.

7.2 Materials and methods

7.2.1 Treatment of EndoC-βH3 cells with placental small extracellular vesicles

7.2.1.1 Reverse transcription quantitative polymerase chain reaction for changes in insulin gene expression

Based on the small extracellular vesicle (sEV) dose optimisation studies conducted using reverse transcription quantitative polymerase chain reaction (RT-qPCR) in Chapter 6, along with the findings from the live-cell psEV uptake assay presented in Chapter 5, I selected an sEV treatment dose of 40 µg/mL. The RNA sequencing experiment presented in Chapter 6 did not detect differences in insulin gene (*INS)* expression at 18 hours and the live-cell psEV uptake assay (Chapter 5) showed that psEV uptake continued up to 18 hours in the 40 µg/mL psEV treatment group. Based on these observations, I postulated that changes in *INS* expression might occur from 24 hours onward, 6 or more hours after maximal psEV internalisation at 18 hours.

First, I performed a time course study to evaluate *INS* expression in normal pregnancy and GDM psEV-treated cells compared to controls (sEV carrier control and red blood cell sEVs (RBCsEVs)) at 24, 30, 36, 48, and 72 hours in normal glucose (5.5 mM) media.

Differentiated EndoC-βH3 cells were seeded into 24-well plates at a density of 2.4 x 10^5 cells per well and treated with GDM psEVs, normal pregnancy psEVs, RBCsEVs, and the sEV carrier control. The reasons for using RBCsEVs and sEV carrier controls as appropriate comparators are detailed in Chapters 5 and 6. Each condition included six biological replicates, representing samples from different patients, and three technical replicates, wherein each sample was assayed in triplicate.

As β cells naturally secrete more insulin in response to higher glucose levels, in a second experiment I aimed to determine if high glucose media would alter the effects of psEVs on *INS* transcription. In this experiment using a different set of biological samples (n = 6 biological replicates per condition), the media were switched to either normal glucose (5.5 mM) or high glucose (20 mM) media 24 hours after treatment. Cells were then lysed at 30 and 36 hours.

Following cell treatments, RNA was extracted, converted to cDNA, and the RT-qPCR was performed using *INS* (Applied Biosystems, cat. no. Hs00355773_m1) and TATA-box binding protein (*TBP)* (Applied Biosystems, cat. no. Hs00427620_m1) TaqMan ™ gene expression assays and analysed as described in Chapter 2. The fold change of *INS* expression in cells treated with normal pregnancy psEVs and GDM psEVs were calculated relative to controls (sEV carrier controls and RBCsEVs) and compared at different time points. Between group differences were analysed using a one-way ANOVA and individual groups were compared to the control group using Tukey's multiple comparisons test.

7.2.1.2 Insulin content and glucose-stimulated insulin secretion assays

Differentiated EndoC-βH3 cells were seeded into 96-well plates at a density of 4 x 10^4 cells per well, with only the 60 central wells seeded to avoid cell loss in the outer wells. Two sets of plates were prepared: one for cell count and insulin content measurements, and the other for glucose-stimulated insulin secretion (GSIS) assays. Using the first set of plates, cells were treated with 40 µg/mL of GDM psEVs, normal pregnancy psEVs, RBCsEVs, and the sEV carrier control. At 40 hours post-treatment, the cell count per well was quantified using the CyQUANT™ Direct Cell Proliferation Assay (Thermo Fisher Scientific, cat. no. C35011). Insulin content was subsequently measured using the Mercodia Insulin ELISA Kit

(Mercodia, cat. no. 10-1113-01). For the second set of plates, cells were treated with 40 μg/mL of normal pregnancy psEVs, RBCsEVs, and the sEV carrier control. GSIS was performed 40 hours post-treatment. For the assay measuring insulin content, six biological replicates, each with at least four technical replicates, were used for psEV treatments. Data points represent the mean of the technical replicates. For the GSIS assay, four biological replicates were used for normal pregnancy psEVs, and three biological replicates were used for RBCsEVs and the sEV carrier control, each with three technical replicates.

7.2.1.2.1 CyQUANT™ direct cell proliferation assay

On the day of the assay, reference standards were prepared by seeding wells with a known number of cells. Cells were counted using a Countess™ 3 Automated Cell Counter (Thermo Fisher Scientific, cat. no. AMQAX2000), and a dilution series was prepared with the following cell numbers per well: 50,000; 25,000; 12,500; 6,250; 3,125; 1,563; 781; 391; 195; 98; 49; and a blank control. These standards were seeded into wells prior to beginning the assay.

The 2X detection reagent was prepared by combining phosphate-buffered saline (PBS) (Gibco, cat. no. 10010023), the CyQUANT Direct nucleic acid stain, and the CyQUANT Background Suppressor I according to the manufacturer's instructions. The 2X detection reagent (100 μL) was added to each well, and the plate was incubated at 37°C for 60 minutes. Using the FLUOstat OPTIMA plate reader (BMG Labtech), fluorescence of the samples was measured using standard "green" filter sets (480/535 nm). A reference standard curve was generated from the prepared standards, and fluorescence values of the samples were compared to the standard curve to calculate the number of cells per well.

7.2.1.2.2 Insulin ELISA

Following the CyQUANT assay, the media and CyQUANT 2X detection reagent were carefully removed. The cells were gently washed with PBS and then lysed using acid ethanol (0.18 M HCL in 96% ethanol, vol/vol). After lysis, the contents of each well were diluted 1:100 in Calibrator 0.

All reagents were brought to room temperature before use. The enzyme conjugate was prepared by mixing the entire content of the conjugate buffer with the enzyme conjugate 11X vial and used within the same day. The wash buffer was prepared by diluting 35 mL of wash buffer concentrate with 700 mL of distilled water.

To conduct the assay, 100 µL of the enzyme conjugate mixture was pipetted into each well. Five calibrators with known insulin concentrations as well as the blank (no insulin) were provided by the manufacturer. Each calibrator or sample was added to the wells (25 µL). The plate was incubated on a plate shaker at 700-900 rpm for 1 hour at room temperature. Following incubation, the plate was washed six times with 700 µL of wash buffer using the BioTek ELx405 Select plate washer with an overflow wash function. After the final wash, the plate was inverted and tapped against absorbent paper to remove any residual buffer. Next, 200 µL of TMB substrate solution was added to each well, and the plate was incubated for 15 minutes at room temperature. Following this, 50 µL of stop solution was added to each well, and the plate was mixed on a plate shaker (Eppendorf MixMate®) for 5 seconds. The optical density was read at 450 nm within 30 minutes of adding the stop solution using the FLUOstat OPTIMA plate reader. Insulin concentrations were determined by computerised data reduction of the absorbance for the calibrators, except for calibrator 0, versus the concentration using cubic spline regression.

7.2.1.2.3 Glucose-stimulated insulin secretion

Controls to assess appropriate insulin secretion were prepared: dimethyl sulfoxide (DMSO) (200 mM) (Sigma, cat. no. D4540**)** was added to both 1 mM and 20 mM glucose media, tolbutamide (200 mM, an insulin secretagogue) (Sigma, cat. no. T 0891) was added to 1 mM glucose media, and diazoxide (200 mM, an inhibitor of insulin secretion) (Sigma, cat. no. D9035) was added to 20 mM glucose media. EndoC-βH3 cells, both pre-treated with normal pregnancy psEVs (n = 4 biological replicates), RBCsEVs (n = 3), sEV controls (n = 3), and untreated cells (to test secretion controls), were placed in starvation low-glucose media (2.8 mM) overnight. The following day, the media was changed to no-glucose media (0 mM), and the cells were incubated for 1 hour at 37°C. After this incubation step, either 1 mM or 20 mM glucose media was added to each experimental group, respectively, and incubated for an additional hour at 37°C to stimulate glucose secretion. Following GSIS, 70 µL of supernatant was removed from each well, placed into a labelled PCR plate and centrifuged at 500 *g* for 5 minutes at 4°C. From this plate, 50 µL of the supernatant was then transferred to a second PCR plate. These steps were performed to ensure that no residual cells remained in the supernatant, thereby representing only the secreted insulin. The remaining media in the wells containing cells was then removed, and the cells lysed using acid ethanol. The lysed cells represented insulin content. Secreted insulin in the supernatant was measured undiluted, and lysed cells containing insulin content was diluted 1:100 prior to measurement. Insulin concentration for each was determined using an insulin ELISA assay as previously described.

7.2.1.2.4 Cell counts, insulin content and glucose-stimulated insulin secretion data processing and analysis

Cell counts between controls, normal pregnancy, and GDM psEV treated differentiated EndoC-βH3 cells were compared using the Kruskal-Wallis test to ensure no difference in cell numbers were present between conditions. For the insulin content assay, insulin content from each well was normalised to the cell count per well, and this value was multiplied by 100 to account for the dilution prior to measurement by insulin ELISA. Insulin content measurements were compared between groups using a the Kruskal-Wallis test followed by post-hoc analysis using Dunn's multiple comparison test to compare individual groups. For the GSIS assay, secreted insulin was normalised to the insulin content per well. To confirm differential insulin secretion between low and high glucose concentrations, insulin secretion at 1 mM glucose was compared to 20 mM glucose. Comparisons of DMSO, tolbutamide, and diazoxide containing media to no-drug controls were conducted using a one-way ANOVA followed by Šídák's multiple comparisons test as a small number of specific comparisons were performed. To assess the effect of normal pregnancy psEVs on insulin secretion, secreted insulin concentrations in normal pregnancy psEV-treated cells were compared to controls at both 1 mM and 20 mM glucose concentrations. Comparisons of normal pregnancy psEVs to controls were performed using a two-way ANOVA, followed by Tukey's multiple comparisons test, as all individual groups were compared to each other.

7.2.2 Liquid chromatography-mass spectrometry of EndoC-βH3 cells treated with placental small extracellular vesicles

Differentiated EndoC-βH3 cells were seeded into 6 cm culture dishes at 3 x 10^6 cells per dish and treated with 40 μg/mL of GDM psEVs, normal pregnancy psEVs, RBCsEVs, and

the sEV carrier control. After 24 hours, cell lysates were prepared, and protein concentration quantified as described in Chapter 2.

7.2.2.1 Sample size calculation

A sample size calculation was performed to determine the appropriate number of samples necessary to detect differentially expressed proteins between groups. Due to the absence of pilot liquid chromatography-mass spectrometry (LC-MS/MS) data, the RNA sequencing dataset, which had the same experimental design, was used to guide the calculation. I aimed to detect a biologically meaningful effect size which I defined as a fold change of 4 (equivalent to a log2 FC of 2). The calculation was performed using a two-tailed t-test comparing two independent means in G*Power (v 3.1.9.6). The parameters set included: a power of 0.8 and an adjusted α error probability (α′) of 0.017, which was used to correct for multiple comparisons (Bonferroni correction), instead of the standard α error probability of 0.05. A standard deviation (SD) of 1.25, calculated based on the RNA sequencing experiment, was also incorporated. Based on these parameters, it was determined that a sample size of six per group would be needed. Owing to the high cost associated with LC-MS/MS, submitting a large number of samples for the initial experiment was not feasible. Instead, I decided to submit a smaller number of samples (n = 3 per treatment group) for LC-MS/MS to identify targets of interest. I would then aim to use a larger sample size for validation of these key targets using immunoblotting.

7.2.2.2 Sample digestion and liquid chromatography-mass spectrometry

LC-MS/MS was performed in collaboration with Ms Svenja Hester and Professor Roman Fischer at the Target Discovery Institute (TDI), Nuffield Department of Medicine, University of Oxford.

Protein digestion and the LC-MS/MS experiment was performed by Ms Svenja Hester, as follows. Protein lysates from EndoC-βH3 cells treated with GDM and normal pregnancy psEVs, RBCsEVs, and the sEV carrier control were prepared using Filter-Aided Sample Preparation (FASP) digestion. The FASP filter (Vivacon® 500, Sartorius, VN01H02, 10 kDa) was washed with 200 µL of 0.1% trifluoroacetic acid (TFA) (Sigma, cat. no. 80457) in 50% acetonitrile (ACN) (Sigma, cat. no. AX0156) and centrifuged at 14,300 *g* for 10 minutes. The sample was loaded onto the filter, and proteins were denatured with 200 µL of 8 M urea (Sigma, cat. no. U4883) (prepared by dissolving 4.8 g of urea in 10 mL of 100 mM triethylammonium bicarbonate (TEAB) (Sigma, cat. no. T7408)) for 30 minutes at room temperature. For reduction, tris (2-carboxyethyl) phosphine (TCEP) (Sigma, cat. no. C7406) was added to a final concentration of 10 mM (by adding 4 µL of 0.5M TCEP) and incubated for 30 minutes at room temperature. Alkylation was carried out by adding chloroacetamide (C-AA) (Sigma, cat. no. 22790) to a final concentration of 50 mM (20.4 µL of 0.5M C-AA) and incubating for 30 minutes in the dark. The liquid was then spun through the filter at 14,300 *g* for 10 minutes. The filter was washed twice with 200 µL of 50 mM TEAB, each wash followed by centrifugation at 14,300 *g* for 10 minutes. The sample was transferred to a fresh tube prior to protease addition. Digestion was performed using 2 µg of trypsin in 200 µL of 50 mM TEAB, incubated overnight at 37°C. After digestion, the liquid was spun through, and the flow-through was retained. The filter was washed with 200 µL of 0.1% TFA, and the flow-through was combined with the initial flow-through. The filter was then washed with 200 µL of 50% ACN in 0.1% TFA, and the flow-through was combined again. The combined flow-through was dried down using a speedvac vacuum concentrator and re-suspended in 50 µL of 5% formic acid (Sigma, cat. no. 5.33002) and 5% DMSO.

Peptides were chromatographically separated and eluted onto a TimsTOF Pro mass spectrometer (Bruker Daltonics). Samples loaded on Evotips were analysed using the high-throughput Evosep One LC system connected to the TimsTOF Pro mass spectrometer. Peptides were analysed using the pre-built 100 samples/day method (EvosepOne) with an 11.5-minute gradient (total cycle time of 14.4 minutes) at a flow rate of 1.2 µL/min. Tryptic peptides were transferred from the pre-loaded C18 evotips to a sample loop and separated on a 150 µm x 8 cm C18 analytical column (Evosep Pepsep, 3 µm beads, 100 µm ID) with a gradient from 3% to 40% acetonitrile.

Mass spectrometry (MS) data were acquired in data-independent acquisition mode with parallel accumulation serial fragmentation (diaPASEF) using oTOF control (v6.0.0.12). The ion mobility window was set to 1/k0 start = 0.85 Vs/cm² to 1/k0 end = 1.3 Vs/cm², ramp time 100 milliseconds with a locked duty cycle, and a mass range of 100-1700 m/z. MS/MS were acquired in four PASEF frames (three cycles overlap). Target intensity was set to 6,000 and threshold intensity to 200.

The raw MS data were analysed using a library-free approach with Data-Independent Acquisition by Neural Networks (DIA-NN, v1.8.1), utilising the UniProt reference proteome for Homo sapiens (UPR_Homo sapiens_9606_UP000005640_20221003.fasta). To ensure high-confidence identifications, the false discovery rate (FDR) was maintained at 0.01. The Match Between Runs (MBR) feature was activated to enhance quantification accuracy across different datasets, and cross-run normalisation was performed using maximal label-free quantification (MaxLFQ) for consistent and precise quantification.

7.2.2.3 Liquid chromatography-mass spectrometry data analysis

I performed the data analysis using Perseus (v2.0.11), a proteomics data analysis and visualisation tool offering a robust set of features for data pre-processing, quality control, and statistical testing to identify differential expression. The raw MS intensity data were log2 transformed to ensure data followed a normal distribution, and biological replicates were grouped as sEV carrier controls, RBCsEVs, normal pregnancy psEVs, and GDM psEVs. Rows were filtered to retain those with at least 50% of valid values per group, followed by imputation assuming a normal distribution. Group comparisons were made using a Student's t-test with permutation-based testing to correct for multiple comparisons. In the interest of discovery an FDR of 0.1 and an S0 parameter of 0.2 were applied to determine statistical significance (202). (The FDR represents the adjusted p-value following correction for multiple comparisons). Principal component analysis (PCA) was performed using the built-in PCA function in Perseus. The 25 proteins with the largest positive and negative log2 fold changes when comparing normal pregnancy psEVs to controls, and GDM psEVs to controls, respectively, were visualised using hierarchical clustering analysis. A subset table containing these proteins and their MS intensities per condition was created. A normalisation z-score was calculated, and the heatmap was generated using the hierarchical clustering function with the following settings: Euclidean distance, average linkage, and no constraints. Volcano plots were generated by plotting the negative log10 FDR against the log2 fold change of the normalised mean MS intensities. A negative log10 FDR of > 1 is equivalent to an FDR < 0.1. Protein profile plots were generated using the protein plot profile function in Perseus by plotting the protein abundance (log2-transformed MS signal intensities) detected for each protein per condition for each sample. Differentially expressed proteins were selected and highlighted. String DB (STRING, v2023) (139) was used to perform a protein clustering analysis of significantly differentially expressed proteins for

detection of interactions of a physical subnetwork. An FDR < 0.05 and required score of 0.4 (medium confidence) was applied.

7.2.3 Immunoblotting to validate an anti-Protein Kinase CAMP-Activated Catalytic Subunit Gamma antibody

Immunoblotting of the recombinant full-length Protein Kinase CAMP-Activated Catalytic Subunit Alpha (PRKACA) protein (H00005566-P01) was performed as described in Chapter 2. Per well, 20 ng of recombinant protein was loaded. The primary and secondary antibodies against both Protein Kinase CAMP-Activated Catalytic Subunit Gamma (PRKACG) and PRKACA used are detailed in Table 7.1

Table 7.1: Antibodies used during immunoblotting for anti-PRKACG antibody validation.

Antibody	Concentration	Manufacturer	Catalog Number	Species	Clonality	Dilution
Primary antibodies						
PRKACG	0.2 mg/mL	Santa Cruz Biotechnology	sc-514087	Mouse	Monoclonal	1 in 250
PRKACG	0.606 mg/mL	Abcam	ab108385	Rabbit	Polyclonal	1 in 1000
PRKACG	4 mg/mL	Abbexa	abx301838	Rabbit	Monoclonal	1 in 1000
PRKACA	1 mg/mL	Proteintech	67491-1-IG	Mouse	Monoclonal	1 in 1000
Secondary antibodies						
IRDye 680 anti-Mouse IgG	10 mg/mL	LI-COR Biosciences	926-68072	Donkey	-	1in 10000
IRDye 800 anti-Rabbit IgG	10 mg/mL	LI-COR Biosciences	926-32213	Donkey	-	1in 10000

**PRKACA* - Protein Kinase CAMP-Activated Catalytic Subunit Alpha, *PRKACG* - Protein Kinase CAMP-Activated Catalytic Subunit Gamma.

7.2.4 Immunofluorescence for the detection of placental small extracellular vesicle markers in islets from pregnant women

7.2.4.1 Immunoblotting to confirm the presence of placental specific markers on placental small extracellular vesicles

Immunoblotting was performed, as described in Chapter 2, to confirm that psEVs were enriched for placental specific markers: placental alkaline phosphatase (PLAP) and chorionic somatomammotropin hormone-like 1 (CSHL1). The following primary antibodies were used: Anti-PLAP antibody (Abcam, cat. no. ab133602) and Anti-CSHL1 (Abcam, cat. no. ab174295).

7.2.4.2 Immunofluorescence of pancreas tissue sections from pregnant women

The formalin-fixed paraffin-embedded (FFPE) human pancreas tissue histology sections, used in Chapter 3 and 4, were analysed by immunofluorescence (IHC-IF) to determine if placental specific markers carried by psEVs (PLAP and CSHL1) could be detected in islets from pregnant women. In addition, FFPE placental tissue sections belonging to the Vatish group were also analysed by IHC-IF for PLAP and CSHL1 (Central Oxfordshire Research Ethics Committee C (REFS: 07/H0607/74 and 07/H0606/148)).

FFPE pancreas and placental tissue sections were processed and imaged as described in Chapter 2 and 4. The anti-PLAP and anti-CSHL1 primary antibodies used are those that were used for immunoblotting described above, and the secondary antibodies used are as previously described (Chapter 5, Table 5.1).

7.2.5 Re-evaluation of proteomics data to identify if protein changes induced by placental small extracellular vesicles in EndoC-βH3 cells are present *ex vivo*

The proteomics data from the LC-MS/MS analysis of human islets, isolated from pregnant women and non-pregnant controls and presented in Chapter 3, was re-evaluated. Proteins significantly expressed in EndoC-βH3 cells following psEV treatment were searched for within the proteomic dataset analysing human islets. If identified, the abundance of the psEV-altered proteins was analysed in the human islet dataset by comparing their expression levels between pregnant and non-pregnant islets, following the methods described in Chapter 3. This analysis aimed to assess whether the changes in protein expression observed in EndoC-βH3 cells following psEV treatments were also reflected in the pregnant islets.

7.3 Results

7.3.1 Insulin gene transcription in EndoC-βH3 cells treated with placental small extracellular vesicles

First, I performed the time course experiment to determine if *INS* expression was altered following treatment with psEVs. The time course showed *INS* transcription increased in normal pregnancy and GDM psEVs at 30 hours relative to *INS* expression in EndoC-βH3 cells treated with controls (sEV carrier control and RBCsEVs). FC = 2.48 in normal pregnancy psEVs versus (vs.) FC = 0.62 in sEV carrier, ($p = 0.0364$) and FC = 0.72 in RBCsEVs ($p = 0.0441$), and FC= 2.42 in GDM psEVs vs. FC in sEV carrier, ($p = 0.0301$) and in RBCsEVs, ($p = 0.0366$), respectively. No significant change in *INS* expression was noted at 36, 48 or 72 hours (Figure 7.1).

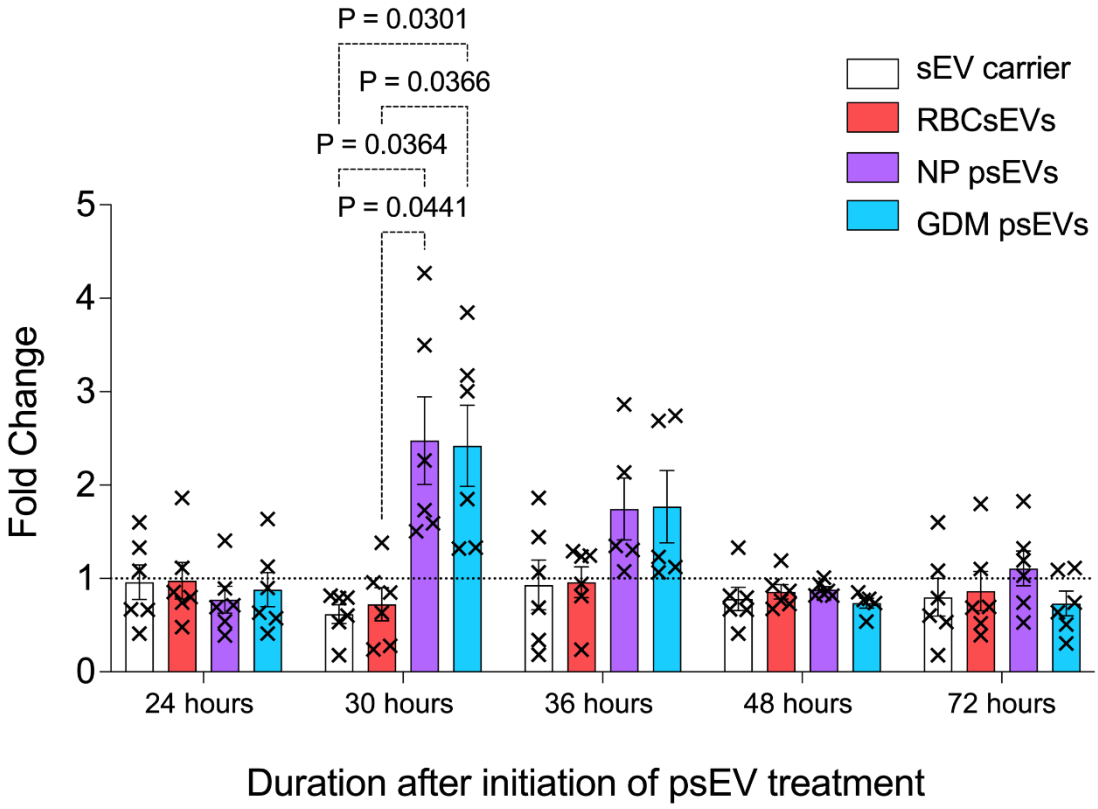

Figure 7.1. Time course of insulin gene (*INS*) transcription in EndoC-βH3 cells treated with normal pregnancy (NP) and gestational diabetes mellitus (GDM) placental small extracellular vesicles (psEVs) compared to the controls (red blood cell small extracellular vesicles (RBCsEVs), and the small extracellular vesicle (sEV) carrier control) showing that *INS* expression is increased in normal pregnancy and GDM psEVs at 30 hours. The fold changes in *INS* expression for cells treated with psEVs from normal pregnancies (purple bar) and GDM (blue bar) are shown relative to the expression in cells treated with the controls (sEV carrier control [white bar] and RBCsEVs [red bar]). Between group differences were analysed using a one-way ANOVA using Tukey's multiple comparisons test to compare individual groups to the control group. Only p-values for significant comparisons are shown. Reproduced from *Seedat et al.*, *Clinical Science* (2024), with permission from Portland Press. This content is distributed under the Creative Commons Attribution License (CC BY 4.0).

I then sought to determine if exposing cells to high glucose media (20mM), to mimic hyperglycaemia, would have any effect on *INS* expression induced by psEVs. Following the psEV treatments, the increase in *INS* transcription was maintained in cells cultured in normal glucose media (5 mM) at 30 hours (FC = 2.27 in normal pregnancy psEVs vs. FC = 0.86 in sEV carrier, $p < 0.0011$ and FC = 0.82 in RBCsEVs, $p < 0.0001$; FC = 2.12 in GDM psEVs vs. FC in sEV carrier, $p = 0.0002$ and RBCsEVs, $p = 0.0001$, respectively)(Figure 7.2A) but was attenuated in cells cultured in high glucose media at 30 hours (FC = 1.62 in normal pregnancy psEVs vs. FC = 0.92 in sEV carrier, $p = 0.1376$ and FC in RBCsEVs = 1.14, $p = 0.6522$; FC = 1.62 in GDM psEVs vs. FC in sEV carrier, $p = 0.1417$ and RBCsEVs, $p = 0.6610$, respectively)(Figure 7.2B).

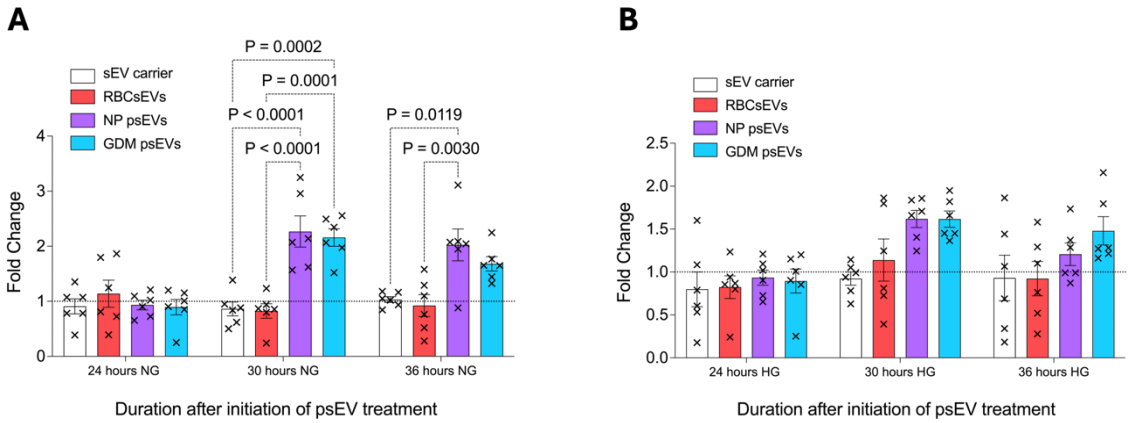

Figure 7.2. Insulin gene (*INS*) transcription in EndoC-βH3 cells exposed to **A.** normal glucose (NG) (5.5 mM) and **B.** high glucose (HG) (20 mM) media following treatments with normal pregnancy (NP) and gestational diabetes mellitus (GDM) placental small extracellular vesicle (psEVs) compared to the controls (red blood cell small extracellular vesicles (RBCsEVs), and the small extracellular vesicle (sEV) carrier control). The fold changes in *INS* expression for cells treated with psEVs from normal pregnancies (purple bar) and GDM (blue bar) are shown relative to the expression in cells treated with the controls (sEV carrier control [white bar] and RBCsEVs [red bar]). Between group differences were analysed using a one-way ANOVA using Tukey's multiple comparisons test to compare individual groups to the control group. Only p-values for significant comparisons are shown. Reproduced from *Seedat et al.*, *Clinical Science* (2024), with permission from Portland Press. This content is distributed under the Creative Commons Attribution License (CC BY 4.0).

In a third replicate experiment performed using additional biological replicates (n = 8), *INS* transcription was once more increased at 30 hours in EndoC-βH3 cells cultured in normal glucose media when treated with normal pregnancy and GDM psEVs (FC = 2.71 in normal pregnancy psEVs vs. FC = 0.89 in sEV carrier, $p < 0.0001$ and FC in RBCsEVs = 1.03, $p < 0.0001$; FC = 2.19 in GDM psEVs vs. FC in sEV carrier, $p < 0.0001$ and RBCsEVs, $p < 0.0001$, respectively). No difference in fold change was observed between normal pregnancy and GDM psEVs at 30 hours ($p = 0.1136$) (Figure 7.3).

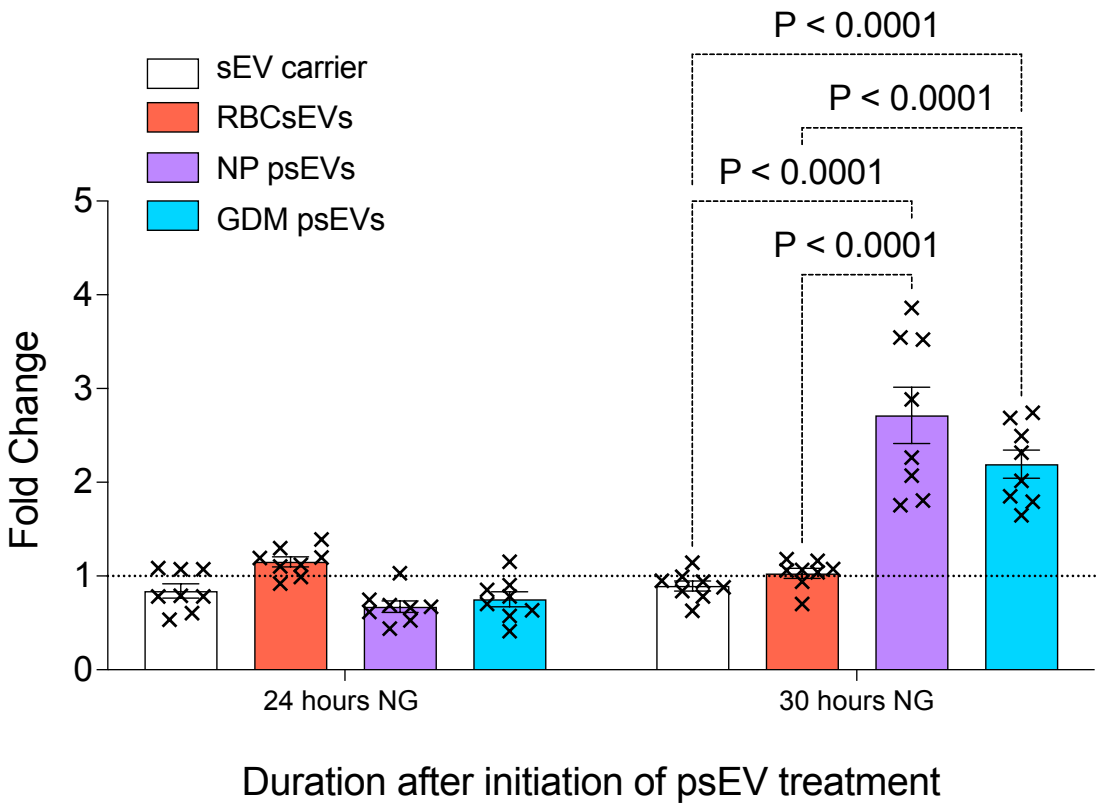

Figure 7.3. Insulin gene (*INS*) transcription at 30 hours in EndoC-βH3 cells cultured in normal glucose (NG) (5.5 mM) media treated with normal pregnancy (NP) and gestational diabetes mellitus (GDM) placental small extracellular vesicles (psEVs) compared to the controls (red blood cell small extracellular vesicles (RBCsEVs) and small extracellular vesicle (sEV) carrier control). The fold changes in *INS* expression for cells treated with psEVs from normal pregnancies (purple bar) and GDM (blue bar) are shown relative to the expression in cells treated with the controls (sEV carrier control [white bar] and RBCsEVs [red bar]). Between group differences were analysed using a one-way ANOVA using Tukey's multiple comparisons test to compare individual groups to the control group. Only p-values for significant comparisons are shown. Reproduced from *Seedat et al.*, *Clinical Science* (2024), with permission from Portland Press. This content is distributed under the Creative Commons Attribution License (CC BY 4.0).

7.3.2 Insulin content in EndoC-βH3 cells treated with placental small extracellular vesicles

I then examined whether increases in *INS* transcription in response to psEVs were translated to an increase in intracellular insulin content.

As *INS* expression peaked at 30 hours, I postulated that changes in insulin levels would be detectable by 40 hours, allowing sufficient time for the genetic changes to translate into alterations in protein levels. I first confirmed that similar cell numbers per well were present between the different treatment conditions ($p = 0.4999$) (Figure 7.4).

Insulin content was increased in EndoC-βH3 cells treated with normal pregnancy (0.48 pmol/L, IQR: 0.36-0.7, $p = 0.026$) and GDM (0.52 pmol/L, IQR: 0.39-0.65, $p=0.0088$) psEVs relative to the control group (sEV carrier controls and RBCsEVs) (0.34 pmol/L, IQR: 0.275-0.46); however, no difference was noted between normal pregnancy and GDM psEVs ($p > 0.99$) (Figure 7.5).

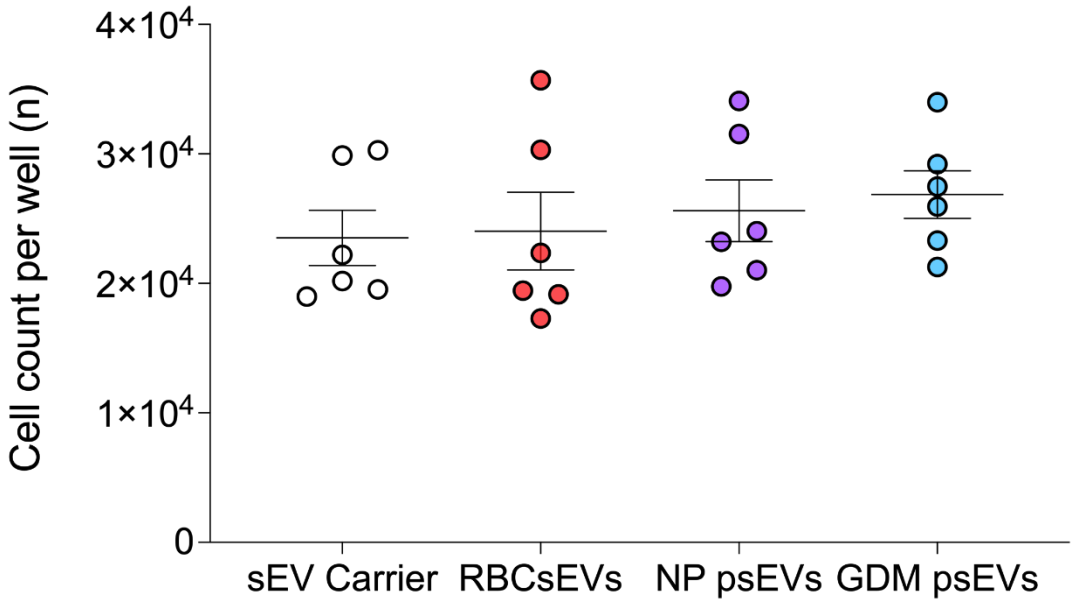

Figure 7.4. Comparison of cell counts in wells for each condition. Individual measures for small extracellular vesicle (sEV) carrier controls (white), red blood cell small extracellular vesicles (RBCsEVs), normal pregnancy (NP) placental small extracellular vesicles (psEVs) (purple), and gestational diabetes mellitus (GDM) psEVs (blue) are shown. No significant differences were observed between conditions analysed using a Kruskal-Wallis test, $p = 0.4999$.

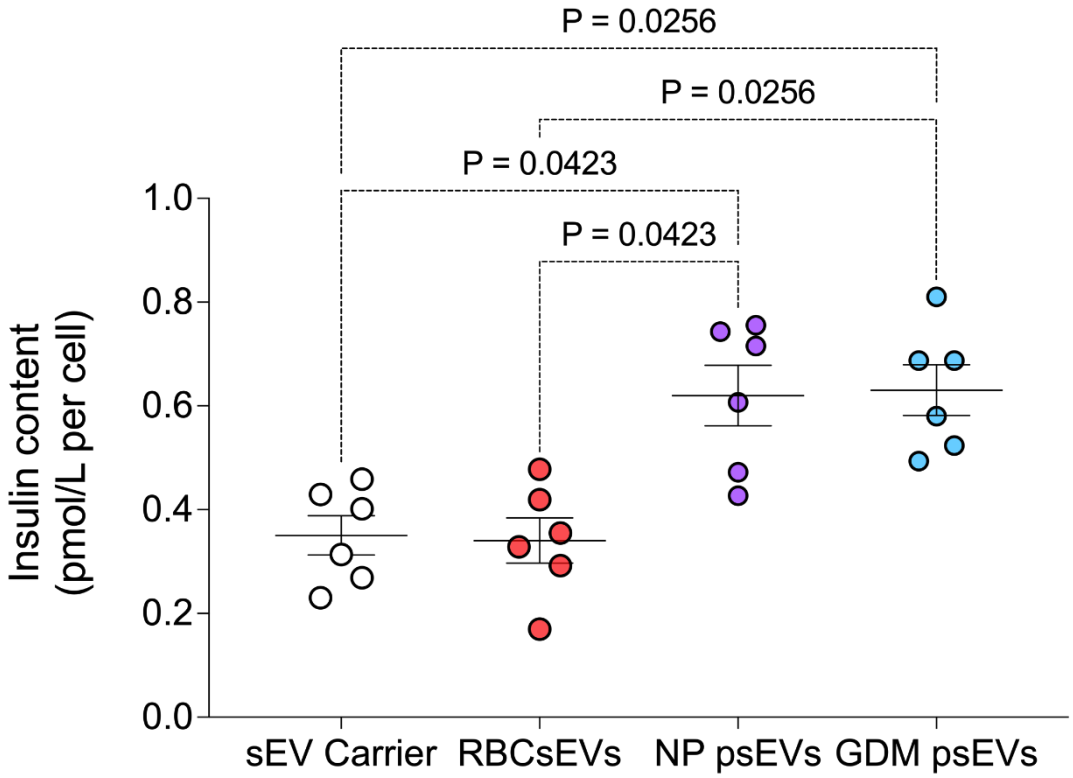

Figure 7.5. Insulin content measured at 40 hours after placental small extracellular vesicle (psEV) treatments. Individual measures for small extracellular vesicle (sEV) carrier controls (white), red blood cell small extracellular vesicles (RBCsEVs) (red), normal pregnancy (NP) psEVs (purple), and gestational diabetes mellitus (GDM) psEVs (blue) are shown. Differences were analysed using a Kruskal-Wallis test, followed by Dunn's multiple comparison test for individual group comparisons. Only p-values for significant comparisons are shown. Reproduced from *Seedat et al.*, *Clinical Science* (2024), with permission from Portland Press. This content is distributed under the Creative Commons Attribution License (CC BY 4.0).

7.3.3 Glucose-stimulated insulin secretion in EndoC-βH3 cells treated with placental small extracellular vesicles

I then examined whether increases in intracellular insulin content following psEV treatments were also associated with changes in insulin secretion.

EndoC-βH3 cells responded appropriately to GSIS controls, including: 1 mM and 20 mM glucose media containing DMSO, as well as to the pharmaceutical drugs added to cell culture media to stimulate or inhibit insulin secretion. Insulin secretion increased in the presence of 20 mM glucose with DMSO relative to 1 mM glucose with DMSO (20 mM glucose with DMSO, 3.066 % ± 0.116 vs. 1 mM glucose with DMSO, 1.166 % ± 0.329, $p < 0.001$). Insulin secretion was stimulated by the secretagogue tolbutamide in 1 mM glucose (tobutamide in 1 mM glucose, 9.722 % ± 0.348 vs. 1 mM glucose only 1.203 % ± 0.196, $p < 0.001$) and inhibited by diazoxide, an inhibitor of insulin secretion, in 20 mM glucose (diaxoxide in 20 mM glucose, 1.177 % ± 0.099 vs. 20 mM glucose only 3.052 % ± 0.034, $p < 0.001$) (Figure 7.6).

GSIS performed using EndoC-βH3 cells treated with controls and normal pregnancy psEVs showed an appropriate reduction in insulin secretion in 1 mM glucose media and an increase in insulin secretion in 20 mM glucose (sEV carrier in 1 mM glucose, 1,046 % ± 0.171 vs. sEV carrier in 20 mM glucose, 2.844 % ± 0.071, $p < 0.0001$; RBCsEVs in 1 mM glucose, 0.092 % ± 0.108 vs. RBCsEV in 20 mM glucose, 2.693 % ± 0.093, $p < 0.0001$; normal pregnancy psEVs in 1 mM glucose, 1.049 % ± 00.153 vs. normal pregnancy psEVs in 20 mM glucose, 2.693 % ± 0.093, $p < 0.0001$). However, when cells treated with controls were compared to those treated with normal pregnancy psEVs at each glucose concentration, no difference in insulin secretion was observed in either low (1 mM) (normal pregnancy psEVs

compared to sEV carrier, p = 0.9107; normal pregnancy psEVs compared to RBCsEVs, p = 0.4156) or high (20 mM) glucose concentrations (normal pregnancy psEVs compared to sEV carrier, p = 0.6451; normal pregnancy psEVs compared to RBCsEVs, p = 0.2273) (Figure 7.7).

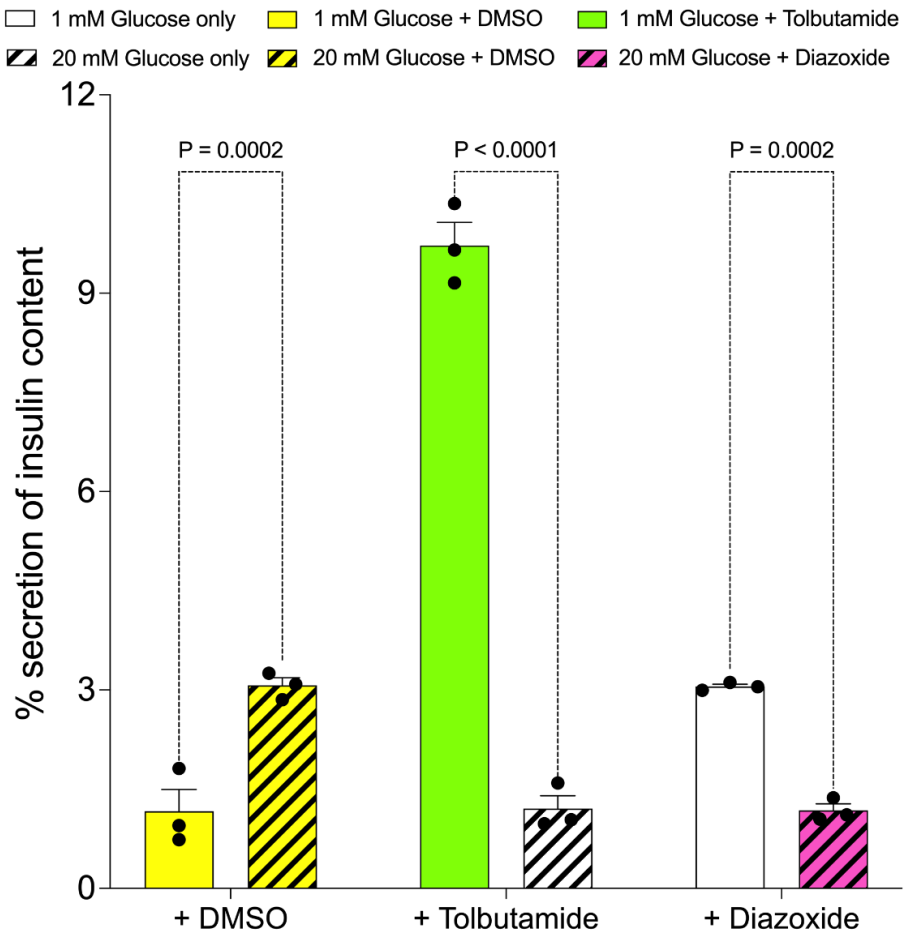

Figure 7.6. Glucose-stimulated insulin secretion assay showing an appropriate response insulin secretory response by EndoC-βH3 cells when cultured in basal 1 mM and 20 mM glucose media. Insulin secretion increased in the presence of 20 mM glucose media with DMSO relative to the 1 mM glucose media containing DMSO. Insulin secretion increased in the presence of tolbutamide in 1 mM glucose media and insulin secretion was reduced in the presence of diazoxide in 20 mM glucose media. Between-group differences were analysed using a one-way ANOVA, followed by Šídák's multiple comparisons test for individual group comparisons. Only p-values for significant comparisons are shown. Reproduced from *Seedat et al.*, *Clinical Science* (2024), with permission from Portland Press. This content is distributed under the Creative Commons Attribution License (CC BY 4.0).

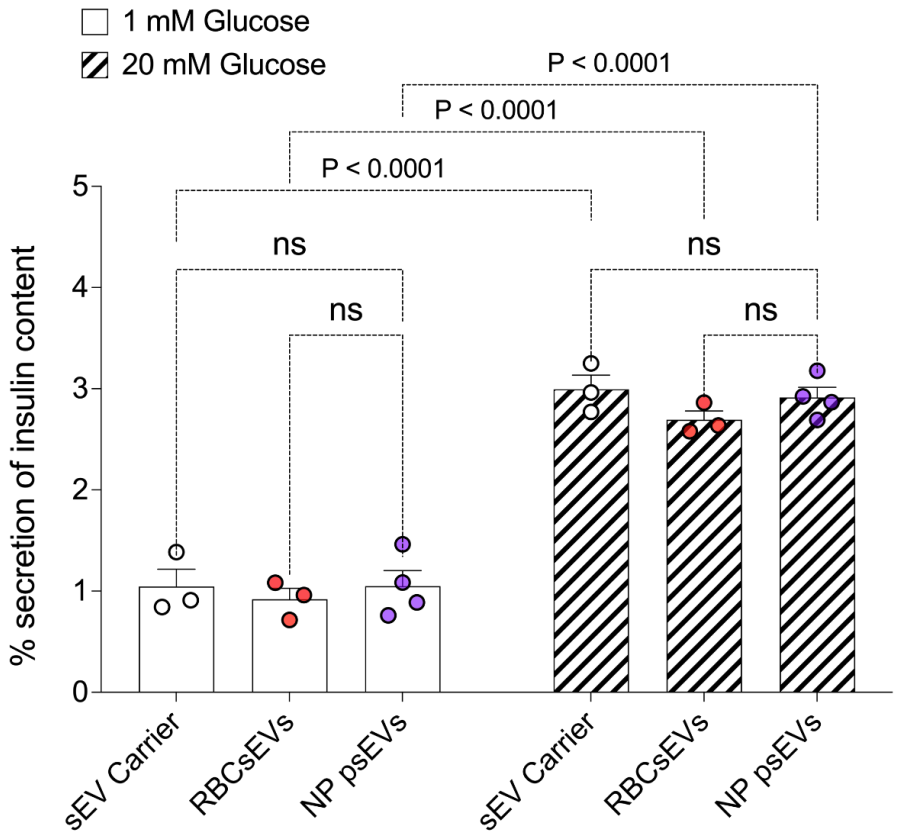

Figure 7.7. Glucose-stimulated insulin secretion assay of insulin secretion by EndoC-βH3 cells following treatment with the small extracellular vesicle (sEV) carrier, red blood cell small extracellular vesicles (RBCsEVs), and normal pregnancy (NP) placental small extracellular vesicles (psEVs). An appropriate increase in insulin secretion was noted when EndoC-βH3 cells were exposed to 20 mM glucose compared to 1 mM glucose containing media for each condition. However, no differences were detected when comparing normal pregnancy psEVs to controls in either 1 mM glucose or 20 mM glucose containing media. Individual measures for sEV carrier controls (white), RBCsEVs (red), and normal pregnancy psEVs (purple) are shown. Differences were analysed using a two-way ANOVA, followed by Tukey's multiple comparisons test for individual group comparisons. Reproduced from *Seedat et al.*, *Clinical Science* (2024), with permission from Portland Press. This content is distributed under the Creative Commons Attribution License (CC BY 4.0).

7.3.4 Liquid chromatography-mass spectrometry of EndoC-βH3 cells treated with placental small extracellular vesicles

In order to identify possible mechanisms contributing to the upregulation of *INS* gene expression and insulin content conferred by psEVs, I conducted a LC-MS/MS experiment to evaluate the proteome of EndoC-βH3 cells following treatment with normal pregnancy psEVs, GDM psEVs, RBCsEVs, and the sEV Carrier control (n = 3 per group). I sought to understand whether psEVs alter the proteome of EndoC-βH3 cells and if any changes in protein abundance could mechanistically contribute to the alterations in *INS* transcription and insulin content. Given that *INS* transcription increased at 30 – 36 hours post-psEV treatment, for any protein to affect *INS* transcription its' abundance would need to be altered at an earlier time point to when we observed the changes in *INS* expression. Hence, I chose to evaluate the proteome of EndoC-βH3 cell at 24 hours after psEV treatments which was 6-12 hours prior to alterations in *INS* transcription.

The data underwent quality control evaluation prior to analysis. The log2 transformed distribution for each condition is shown in Figure 7.8. The principal component analysis demonstrated that samples used as controls (sEV carrier controls and RBCsEVs) each clustered together and were separated from psEV-treated samples. However, some overlap between the normal pregnancy and GDM psEV samples was noted (Figure 7.9). Hierarchical clustering analysis of the 25 proteins with the largest positive and negative log2 fold changes in psEV-treated cells compared to controls are shown in Figures 7.10 (normal pregnancy psEV compared to controls) and 7.11 (GDM psEV compared to controls), respectively.

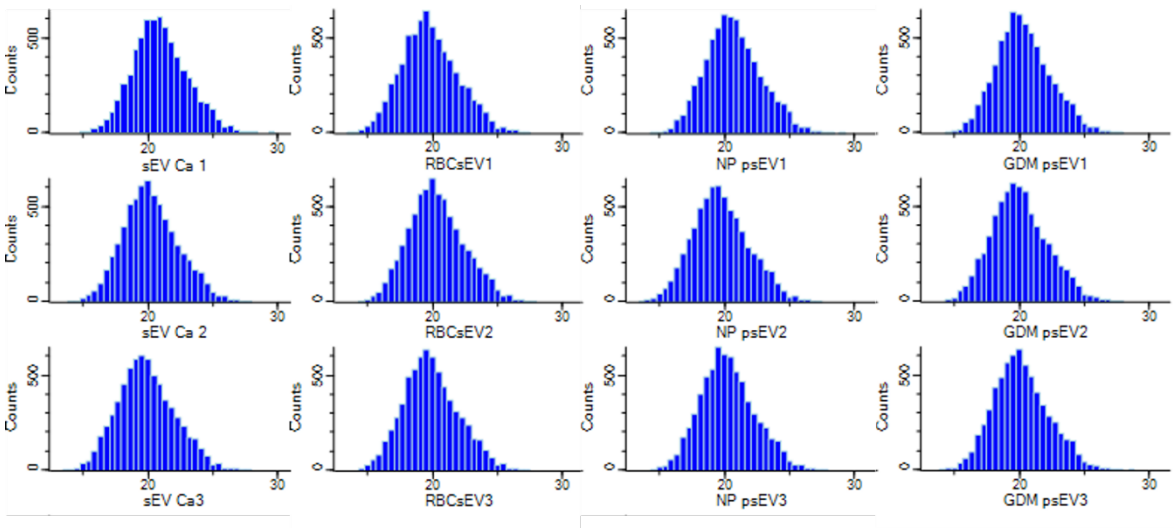

Figure 7.8. Histograms of normalised protein abundance for each condition which is normally distributed in all treatment conditions.

*GDM – gestational diabetes mellitus, NP – normal pregnancy, psEV – placental small extracellular vesicle, RBCsEV - red blood cell small extracellular vesicles, sEV Ca – small extracellular vesicle carrier control.

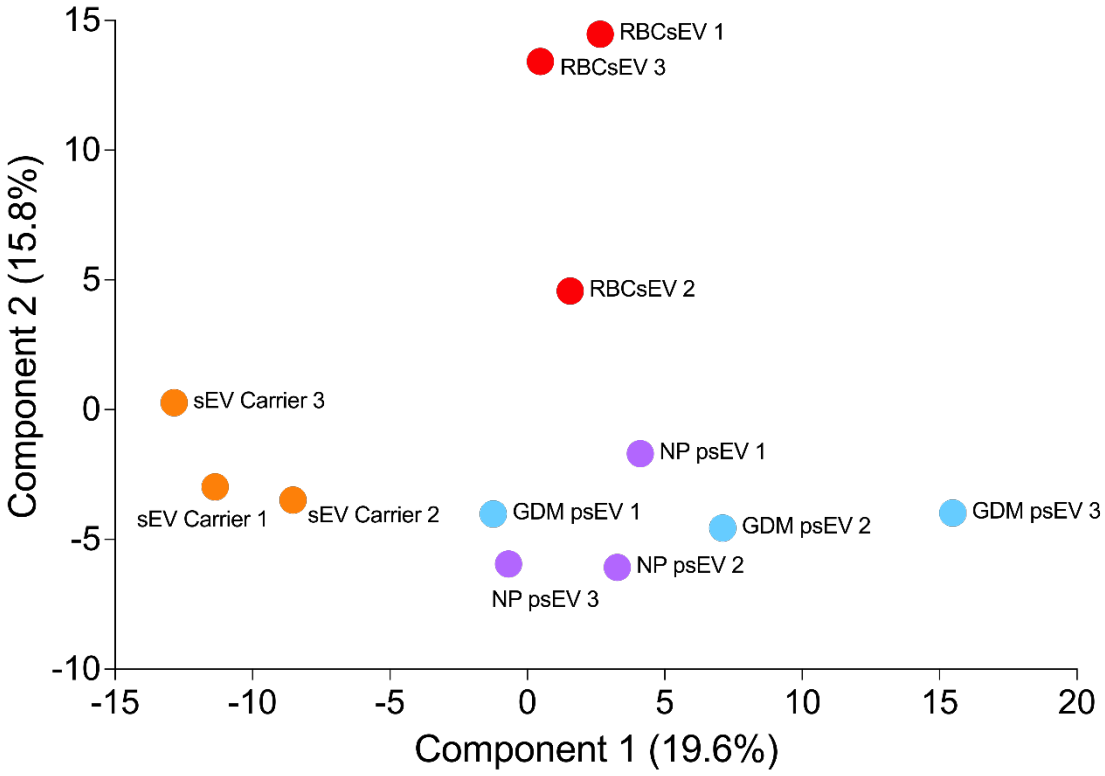

Figure 7.9. Principal component analysis showing clustering of proteomic profiles of all treatment conditions, – small extracellular vesicle (sEV) carrier controls (orange), red blood cell small extracellular vesicles (RBCsEVs) (red), normal pregnancy (NP) placental small extracellular vesicle (psEVs) (purple), and gestational diabetes mellitus (GDM) psEVs (blue). Reproduced from *Seedat et al.*, *Clinical Science* (2024), with permission from Portland Press. This content is distributed under the Creative Commons Attribution License (CC BY 4.0).

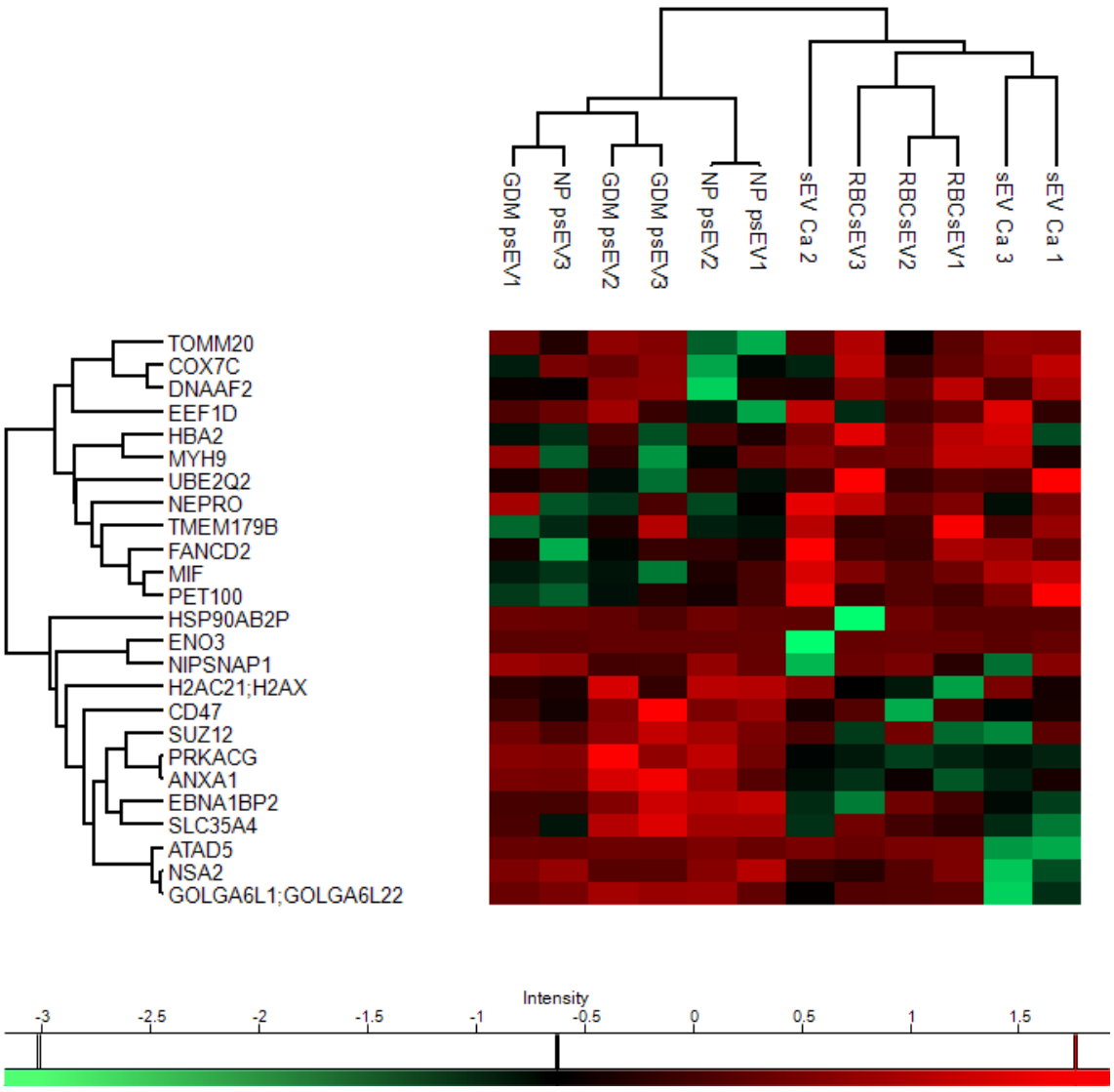

Figure 7.10. Hierarchical clustering of the 25 proteins with the greatest positive and negative log2 fold changes when comparing normal pregnancy (NP) placental small extracellular vesicles (psEVs) to controls (small extracellular vesicle carrier control (sEV Ca) and red blood cell small extracellular vesicles (RBCsEVs)). Warmer colours (red) represent higher expression, while cooler colours (green) indicate lower expression.

*GDM – gestational diabetes mellitus.

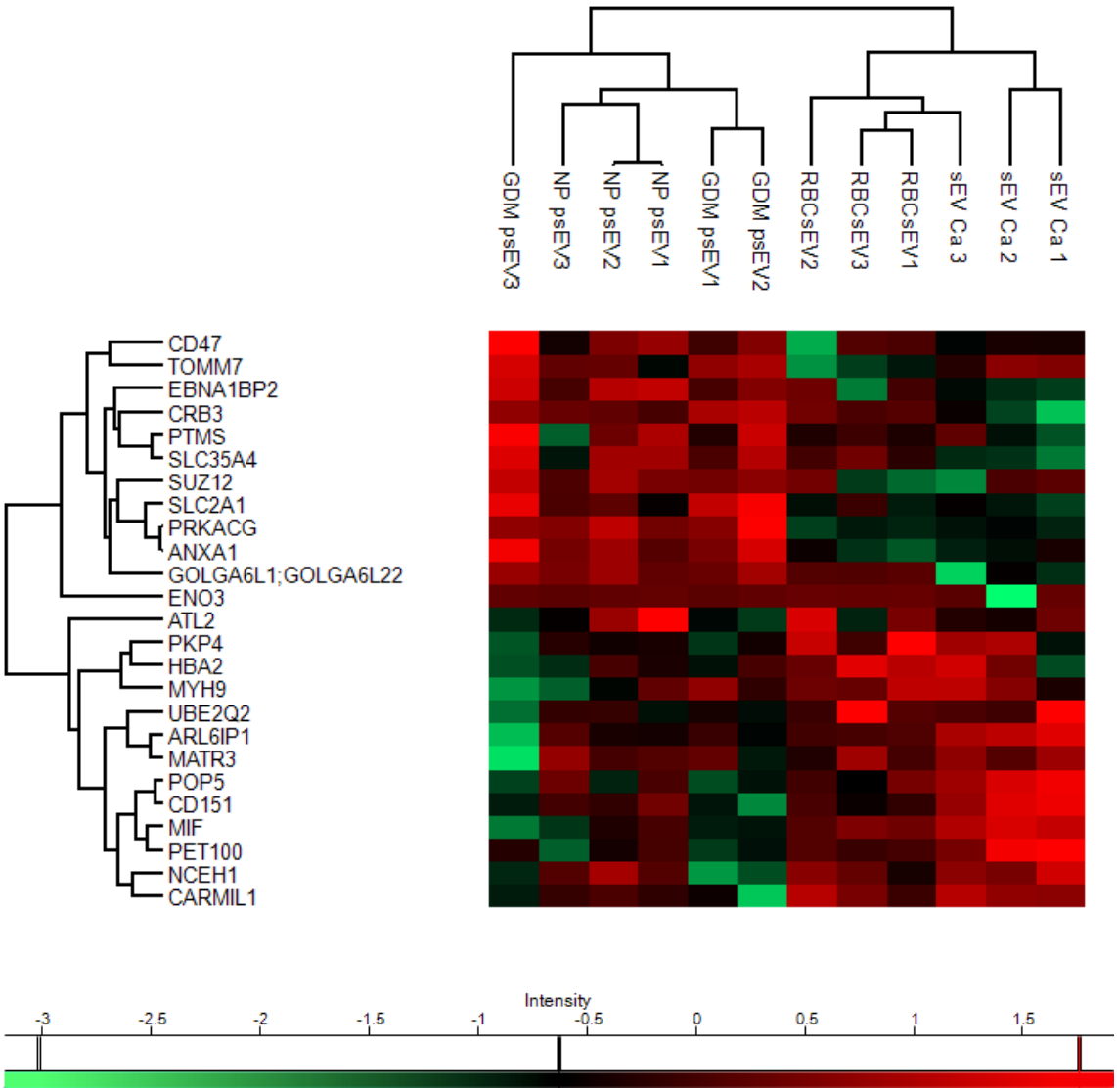

Figure 7.11. Hierarchical clustering of the 25 proteins with the greatest positive and negative log2 fold changes when comparing gestational diabetes mellitus (GDM) placental small extracellular vesicles (psEVs) to controls (small extracellular vesicle carrier control (sEV Ca) and red blood cell small extracellular vesicles (RBCsEVs)). Warmer colours (red) represent higher expression, while cooler colours (green) indicate lower expression.

*NP – normal pregnancy.

I then compared the treatment groups to determine if significant differences in protein expression were present. I compared protein abundance in psEV-treated cells to both the controls (sEV carrier and RBCsEV) and only considered proteins that were increased relative to both controls as significant. I observed that the abundance of Annexin A1 (ANXA1) and PRKACG were increased. Specifically, in normal pregnancy psEV-treated cells, ANXA1 abundance increased by a log2 FC of 1.85 (-log p-value = 2.02) compared to the sEV carrier control and by a log2 FC of 2.34 (-log p-value = 1.97) compared to RBCsEVs. In GDM psEV-treated cells, ANXA1 increased by a log2 FC of 2.92 (-log p-value = 2.11) compared to the sEV carrier control and by a log2 FC of 3.44 (-log p-value = 2.13) compared to RBCsEVs. PRKACG abundance increased by a log2 FC of 1.54 (-log p-value = 2.52) in normal pregnancy psEV-treated cells compared to the sEV carrier control and by a log2 FC of 1.75 (-log p-value = 2.67) in normal pregnancy psEV-treated cells compared to RBCsEVs. In GDM psEV-treated cells, PRKACG abundance increased by a log2 FC of 1.85 (-log p-value = 2.13) compared to the sEV carrier control and increased by a log2 FC of 2.06 (-log p-value = 2.27) compared to RBCsEVs. Additionally, in GDM psEV-treated cells, solute carrier family 2, facilitated glucose transporter member 1 (SLC2A1), also known as glucose transporter 1 (GLUT1), abundance was increased (log2 FC = 1.28, -log p-value = 3.24 compared to the sEV carrier control and log2 FC = 1.11, -log2 FC = 2.69 compared to RBCsEVs) (Figures 7.12 and 7.13). No differentially expressed proteins were detected when normal pregnancy and GDM psEVs were compared. Figure 7.14 displays a protein profile plot that illustrates protein abundance per sample, the differentially expressed proteins are highlighted. Protein network analysis did not reveal any connections among the differentially expressed proteins, suggesting they do not function as a coordinated physical subnetwork (Figure 7.15).

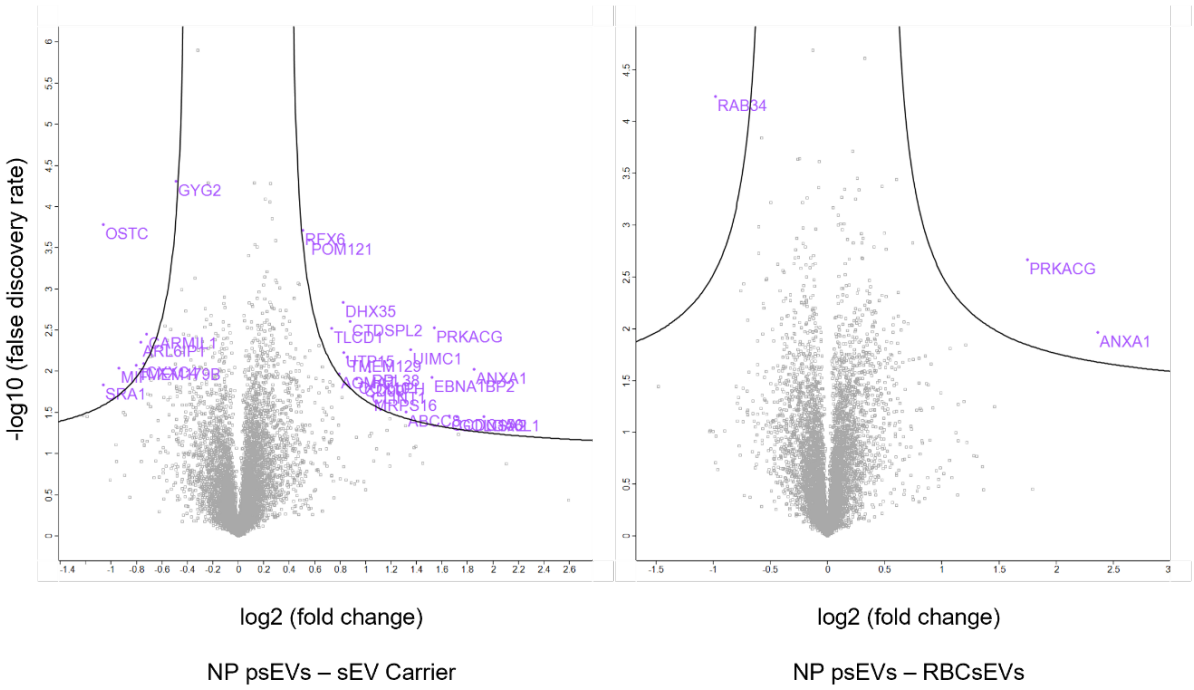

Figure 7.12. Volcano plots showing differentially expressed proteins when comparing EndoC-βH3 cells treated with normal pregnancy (NP) placental small extracellular vesicles (psEVs) to cells treated with controls (small extracellular vesicle (sEV) carrier control and red blood cell extracellular vesicles (RBCsEVs)). This analysis was conducted using n = 3 biological replicates for each group. Significance was determined using a false discovery rate (FDR) < 0.1, where FDR < 0.1 = -log 10 FDR > 1, and S0 = 0.2. Proteins that met both the FDR and fold change thresholds are highlighted, indicating those that are significantly upregulated or downregulated.

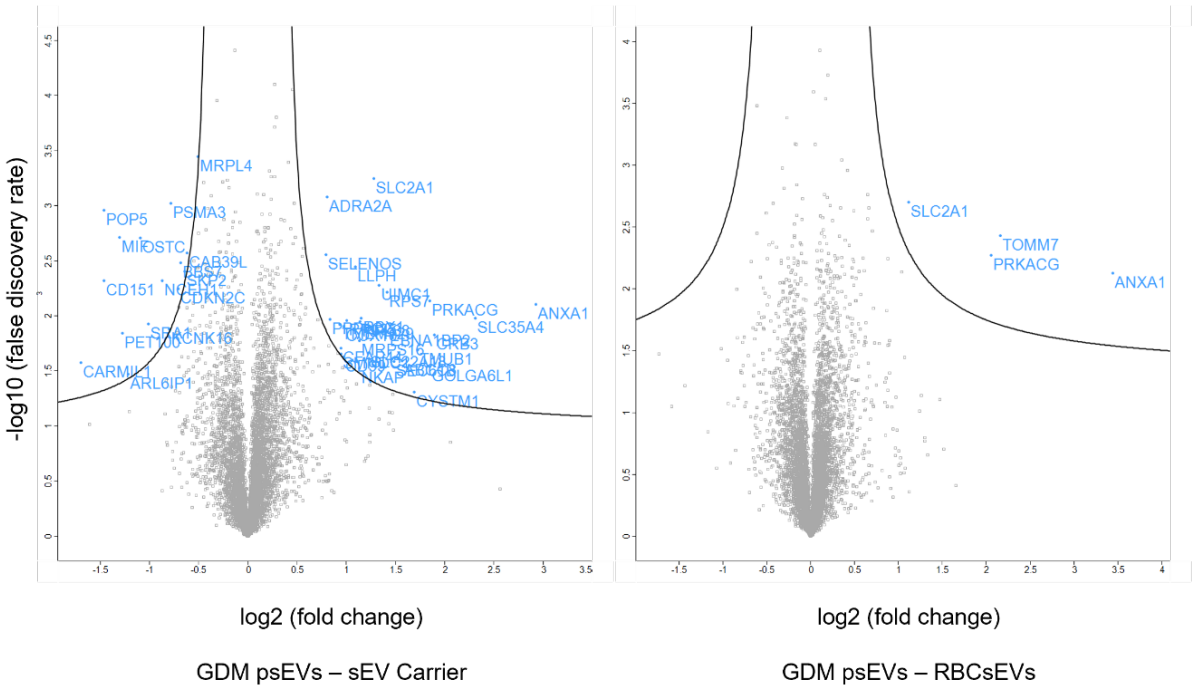

Figure 7.13. Volcano plots showing differentially expressed proteins when comparing EndoC-βH3 cells treated with gestational diabetes mellitus (GDM) placental small extracellular vesicles (psEVs) to cells treated with controls (small extracellular vesicle (sEV) carrier control and red blood cell extracellular vesicles (RBCsEVs)). This analysis was conducted using n = 3 biological replicates for each group. Significance was determined using a false discovery rate (FDR) < 0.1, where FDR < 0.1 = -log 10 FDR > 1, and S0 = 0.2. Proteins that met both the FDR and fold change thresholds are highlighted, indicating those that are significantly upregulated or downregulated.

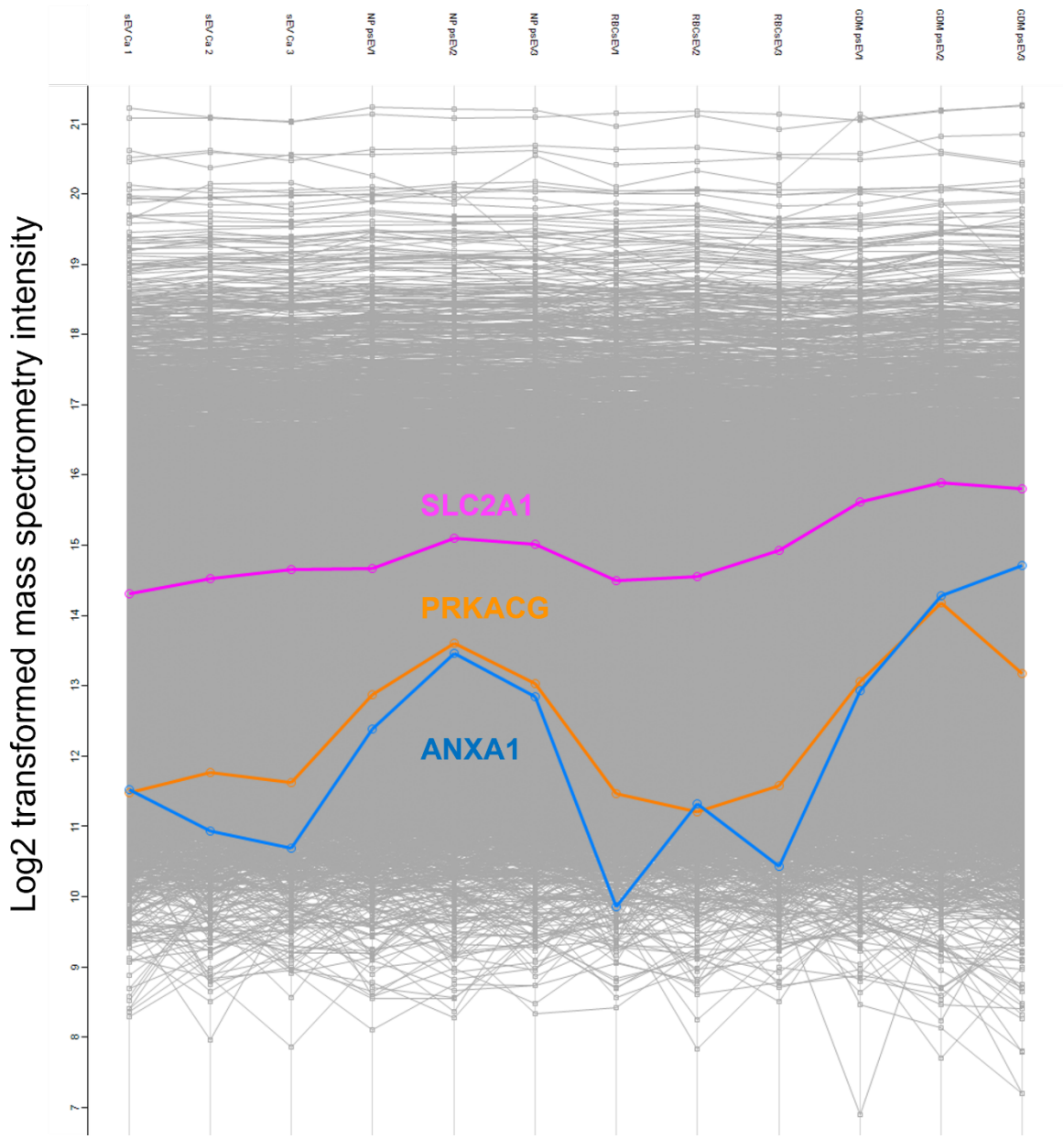

Figure 7.14. Protein profile plot of protein abundance per sample, profiles for the proteins in which differences in abundance were statistically significant are highlighted.

*ANXA1 - Annexin A1, GDM – gestational diabetes mellitus, NP – normal pregnancy, psEVs – placental small extracellular vesicles, PRKACG - Protein Kinase CAMP-Activated Catalytic Subunit Gamma, RBCsEVs – red blood cell extracellular vesicles, sEV Ca – small extracellular vesicle carrier control, SLC2A1 - Solute carrier family 2, facilitated glucose transporter member 1 (Glucose transporter 1).

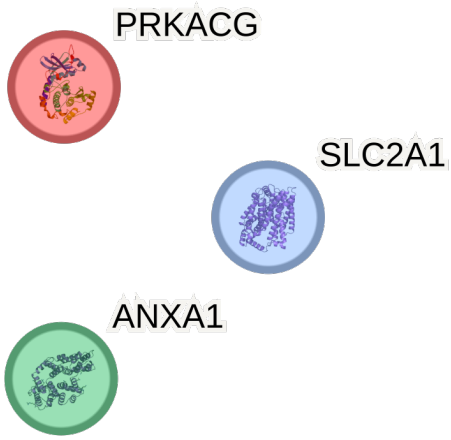

Figure 7.15. Protein network analysis using String DB. No physical subnetwork connections between proteins with statistically significant abundance were detected.

*ANXA1 - Annexin A1, PRKACG - Protein Kinase CAMP-Activated Catalytic Subunit Gamma, SLC2A1 - Solute carrier family 2, facilitated glucose transporter member 1 (Glucose transporter 1).

7.3.4 Liquid chromatography-mass spectrometry validation by immunoblotting

I aimed to validate the LC-MS/MS data in an independent replicate experiment with different biological samples using immunoblotting. Prior to purchasing antibodies, I began assessing the proteins of interest in detail to identify antibodies that could both detect and were specific to the protein of interest. Owing to the well-established link between protein kinase A (PKA), *INS* expression, and insulin synthesis (203) I first assessed PRKACG, the gamma catalytic subunit of PKA. The amino acid sequence of PRKACG is more than 80% similar with the alpha (PRKACA) and beta subunits (Protein Kinase CAMP-Activated Catalytic Subunit Beta (PRKCB)) (Figure 7.16) (203, 204). To select a PRKACG specific antibody, I compared the known immunogen of numerous commercial antibodies to the aligned amino acid sequences of PRKACG, PRKACA and PRKACB to identify a region where little sequence overlap was present (Figure 7.16). Two antibodies (Table 7.1) were selected based on specific regions which had the least sequence overlap, while a third was chosen due to positive previous experience with antibodies from the same manufacturer (205). These antibodies were tested against recombinant full-length PRKACA protein (H00005566-P01) to determine antibody specificity, and all three antibodies were not specific to PRKACG as they detected the recombinant PRKACA protein. An anti-PRKACA antibody (Table 7.1) also produced a band at the same molecular weight as the three anti- PRKACG antibodies (Figure 7.17). Hence, it was unlikely that a commercial antibody was available that could reliably detect PRKACG and validating the increase in PRKACG expression in psEV treated EndoC-βH3 cells, detected by LC-MS/MS, using immunoblotting would not be possible.

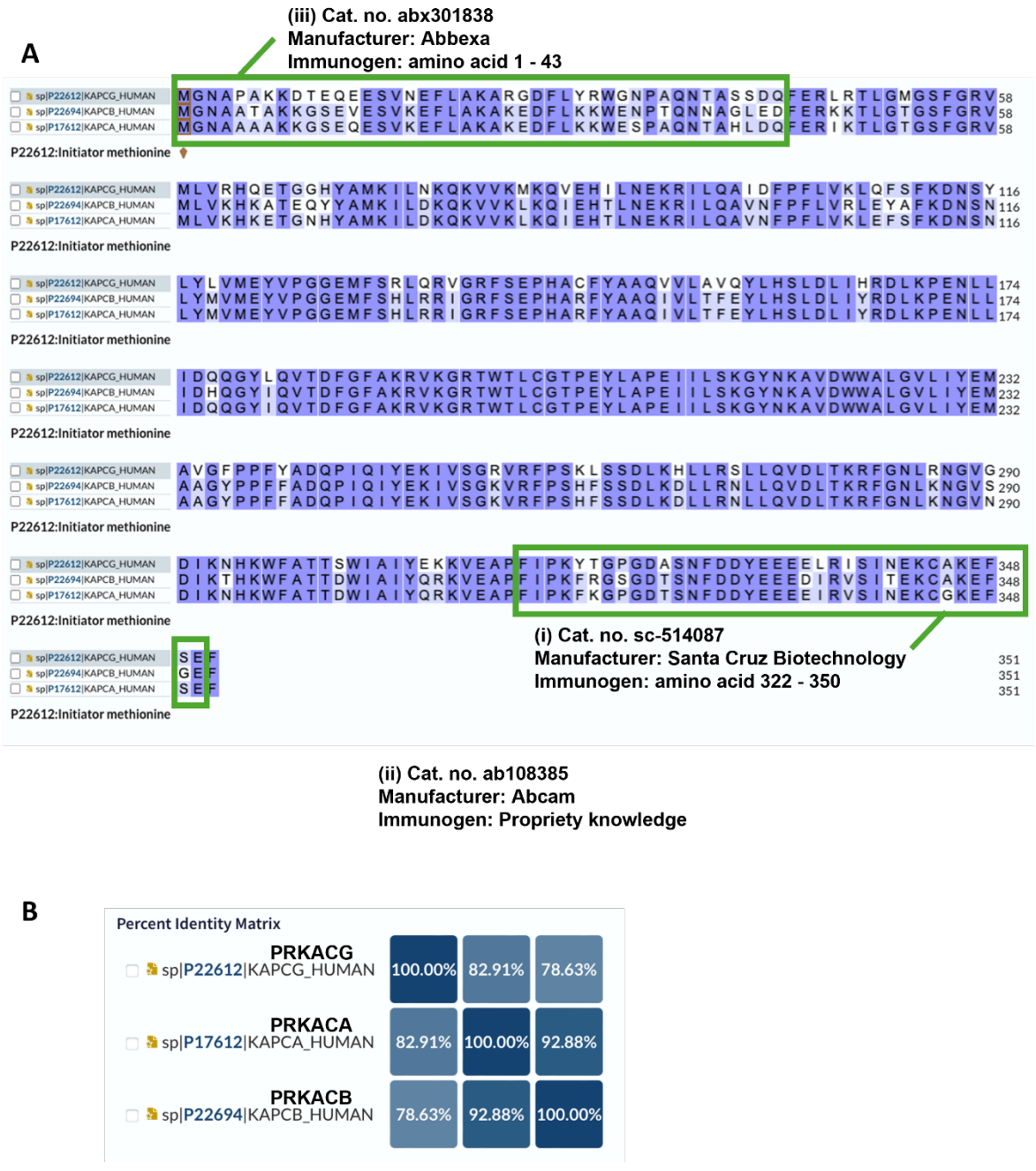

Figure 7.16. A. Protein alignment generated using UniProt demonstrating similarities in amino acid sequences between PKA catalytic subunits, PRKACG Protein Kinase CAMP-Activated Catalytic Subunit Gamma) (top), Protein Kinase CAMP-Activated Catalytic Subunit Beta (PRKACB) (middle), and Protein Kinase CAMP-Activated Catalytic Subunit Alpha (PRKACA) (bottom) (206). The details of the antibodies used and the immunogens against which they were raised are provided and indicted in green boxes on the amino acid

alignment. **B.** Percentage identity matrix generated using UniProt showing percentage similarity between PRKACG, PRKACA, and PRKACB (206).

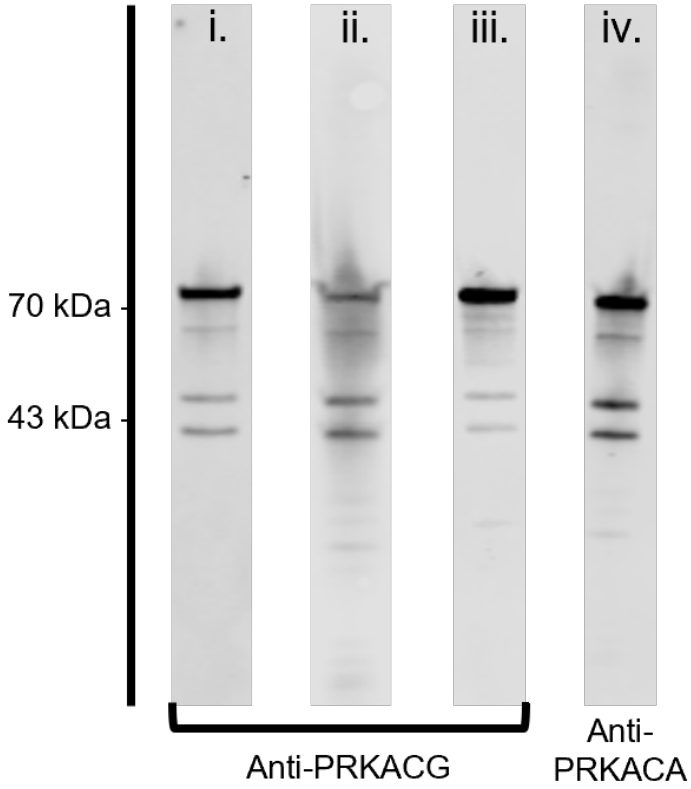

Figure 7.17. Immunoblot of recombinant Protein Kinase CAMP-Activated Catalytic Subunit Alpha (PRKACA) protein (H00005566-P01) using anti- Protein Kinase CAMP-Activated Catalytic Subunit Gamma (PRKACG) antibodies: i. sc-514087 (Santa Cruz Biotechnology USA), ii. ab108385 (Abcam UK), iii. abx301838 (Abbexa UK), and the iv. Anti- PRKACA antibody (67491-1-IG, Proteintech USA). A band at the predicted molecular weight of PRKACA + GST tag (70 kDa) is seen for all antibodies used, demonstrating non-specific binding by anti- PRKACG antibodies to the PRKACA recombinant protein. Molecular weight markers in kDa is shown as a ladder on the left. Reproduced from *Seedat et al.*, *Clinical Science* (2024), with permission from Portland Press. This content is distributed under the Creative Commons Attribution License (CC BY 4.0).

7.3.5 Validation of initial experiment by repeat liquid chromatography-mass spectrometry

Owing to the inability to validate a commercial antibody to reliably identify PRKACG, and considering that ANXA1 belongs to a family of 12 proteins with sequence similarities of more than 50% (207) it was clear that immunoblotting would not be suitable for validating the LC-MS/MS findings. After conducting a replicate experiment with different biological samples (n = 4 per treatment group), I once again utilised LC-MS/MS to analyse the proteome of psEV-treated EndoC-βH3 cells, aiming to validate the results from the original experiment.

In the replicate experiment, ANXA1 was once more upregulated in EndoC-βH3 cells treated with normal pregnancy psEVs relative to the sEV carrier (log2 FC = 3.25, -log p-value = 3.20) and RBCsEVs (log2 FC = 3.45, -log p-value = 2.59), as well as in GDM psEVs relative to the sEV carrier (log2 FC = 3.76, -log p-value = 4.17) and RBCsEVs (log2 FC = 3.96, -log p-value = 3.16). In GDM psEV treated cells, although SLC2A1 (GLUT1) abundance was increased relative to the sEV carrier control (log2 FC = 2.12, -log p-value = 2.97) it was not above the S0 threshold of significance, moreover it was not increased relative to RBCsEVs (log2 FC = 0.78, -log p-value = 1.14). PRKACG was not detected in any samples. Other differentially expressed proteins were also observed in this experiment (Figure 7.18 and 7.19). However, these were not considered for further analysis, as their abundance was unchanged during the initial LC-MS/MS experiment and hence changes in their abundance had not been replicated across experiments. Figure 7.20 displays a protein profile plot from the validation replicate experiment that illustrates protein abundance per sample. The differentially expressed proteins from the original experiment are highlighted. Based on the results of the validation experiment, only ANXA1 was consistently increased by psEV

treatments across multiple experiments. After combining the samples size from the two replicate experiments, the total number of biological replicates used to demonstrate an upregulation of ANXA1 in EndoC-βH3 cells following psEV-treatments totalled n = 7. This was greater than the minimum sample size suggested would be needed to detect statistically significant differences in protein abundance by the initial sample size calculation.

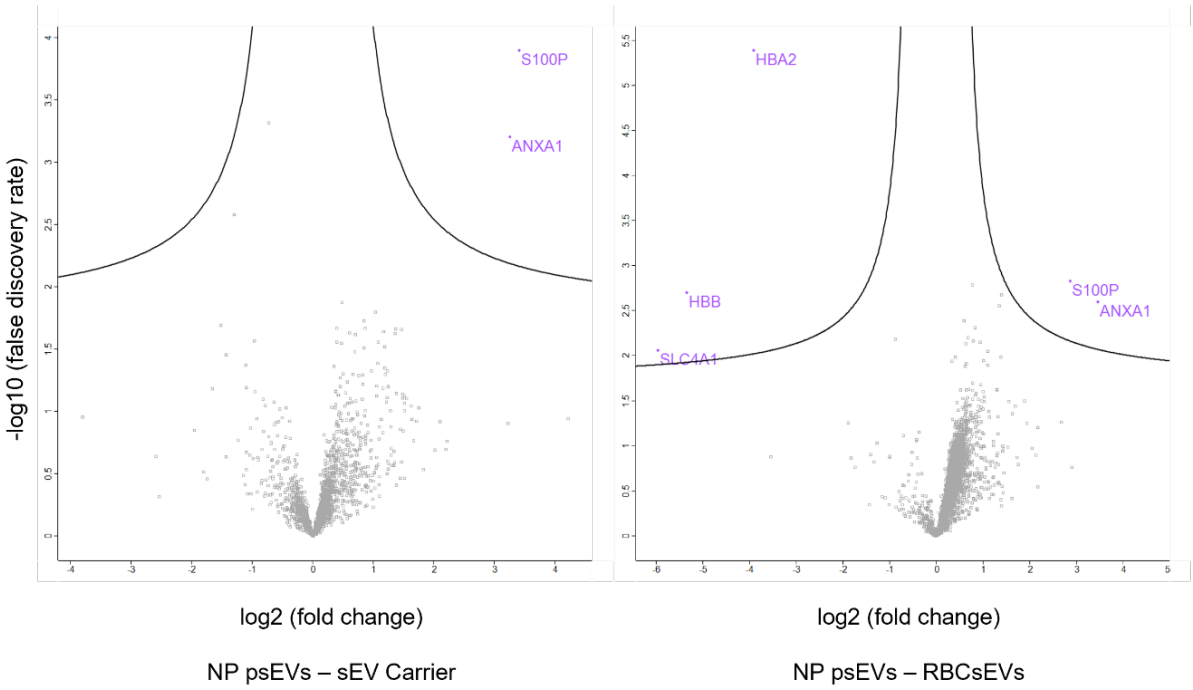

Figure 7.18. Volcano plots showing differentially expressed proteins from the validation replicate liquid chromatography-mass spectrometry experiment (experiment 2) which was conducted to replicate and validate the findings from the first experiment. Cells treated with normal pregnancy (NP) placental small extracellular vesicles (psEVs) were compared to cells treated with controls (small extracellular vesicle (sEV) carrier control and red blood cell extracellular vesicles (RBCsEVs)). This experiment used a different set of biological replicates, with n = 4 biological replicates for each group. Significance was determined using a false discovery rate (FDR) < 0.1, where FDR < 0.1 = -log 10 FDR > 1, and S0 = 0.2. Proteins that met both the FDR and fold change thresholds are highlighted, indicating those that are significantly upregulated or downregulated.

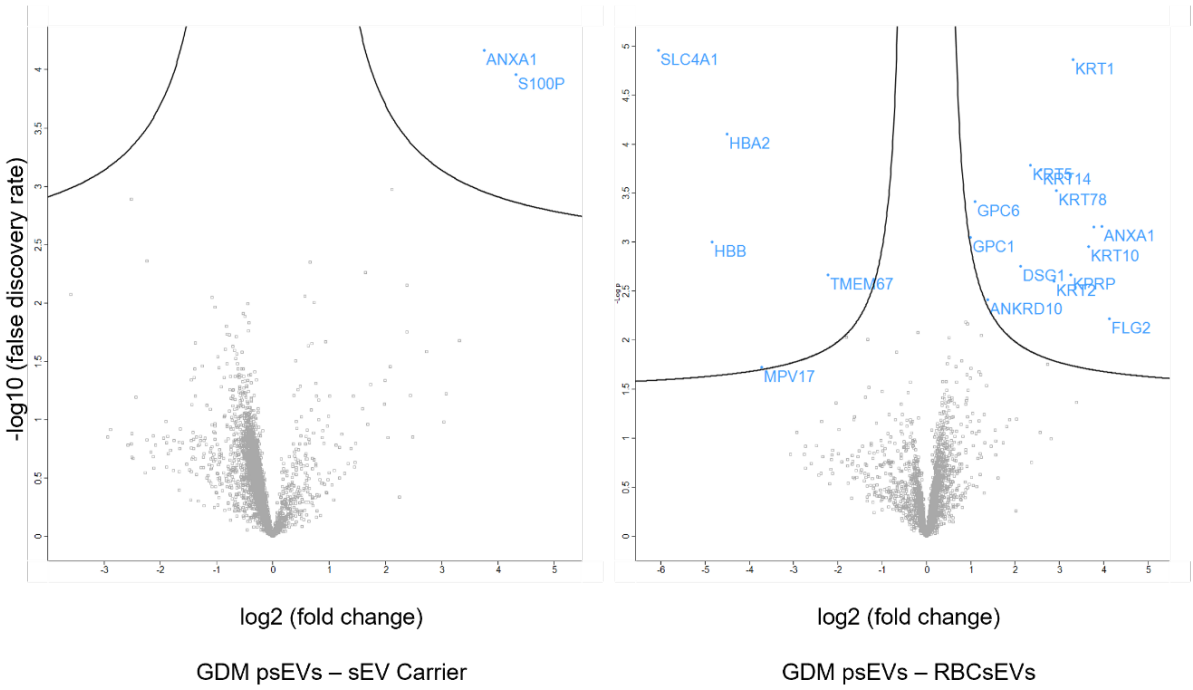

Figure 7.19. Volcano plots showing differentially expressed proteins from the validation replicate liquid chromatography-mass spectrometry experiment (experiment 2) which was conducted to replicate and validate the findings from the first experiment. Cells treated with gestational diabetes mellitus (GDM) placental small extracellular vesicles (psEVs) were compared to cells treated with controls (small extracellular vesicle (sEV) carrier control and red blood cell extracellular vesicles (RBCsEVs)). This experiment used a different set of biological replicates, with n = 4 biological replicates for each group. Significance was determined using a false discovery rate (FDR) < 0.1, where FDR < 0.1 = -log 10 FDR > 1 and S0 = 0.2. Proteins that met both the FDR and fold change thresholds are highlighted, indicating those that are significantly upregulated or downregulated.

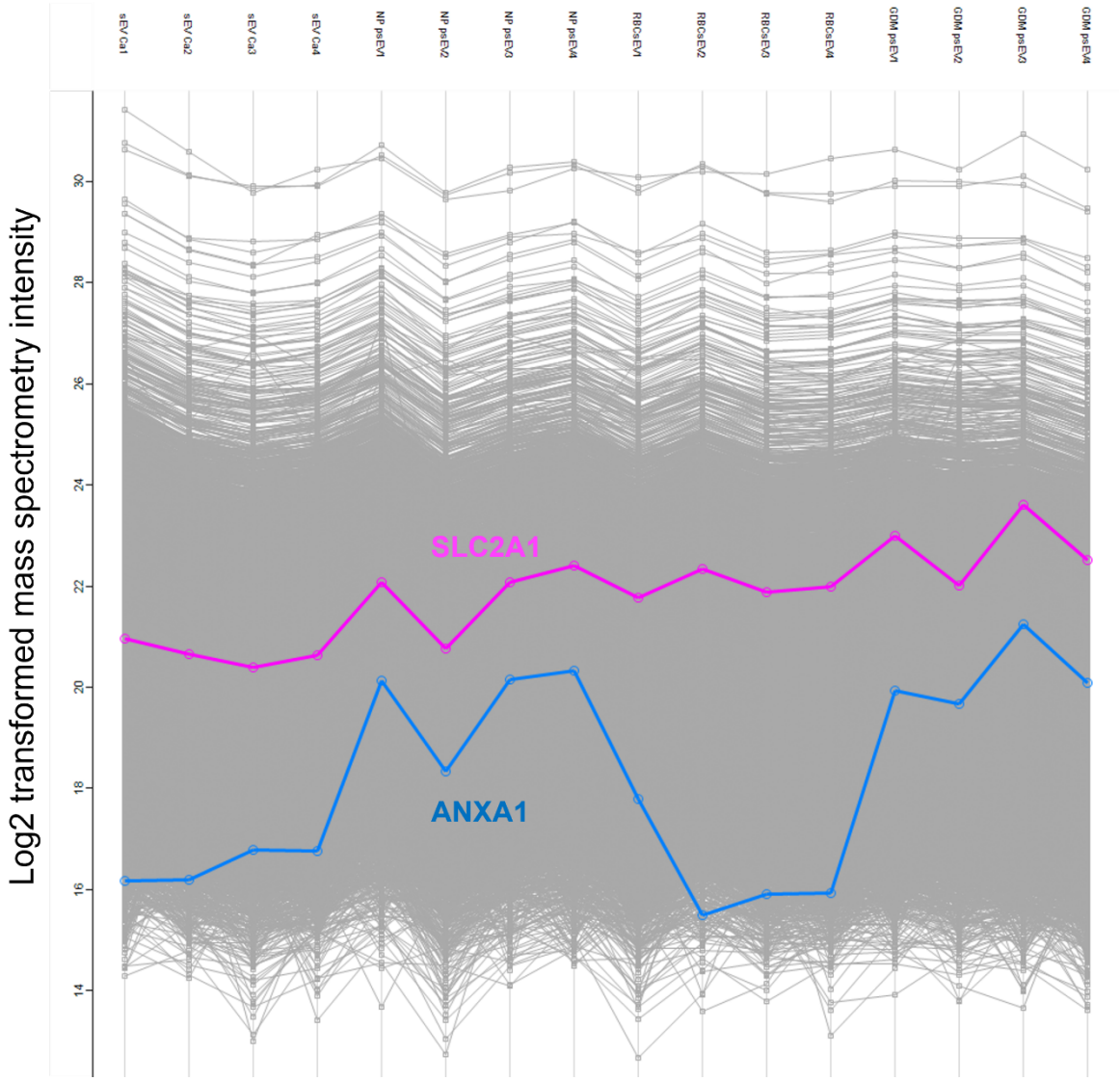

Figure 7.20. Protein profile plot of protein abundance per sample from the validation replicate experiment. Profiles for proteins in which differences in abundance were statistically significant in the first liquid chromatography-mass spectrometry experiment, are highlighted. Protein Kinase CAMP-Activated Catalytic Subunit Gamma (PRKACG) is not shown as it was not detected in the replicate experiment.

*ANXA1 - Annexin A1, GDM – gestational diabetes mellitus, NP – normal pregnancy, psEVs – placental small extracellular vesicles, RBCsEVs – red blood cell extracellular vesicles, sEV Ca – small extracellular vesicle carrier control, SLC2A1 - Solute carrier family 2, facilitated glucose transporter member 1 (Glucose transporter 1).

7.3.6 Placental small extracellular vesicles are enriched for placental alkaline phosphatase and chorionic somatomammotropin hormone-like 1

My aim was to determine whether psEVs could be detected in islets from pregnant women. Building on the data showing psEV internalisation by EndoC-βH3 cells, I utilised PLAP, a psEV-specific marker, to represent psEVs *in vivo*. Additionally, I sought to identify a second placental-specific marker to further confirm psEV presence within pancreatic islets from pregnant women *in vivo*. Upon reviewing the placenta-specific proteome in the Human Protein Atlas database, I identified CSHL1 as a placental-specific protein detected in the syncytiotrophoblast layer, making it a suitable marker for placental specificity of psEVs (208). To ensure that both these markers could reliably represent psEVs in the IHC-IF analysis, I first confirmed, by immunoblotting, that psEVs were enriched for CSHL1 (Figure 7.21). While I had already demonstrated PLAP enrichment in psEVs in Chapter 5 using a polyclonal anti-PLAP antibody, the new data presented here, using a monoclonal anti-PLAP antibody, reaffirms this finding (Figure 7.21).

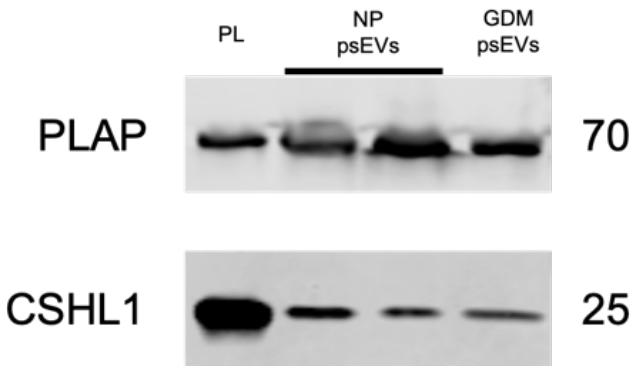

Figure 7.21. Immunoblot of normal pregnancy (NP) and gestational diabetes mellitus (GDM) placental small extracellular vesicles (psEVs) showing that they are enriched for the placental specific markers placental alkaline phosphatase (PLAP) and chorionic somatomammotropin hormone-like 1 (CSHL1). Placental lysate (PL) is used as a positive control. The molecular weight in kDa is shown for each protein.

7.3.7 Immunofluorescence to detect the presence of placental small extracellular vesicle specific markers in islets from pregnant women

PLAP and CSHL1 protein was detected in the syncytiotrophoblast layer of FFPE placental tissue, which were processed in parallel to the pancreas sections, and served as a positive control to demonstrate efficacy of the antibody under the same experimental conditions (Figure 7.22). However, no signal for PLAP or CSHL1 was detected within any pancreatic islets in the FFPE pancreatic tissue sections (Figure 7.23).

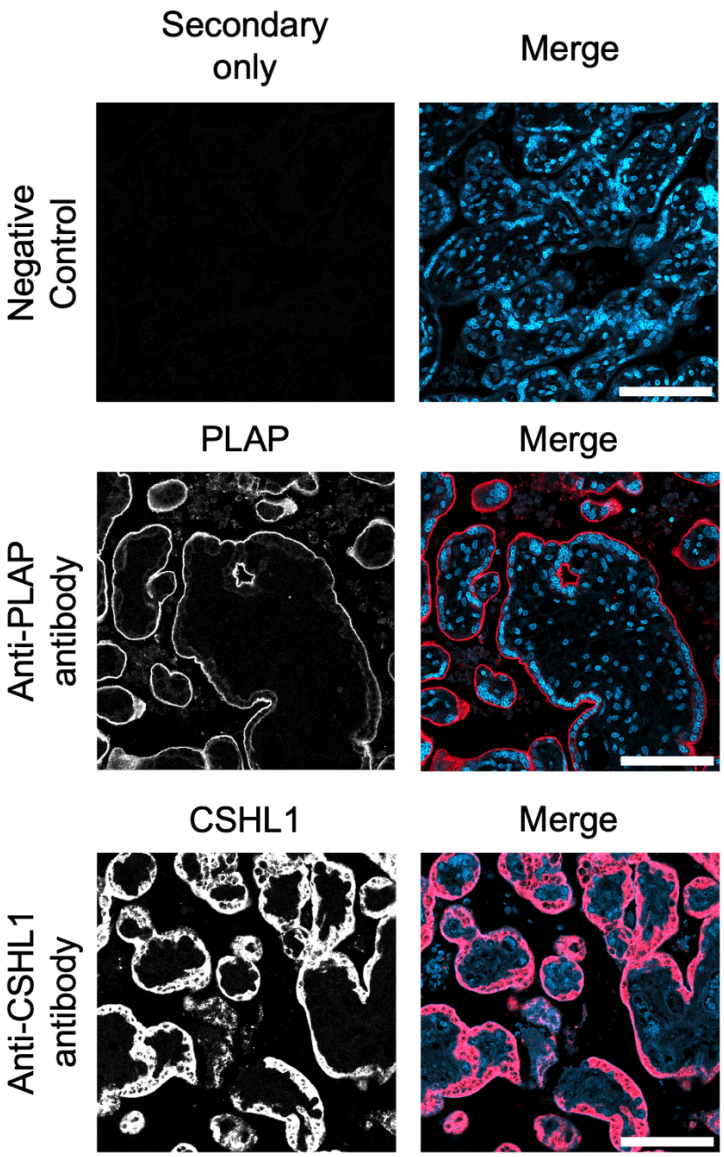

Figure 7.22. Immunofluorescence staining was performed on formalin-fixed, paraffin-embedded placental tissue sections. The syncytiotrophoblast layer was labelled with antibodies against placental alkaline phosphatase (PLAP) and chorionic somatomammotropin hormone-like 1(CSHL1), with no detectable signal observed in the secondary antibody-only control. Grayscale images for the negative control, PLAP, and CSHL1 channels are presented, while a composite colour image displays the merged signals (nuclei are labelled by DAPI in blue, and PLAP/CSHL1 in red). Scale bar = 100 μm.

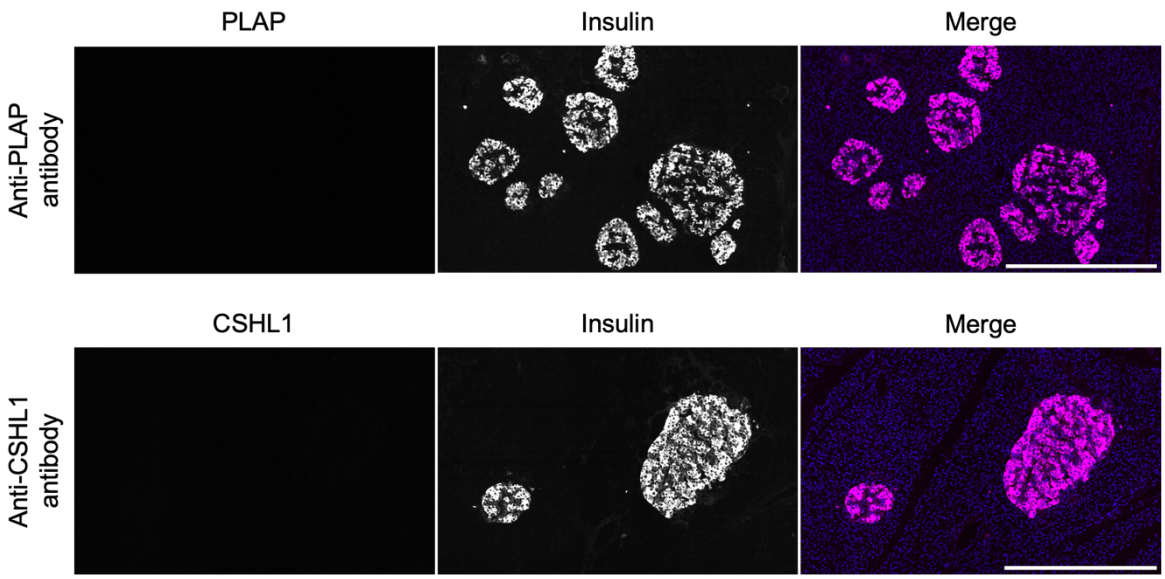

Figure 7.23. Immunofluorescence analysis was performed on formalin-fixed, paraffin-embedded pancreatic tissue sections from pregnant women. No signal for the placental small extracellular vesicles (psEV) specific proteins, placental alkaline phosphatase (PLAP) and chorionic somatomammotropin hormone-like 1(CSHL1), was detected in any islets across the entire tissue section. A representative image of a few islets is shown. Grayscale images for the PLAP, CSHL1, and insulin (representing islets) channels are provided, alongside a colour merged image (nuclei are labelled by DAPI in blue, insulin in magenta, and PLAP/CSHL1 in red). Scale bar = 500 µm.

7.3.8 Re-evaluation of proteomics data from human islets for the presence of and quantification of Annexin A1 abundance in islets from pregnant women

I sought to determine whether the findings from *in vitro* studies using psEVs and EndoC-βH3 cells were replicated *ex vivo*. Having already conducted high-quality LC-MS/MS analysis on pancreatic islets from pregnant women (Chapter 3), I re-examined the dataset to assess whether ANXA1 could be reliably detected in the islets and, if so, whether the abundance of ANXA1 was increased in samples from pregnant women, consistent with the *in vitro* data.

ANXA1 was consistently detected by LC-MS/MS within all the islets samples isolated from pregnant and non-pregnant women (Figure 7.24). However, no difference in abundance was observed between islets isolated from pregnant women versus non-pregnant controls (log2 FC = -0.3, -log p-value = 0.612179).

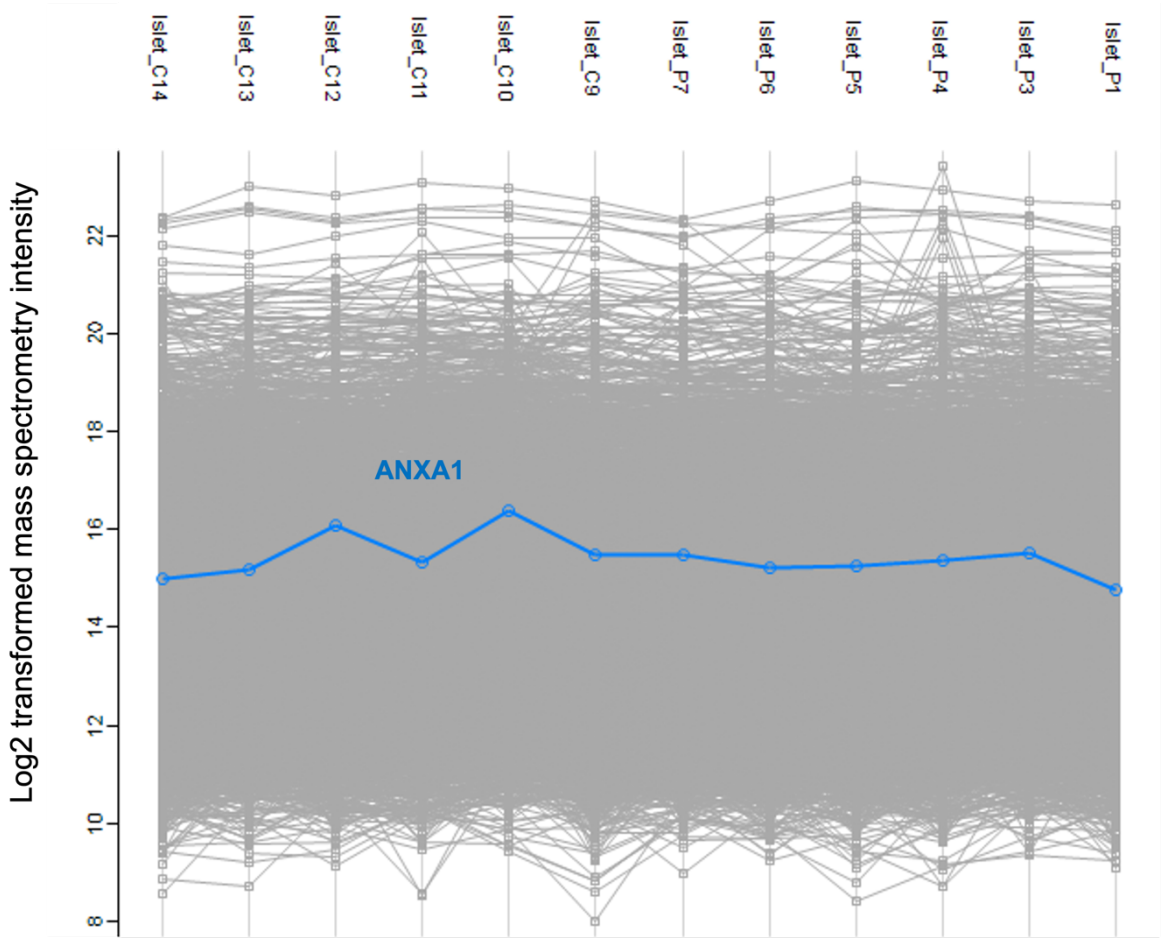

Figure 7.24. Protein profile plot of protein abundance per sample from the liquid chromatography-mass spectrometry of islets isolated by laser capture microdissection from pregnant women (P) and non-pregnant controls (C). The profiles for Annexin A1 (ANXA1) is highlighted showing that ANXA1 was consistently detected in all samples.

7.4 Discussion

In this chapter, I investigated the effect of psEVs on insulin gene expression, synthesis and secretion in a human β cell line. The results demonstrate that psEVs from normal pregnancy and GDM placentae upregulate *INS* expression and increase β-cell insulin content. However, there was no detected change in insulin secretion. Additionally, the protein ANXA1 was upregulated in EndoC-βH3 cells following treatment with psEVs which occurs at an earlier time point to the observed increases of *INS* and insulin content. The increase in ANXA1 following psEV treatments may mechanistically explain the psEV associated increases in *INS* transcription and insulin content.

Insulin secretion and the number of circulating psEVs both increase as pregnancy progresses, with higher levels observed in women with GDM compared to those with normal pregnancy (57). Despite this association, the impact of psEVs on β cells is not well-documented. In pancreatic islets from mice infused for four days with psEVs, isolated from the plasma of women with normal pregnancy and GDM, insulin secretion increased in the normal pregnancy group, but no change in secretion was seen in the GDM group (85). miR-320b was found to be differentially expressed in GDM versus normal pregnancy psEVs isolated from human placental explants. On transfecting mouse islets and β cells with miR-320b a decrease in GSIS was observed but no changes in insulin synthesis or content were noted (66).

The data I report in this study is the first to show that both normal pregnancy and GDM psEVs enhance *INS* transcription and increase insulin content in human β cells. However, unlike previous studies (66, 85), no increase in GSIS was observed following treatment with normal pregnancy psEVs. Additionally, no differences were found between the effects of

normal pregnancy and GDM psEVs, suggesting that their impact on insulin biosynthetic pathways is similar. This finding contrasts with previous observations in mice (66, 85), where only normal pregnancy psEVs increased GSIS, while GDM psEVs reduced it. The lack of a significant effect on GSIS despite increased insulin content suggests that psEVs primarily modulate insulin synthesis rather than secretion dynamics.

The contrasts between the data presented in this chapter and previously published data may be explained by several reasons. The studies using mice models primarily examined insulin secretion rather than changes in insulin content. Changes in insulin synthesis and secretion may not directly correlate, hence observed differences in secretion cannot be extrapolated to expect differences in insulin content. This may explain why I observed no differences in *INS* transcription or insulin content between cells treated with normal pregnancy and GDM psEVs despite mice studies observing increased insulin secretion following normal pregnancy psEV treatments and no effect after GDM psEV treatments. Additionally, the lack of an effect on GSIS by psEVs and the similar effect conferred by normal pregnancy and GDM psEVs on *INS* gene transcription and insulin content, may also be attributed to the inherent biological distinctions between human and mouse β cells and their differing behaviour during mouse versus human pregnancy (114, 119). Furthermore, previous mouse studies used whole islets rather than isolated β cells. In whole islets, β-cell function could be influenced by paracrine signalling from other islet cell types or the surrounding islet microenvironment (8). Moreover, observed differences may be explained by the varying methodologies used to isolate psEVs. In the murine studies, psEVs were isolated from human plasma and human placental explants. I isolated psEVs using placental perfusion from a fresh placenta immediately following delivery, aiming to mimic the physiology of pregnancy. sEVs isolated from plasma samples may be contaminated with sEVs from other

sources, such as lipoproteins or other nano-sized particles. EVs from placental explants, which are cultured over days, may be affected by the placental viability and culture conditions (70, 73).

It is a limitation that I did not perform GSIS on EndoC-βH3 cells treated with GDM psEVs. However, since I observed no differences in the effects on *INS* expression or insulin synthesis between normal pregnancy and GDM psEVs, I deemed it unlikely that GDM psEVs would affect GSIS as normal pregnancy psEVs had no effect on insulin secretion. Given the expense of insulin ELISA assays, I allocated resources to validating the LC-MS/MS results instead of performing GSIS on EndoC-βH3 cells treated with GDM psEVs.

I found that *INS* expression remained unchanged in high glucose media following psEV treatments. This implies that elevated blood sugar levels negate the impact of psEVs on insulin biosynthesis observed in β cells cultured in normal glucose media. This data illustrates that glucotoxicity diminishes psEV-induced upregulation of *INS* and insulin synthesis, which potentially explains the β-cell dysfunction observed in patients with GDM. This also clarifies why patients with GDM, who experience hyperglycaemia due to insulin resistance, show impaired β-cell function despite the similar effects of psEVs from women with normal pregnancies and those with GDM (10).

I observed that psEVs increased ANXA1 expression in β cells, followed by increases in *INS* expression and insulin content. ANXA1, a 37 kDa protein belonging to the annexin superfamily, is known for its anti-inflammatory effects (207). It is found in circulation and also localises to the cell membrane, cytoplasm, and nucleus (209). ANXA1 is linked to β-cell function and glucose homeostasis, with higher levels observed in type 2 diabetes-related

obesity (210). In a murine model, ANXA1 has been identified as a key mediator of glucose homeostasis. ANXA1 knockout (ANXA1-/-) mice fed a high sugar, high-fat diet exhibited greater glucose intolerance compared to wild-type high-fat diet fed mice. Treatment with human recombinant ANXA1 improved glucose levels and OGTT results in high-fat diet fed ANXA-/- mice (211). In rat islets, ANXA1 is colocalised with insulin-containing secretory vesicles and found at high levels within the cytosol and nucleus (212). Glucose-induced phosphorylation at ANXA1's serine residue is associated with increased insulin secretion (212). In MIN6N8a cells, a mouse pancreatic β cell line, ANXA1 was shown to enhance the second phase of insulin secretion by mobilising insulin vesicles and regulate insulin secretion through cell surface receptor binding (213, 214). Similar findings were reported in rat islets (215, 216). Notably, insulin content was higher in rat islets co-cultured with ANXA1 for 72 hours compared to controls (216).

In immune cells, ANXA1 activates the G-protein coupled formyl peptide receptor 2 in an autocrine/paracrine manner (207). In rat islets, intracellular ANXA1 stimulates insulin secretion in an autocrine fashion (215). Additionally, intracellular ANXA1 may alter cell function through nuclear translocation, with both intra- and extracellular ANXA1 potentially translocating to the nucleus (209, 217). Nuclear translocation can occur in response to DNA damage, proliferative/mitogenic stimuli or phosphorylation (209, 217). ANXA1 contains a sequence capable of binding to DNA and/or RNA and exhibits helicase activity within the nucleus, which is essential for DNA replication and repair (217) and can regulate both transcription factors and downstream gene expression (209, 218). Cell proliferation was reduced in MIN6N8a cells with siRNA knockdown of ANXA1 expression, and ANXA1 protein expression correlated with cell cycle proteins cyclin D1, cyclin E, and cyclin-dependent kinase 2 (CDK2) (219). In an overexpression model, ANXA1 regulated

miR-26b expression (218). miR-26 is implicated in *INS* expression, with miR-26 knockdown downregulating insulin promoter activity and insulin mRNA synthesis (220). The current literature on ANXA1 indicates that it could be a particularly intriguing target in β cells, with a possible mechanistic link between psEV-induced ANXA1 expression and *INS* expression. However, further research is needed to clarify this relationship before definitive conclusions can be made. Understanding the interaction between psEV-induced upregulation of ANXA1 and the resulting increase in insulin synthesis could offer new avenues for developing therapies to treat diabetes.

I also investigated whether psEVs could be detected within pancreatic islets from pregnant women and whether the increase in ANXA1 abundance observed *in vitro* was similarly present *ex vivo*. Following the use of IHC-IF to analyse FFPE pancreas tissue from pregnant women, psEV-specific proteins, PLAP and CSHL1, were not detected in the pancreatic islets. This may be due to degradation of these proteins by islet cells upon psEV entry or their presence being delivered by psEVs at levels too low to be detected by IHC-IF. Alternatively, using psEV specific C19 miRNA, as shown in Chapter 5, could be a more effective marker for psEVs. The amplification capability of RT-qPCR may increase the likelihood of detecting this psEV specific marker (221). However, I chose not to perform RT-qPCR on the pancreatic islets I had isolated, as they were FFPE tissue samples, and it is well described that FFPE tissue processing and sample storage results in highly degraded RNA (222). For future studies, islets preserved in RNAlater or fresh-frozen tissue would be more suitable for RNA analysis.

While ANXA1 was detected in both pregnant and non-pregnant islets by LC-MS/MS, no increase in ANXA1 abundance was observed in the islets from pregnant women. This could

be because the protein profiles of whole islets were analysed by LC-MS/MS which lacked the single-cell resolution necessary to distinguish differences in protein levels between different islet cell types. I observed an increase in ANXA1 abundance in EndoC-βH3 cells, which specifically represent β cells. Future work will focus on using single-cell resolution techniques, such as single cell proteomics (223), to quantify ANXA1 expression in human pregnancy islets. If IHC-IF is employed, it is essential to first robustly validate the anti-ANXA1 antibody before applying it to tissue sections from pregnant women.

The strengths of the studies in this chapter include the use of a human model system, specifically psEVs isolated from fresh human placentae and the use of a human β cell line. Additionally, employing a placental perfusion-based system employs a physiologically representative method to isolate psEVs and minimises contamination from other sources of sEVs. While psEVs are detectable in the plasma of pregnant women, investigating their effects on maternal pancreata *ex vivo* presents significant ethical and practical challenges associated with studying pregnant human subjects. Therefore, I employed an *in vitro* experimental design. However, this approach has limitations, and further validation of these findings is required through *in vivo* studies. Moreover, as a proliferative β-cell line, EndoC-βH3 cells may not fully recapitulate primary human β-cell responses to psEVs, necessitating validation in primary islets.

I was unable to validate the findings using the FFPE pancreas tissue available to me because these samples were not ideal for applying the most sensitive techniques needed to confirm the *in vitro* model. Ideally, future studies should involve human subjects or ethically appropriate animal models that closely mimic human biology, allowing the use of highly sensitive techniques to detect psEV-specific C19 miRNA in β cells and to validate the

observed increase in ANXA1 abundance specifically within β cells, rather than in whole islets. Owing to the absence of previous LC-MS/MS pilot data, I used the results from the RNA sequencing experiment conducted on EndoC-βH3 cells treated with psEVs to calculate the SD, which was then used to determine the required sample size for the LC-MS/MS experiment. Although the experimental design of the RNA sequencing experiment closely mirrored that of the LC-MS/MS experiment, fold changes in RNA and protein changes may not necessarily correlate. Ideally, conducting a pilot LC-MS/MS experiment to aid in sample size calculation would have been preferable, but due to the cost of LC-MS/MS I did not have the capacity to perform a pilot experiment. Moreover, although the combined sample size from the two proteomics experiments exceeded the calculated minimum required, it would have been preferable to conduct a single experiment with a larger sample size, rather than combining data from two separate experiments to meet the required sample size. The reasons for this approach have already been discussed previously (see 7.2.2.1 Sample size calculation). However, it is reassuring that despite the small sample size used in each of the two LC-MS/MS experiments, the abundance of ANXA1 was consistently increased across the two independent experiments. Finally, the challenges posed by isolating psEVs using a placental perfusion system also limited the possible sample size included in this study.

In this chapter, I have demonstrated that, following internalisation, psEVs increase the expression of *INS* and insulin content in β-cells. Additionally, psEVs upregulate ANXA1, potentially providing insight into the mechanism underlying these effects on insulin biosynthesis. Further studies will focus on characterising the psEV-induced increase in ANXA1 expression in β cells, including investigating ANXA1 signalling by analysing extracellular and nuclear levels of ANXA1 after psEV treatment. To confirm ANXA1 as a

key mediator of the psEV-induced increases in *INS* expression and insulin content, an ANXA1 knockdown model will be employed.

These findings should ideally be verified *in vivo*. Future work will aim to examine ANXA1 expression in human β cells from pregnant women using single-cell resolution techniques, such as single-cell proteomics or IHC-IF. If IHC-IF is employed, it would be essential to first validate an anti-ANXA1 antibody, ideally in a knockout model. Quantification of ANXA1 expression can then be performed using the IHC-IF analysis pipeline described in Chapter 4.

Chapter 8

General discussion

8.1 Summary

I aimed to characterise the alterations in pancreatic islets during human pregnancy, with a particular focus on how these changes are mediated by placental-pancreatic communication. First, I examined changes in α- and β-cell area, receptor expression, and global protein abundance in human islets during pregnancy. I analysed rare pancreatic tissue sections from pregnant women, which served as a valuable *ex vivo* model, providing new insights into islet adaptations during pregnancy. Furthermore, I investigated the role of placental small extracellular vesicles (psEVs) as additional mediators of placental communication, specifically I analysed their effects on insulin producing pancreatic β cells. By isolating psEVs from human placentae and using a human β-cell line (EndoC-βH3), I developed a human-based model system to explore their effects on insulin synthesis and secretion, as well as their impact on the β-cell transcriptome and proteome. Throughout, I also compared the differences observed in human pancreatic islets and the effects of psEVs on β cells between women with gestational diabetes mellitus (GDM) to those with normal pregnancies.

8.1.1 *Ex vivo* alterations in pancreatic islets during pregnancy

Integrating proteomics, immunofluorescence of tissue sections (IHC-IF), advanced imaging techniques, and a non-biased reproducible quantitative computational analysis pipeline, the studies presented in this thesis provide the most detailed characterisation of the proteomic and cellular alterations in human pancreatic islets during pregnancy to date. This comprehensive approach has led to novel discoveries and provided validation data that challenge findings from mouse models.

In Chapter 3, laser capture microdissection (LCM) was used to successfully isolate islets from formalin-fixed paraffin-embedded (FFPE) pancreatic tissues, which were then

analysed by liquid chromatography-tandem mass spectrometry (LC-MS/MS). This is the first time LC-MS/MS has been applied to islets isolated from FFPE pancreatic tissue, marking a significant technical achievement. Currently, these data represent the most in-depth proteomic characterisation of human islet proteins during pregnancy. I observed that only four proteins showed significant differences in abundance between the islet proteomes of pregnant and non-pregnant women. This outcome contrasts with previous reports in mice, in which significant proteomic alterations in islets have been documented during pregnancy (22). While surprising, these findings highlight key differences between species and suggest that the mechanisms of islet adaptation in humans may differ fundamentally from those in mice.

The data presented in Chapter 4, replicated the well-known observation of increased β-cell area in human pregnancy, aligning with previous studies (26, 27). However, a novel discovery was the increase in α-cell area during pregnancy. I observed that the increase in both α and β cell area was attributed to an increase in α and β cell numbers. The underlying mechanisms driving this increase in cell numbers, however, remain unclear and warrant further investigation. Among the observed changes in α cells, I noted an increased abundance of glucagon-like peptide 1 (GLP-1) during pregnancy. I also observed an increase in the proportion of α cells expressing the prolactin receptor (PRLR) and serotonin 2B (5-HT2B) receptor during pregnancy, a novel finding that warrants further functional investigation. Notably, PRLR did not show increased expression in β-cells, and no 5-HT2B receptors were detected in β-cells at all, which contrasts sharply with findings in mice. The antibodies used in this study were thoroughly validated, ensuring the robustness and reliability of the findings presented.

Taken together, these findings highlight an essential species-specific difference in islet adaptative mechanisms between human and mouse pregnancy. While mice exhibit distinct mechanisms of islet adaptation during pregnancy, human islets likely undergo a different set of changes (120). The potential for functional plasticity in human islets may involve GLP-1-mediated paracrine signalling between α and β cells. These processes may play a critical role in human pregnancy, warranting further investigation into the unique adaptations of human islets.

8.1.2 Placental small extracellular vesicles and insulin synthesis in β cells

In Chapter 5, I isolated placental small extracellular vesicles (psEVs) from human placentae of normal pregnancies and those affected by GDM, and characterised them immunophenotypically to validate their identity as psEVs. I demonstrated that differentiated EndoC-βH3 cells internalise psEVs in a time- and dose-dependent manner, as observed through live-cell imaging and computational analysis. To my knowledge, this was the first application of these advanced imaging and computational analysis techniques to psEV research.

Chapter 6 explored the impact of psEVs on β-cell transcriptomics. I demonstrated that internalised psEVs induced transcriptomic changes in EndoC-βH3 cells, marking the first demonstration of psEV-mediated gene expression changes in β cells. However, the magnitude of these changes was small, even after optimising the RNA isolation time and psEV dosage. Consequently, I shifted my focus to assessing the functional impact of psEVs on insulin content and secretion.

In Chapter 7, I demonstrated that both normal pregnancy and GDM-derived psEVs upregulate insulin gene (*INS*) expression and increase intracellular insulin content in EndoC-βH3 cells. However, psEVs had no effect on glucose-stimulated insulin secretion (GSIS). In order to uncover the underlying mechanisms behind the upregulation of insulin synthesis, I conducted a proteomic analysis and identified Annexin A1 (ANXA1) as a key molecule upregulated by psEVs. ANXA1 has been linked to insulin biology and may be responsible for the psEV-induced changes in *INS* expression and insulin content. However, attempts to verify ANXA1 upregulation in β cells *ex vivo* during pregnancy by re-evaluating the islet LC-MS/MS data from Chapter 3 were inconclusive, likely due to the limitations of LC-MS/MS in detecting low-abundance proteins and achieving single-cell resolution. Further *in vivo* studies are needed to investigate the role of ANXA1 in β cell function during pregnancy.

8.1.3 Limitations

First, the small sample size and consequent heterogeneity in the cohorts compared used to study human pancreatic tissue by LC-MS/MS and IHC-IF is a limitation, though this was an unavoidable consequence of the rarity of these samples.

The small changes in gene expression observed in the RNA sequencing experiment presented in Chapter 6 limited the conclusions that could be drawn from the data. Future studies should consider experimental designs that better mimic human biology, such as continuous psEV supply using cell infusion systems, rather than single-dose treatments, to better capture their sustained effects on the cell transcriptome.

Additionally, I chose to focus exclusively on small extracellular vesicles (sEVs) and excluded medium and large EVs. This decision was influenced by two key factors: first, as previously discussed, studies indicate that medium/large EVs are not consistently detected in peripheral organs such as the spleen or kidneys, whereas sEVs are reliably identified and exhibit greater cellular motility, enhancing their uptake and cargo delivery to distant tissues (63, 65). Additionally, psEVs have been detected in the pancreas using an *in vivo* model (66). Moreover, it is sEVs rather than medium/large EVs have been specifically linked to pancreatic islet changes in insulin secretion (66, 85). Therefore, I concluded that it was more relevant to study sEVs as they were more likely to reach and affect pancreatic β cells *in vivo*. Second, practical considerations such as time constraints and the cost of duplicating experiments influenced this choice. Future studies, however, should aim to investigate the effects of these larger vesicle populations to provide a more comprehensive understanding of placental EV-mediated signalling in β cells.

Finally, I chose to measure EV concentration by protein content rather than nanoparticle tracking analysis (NTA). While there is ongoing debate regarding the best method for quantifying EVs, consistency across experiments was maintained, which is key to the reliability of my findings.

8.1.4 Future work

Future research should build upon the discoveries of this thesis in several important ways. First, it is essential to investigate the functional impact of increased GLP-1 abundance in α cells during pregnancy on β cell function through mechanistic studies, using both *in vitro* and *in vivo* models. Additionally, performing single-cell proteomics would allow for the detailed characterisation of protein changes within distinct islet cell populations during

pregnancy, elucidating cell-type-specific proteomic alterations rather than generalised changes across the islet's heterogeneous cell population. Exploring the role of other islet cell types, such as δ cells, is also crucial, as paracrine signalling may play an important role in islet adaptation during pregnancy.

Further experiments using ANXA1 knockout models treated with psEVs will help confirm whether ANXA1 is the key mediator of psEV-induced changes in *INS* expression and insulin content, consistent with the methodology utilised in a recent study (224). Investigating ANXA1 expression in β cells in pancreatic tissue as an *ex vivo* model, through single-cell proteomics or IHC-IF combined with computational analysis, will provide additional insights. Exploration of the roles of ANXA1 in β cells in greater detail, including through overexpression models, will be important to fully elucidate its role in insulin regulation during pregnancy.

My results improve our understanding of the molecular communication between the placenta and pancreatic islets during pregnancy. By characterising the proteomic changes in islets and the effects of psEVs on β cells, this work lays the groundwork for future studies that may lead to enhancing our understanding of β-cell adaptation during pregnancy and new therapeutic targets for managing GDM.

Appendix

List of publications

1. **Seedat F**, Holden K, Davis S, Fischer R, Bancroft J, Drydale E, et al. A new paradigm of islet adaptations in human pregnancy: insights from immunohistochemistry and proteomics. Nature Communications. 2025. Accepted for publication.
2. **Seedat F**, Holden K, Davis S, Fischer R, Bancroft J, Drydale E, et al. Redefining islet adaptations in human pregnancy: insights from immunohistochemistry and proteomics. 2025. European Society of Endocrinology Conference, Copenhagen, Denmark. Oral presentation.
3. **Seedat F**, Kandzija N, Ellis MJ, Jiang S, Sarbalina A, Bancroft J, et al. Placental small extracellular vesicles from normal pregnancy and gestational diabetes increase insulin gene transcription and content in β cells. Clin Sci (Lond). 2024;138(22):1481-502.
4. Ellis MJ, Lekka C, Holden KL, Tulmin H, **Seedat F**, O'Brien DP, et al. Identification of high-performing antibodies for the reliable detection of tau proteoforms by western blotting and immunohistochemistry. Acta Neuropathol. 2024. 147(1):87.
5. Kandzija N, Payne S, Cooke WR, **Seedat F**, Fischer R, Vatish M. Protein Profiling of Placental Extracellular Vesicles in Gestational Diabetes Mellitus. Int J Mol Sci. 2024;25(4).
6. **Seedat F**, Kandzija N, Ellis MJ, Jiang S, Sarbalina A, Bancroft J, et al. Placental small extracellular vesicles from normal pregnancy and gestational diabetes increase insulin gene transcription and content in β cells. 2024. European Placenta Group Conference, Hradec Králové, Czech Republic. Oral presentation.
7. **Seedat F**, Kandzija N, Ellis M.J, Wade A, Taylor A, Todd JA, Stefana MI, Vatish M. Placental small extracellular vesicles are internalized by human pancreatic beta cells and

trigger transcriptional changes in recipient cells. 2023. UKEV Forum, Cambridge, United Kingdom. Poster presentation.

8. Lokeswara A, **Seedat F**, Zhang W, Holloway P, Couch Y, Dallmann R, Vatish M. Are pericytes involved in the pathogenesis of preeclampsia? *J Obstet Gynaecol*. 2024;44(1):2432795. doi:10.1080/01443615.2024.2432795.

References

1. Napso T, Yong HEJ, Lopez-Tello J, Sferruzzi-Perri AN. The role of placental hormones in mediating maternal adaptations to support pregnancy and lactation. Front Physiol. 2018;9:1091.
2. Soma-Pillay P, Nelson-Piercy C, Tolppanen H, Mebazaa A. Physiological changes in pregnancy. Cardiovasc J Afr. 2016;27(2):89-94.
3. Da Silva Xavier G. The cells of the islets of langerhans. J Clin Med. 2018;7(3).
4. Ionescu-Tirgoviste C, Gagniuc PA, Gubceac E, Mardare L, Popescu I, Dima S, et al. A 3d map of the islet routes throughout the healthy human pancreas. Sci Rep. 2015;5:14634.
5. Lehrstrand J, Davies WIL, Hahn M, Korsgren O, Alanentalo T, Ahlgren U. Illuminating the complete β-cell mass of the human pancreas- signifying a new view on the islets of langerhans. Nat Commun. 2024;15(1):3318.
6. Wang X, Misawa R, Zielinski MC, Cowen P, Jo J, Periwal V, et al. Regional differences in islet distribution in the human pancreas--preferential beta-cell loss in the head region in patients with type 2 diabetes. PLoS One. 2013;8(6):e67454.
7. Bonner-Weir S. The islets of langerhans continue to reveal their secrets. Nat Rev Endocrinol. 2020;16(2):73-4.
8. Campbell JE, Newgard CB. Mechanisms controlling pancreatic islet cell function in insulin secretion. Nat Rev Mol Cell Biol. 2021;22(2):142-58.
9. Gilon P. The role of alpha-cells in islet function and glucose homeostasis in health and type 2 diabetes. J Mol Biol. 2020;432(5):1367-94.
10. Hivert M-F, Backman H, Benhalima K, Catalano P, Desoye G, Immanuel J, et al. Pathophysiology from preconception, during pregnancy, and beyond. The Lancet. 2024.

11. Salazar-Petres ER, Sferruzzi-Perri AN. Pregnancy-induced changes in beta-cell function: what are the key players? J Physiol. 2022;600(5):1089-117.
12. Baeyens L, Hindi S, Sorenson RL, German MS. Beta-cell adaptation in pregnancy. Diabetes Obes Metab. 2016;18 Suppl 1:63-70.
13. Banerjee RR. Piecing together the puzzle of pancreatic islet adaptation in pregnancy. Ann N Y Acad Sci. 2018;1411(1):120-39.
14. Sweeting A, Wong J, Murphy HR, Ross GP. A clinical update on gestational diabetes mellitus. Endocr Rev. 2022;43(5):763-93.
15. Powe CE, Huston Presley LP, Locascio JJ, Catalano PM. Augmented insulin secretory response in early pregnancy. Diabetologia. 2019;62(8):1445-52.
16. Lain KY, Catalano PM. Metabolic changes in pregnancy. Clin Obstet Gynecol. 2007;50(4):938-48.
17. Luyckx AS, Gerard J, Gaspard U, Lefebvre PJ. Plasma glucagon levels in normal women during pregnancy. Diabetologia. 1975;11(6):549-54.
18. Daniel RR, Metzger BE, Freinkel N, Faloona GR, Unger RH, Nitzan M. Carbohydrate metabolism in pregnancy. XI. Response of plasma glucagon to overnight fast and oral glucose during normal pregnancy and in gestational diabetes. Diabetes. 1974;23(9):771-6.
19. Kuhl C, Holst JJ. Plasma glucagon and the insulin:glucagon ratio in gestational diabetes. Diabetes. 1976;25(1):16-23.
20. Kampmann U, Knorr S, Fuglsang J, Ovesen P. Determinants of maternal insulin resistance during pregnancy: an updated overview. J Diabetes Res. 2019;2019:5320156.
21. Rieck S, White P, Schug J, Fox AJ, Smirnova O, Gao N, et al. The transcriptional response of the islet to pregnancy in mice. Mol Endocrinol. 2009;23(10):1702-12.

22. Horn S, Kirkegaard JS, Hoelper S, Seymour PA, Rescan C, Nielsen JH, et al. Research resource: A dual proteomic approach identifies regulated islet proteins during beta-cell mass expansion in vivo. Mol Endocrinol. 2016;30(1):133-43.

23. Qiao L, Saget S, Lu C, Zang T, Dzyuba B, Hay WW, et al. The essential role of pancreatic alpha-cells in maternal metabolic adaptation to pregnancy. Diabetes. 2022;71(5):978-88.

24. Quesada-Candela C, Tuduri E, Marroqui L, Alonso-Magdalena P, Quesada I, Nadal A. Morphological and functional adaptations of pancreatic alpha-cells during late pregnancy in the mouse. Metabolism. 2020;102:153963.

25. Ruiz-Otero N, Tessem JS, Banerjee RR. Pancreatic islet adaptation in pregnancy and postpartum. Trends Endocrinol Metab. 2024.

26. Van Assche FA, Aerts L, De Prins F. A morphological study of the endocrine pancreas in human pregnancy. Br J Obstet Gynaecol. 1978;85(11):818-20.

27. Butler AE, Cao-Minh L, Galasso R, Rizza RA, Corradin A, Cobelli C, et al. Adaptive changes in pancreatic beta cell fractional area and beta cell turnover in human pregnancy. Diabetologia. 2010;53(10):2167-76.

28. Parsons JA, Brelje TC, Sorenson RL. Adaptation of islets of langerhans to pregnancy: increased islet cell proliferation and insulin secretion correlates with the onset of placental lactogen secretion. Endocrinology. 1992;130(3):1459-66.

29. Sorenson RL, Brelje TC. Prolactin receptors are critical to the adaptation of islets to pregnancy. Endocrinology. 2009;150(4):1566-9.

30. Vasavada RC, Garcia-Ocaña A, Zawalich WS, Sorenson RL, Dann P, Syed M, et al. Targeted expression of placental lactogen in the beta cells of transgenic mice results in beta cell proliferation, islet mass augmentation, and hypoglycemia. J Biol Chem. 2000;275(20):15399-406.

31. Huang C, Snider F, Cross JC. Prolactin receptor is required for normal glucose homeostasis and modulation of beta-cell mass during pregnancy. Endocrinology. 2009;150(4):1618-26.

32. Banerjee RR, Cyphert HA, Walker EM, Chakravarthy H, Peiris H, Gu X, et al. Gestational diabetes mellitus from inactivation of prolactin receptor and mafb in islet beta-cells. Diabetes. 2016;65(8):2331-41.

33. Nteeba J, Kubota K, Wang W, Zhu H, Vivian J, Dai G, et al. Pancreatic prolactin receptor signaling regulates maternal glucose homeostasis. J Endocrinol. 2019.

34. Shrivastava V, Lee M, Lee D, Pretorius M, Radford B, Makkar G, et al. Beta cell adaptation to pregnancy requires prolactin action on both beta and non-beta cells. Sci Rep. 2021;11(1):10372.

35. Arumugam R, Fleenor D, Freemark M. Knockdown of prolactin receptors in a pancreatic beta cell line: effects on DNA synthesis, apoptosis, and gene expression. Endocrine. 2014;46(3):568-76.

36. Hughes E, Huang C. Participation of akt, menin, and p21 in pregnancy-induced beta-cell proliferation. Endocrinology. 2011;152(3):847-55.

37. Zhang H, Zhang J, Pope CF, Crawford LA, Vasavada RC, Jagasia SM, et al. Gestational diabetes mellitus resulting from impaired beta-cell compensation in the absence of foxm1, a novel downstream effector of placental lactogen. Diabetes. 2010;59(1):143-52.

38. Karnik SK, Chen H, McLean GW, Heit JJ, Gu X, Zhang AY, et al. Menin controls growth of pancreatic beta-cells in pregnant mice and promotes gestational diabetes mellitus. Science. 2007;318(5851):806-9.

39. Schindler C, Darnell JE, Jr. Transcriptional responses to polypeptide ligands: the jak-stat pathway. Annu Rev Biochem. 1995;64:621-51.

40. Usman TO, Chhetri G, Yeh H, Dong HH. Beta-cell compensation and gestational diabetes. J Biol Chem. 2023;299(12).

41. Moon JH, Kim YG, Kim K, Osonoi S, Wang S, Saunders DC, et al. Serotonin regulates adult beta-cell mass by stimulating perinatal beta-cell proliferation. Diabetes. 2020;69(2):205-14.

42. Bennet H, Mollet IG, Balhuizen A, Medina A, Nagorny C, Bagge A, et al. Serotonin (5-ht) receptor 2b activation augments glucose-stimulated insulin secretion in human and mouse islets of langerhans. Diabetologia. 2016;59(4):744-54.

43. Yabut JM, Crane JD, Green AE, Keating DJ, Khan WI, Steinberg GR. Emerging roles for serotonin in regulating metabolism: new implications for an ancient molecule. Endocr Rev. 2019;40(4):1092-107.

44. Kim H, Toyofuku Y, Lynn FC, Chak E, Uchida T, Mizukami H, et al. Serotonin regulates pancreatic beta cell mass during pregnancy. Nat Med. 2010;16(7):804-8.

45. Ohara-Imaizumi M, Kim H, Yoshida M, Fujiwara T, Aoyagi K, Toyofuku Y, et al. Serotonin regulates glucose-stimulated insulin secretion from pancreatic beta cells during pregnancy. Proc Natl Acad Sci U S A. 2013;110(48):19420-5.

46. Goyvaerts L, Schraenen A, Lemaire K, Veld PI, Smolders I, Maroteaux L, et al. Normal pregnancy-induced islet beta cell proliferation in mouse models that are deficient in serotonin-signaling. Int J Mol Sci. 2022;23(24).

47. Kwak SH, Park BL, Kim H, German MS, Go MJ, Jung HS, et al. Association of variations in tph1 and htr2b with gestational weight gain and measures of obesity. Obesity (Silver Spring). 2012;20(1):233-8.

48. Welsh JA, Goberdhan DCI, O'Driscoll L, Buzas EI, Blenkiron C, Bussolati B, et al. Minimal information for studies of extracellular vesicles (misev2023): from basic to advanced approaches. J Extracell Vesicles. 2024;13(2):e12404.

49. Thery C, Witwer KW, Aikawa E, Alcaraz MJ, Anderson JD, Andriantsitohaina R, et al. Minimal information for studies of extracellular vesicles 2018 (misev2018): a position statement of the international society for extracellular vesicles and update of the misev2014 guidelines. J Extracell Vesicles. 2018;7(1):1535750.

50. Teng F, Fussenegger M. Shedding light on extracellular vesicle biogenesis and bioengineering. Adv Sci (Weinh). 2020;8(1):2003505.

51. El Andaloussi S, Mäger I, Breakefield XO, Wood MJ. Extracellular vesicles: Biology and emerging therapeutic opportunities. Nat Rev Drug Discov. 2013;12(5):347-57.

52. Simeone P, Bologna G, Lanuti P, Pierdomenico L, Guagnano MT, Pieragostino D, et al. Extracellular vesicles as signaling mediators and disease biomarkers across biological barriers. Int J Mol Sci. 2020;21(7).

53. Kumar MA, Baba SK, Sadida HQ, Marzooqi SA, Jerobin J, Altemani FH, et al. Extracellular vesicles as tools and targets in therapy for diseases. Signal Transduct Target Ther. 2024;9(1):27.

54. Czernek L, Duchler M. Exosomes as messengers between mother and fetus in pregnancy. Int J Mol Sci. 2020;21(12).

55. Familari M, Cronqvist T, Masoumi Z, Hansson SR. Placenta-derived extracellular vesicles: their cargo and possible functions. Reprod Fertil Dev. 2017;29(3):433-47.

56. Adamova P, Lotto RR, Powell AK, Dykes IM. Are there foetal extracellular vesicles in maternal blood? Prospects for diagnostic biomarker discovery. J Mol Med (Berl). 2023;101(1-2):65-81.

57. Kupper N, Huppertz B. The endogenous exposome of the pregnant mother: Placental extracellular vesicles and their effect on the maternal system. Mol Aspects Med. 2022;87:100955.

58. Ouyang Y, Mouillet JF, Coyne CB, Sadovsky Y. Review: Placenta-specific micrornas in exosomes - good things come in nano-packages. Placenta. 2014;35 Suppl:S69-73.

59. Cronqvist T, Tannetta D, Mörgelin M, Belting M, Sargent I, Familari M, et al. Syncytiotrophoblast derived extracellular vesicles transfer functional placental mirnas to primary human endothelial cells. Sci Rep. 2017;7(1):4558.

60. Barnes MVC, Pantazi P, Holder B. Circulating extracellular vesicles in healthy and pathological pregnancies: a scoping review of methodology, rigour and results. J Extracell Vesicles. 2023;12(11):e12377.

61. Ortega MA, Fraile-Martinez O, Garcia-Montero C, Paradela A, Asuncion Sanchez-Gil M, Rodriguez-Martin S, et al. Unfolding the role of placental-derived extracellular vesicles in pregnancy: from homeostasis to pathophysiology. Front Cell Dev Biol. 2022;10:1060850.

62. Elfeky O, Longo S, Lai A, Rice GE, Salomon C. Influence of maternal bmi on the exosomal profile during gestation and their role on maternal systemic inflammation. Placenta. 2017;50:60-9.

63. Kang M, Jordan V, Blenkiron C, Chamley LW. Biodistribution of extracellular vesicles following administration into animals: a systematic review. J Extracell Vesicles. 2021;10(8):e12085.

64. Kang M, Blenkiron C, Chamley LW. The biodistribution of placental and fetal extracellular vesicles during pregnancy following placentation. Clin Sci (Lond). 2023;137(5):385-99.

65. Liu YJ, Wang C. A review of the regulatory mechanisms of extracellular vesicles-mediated intercellular communication. Cell Commun Signal. 2023;21(1):77.

66. Wang Y, Yuan Y, Shen S, Ge Z, Zhu D, Bi Y. Placenta-derived exosomes exacerbate beta cell dysfunction in gestational diabetes mellitus through delivery of mir-320b. Front Endocrinol (Lausanne). 2023;14:1282075.

67. Martin C, Bergamelli M, Malnou CE, D'Angelo G. Placental extracellular vesicles in maternal-fetal communication during pregnancy. Biochem Soc Trans. 2022;50(6):1785-95.

68. Gupta AK, Rusterholz C, Huppertz B, Malek A, Schneider H, Holzgreve W, et al. A comparative study of the effect of three different syncytiotrophoblast micro-particles preparations on endothelial cells. Placenta. 2005;26(1):59-66.

69. Dragovic RA, Collett GP, Hole P, Ferguson DJ, Redman CW, Sargent IL, et al. Isolation of syncytiotrophoblast microvesicles and exosomes and their characterisation by multicolour flow cytometry and fluorescence nanoparticle tracking analysis. Methods (San Diego, Calif). 2015;87:64-74.

70. Tekkatte C, Lindsay SA, Duggan E, Castro-Martínez A, Hakim A, Saldana I, et al. Identification of optimal conditions for human placental explant culture and extracellular vesicle release. iScience. 2023;26(10):108046.

71. Block LN, Bowman BD, Schmidt JK, Keding LT, Stanic AK, Golos TG. The promise of placental extracellular vesicles: models and challenges for diagnosing placental dysfunction in utero†. Biol Reprod. 2021;104(1):27-57.

72. Burton GJ, Sebire NJ, Myatt L, Tannetta D, Wang YL, Sadovsky Y, et al. Optimising sample collection for placental research. Placenta. 2014;35(1):9-22.

73. Brennan K, Martin K, FitzGerald SP, O'Sullivan J, Wu Y, Blanco A, et al. A comparison of methods for the isolation and separation of extracellular vesicles from protein and lipid particles in human serum. Sci Rep. 2020;10(1):1039.

74. Simonsen JB. What are we looking at? Extracellular vesicles, lipoproteins, or both? Circ Res. 2017;121(8):920-2.

75. Simon C, Greening DW, Bolumar D, Balaguer N, Salamonsen LA, Vilella F. Extracellular vesicles in human reproduction in health and disease. Endocr Rev. 2018;39(3):292-332.

76. Hendrix A, Lippens L, Pinheiro C, Théry C, Martin-Jaular L, Lötvall J, et al. Extracellular vesicle analysis. Nat Rev Methods Primers. 2023;3(1):56.

77. Nair S, Ormazabal V, Carrion F, Handberg A, McIntyre HD, Salomon C. Extracellular vesicle-mediated targeting strategies for long-term health benefits in gestational diabetes. Clin Sci (Lond). 2023;137(16):1311-32.

78. Palma C, McIntyre HD, Salomon C. Extracellular vesicles-new players in cell-to-cell communication in gestational diabetes mellitus. Biomedicines. 2022;10(2).

79. Bathla T, Abolbaghaei A, Reyes AB, Burger D. Extracellular vesicles in gestational diabetes mellitus: a scoping review. Diab Vasc Dis Res. 2022;19(1):14791641221093901.

80. Gillet V, Ouellet A, Stepanov Y, Rodosthenous RS, Croft EK, Brennan K, et al. Mirna profiles in extracellular vesicles from serum early in pregnancies complicated by gestational diabetes mellitus. J Clin Endocrinol Metab. 2019;104(11):5157-69.

81. Kandzija N, Payne S, Cooke WR, Seedat F, Fischer R, Vatish M. Protein profiling of placental extracellular vesicles in gestational diabetes mellitus. Int J Mol Sci. 2024;25(4).

82. Liu X, Qiu H. Placenta-derived exosomes and gestational diabetes mellitus. Diabetes Metab Syndr Obes. 2022;Volume 15:1391-404.

83. Salomon C, Torres MJ, Kobayashi M, Scholz-Romero K, Sobrevia L, Dobierzewska A, et al. A gestational profile of placental exosomes in maternal plasma and their effects on endothelial cell migration. PLoS One. 2014;9(6):e98667.

84. Razo-Azamar M, Nambo-Venegas R, Quevedo IR, Juárez-Luna G, Salomon C, Guevara-Cruz M, et al. Early-pregnancy serum maternal and placenta-derived exosomes mirnas vary based on pancreatic β-cell function in gdm. J Clin Endocrinol Metab. 2024;109(6):1526-39.

85. James-Allan LB, Rosario FJ, Madi L, Barner K, Nair S, Lai A, et al. A novel technique using chronic infusion of small extracellular vesicles from gestational diabetes mellitus causes glucose intolerance in pregnant mice. Clin Sci (Lond). 2022;136(21):1535-49.

86. Buteau J. Glp-1 receptor signaling: Effects on pancreatic beta-cell proliferation and survival. Diabetes Metab. 2008;34 Suppl 2:S73-7.

87. Kandzija N, Zhang W, Motta-Mejia C, Mhlomi V, McGowan-Downey J, James T, et al. Placental extracellular vesicles express active dipeptidyl peptidase iv; levels are increased in gestational diabetes mellitus. J Extracell Vesicles. 2019;8(1):1617000.

88. Sweeting A, Hannah W, Backman H, Catalano P, Feghali M, Herman WH, et al. Epidemiology and management of gestational diabetes. The Lancet. 2024.

89. Idf atlas, 10th edition 2021.

90. Metzger BE, Lowe LP, Dyer AR, Trimble ER, Chaovarindr U, Coustan DR, et al. Hyperglycemia and adverse pregnancy outcomes. N Engl J Med. 2008;358(19):1991-2002.

91. Simmons D, Gupta Y, Hernandez TL, Levitt N, van Poppel M, Yang X, et al. Call to action for a life course approach. The Lancet. 2024.

92. Metzger BE, Gabbe SG, Persson B, Buchanan TA, Catalano PA, Damm P, et al. International association of diabetes and pregnancy study groups recommendations on the diagnosis and classification of hyperglycemia in pregnancy. Diabetes Care. 2010;33(3):676-82.

93. Benhalima K, Mathieu C, Damm P, Van Assche A, Devlieger R, Desoye G, et al. A proposal for the use of uniform diagnostic criteria for gestational diabetes in europe: an opinion paper by the european board & college of obstetrics and gynaecology (ebcog). Diabetologia. 2015;58(7):1422-9.

94. Diagnostic criteria and classification of hyperglycaemia first detected in pregnancy: a world health organization guideline. Diabetes Res Clin Pract. 2014;103(3):341-63.

95. Hod M, Kapur A, Sacks DA, Hadar E, Agarwal M, Di Renzo GC, et al. The international federation of gynecology and obstetrics (figo) initiative on gestational diabetes mellitus: a pragmatic guide for diagnosis, management, and care. Int J Gynaecol Obstet. 2015;131 Suppl 3:S173-211.

96. Nankervis A, Mcintyre HD, Moses R, Ross GP, Callaway L, C. P, et al. Adips consensus guidelines for the testing and diagnosis of gestational diabetes mellitus in australia. 2014.

97. American Diabetes A. 14. Management of diabetes in pregnancy: Standards of medical care in diabetes-2020. Diabetes Care. 2020;43(Suppl 1):S183-S92.

98. Araki E, Goto A, Kondo T, Noda M, Noto H, Origasa H, et al. Japanese clinical practice guideline for diabetes 2019. J Diabetes Investig. 2020;11(4):1020-76.

99. Blumer I, Hadar E, Hadden DR, Jovanovič L, Mestman JH, Murad MH, et al. Diabetes and pregnancy: an endocrine society clinical practice guideline. J Clin Endocrinol Metab. 2013;98(11):4227-49.

100. Diabetes in pregnancy: Management from preconception to the postnatal period London: National Institute for Health and Care Excellence (NICE). 2020 Dec 16. PMID: 32212588.

101. Crowther CA, Samuel D, McCowan LME, Edlin R, Tran T, McKinlay CJ. Lower versus higher glycemic criteria for diagnosis of gestational diabetes. N Engl J Med. 2022;387(7):587-98.

102. Hillier TA, Pedula KL, Ogasawara KK, Vesco KK, Oshiro CES, Lubarsky SL, et al. A pragmatic, randomized clinical trial of gestational diabetes screening. N Engl J Med. 2021;384(10):895-904.

103. Ye W, Luo C, Huang J, Li C, Liu Z, Liu F. Gestational diabetes mellitus and adverse pregnancy outcomes: systematic review and meta-analysis. Bmj. 2022;377:e067946.

104. Hannah W, Bhavadharini B, Beks H, Deepa M, Anjana RM, Uma R, et al. Global burden of early pregnancy gestational diabetes mellitus (egdm): a systematic review. Acta Diabetol. 2022;59(3):403-27.

105. Immanuel J, Simmons D. Screening and treatment for early-onset gestational diabetes mellitus: a systematic review and meta-analysis. Curr Diab Rep. 2017;17(11):115.

106. Crowther CA, Hiller JE, Moss JR, McPhee AJ, Jeffries WS, Robinson JS. Effect of treatment of gestational diabetes mellitus on pregnancy outcomes. N Engl J Med. 2005;352(24):2477-86.

107. Simmons D, Immanuel J, Hague WM, Teede H, Nolan CJ, Peek MJ, et al. Treatment of gestational diabetes mellitus diagnosed early in pregnancy. N Engl J Med. 2023;388(23):2132-44.

108. Ravi PK, Purkait S, Singh SR, Mishra PR. Decay score: A guide to the immunoreactivity of human pancreatic islets in autopsy specimen. Folia Morphol (Warsz). 2022;81(1):101-6.

109. Aamodt KI, Powers AC. Signals in the pancreatic islet microenvironment influence beta-cell proliferation. Diabetes Obes Metab. 2017;19 Suppl 1(Suppl 1):124-36.

110. Noguchi GM, Huising MO. Integrating the inputs that shape pancreatic islet hormone release. Nat Metab. 2019;1(12):1189-201.

111. Malassiné A, Frendo JL, Evain-Brion D. A comparison of placental development and endocrine functions between the human and mouse model. Hum Reprod Update. 2003;9(6):531-9.

112. Schmidt A, Morales-Prieto DM, Pastuschek J, Fröhlich K, Markert UR. Only humans have human placentas: molecular differences between mice and humans. J Reprod Immunol. 2015;108:65-71.

113. Moede T, Leibiger IB, Berggren PO. Alpha cell regulation of beta cell function. Diabetologia. 2020;63(10):2064-75.

114. Benner C, van der Meulen T, Cacéres E, Tigyi K, Donaldson CJ, Huising MO. The transcriptional landscape of mouse beta cells compared to human beta cells reveals notable species differences in long non-coding rna and protein-coding gene expression. BMC Genomics. 2014;15(1):620.

115. Wieland FC, van Blitterswijk CA, van Apeldoorn A, LaPointe VLS. The functional importance of the cellular and extracellular composition of the islets of langerhans. J Immunol Regen Med. 2021;13.

116. Baeyens L, Lemper M, Staels W, De Groef S, De Leu N, Heremans Y, et al. (re)generating human beta cells: status, pitfalls, and perspectives. Physiol Rev. 2018;98(3):1143-67.

117. Sasaki H, Saisho Y, Inaishi J, Itoh H. Revisiting regulators of human beta-cell mass to achieve beta-cell-centric approach toward type 2 diabetes. J Endocr Soc. 2021;5(10):bvab128.

118. Huising MO. Paracrine regulation of insulin secretion. Diabetologia. 2020;63(10):2057-63.

119. Genevay M, Pontes H, Meda P. Beta cell adaptation in pregnancy: a major difference between humans and rodents? Diabetologia. 2010;53(10):2089-92.

120. Bonner-Weir S, Guo L, Li WC, Ouziel-Yahalom L, Lysy PA, Weir GC, et al. Islet neogenesis: a possible pathway for beta-cell replenishment. Rev Diabet Stud. 2012;9(4):407-16.

121. Aldous N, Moin ASM, Abdelalim EM. Pancreatic β-cell heterogeneity in adult human islets and stem cell-derived islets. Cell Mol Life Sci. 2023;80(6):176.

122. Roberts L. Small, furry and powerful: are mouse lemurs the next big thing in genetics? Nature. 2019;570(7760):151-4.

123. Carter AM. Animal models of human pregnancy and placentation: alternatives to the mouse. Reproduction. 2020;160(6):R129-R43.

124. Campbell-Thompson M, Wasserfall C, Kaddis J, Albanese-O'Neill A, Staeva T, Nierras C, et al. Network for pancreatic organ donors with diabetes (npod):

developing a tissue biobank for type 1 diabetes. Diabetes Metab Res Rev. 2012;28(7):608-17.

125. Pugliese A, Yang M, Kusmarteva I, Heiple T, Vendrame F, Wasserfall C, et al. The juvenile diabetes research foundation network for pancreatic organ donors with diabetes (npod) program: goals, operational model and emerging findings. Pediatr Diabetes. 2014;15(1):1-9.

126. Benazra M, Lecomte MJ, Colace C, Müller A, Machado C, Pechberty S, et al. A human beta cell line with drug inducible excision of immortalizing transgenes. Mol Metab. 2015;4(12):916-25.

127. Ravassard P, Hazhouz Y, Pechberty S, Bricout-Neveu E, Armanet M, Czernichow P, et al. A genetically engineered human pancreatic β cell line exhibiting glucose-inducible insulin secretion. J Clin Invest. 2011;121(9):3589-97.

128. Skelin M, Rupnik M, Cencic A. Pancreatic beta cell lines and their applications in diabetes mellitus research. Altex. 2010;27(2):105-13.

129. Sferruzzi-Perri AN, Lopez-Tello J, Napso T, Yong HEJ. Exploring the causes and consequences of maternal metabolic maladaptations during pregnancy: lessons from animal models. Placenta. 2020;98:43-51.

130. Schraenen A, de Faudeur G, Thorrez L, Lemaire K, Van Wichelen G, Granvik M, et al. Mrna expression analysis of cell cycle genes in islets of pregnant mice. Diabetologia. 2010;53(12):2579-88.

131. Chung JY, Ma Y, Zhang D, Bickerton HH, Stokes E, Patel SB, et al. Pancreatic islet cell type-specific transcriptomic changes during pregnancy and postpartum. iScience. 2023;26(4):106439.

132. Payne SH. The utility of protein and mrna correlation. Trends Biochem Sci. 2015;40(1):1-3.

133. Liotta LA, Pappalardo PA, Carpino A, Haymond A, Howard M, Espina V, et al. Laser capture proteomics: Spatial tissue molecular profiling from the bench to personalized medicine. Expert Rev Proteomics. 2021;18(10):845-61.

134. Davis S, Scott C, Oetjen J, Charles PD, Kessler BM, Ansorge O, et al. Deep topographic proteomics of a human brain tumour. Nat Commun. 2023;14(1):7710.

135. Rosenberger FA, Thielert M, Strauss MT, Schweizer L, Ammar C, Mädler SC, et al. Spatial single-cell mass spectrometry defines zonation of the hepatocyte proteome. Nat Methods. 2023;20(10):1530-6.

136. Meier F, Brunner A-D, Frank M, Ha A, Bludau I, Voytik E, et al. Diapasef: parallel accumulation–serial fragmentation combined with data-independent acquisition. Nat Methods. 2020;17(12):1229-36.

137. Demichev V, Messner CB, Vernardis SI, Lilley KS, Ralser M. Dia-nn: Neural networks and interference correction enable deep proteome coverage in high throughput. Nat Methods. 2020;17(1):41-4.

138. Tyanova S, Temu T, Sinitcyn P, Carlson A, Hein MY, Geiger T, et al. The perseus computational platform for comprehensive analysis of (prote)omics data. Nat Methods. 2016;13(9):731-40.

139. Szklarczyk D, Kirsch R, Koutrouli M, Nastou K, Mehryary F, Hachilif R, et al. The string database in 2023: Protein-protein association networks and functional enrichment analyses for any sequenced genome of interest. Nucleic Acids Res. 2023;51(D1):D638-d46.

140. Utriainen M, Morris JH. Clustermaker2: a major update to clustermaker, a multi-algorithm clustering app for cytoscape. BMC Bioinformatics. 2023;24(1):134.

141. Rorsman P, Ashcroft FM. Pancreatic beta-cell electrical activity and insulin secretion: Of mice and men. Physiol Rev. 2018;98(1):117-214.

142. Coscia F, Doll S, Bech JM, Schweizer L, Mund A, Lengyel E, et al. A streamlined mass spectrometry-based proteomics workflow for large-scale ffpe tissue analysis. J Pathol. 2020;251(1):100-12.

143. Pujari GP, Mangalaparthi KK, Madden BJ, Bhat FA, Charlesworth MC, French AJ, et al. A high-throughput workflow for ffpe tissue proteomics. J Am Soc Mass Spectrom. 2023;34(7):1225-9.

144. Kuras M, Woldmar N, Kim Y, Hefner M, Malm J, Moldvay J, et al. Proteomic workflows for high-quality quantitative proteome and post-translational modification analysis of clinically relevant samples from formalin-fixed paraffin-embedded archives. J Proteome Res. 2021;20(1):1027-39.

145. Cho A, Ahn J, Kim A, Lee JH, Ryu HS, Kim KM, et al. Proteomics analysis of an individual formalin-fixed paraffin-embedded tissue section using isobaric-tag amplification. Rapid Commun Mass Spectrom. 2023;37(22):e9616.

146. Mund A, Brunner AD, Mann M. Unbiased spatial proteomics with single-cell resolution in tissues. Mol Cell. 2022;82(12):2335-49.

147. Griesser E, Wyatt H, Ten Have S, Stierstorfer B, Lenter M, Lamond AI. Quantitative profiling of the human substantia nigra proteome from laser-capture microdissected ffpe tissue. Mol Cell Proteomics. 2020;19(5):839-51.

148. Nyalwidhe JO, Grzesik WJ, Burch TC, Semeraro ML, Waseem T, Gerling IC, et al. Comparative quantitative proteomic analysis of disease stratified laser captured microdissected human islets identifies proteins and pathways potentially related to type 1 diabetes. PLoS One. 2017;12(9):e0183908.

149. Zhang L, Lanzoni G, Battarra M, Inverardi L, Zhang Q. Proteomic profiling of human islets collected from frozen pancreata using laser capture microdissection. J Proteomics. 2017;150:149-59.

150. Swensen AC, Velickovic D, Williams SM, Moore RJ, Day LZ, Niessen S, et al. Proteomic profiling of intra-islet features reveals substructure-specific protein signatures. Mol Cell Proteomics. 2022;21(12):100426.

151. Waanders LF, Chwalek K, Monetti M, Kumar C, Lammert E, Mann M. Quantitative proteomic analysis of single pancreatic islets. Proc Natl Acad Sci U S A. 2009;106(45):18902-7.

152. Uhlén M, Fagerberg L, Hallström BM, Lindskog C, Oksvold P, Mardinoglu A, et al. Proteomics. Tissue-based map of the human proteome. Science. 2015;347(6220):1260419.

153. Gosline SJC, Velickovic M, Pino JC, Day LZ, Attah IK, Swensen AC, et al. Proteome mapping of the human pancreatic islet microenvironment reveals endocrine-exocrine signaling sphere of influence. Mol Cell Proteomics. 2023;22(8):100592.

154. Kolic J, Sun WG, Cen HH, Ewald JD, Rogalski JC, Sasaki S, et al. Proteomic predictors of individualized nutrient-specific insulin secretion in health and disease. Cell Metab. 2024;36(7):1619-33.e5.

155. Akkari L, Gocheva V, Kester JC, Hunter KE, Quick ML, Sevenich L, et al. Distinct functions of macrophage-derived and cancer cell-derived cathepsin z combine to promote tumor malignancy via interactions with the extracellular matrix. Genes Dev. 2014;28(19):2134-50.

156. Carter AM, Kumar N, Herring B, Tan C, Guenter R, Telange R, et al. Cdk5 drives formation of heterogeneous pancreatic neuroendocrine tumors. Oncogenesis. 2021;10(12):83.

157. Daval M, Gurlo T, Costes S, Huang CJ, Butler PC. Cyclin-dependent kinase 5 promotes pancreatic β-cell survival via fak-akt signaling pathways. Diabetes. 2011;60(4):1186-97.

158. Ubeda M, Kemp DM, Habener JF. Glucose-induced expression of the cyclin-dependent protein kinase 5 activator p35 involved in alzheimer's disease regulates insulin gene transcription in pancreatic beta-cells. Endocrinology. 2004;145(6):3023-31.

159. Draney C, Hobson AE, Grover SG, Jack BO, Tessem JS. Cdk5r1 overexpression induces primary β-cell proliferation. J Diabetes Res. 2016;2016:6375804.

160. Wei FY, Nagashima K, Ohshima T, Saheki Y, Lu YF, Matsushita M, et al. Cdk5-dependent regulation of glucose-stimulated insulin secretion. Nat Med. 2005;11(10):1104-8.

161. Lilja L, Yang SN, Webb DL, Juntti-Berggren L, Berggren PO, Bark C. Cyclin-dependent kinase 5 promotes insulin exocytosis. J Biol Chem. 2001;276(36):34199-205.

162. Liu SY, Cao SL, Luo HY, Bao L, E J, Li B, et al. Tfp5, a peptide derived from cdk5 activator p35, protects pancreatic beta cells from glucose toxicity. Bull Exp Biol Med. 2023;176(1):19-25.

163. Goddi A, Schroedl L, Brey EM, Cohen RN. Laminins in metabolic tissues. Metabolism. 2021;120:154775.

164. Thaweethai T, Soetan Z, James K, Florez JC, Powe CE. Distinct insulin physiology trajectories in euglycemic pregnancy and gestational diabetes mellitus. Diabetes Care. 2023;46(12):2137-46.

165. Nordmann TM, Schweizer L, Metousis A, Thielert M, Rodriguez E, Rahbek-Gjerdrum LM, et al. A standardized and reproducible workflow for membrane

glass slides in routine histology and spatial proteomics. Mol Cell Proteomics. 2023;22(10):100643.

166. Havnar C, Hotzel K, Espiritu C, Lo A, Webster JD. Standardized processing for formalin-fixed, paraffin-embedded cell pellet immunohistochemistry controls. J Vis Exp. 2022(185).

167. Alavi SE, Ebrahimi Shahmabadi H. Glp-1 peptide analogs for targeting pancreatic beta cells. Drug Discov Today. 2021;26(8):1936-43.

168. Rosselot C, Li Y, Wang P, Alvarsson A, Beliard K, Lu G, et al. Harmine and exendin-4 combination therapy safely expands human β cell mass *in vivo* in a mouse xenograft system. Sci Transl Med. 2024;16(755):eadg3456.

169. Campbell SA, Golec DP, Hubert M, Johnson J, Salamon N, Barr A, et al. Human islets contain a subpopulation of glucagon-like peptide-1 secreting alpha cells that is increased in type 2 diabetes. Mol Metab. 2020;39:101014.

170. Marchetti P, Lupi R, Bugliani M, Kirkpatrick CL, Sebastiani G, Grieco FA, et al. A local glucagon-like peptide 1 (glp-1) system in human pancreatic islets. Diabetologia. 2012;55(12):3262-72.

171. Mayendraraj A, Rosenkilde MM, Gasbjerg LS. Glp-1 and gip receptor signaling in beta cells - a review of receptor interactions and co-stimulation. Peptides. 2022;151:170749.

172. Rodriguez-Diaz R, Molano RD, Weitz JR, Abdulreda MH, Berman DM, Leibiger B, et al. Paracrine interactions within the pancreatic islet determine the glycemic set point. Cell Metab. 2018;27(3):549-58.e4.

173. Agha-Jaffar R, Oliver N, Johnston D, Robinson S. Gestational diabetes mellitus: does an effective prevention strategy exist? Nat Rev Endocrinol. 2016;12(9):533-46.

174. Jiang SH, Li J, Dong FY, Yang JY, Liu DJ, Yang XM, et al. Increased serotonin signaling contributes to the warburg effect in pancreatic tumor cells under metabolic stress and promotes growth of pancreatic tumors in mice. Gastroenterology. 2017;153(1):277-91 e19.

175. Voskuil J. Commercial antibodies and their validation. F1000Res. 2014;3:232.

176. Almaca J, Molina J, Menegaz D, Pronin AN, Tamayo A, Slepak V, et al. Human beta cells produce and release serotonin to inhibit glucagon secretion from alpha cells. Cell Rep. 2016;17(12):3281-91.

177. Karmakar S, Lal G. Role of serotonin receptor signaling in cancer cells and anti-tumor immunity. Theranostics. 2021;11(11):5296-312.

178. Rorsman P, Braun M, Zhang Q. Regulation of calcium in pancreatic α- and β-cells in health and disease. Cell Calcium. 2012;51(3-4):300-8.

179. Rohli KE, Boyer CK, Blom SE, Stephens SB. Nutrient regulation of pancreatic islet β-cell secretory capacity and insulin production. Biomolecules. 2022;12(2).

180. Bolte S, Cordelières FP. A guided tour into subcellular colocalization analysis in light microscopy. J Microsc. 2006;224(3):213-32.

181. Laiginhas R, Cabral D, Falcão M. Evaluation of the different thresholding strategies for quantifying choriocapillaris using optical coherence tomography angiography. Quant Imaging Med Surg. 2020;10(10):1994-2005.

182. Wickham H. Ggplot2: Elegant graphics for data analysis. 2nd ed Cham, Switzerland: Springer Int Publ. 2016:260 p. (Use R!).

183. Hromadnikova I, Kotlabova K, Ondrackova M, Pirkova P, Kestlerova A, Novotna V, et al. Expression profile of c19mc micrornas in placental tissue in pregnancy-related complications. DNA Cell Biol. 2015;34(6):437-57.

184. Lukinavicius G, Reymond L, D'Este E, Masharina A, Gottfert F, Ta H, et al. Fluorogenic probes for live-cell imaging of the cytoskeleton. Nat Methods. 2014;11(7):731-3.

185. Tersigni C, Furqan Bari M, Cai S, Zhang W, Kandzija N, Buchan A, et al. Syncytiotrophoblast-derived extracellular vesicles carry apolipoprotein-e and affect lipid synthesis of liver cells in vitro. J Cell Mol Med. 2022;26(1):123-32.

186. Motta-Mejia C, Kandzija N, Zhang W, Mhlomi V, Cerdeira AS, Burdujan A, et al. Placental vesicles carry active endothelial nitric oxide synthase and their activity is reduced in preeclampsia. Hypertension. 2017;70(2):372-81.

187. Awoyemi T, Motta-Mejia C, Zhang W, Kouser L, White K, Kandzija N, et al. Syncytiotrophoblast extracellular vesicles from late-onset preeclampsia placentae suppress pro-inflammatory immune response in thp-1 macrophages. Front Immunol. 2021;12:676056.

188. Puzar Dominkus P, Stenovec M, Sitar S, Lasic E, Zorec R, Plemenitas A, et al. Pkh26 labeling of extracellular vesicles: characterization and cellular internalization of contaminating pkh26 nanoparticles. Biochim Biophys Acta Biomembr. 2018;1860(6):1350-61.

189. Simonsen JB. Pitfalls associated with lipophilic fluorophore staining of extracellular vesicles for uptake studies. J Extracell Vesicles. 2019;8(1):1582237.

190. Dehghani M, Gulvin SM, Flax J, Gaborski TR. Systematic evaluation of pkh labelling on extracellular vesicle size by nanoparticle tracking analysis. Sci Rep. 2020;10(1):9533.

191. Tertel T, Schoppet M, Stambouli O, Al-Jipouri A, James PF, Giebel B. Imaging flow cytometry challenges the usefulness of classically used extracellular vesicle

labeling dyes and qualifies the novel dye exoria for the labeling of mesenchymal stromal cell-extracellular vesicle preparations. Cytotherapy. 2022;24(6):619-28.

192. Jurgielewicz BJ, Yao Y, Stice SL. Kinetics and specificity of hek293t extracellular vesicle uptake using imaging flow cytometry. Nanoscale Res Lett. 2020;15(1):170.

193. Awoyemi T, Cerdeira AS, Zhang W, Jiang S, Rahbar M, Logenthiran P, et al. Preeclampsia and syncytiotrophoblast membrane extracellular vesicles (stb-evs). Clin Sci (Lond). 2022;136(24):1793-807.

194. Cooke WR, Jiang P, Ji L, Bai J, Jones GD, Lo YMD, et al. Differential 5'-trna fragment expression in circulating preeclampsia syncytiotrophoblast vesicles drives macrophage inflammation. Hypertension. 2024;81(4):876-86.

195. Godakumara K, Ord J, Lättekivi F, Dissanayake K, Viil J, Boggavarapu NR, et al. Trophoblast derived extracellular vesicles specifically alter the transcriptome of endometrial cells and may constitute a critical component of embryo-maternal communication. Reprod Biol Endocrinol. 2021;19(1):115.

196. Krenning L, Sonneveld S, Tanenbaum ME. Time-resolved single-cell sequencing identifies multiple waves of mrna decay during the mitosis-to-g1 phase transition. Elife. 2022;11.

197. Mi H, Muruganujan A, Ebert D, Huang X, Thomas PD. Panther version 14: More genomes, a new panther go-slim and improvements in enrichment analysis tools. Nucleic Acids Res. 2019;47(D1):D419-d26.

198. Haider S, Pal R. Integrated analysis of transcriptomic and proteomic data. Curr Genomics. 2013;14(2):91-110.

199. Vogel C, Marcotte EM. Insights into the regulation of protein abundance from proteomic and transcriptomic analyses. Nat Rev Genet. 2012;13(4):227-32.

200. Perl K, Ushakov K, Pozniak Y, Yizhar-Barnea O, Bhonker Y, Shivatzki S, et al. Reduced changes in protein compared to mrna levels across non-proliferating tissues. BMC Genomics. 2017;18(1):305.

201. Morris R, Black KA, Stollar EJ. Uncovering protein function: From classification to complexes. Essays Biochem. 2022;66(3):255-85.

202. Tusher VG, Tibshirani R, Chu G. Significance analysis of microarrays applied to the ionizing radiation response. Proc Natl Acad Sci U S A. 2001;98(9):5116-21.

203. Yang H, Yang L. Targeting camp/pka pathway for glycemic control and type 2 diabetes therapy. J Mol Endocrinol. 2016;57(2):R93-R108.

204. Hansson V, Skålhegg BS, Taskén K. Cyclic-amp-dependent protein kinase (pka) in testicular cells. Cell specific expression, differential regulation and targeting of subunits of pka. J Steroid Biochem Mol Biol. 2000;73(1-2):81-92.

205. Ellis MJ, Lekka C, Holden KL, Tulmin H, Seedat F, O'Brien DP, et al. Identification of high-performing antibodies for the reliable detection of tau proteoforms by western blotting and immunohistochemistry. Acta Neuropathol. 2024;147(1):87.

206. UniProt. 2024 [KAPCG, KAPCA, and KAPCB alignment results]. Available from: https://www.uniprot.org/align/clustalo-R20240727-121144-0489-42747133-p1m/overview.

207. Kelly L, McGrath S, Rodgers L, McCall K, Tulunay Virlan A, Dempsey F, et al. Annexin-a1: the culprit or the solution? Immunology. 2022;166(1):2-16.

208. Human protein atlas, the placenta-specific proteome. 2024.

209. Sousa SO, Santos MRD, Teixeira SC, Ferro EAV, Oliani SM. Annexin a1: Roles in placenta, cell survival, and nucleus. Cells. 2022;11(13).

210. Pietrani NT, Ferreira CN, Rodrigues KF, Perucci LO, Carneiro FS, Bosco AA, et al. Proresolving protein annexin a1: the role in type 2 diabetes mellitus and obesity. Biomed Pharmacother. 2018;103:482-9.

211. Purvis GSD, Collino M, Loiola RA, Baragetti A, Chiazza F, Brovelli M, et al. Identification of annexina1 as an endogenous regulator of rhoa, and its role in the pathophysiology and experimental therapy of type-2 diabetes. Front Immunol. 2019;10:571.

212. Ohnishi M, Tokuda M, Masaki T, Fujimura T, Tai Y, Itano T, et al. Involvement of annexin-i in glucose-induced insulin secretion in rat pancreatic islets. Endocrinology. 1995;136(6):2421-6.

213. Kang Nn, Won JH, Park YM. Annexin i stimulates insulin secretion through regulation of cytoskeleton and pkc activity. Anim Cells Syst. 2010;13(1):17-23.

214. Won JH, Kang NN, Auh CK, Park YM. The surface receptor is involved in annexin i-stimulated insulin secretion in min6n8a cells. Biochem Biophys Res Commun. 2003;307(2):389-94.

215. Hong SH, Won JH, Yoo SA, Auh CK, Park YM. Effect of annexin i on insulin secretion through surface binding sites in rat pancreatic islets. FEBS Lett. 2002;532(1-2):17-20.

216. Rackham CL, Vargas AE, Hawkes RG, Amisten S, Persaud SJ, Austin AL, et al. Annexin a1 is a key modulator of mesenchymal stromal cell-mediated improvements in islet function. Diabetes. 2016;65(1):129-39.

217. Moreli JB, Santos MRD, Calderon IMP, Hebeda CB, Farsky SHP, Bevilacqua E, et al. The role of annexin a1 in DNA damage response in placental cells: Impact on gestational diabetes mellitus. Int J Mol Sci. 2023;24(12).

218. Anbalagan D, Yap G, Yuan Y, Pandey VK, Lau WH, Arora S, et al. Annexin-a1 regulates microrna-26b* and microrna-562 to directly target nf-kappab and angiogenesis in breast cancer cells. PLoS One. 2014;9(12):e114507.

219. Gu ZY, Miao XY, Ma LC, Gao JJ, Gong YP, Li CL. Maintenance of cellular annexin a1 level is essential for pi3k/akt/mtor-mediated proliferation of pancreatic beta cells. J Biol Regul Homeost Agents. 2021;35(3):1011-9.

220. Melkman-Zehavi T, Oren R, Kredo-Russo S, Shapira T, Mandelbaum AD, Rivkin N, et al. Mirnas control insulin content in pancreatic beta-cells via downregulation of transcriptional repressors. EMBO J. 2011;30(5):835-45.

221. VanGuilder HD, Vrana KE, Freeman WM. Twenty-five years of quantitative pcr for gene expression analysis. Biotechniques. 2008;44(5):619-26.

222. Pennock ND, Jindal S, Horton W, Sun D, Narasimhan J, Carbone L, et al. Rna-seq from archival ffpe breast cancer samples: Molecular pathway fidelity and novel discovery. BMC Med Genomics. 2019;12(1):195.

223. Bennett HM, Stephenson W, Rose CM, Darmanis S. Single-cell proteomics enabled by next-generation sequencing or mass spectrometry. Nat Methods. 2023;20(3):363-74.

224. Ma Z, Sun Y, Yu Y, Xiao W, Xiao Z, Zhong T, et al. Extracellular vesicles containing mfge8 from colorectal cancer facilitate macrophage efferocytosis. Cell Commun Signal. 2024;22(1):295.